ETUDE DES REACTIONS COMPLEXES EN PHASE SOLIDE POUR LE STOCKAGE D'HYDROGENE

Abdelouahab El Kharbachi

UNIVERSITÉ DE GRENOBLE

THÈSE

Pour obtenir le grade de

DOCTEUR DE L'UNIVERSITÉ DE GRENOBLE

Spécialité : **Matériaux, Mécanique, Génie civil, Electrochimie**

Arrêté ministériel : 7 août 2006

Présentée par

Abdelouahab EL KHARBACHI

Thèse dirigée par **« Alain Reza YAVARI »** et
codirigée par **« Ioana NUTA »**

préparée au sein du **Laboratoire de Science et Ingénierie des Matériaux et Procédés**
dans **l'École Doctorale « Ingénierie - Matériaux, Mécanique, Environnement, Energétique, Procédés, Production »**

ETUDE DES REACTIONS COMPLEXES EN PHASE SOLIDE POUR LE STOCKAGE D'HYDROGENE

Thèse soutenue publiquement le **« 25 mars 2011 »**,
devant le jury composé de :

M. Michel PONS	
Directeur de recherche, SIMaP/CNRS-Grenoble	Président
M. Marcello BARICCO	
Professeur, Université de Turin (Italie)	Rapporteur
M. Jean-Claude TEDENAC	
Professeur, Université de Montpellier II	Rapporteur
M. Olivier DEZELLUS	
Maître de conférences, Université Claude Bernard Lyon I	Examinateur
M. Christian CHATILLON	
Directeur de recherche, SIMaP/CNRS-Grenoble	Invité

I would like to express my gratitude to my supervisor Mr Alain Yavari for allowing me this chance to make a Ph.D thesis within the SIMaP Laboratory in parallel to the COSY-European Project contract.

I thank Ms Ioana Nuta for accepting to take the responsibility of co-supervisor of the thesis and for technical and moral support, and for the latitude allowed to experiment and develop personal approaches.

I am ever so grateful to Mr Christian Chatillon for the time spent reading and discussing my work, and for giving me fruitful input. His guidance has prepared me well for the challenges that lie ahead. Thanks very much.

Especial acknowledgments are directed to Mr Marcello Baricco for receiving me in his laboratory for initiating on using Thermo-Calc software during the exchange visit at the University of Torino. I could also benefit from constructive and helpful discussions together with Eugenio and Daphiny all along my presence in his Lab.

The members of the TOP group, both past and present, are also given thanks for their insights on various issues as well as for their friendship. I would like to express special thanks to Perrine for here precious help regarding computing and to Laurent, Hervé and Alain LeMoulec for technical support and discussions and for friend, whose constructive discussions and kindness helped me all along my work.

I give all my local (Fabrice, Fatima-Zahra, Denis, Moustafa, Kostas, Ayoub, Jia, Melany, Viviana, Thuy, Nourhane, Magalie, ..) and abroad colleagues of the COSY Project (Sebastiano, Emilie, Carine, Christian, Claudio, Francesco, Daphiny, Christopher and Marta) a big thank-you for their encouragement and close collaboration.

Lastly, I wish to express my affectionate thankfulness to my parents and my wife for their love, understanding and constant support.

To Soumaya and .. company !

Table of contents

RESUME DE LA THESE

INTRODUCTION

Le réchauffement global et le changement climatique mondial avec des conséquences non prévisibles imposent aux politiques nationales et intergouvernementales, des réductions obligatoires des émissions de gaz polluants issues des milieux industriels et de l'activité de transport. Cela suppose que les énergies classiques doivent être remplacées par des énergies alternatives. Une partie de l'obligation de l'humanité est d'alléger les conséquences écologiques et d'acquérir de nouvelles connaissances scientifiques et technologiques pour la mise en place d'une base de notre économie future. L'un des scénarios futurs prometteur est l'économie de l'hydrogène. D'un point de vue de concept de l'énergie propre, l'hydrogène est un moyen idéal pour le stockage de l'énergie, son transport et sa conversion. Sa combustion génère de l'eau et il est donc un système non polluant qui peut être appliqué dans l'avenir pour des véhicules dit à « zéro émission». H_2 est abondant et peut être produit dans une variété de sources d'énergie conventionnelles et renouvelables. Les raisons pour lesquelles, il y a maintenant un large accord que l'hydrogène jouera un rôle clé dans la politique énergétique réelle de l'Union Européen. Cependant, le stockage de l'hydrogène est encore un grand défit.

Le point d'ébullition très faible de l'hydrogène liquide, environ -250℃, rend son stockage sous forme liquide inefficace et très coûteux vu qu'il nécessite un système de réfrigération en continu. Sa faible densité à l'état gazeux peut requérir un stockage dans des compresseurs à haute pression, mais avec des inconvénients d'ordre sécuritaire et liés à son stockage dans les applications mobiles.

Une des solutions sans danger pour le transport et le stockage de l'hydrogène est le stockage sous forme d'hydrure. Parmi les systèmes en discussion, l'hydrogène absorbé sous forme d'hydrures métalliques (à base de métaux de transition ou encore d'hydrures complexe) est une idée prometteuse. Ces hydrures complexes de poids léger ont une capacité gravimétrique de stockage élevée. Par exemple, la décomposition partielle du $LiBH_4$ en donnant du $LiH + B + 1.5H_2$ pourrait engendrer 13,6 % d'hydrogène en masse. Néanmoins, l'utilisation des hydrures complexes pour le stockage de l'hydrogène est difficile à cause des limitations cinétiques et thermodynamiques. Une forte amélioration cinétique est possible en présence de catalyseurs convenables. Le second problème est la chaleur libérée durant la formation de l'hydrure où l'enthalpie de la réaction est d'environ -67 $kJ.mol^{-1}$ H_2 et par consé-

quent, si réversible, une pression de 1 bar obligerait une température > 400℃. La température élevée de désorption porte deux problèmes : (i) la perte de l'énergie pendant la désorption réduit l'efficacité du processus de stockage totale. (ii) la même quantité d'énergie est libérée sous forme de chaleur au cours de l'absorption, ce qui provoque d'énormes problèmes techniques pendant le remplissage du réservoir (environ 1 MW thermique doit être dissipée dans une cuve typique de la voiture).

Les problèmes mentionnés sont typiques aux hydrures complexes et démontrent clairement la nécessité de trouver des matériaux avec des propriétés thermodynamiques convenables aux besoins techniques. L'Union Européen est conscient de l'importance de cette recherche et, par conséquent, a soutenu le projet : «*Complex Solid State Reactions for Energy Efficient Hydrogen Storage*» (COSY). Le principal objectif de ce réseau est de parvenir à une compréhension fondamentale des processus de sorption de composites d'hydrures et des systèmes connexes au moyen de différentes stratégies.

Ce travail dans le cadre du projet COSY est centré sur l'étude du système composite MgH_2-$LiBH_4$. Dans cette thèse seront présenté, d'abord la caractérisation microstructurale et thermique des phases, ensuite une étude thermodynamique du système Mg-B-H-Li. Chaque point soulevé sera approfondie dans la poursuite du manuscrit qui se compose de six chapitres. Leur contenu respectif est résumé ci-dessous.

Le chapitre 1 présente la partie bibliographie du système d'hydrures à étudier. Il donne un rapport progressif sur la caractérisation des matériaux impliqués, leurs propriétés structurales et thermodynamiques. Les mécanismes des réactions de sorption sont également abordés avec des spécificités liées à l'utilisation de catalyseurs. Le chapitre 2 décrit les techniques expérimentales et méthodes utilisées au cours de ce travail de thèse en mettant l'accent sur les techniques thermiques et de spectrométrie de masse. Dans le chapitre 3 nous présentons comment le système d'hydrures a été approché par traitement mécanique (broyage à bille de haute énergie) et analyse thermique à des compositions variables. Les caractéristiques microstructurales et stabilité des phases en fonction de la température ont été également abordés pour d'avantage d'informations. Le chapitre 4 rapporte des mesures de capacité calorifique et une évaluation critique de la thermodynamique du composé $LiBH_4$. Une étude rigoureuse de la stabilité des réactions de décomposition dans le système Li-B-H est regroupé sous le chapitre 5 où la spectrométrie de masse, en parallèle avec la méthode d'effusion de Knudsen, sont utilisé pour étudier la décomposition du composé $LiBH_4$. Le chapitre 6 est consacrée au nouveau projet dédié aux hydrures concernant la construction d'un réacteur mécano-chimique couplé à un spectromètre de masse par le biais d'un tube

capillaire. Tout d'abord, il sera présenté un calcul détaillé des écoulements gazeux essentiel pour la conception de l'ensemble de l'instrumentation et de la faisabilité de la connexion entre les deux dispositifs (réacteur-broyeur et une cellule d'effusion d'un spectromètre de masse). Une conclusion générale est présentée comme dernier chapitre de ce manuscrit. Enfin, les références et les annexes contenant des compléments sont données à la fin de chaque chapitre.

Proprement à cette partie «RESUME DE LA THESE », un résumé de chaque chapitre de la thèse est poursuivi ci-après en clôturant à la fin par une conclusion générale.

1 CARACTERISATION MICROSTRUCTURALE DES COMPOSES D'HYDRURES

Dans le but d'étudier le comportement de désorption d'hydrogène à partir du système d'hydrure complexe MgH_2-$xLiBH_4$ ($0 < x < 3,5$) des expériences préliminaires ont été effectué d'abord avec MgH_2 seul ensuite avec des ajouts progressifs de $LiBH_4$, composé de grande capacité gravimétrique d'absorption d'hydrogène. Dans cette partie, nous étudions l'interaction thermique entre les deux hydrures dans un domaine de températures allant jusqu'à 500℃. Cette étude va nous permettre de faire le ch oix du rapport stœchiométrique appropriés pour réaliser un composite de mélange de ces deux hydrures possédant des propriétés réactionnelles les plus favorables. L'ajout de certains additifs pour but catalytique sera également présenté.

1.1 Réactivation des composites MgH_2-$xLiBH_4$

Le composite MgH_2-$xLiBH_4$ avec $x = 2$ est prévue dans la littérature d'être la composition la plus favorable au cours d'un processus d'échange d'hydrogène. Des expériences ont été faites en préparant des quantités de mélanges dans différents rapports $x = \{0,5 ; 1 ; 2 ; 2,5\}$. Les deux composés sont pré-broyés auparavant par broyage à bille de haute énergie, ensuite les deux poudres sont mélangés manuellement en boîte à gants jusqu'à ce qu'un mélange homogène est obtenu avant de recommencer le broyage pendant 24 heures. Les composites formés seront ainsi étudiés par analyse thermique à différentes températures par ATD/ATG ou DSC. La diffraction des rayons X a aussi été utilisée pour l'identification des phases à différents stade de traitement thermique.

1.1.1 MgH_2 : $xLiBH_4$ ($x = 2$)

La courbe de DSC de l'échantillon préparé est illustrée dans la figure 1 qui montre les différentes transformations qui se déroulent au cours du chauffage. L'analyse calorimétrique révèle quatre événements thermiques distincts. Les deux premiers correspondent respectivement à la transition de phase et à la fusion de $LiBH_4$. Les événements suivants sont la désorption complète d'hydrogène du composite, premièrement du MgH_2 puis du $LiBH_4$.

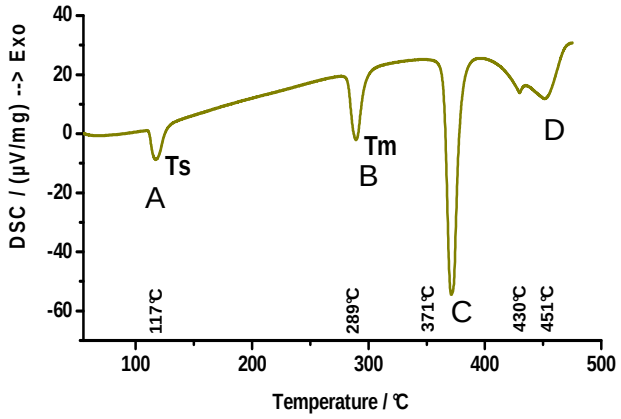

Figure 1. Courbe de DSC du composite MgH_2-$2LiBH_4$ (sous argon 100 ml.min^{-1}, chauffe 5 K.min^{-1})

La réaction de désorption de $LiBH_4$ suivi de la formation de MgB_2 se produit en deux étapes selon les réactions suivantes :

$$2LiBH_4 \rightarrow 2LiH + B_2H_6 \rightarrow 2LiH + 2B + 3H_2 \quad (1)$$

$$Mg + 2B \rightarrow MgB_2 \quad (2)$$

où la réaction totale, la plus favorable thermodynamiquement est [1,2]:

$$2LiBH_4+MgH_2 \rightarrow MgB_2+2LiH+4H_2 \quad (3)$$

Il a été rapporté dans la littérature que le bore amorphe est formé durant la décomposition de $LiBH_4$ et la recombinaison de LiH avec B se fait selon une cinétique très faible [3]. La présence de Mg s'est avérée avantageux pour la décomposition de $LiBH_4$ à basse température. La formation de MgB_2 conserve une présence de B disponible pour la réaction d'hydrogénation. Ces auteurs ont également constaté que les échantillons déshydrogénés sous He donne lieu seulement à Mg, LiH et du bore probablement amorphe [3]. Par contre la formation de MgB_2 a été observée sous une atmosphère de H_2. Peut-être que cela est due aux propriétés réductrices de l'hydrogène. La présence d'oxygène pourrait également restreindre les réactions qui se produisent dans des conditions normales. Compte tenu de l'importance de la formation de MgB_2 en diminuant l'enthalpie de la réaction de désorption, nous avons cherché davantage la présence de cette phase. Les autres espèces probables qui pourraient se former en présence de traces d'humidité et d'oxygène seront également considérées. Il s'agit d'entités d'oxydes et hydroxydes tel que MgO, B_2O_3 et LiOH qui puissent coexister dans la matrice.

Sans additifs

Nous avons comparé nos échantillons avec ceux reçues du partenaire du projet GKSS- Research Center, en utilisant l'analyse DRX, MEB et DSC car les préparations des poudres ne sont pas tout à fait similaires. Après analyse en DSC et MEB, nous avons observé l'importance du pré-broyage des composés seule avant d'être mélanger.

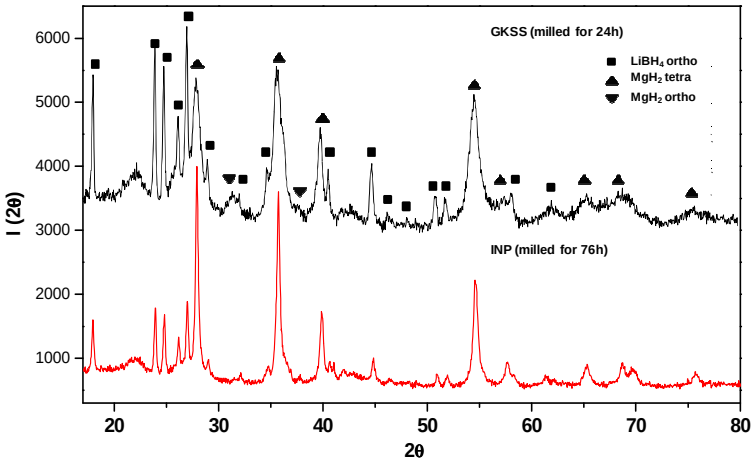

Figure 2. DRX d'échantillon reçu de GKSS comparé à le nôtre préparé au SIMaP

Les pics de Bragg (Fig.2) montrent la présence des phases de départ avant broyage pour les deux échantillons. Une différence au niveau de la largeur des pics est observée. Il semble que la procédure de préparation pourrait affecter la taille des grains des poudres qui en résultent par effet du broyage. En fait, en utilisant la formule de Scherrer, l'échantillon de GKSS présente des cristallites plus fines au sujet de MgH_2 et moins fine vis-à-vis de $LiBH_4$. Ce résultat est en accord avec la procédure de préparation des poudres de GKSS ayant utilisé $LiBH_4$ sans pré-broyage. Les analyses de DSC des deux poudres sont illustrées dans la figure 3.

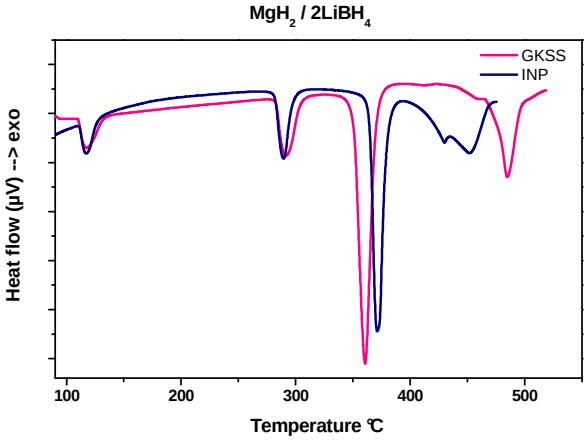

Figure 3. Analyse de DSC des deux échantillons

Comme seulement MgH_2 est pré-broyé pour les échantillons provenant de GKSS, nous avons observé à l'aide de la DSC des comportements thermiques différents pour les deux poudres avec des décalages en température. Par conséquent, le pré-broyage de $LiBH_4$ permet une diminution considérable de la température de désorption qui est d'environ 40℃. Il est clair que la méthode de préparation influence les températures opérationnelles de désorption de ces hydrures.

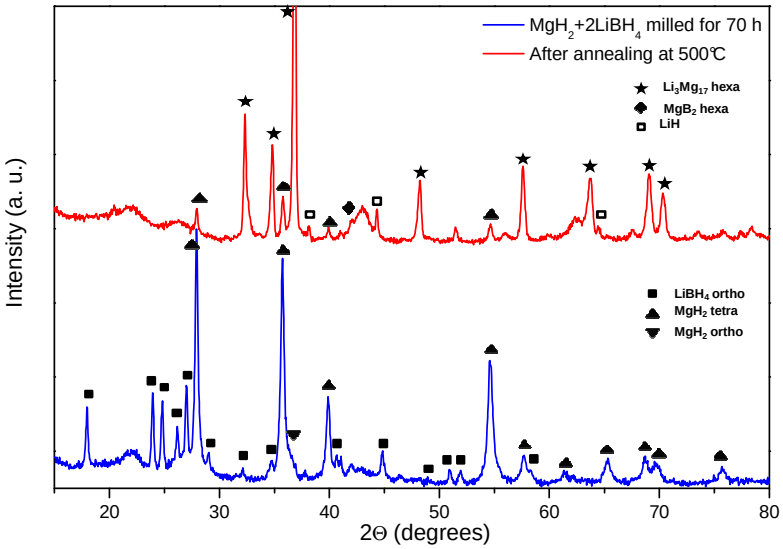

Figure 4. DRX du composite, avant et après traitement thermique à 500℃

Après un traitement thermique à 500℃ (Fig.4), le c omposite d'hydrures est totalement déhydruré. Mg et B se combinent pour former le composé MgB_2. Le seul hydrure encore présent à cette température élevée est LiH provenant de la décomposition consécutive du $LiBH_4$.

Néanmoins, la formation de l'alliage Li_3Mg_{17}, à une telle composition est liée à la présence de Li élémentaire, mais probablement à faible teneur. Comme une quantité conséquente de Mg s'allie à Li pour former Li_3Mg_{17}, dans ce cas l'échantillon résiduel doit contenir des quantités non négligeables de bore pur. Comme il n'y a aucune signature de ce dernier par DRX, le bore est peut être présent sous forme amorphe. A moins que certaines quantités disparaissent en espèces gazeuses B_2H_6 ou BH_3, sachant que la thermodynamique fournit de très basses pressions pour ces espèces.

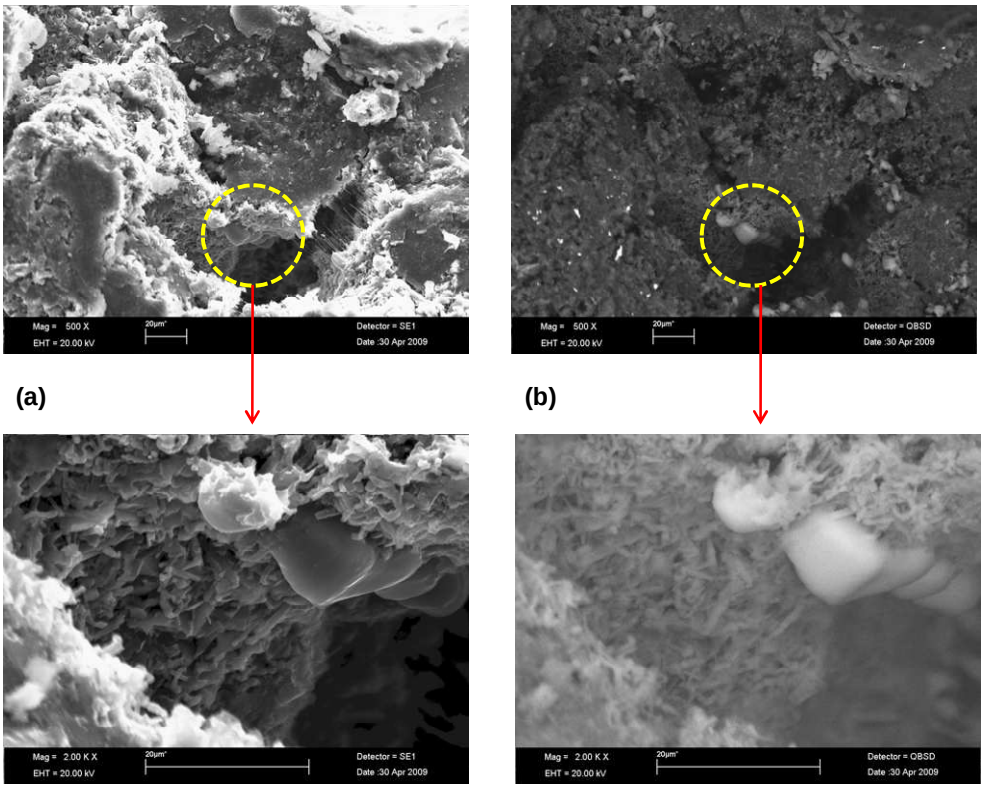

Figure 5. Images du MEB du composite après traitement thermique à 500℃ dans le DSC en mode: (a) SE et (b) BSE (Mag. x500 and x2.10^3)

Pour plus d'informations, l'échantillon chauffé à 500℃ dans le DSC est également observé par MEB (Fig.5). En analysant les images, un échantillon solide a été obtenu après chauffage et présente différentes morphologies. Des fissures et germes peuvent être observés résultant de phénomènes de nucléation. L'analyse EDAX prouve que ces germes formés sont riches en Mg et contiennent des quantités de bore. De notre côté, nous pensons que les germes correspondent à la croissance de grains de MgB_2 au cours du chauffage. Il convient de mentionner que des aspects de relaxation-décontraction en raison du refroidissement

sont observés par le microscope électronique. Ce qui est due à la solidification du matériau après la formation du composé fondu, ayant probablement une densité plus faible.

Avec additifs

Nous avons aussi étudié le composite en y ajoutant des additifs pour la catalyse des réactions. En général, le choix de ces matériaux est basé sur des données existantes relatives à leur affinité vis-à-vis de l'hydrogène pour induire des conversions réactionnelles ainsi que leur régénération pendant le traitement thermique (les cycles de déchargement). Plusieurs additifs ont été testés, mais seulement ceux à base de Ti, Ni et C, ont provoqué un effet cinétique positif.

Isopropoxyde de titane (Tiso)

Cet additif a été proposé par l'équipe de GKSS. Ils ont constaté qu'une amélioration de la cinétique et une diminution de la température de travail ont été obtenus lorsque l'isopropoxyde de titane (Tiso), comparable à VCl_3 , a été ajouté comme catalyseurs à ce système d'hydrures [2]. Nous avons également testé dans notre laboratoire l'effet de cet additif sur le composite. Faisant ainsi, nous pensons que cela pourrait clarifier les points suivants :

- confirmer la méthode de préparation de nos échantillons, étant donné que l'ajout de cet additif doit interagir de la même façon au moins en ce qui concerne l'aspect rhéologique et chimique
- vérifier l'effet catalytique de l'additif
- et si ce dernier point est vérifié, rechercher à comprendre le mécanisme d'intervention de cet additif.

L'isopropoxyde de titane (10 mol.%) qui est liquide à la température ambiante est ajouté aux composites puis broyé pendant 24 h. Après broyage, la poudre observée a un aspect sec ce qui suppose une décomposition de l'additif au cours du broyage. Par addition de Tiso aux deux poudres (nôtre et reçu de GKSS), des comportements thermiques comparables ont été obtenus (Fig.4). Les isothermes identifiées montrent une bonne concordance entre les deux poudres. La désorption de MgH_2 est plus proche de l'événement de fusion de $LiBH_4$ dans le cas de la poudre GKSS. Ce qui est en accord avec les courbes de DSC observées

pour les poudres sans additifs dans la figure 3. Deux événements exothermiques consécutifs sont également identifiés dans les deux cas.

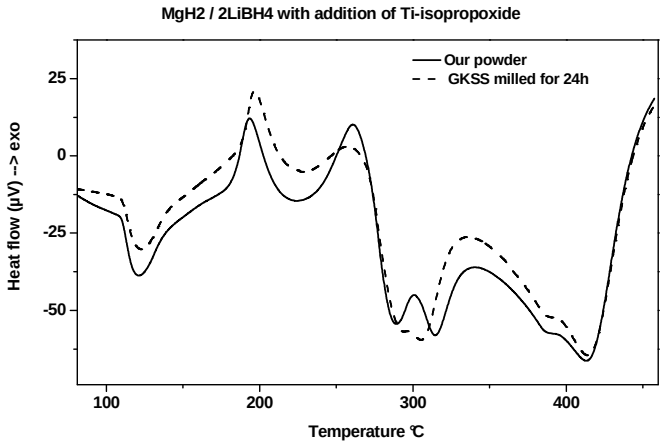

Figure 6. DSC du composite MgH_2-$2LiBH_4$ avec ajout de Tiso (sous flux Ar, 10 $K.min^{-1}$)

En examinant le spectre de masse de Tiso chauffé à 180 °C, il montre la présence de plusieurs fragments (hydrocarbures) possibles avec ou sans titane [4]. Pour le moment, on n'est pas capable d'expliquer les transformations impliquées dans ces événements. Probablement à de telle température de chauffage, Tiso agit dans la poudre sous forme d'oxyde et le reste des hydrocarbures s'évaporent avec un résidu carboné. Par conséquent, ce catalyseur agit peut être par deux composantes distinctes. Comme les métaux de transition ont montré une amélioration de la cinétique de sorption des hydrures, l'introduction de Ti a un effet considérable, probablement rehaussé par la présence de composés carbonés. En outre, le résultat de désorption d'hydrogène du composite en présence de Tiso est comparable à celui des nanotubes de carbone [5].

A partir de l'étude bibliographique, le rôle des métaux de transition est de faciliter la rupture de la liaison H-H ainsi que la chimisorption de la molécule d'hydrogène. En plus de son avantage thermique, le rôle du carbone est probablement d'améliorer la dispersion des éléments en évitant des aspects de frittage massif du matériau. En effet, des phénomènes de nucléation et de croissance sont observés plus clairement pour le composite sans additifs.

2 THERMODYNAMIQUE DU COMPOSE $LiBH_4$

Ce chapitre rapporte la capacité calorifique C_p au-dessus de la température ambiante du composé $LiBH_4$, contenant moins de 0,02 fraction massique d'impuretés. Le présent travail propose une nouvelle expression analytique de la capacité calorifique sélectionnée pour les différentes phases condensées (orthorhombique, hexagonale et liquide) à partir de nos propres mesures supplémentaires [6]. Les mesures ont été réalisées avec un appareil de DSC par deux méthodes de programmation de température: par rampe linéaire et méthode enthalpique (Fig.7). Une nette amélioration a été apportée pour la phase hexagonale dans l'intervalle de température court de son existence de 386.6 K jusqu'à la fusion du composé à 553 K. L'anomalie observée avant la transition de phase polymorphique à 386.6 K a été discutée et attribuée à une tendance « anormale » indépendante de la transition principale : cette tendance est probablement due à l'existence d'un domaine d'hypo-stœchiométrie suite à l'augmentation de défauts dans le réseau cristallin pour le composé $LiBH_4$ (réseau non-cubique). Nos résultats conduisent à modifier les incréments d'enthalpie retenus précédemment et ceci par la méthode d'intégration ainsi que la température de début de la transition. Par conséquent, une nouvelle enthalpie pour la transition polymorphique est proposée (5069 ± 76 $J \cdot mol^{-1}$) avec une température de transition de 386.6 ± 1 K.

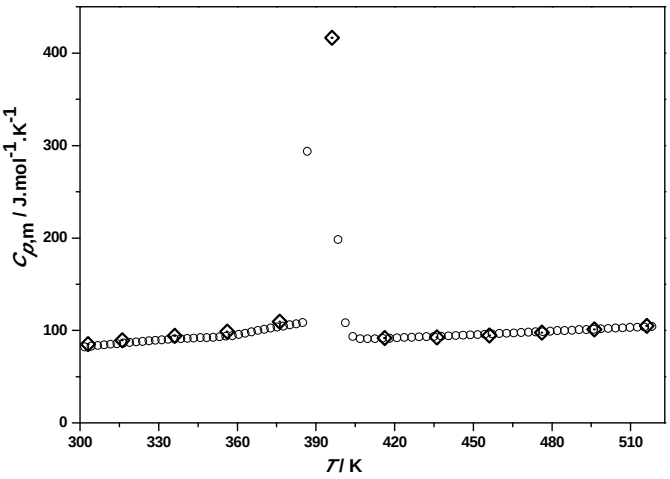

Figure 7. Capacité calorifique expérimentale à haute température du composé $LiBH_4$: ◦, rampe linéaire et ◇, méthode enthalpique.

Après les mesures de C_p, une évaluation critique des propriétés thermodynamiques du composé $LiBH_4$ a été réalisée en tenant compte de toutes les données disponibles dans la littérature. Ce travail peut constituer un bon complément de données des tables thermochimiques

NIST-JANAF pour $LiBH_4$ qui n'ont pas été revu depuis décembre 1964, sachant que leur capacité calorifique au-dessus de l'ambiante était estimée à ce moment-là par analogie avec $NaBH_4$ solide. Le présent travail propose une sélection d'un nouvel ensemble de données pour les différentes phases condensées (orthorhombiques, hexagonales et liquides). Des compilations de littérature de différentes valeurs d'enthalpies de formation du composé provenant seulement d'un travail original unique ont été également examinées. Enfin, nous présentons une fonction de Gibbs des phases avec ajout, à une base de données SGTE, des phases hexagonale et liquide observés jusqu'à la décomposition du composé autour de 756 K [7]. Cette fonction communément appelée *GHSER* prend la forme analytique suivante selon l'approche CALPHAD :

$$GHSER(T) = \mathrm{A} + \mathrm{B}T + \mathrm{C}T\,lnT + \mathrm{D}T^{2} + \mathrm{E}T^{3} + \mathrm{F}T^{-1}$$

Les nouvelles fonctions thermodynamiques ajoutées vont fournir de nouveaux aperçus sur la modélisation des réactions impliquant la désorption et la chimisorption de l'hydrogène à partir de composites à base de $LiBH_4$, matériaux prometteur pour le stockage de l'hydrogène.

3 STABILITE DES PHASES ET REACTIONS DE DECOMPOSITION

3.1 TRIPHASE $LiBH_4$-LiH-B

Dans un diagramme de phase, la principale particularité des hydrures consiste à se déplacer dans leurs compositions par évolution suite à une perte d'hydrogène. Avec ces transformations, nouvelles phases pourraient apparaître. Pour comprendre les produits résultants de l'absorption ou désorption d'hydrogène dans le cas du composé $LiBH_4$, nous examinons le diagramme de phase ternaire Li-B-H, au moins pour des compositions proches de la phase $LiBH_4$ ou des phases en équilibre avec ce composé. La figure ci-dessous (Fig.8) montre le diagramme de phase du système ternaire à la température ambiante comprenant des composés hypothétiques $LiBH_{4-x}$ (0<x<4). L'existence du composé "$LiBH_2$" boryle de lithium est en cours de discussion dans la littérature [8,9].

.

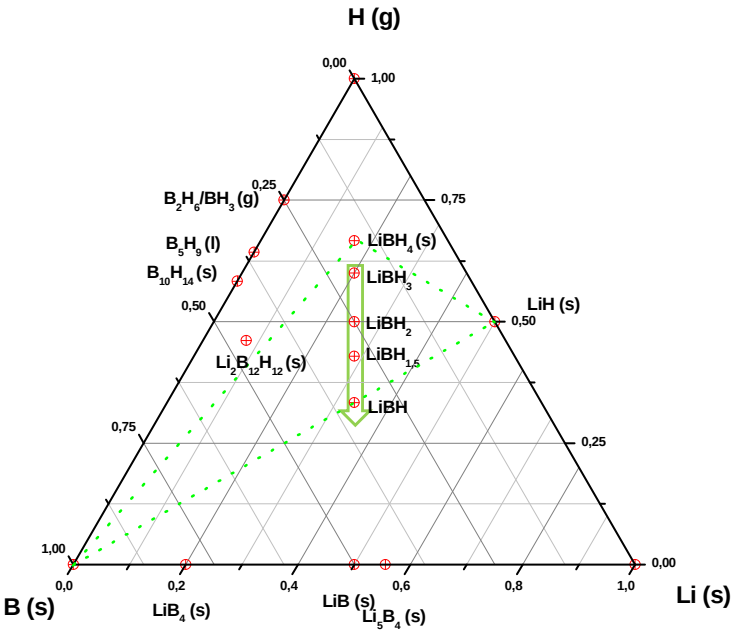

Figure 8. Diagramme de phase du system Li-B-H incluant les composés hypothétiques $LiBH_{4-\varepsilon}$

Cette partie vise à étudier les différentes réactions au cours de la décomposition du $LiBH_4$. D'autre part, nous présentons quelques expériences liées à la stabilité du système Li-B-H dans le triangle triphasique $LiBH_4$-LiH-B. Le composé $LiBH_{4-\varepsilon}$ hypo-stoechiométrique analysé par diffraction est aussi discuté dans cette partie, lorsque des échantillons « purs » de $LiBH_4$ seul sont recuits en ampoule scellée. Une analyse qualitative par spectrométrie de masse est également entreprise pour l'identification des différentes espèces qui peuvent exister en

phase gazeuse. En parallèle, la méthode d'effusion de Knudsen a été utilisée pour quantifier la pression de vapeur totale.

Cinq échantillons ont été traités thermiquement au-dessous et au-dessus de la température de fusion de $LiBH_4$. Deux séries d'échantillons ont été préparés. La première série a été chauffée à 250±2,5℃ pendant 4 heures. À cette temp érature aucune fusion n'a été observée visuellement. Pour ces échantillons un dégagement gazeux léger du mélange solide a été observé à la rupture des ampoules en boîte à gants. La figure suivante montre la DRX de l'un des échantillons (Ech. 1) du triphasé. L'échantillon après broyage présente toutes les phases de départ sans modification. Après chauffage dans une ampoule en quartz scellée, les pics de DRX restent presque inchangés. Seulement une légère modification dans les intensités relatives des phases est observée (fig.9).

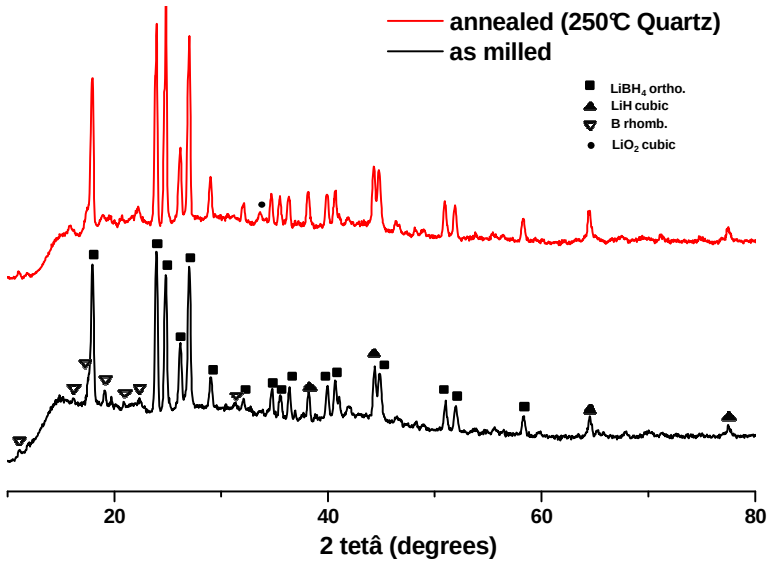

Figure 9. DRX de l'éch.1 avant et après recuit

Pour cette première série, il a été remarqué que les pics de $LiBH_4$ subissent un déplacement selon l'axe 2 thêta. Des observations similaires ont été remarquées pour les autres échantillons à cette température. En outre, l'échantillon riche en B montre une diminution de l'intensité relative de bore. Ceci peut être dû à une transformation vers le bore amorphe pendant le chauffage. A partir de cette analyse, nous pouvions conclure que le $LiBH_4$–LiH–B pseudo-ternaire est stable dans le domaine de température inférieure à la température de fusion de $LiBH_4$.

Dans la deuxième série, les échantillons sont chauffés jusqu'à 300±5℃. Tous les échantillons, sauf éch.5 (riche en Li), ont montré une réactivité avec le tube de quartz révélé par

l'attaque du verre et par la présence du composé Li_3BO_3 notamment pour l'échantillon riche en B (éch.4). Après fusion, les échantillons ont formé une couche protectrice sombre qui a empêché la fusion de la totalité de la poudre. L'échantillon riche en Li (éch.5) n'a pas fondu à cette température, mais il a formé une sorte de produit fritté.

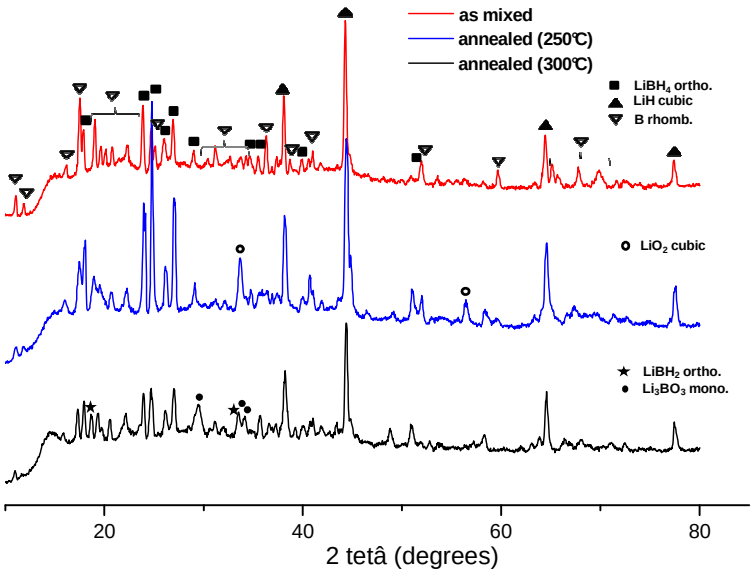

Figure 10. DRX de l'éch.3 avant et après recuit à 250 et 300℃

L'éch.3 analysé par DRX (Fig.10) montre la disparition de certains pics du B tel que mentionné pour la première série. Pour l'échantillon chauffé à 300℃, la présence de $LiBH_2$ dans l'échantillon est probable où deux pics de Bragg sont indexés pour ce composé. Les intensités des pics de $LiBH_4$ sont également affectées à cette température. L'étude thermique des échantillons « purs » de $LiBH_4$ à 270±2,5℃ (juste au-dessous de la température de fusion) pendant 3 jours, ne montrent aucune présence de nouvelle phase, bien qu'un déplacement des pics soit observé. Pour un tel traitement, ce changement peut être attribué à une hypostœchiométrie du composé tel que supposé dans la littérature [10]. Comme il est indiqué pour le triphasé, la présence de $LiBH_2$ est également probable pour cet échantillon. Dans une autre étape, $LiBH_4$ liquide a été étudié sous vide statique. Ce sujet sera abordé dans la partie de mesures de pression totale. Dans ce cas, une composition nominale $LiBH_{3,96}$ a été calculée en accord avec le déplacement des pics de diffraction mais dans ce cas sans aucune signature de la phase $LiBH_2$.

3.2 MESURES DE PRESSION DE VAPEUR DE $LiBH_4$

3.2.1 Spectrométrie de masse

Onze expériences d'évaporation de $LiBH_4$ ont été réalisées. Dans chaque expérience, la cellule a été chargée avec une nouvelle poudre de $LiBH_4$. Les intensités ioniques mesurées sont indiquées dans le tableau 1. Pour faciliter le travail de l'attribution des masses détectées par spectrométrie de masse, une liste des masses de toutes les espèces probables et leurs isotopes pour le système Li-B-H avec les probabilités correspondantes a été réalisé avant expérience. L'oxygène est également considéré dans les combinaisons théoriques possibles des éléments du système de base. L'espèce H_2 a été détecté avec de très faibles intensités ioniques ($pH_2 < 10^{-7}$ bar) et qui augmentent avec la température.

Tableau 1. Analyse par spectrométrie de masse de $LiBH_4$ à des températures variables (156, 185 et 205℃). Les intensités ioniques sont rapportées à l'intensité relative de H_2.

Espèce	Masse (u.a.)	I/I(H_2) vs. T/℃		
		156	185	205
H	0.95	11.4	1.02	0.1
BH_3	13.9	--	--	0.14
?	19	--	--	0.1
?	25.7	0.05	0.1	--
B_2H_5	26.7	0.03	0.1	--
?	28.9	0.39	--	--
?	29.7	--	0.22	--
?	39.7	0.51	0.66	--
$Li_2B_2H_8$?	43.9	0.74	1.56	0.14

L'espèce BH_3 est observée seulement pour l'échantillon broyé et chauffé à 205℃ en utilisant le mode obturateur du spectromètre de masse. Selon la thermodynamique, le dimère B_2H_6 est plus stable que l'espèce BH_3, mais sa présence est difficile à confirmer en raison de la présence abondante de N_2 qui a presque la même masse, espèce constamment présente dans l'atmosphère du spectromètre. À première vue, l'espèce BH_3 observée est en accord avec les mesures de spectrométrie de masse rapporté par Mitrofanova et al.[11] dans le do-

maine de température 110-200℃. Dans le domaine de température de 25-450℃, l'espèce B_2H_6 est toujours observée avec une décomposition à partir de 220℃ en faveur des fragments : BH_2, BH_3 et BH_4. Néanmoins, la méthode de ces auteurs pour la détermination des intensités par soustraction du fond sans obturateur reste douteuse. En outre, une attribution erronée a été signalée dans leurs travaux antérieurs pour l'espèce BH_7 (M = 18 u.a.) alors qu'il s'agissait de la molécule d'eau [12], molécule abondamment présente dans le fond résiduel (vide).

L'espèce B_2H_6 disparaît en même temps qu'une précipitation de Li (s,l) selon les calculs thermodynamiques. La présence de B_2H_6 a été prouvé par le fait que les masses 26.7 et 25.7 u.a. sont, raisonnablement, en accord avec la distribution isotopique de B_2H_5.

B_2H_5 est probablement le résultat d'un processus d'ionisation dissociative, B_2H_6 (g) + e^- → $B_2H_5^+$ + H + 2e^-.

3.2.2 Méthode d'évaporation de type Knudsen

Durant les mesures de spectrométrie de masse aucune perte de masse n'a été enregistré dans la gamme de température 100-205℃. Dans cette partie, seule la méthode Knudsen a été effectuée à l'aide d'une cellule simple (conventionnelle) pour la quantification de la perte de masse à des températures au-delà de 200℃. Après le chargement de l'échantillon, la cellule a été scellée avec de la paraffine pour l'étanchéité (orifice et bords) et ensuite placer sous vide dans un réacteur équipé d'un four de haute température. Pour $LiBH_4$ solide, trois expériences ont été effectués à des températures inférieures au point de fusion : 223, 245 et 255℃. La pression de vapeur approximative à 185℃, déduite de l'expérience précédente pour le composé non broyé, est également ajoutée au diagramme log *p* vs. 1/T dans la figure 12. La pression de vapeur tel que mentionné au début de ce chapitre est due à l'espèce majoritaire H_2 issue de la décomposition par évaporation de $LiBH_4$. L'évaporation de la phase liquide sous vide n'a pas réussie. En effet, le liquide avait subit une effervescence/débordement spontanée à la fusion qui a causé sa dispersion tout autour du four-réacteur. Après refroidissement seulement quelques quantités de $LiBH_4$ sont encore présentes dans le creuset.

Afin d'éviter ce phénomène de débordement de la cellule qui pourra endommager le réacteur, nous avons fondu le composé dans un creuset en Pt inséré dans une ampoule de verre. La cellule est chargée soigneusement en boîte à gants, et ensuite scellée sous vide. L'ampoule est placée dans un lit d'alumine (conteneur + poudre) et maintenue verticalement

afin d'assurer une température homogène (Fig.11). L'ensemble (creuset, ampoule et bain d'alumine) est introduit dans le four avec une rampe de chauffe de 0,4 °C/min, suivie d'un isotherme à 290℃ pendant 4 heures. Après avoir tre mpée l'ampoule dans l'azote liquide pour figer l'échantillon, le creuset est pesé en boîte à gants et un échantillon est prélevé pour analyse par DRX.

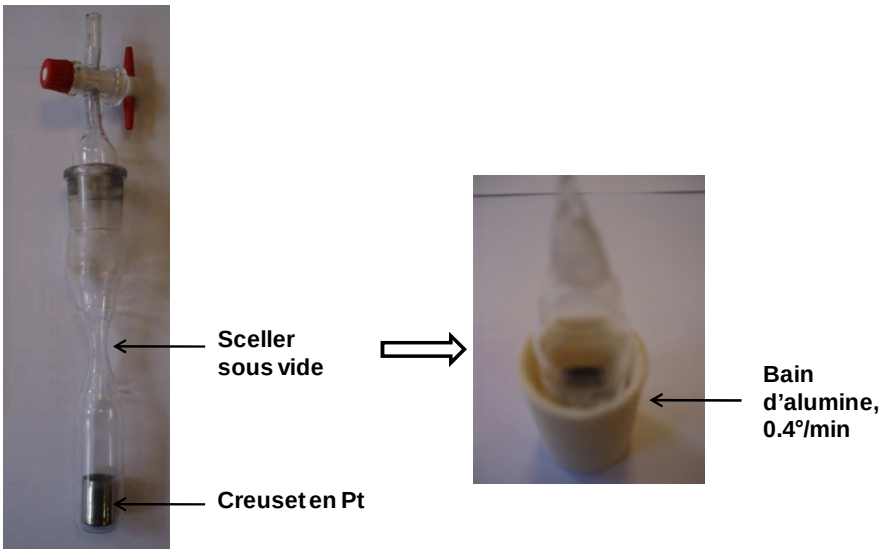

Figure 11. Expérience de la formation du $LiBH_4$ liquide sous vide statique

On a observé que le liquide refroidi a formé un ménisque concave au fond du creuset sans projections notables comme observé sous vide dynamique. Néanmoins, quelques dispersions brunes sont visibles sur les parois de l'ampoule de verre ce qui est peut être un indicateur de la présence du bore. Dans ce cas, la source de bore est probablement une espèce gazeuse (type B_nH_m), qui est déposé sur les parois. Pour cette partie de l'étude notre intérêt est la détermination de la pression totale. Comme la vaporisation est différente des conditions de Knudsen, la pression de H_2 est calculée par volumétrie par la Loi des gaz parfaits sachant le volume de l'ampoule (estimé). Les résultats de DRX ne montrent aucune phase supplémentaire outre que le déplacement des pics du $LiBH_4$. Un composé hypostœchiométrique est probablement formé pendant la fusion avec la composition nominale $LiBH_{3,96}$. Enfin, une donnée expérimentale de pression est obtenue pour la phase liquide et est ajouté à la figure 12.

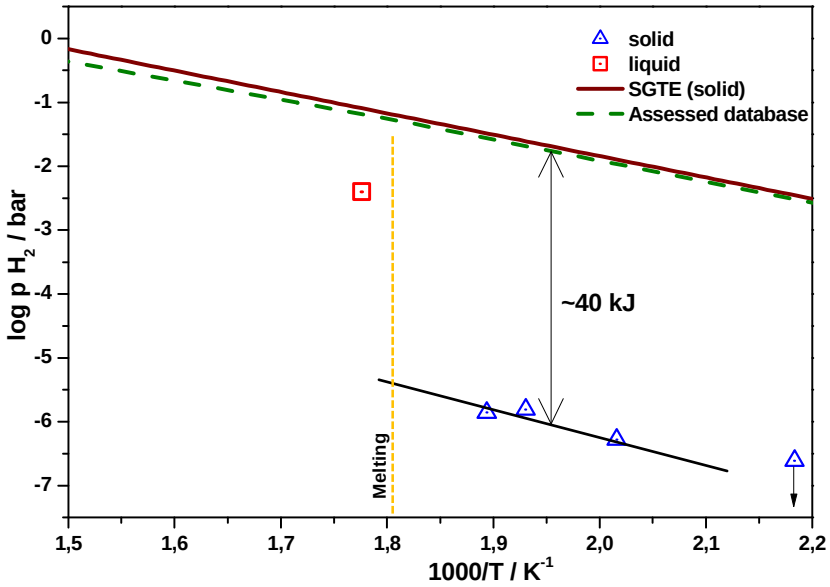

Figure 12. Pressions totales mesurées pendant l'évaporation de $LiBH_4$ par la méthode de Knudsen (solide) et volumétrie (liquide)

Dans la figure ci-dessus, nous observons une pression de vapeur du solide très éloignée des données existantes de SGTE et de la base de données construite au cours de l'évaluation critique du composé. La différence logarithmique, convertie en incrément d'enthalpie libre (environ 40 kJ), est importante. Le coefficient de vaporisation α donnée par la relation de Motzfeldt a été utilisé dans ce cas pour interpréter le phénomène apparent. Le coefficient de vaporisation calculé est de l'ordre de 10^{-8}, qui est probablement lié à une étape limitante avec une faible cinétique. A priori, nous pouvons déduire que les limitations ne sont pas dues à des réactions dans la couche mobile adsorbée de gaz. La seule explication est que les grains de $LiBH_4$ sont recouverts d'impuretés (1,9 %, fiche d'analyse fournisseur) ou par la création de couches protectrices (LiH, B or Li) suite à une évolution par perte de H_2. Cette observation est également justifiée par l'augmentation de la pression dans la phase liquide.

4 PROJET: REACTEUR-BROYEUR COUPLE AU SPECTROMETRE DE MASSE

Pour identifier par spectrométrie de masse les espèces gazeuses émises par les hydrures complexes en cours de broyage, nous envisageons le couplage d'un réacteur mécanique de broyage (broyeur à bille) à un spectromètre de masse. Le but principal de cette étude est d'étudier les réactions chimiques de décomposition ou de recomposition des hydrures complexes pour accéder à des données thermodynamiques et cinétiques. Pour ce type d'étude, un dispositif adéquat de couplage du réacteur doit être conçu. En d'autres termes, nous voudrions relier le réacteur, fonctionnant à des pressions aux environs de l'atmosphère, à un spectromètre de masse où la chambre d'ionisation fonctionne habituellement dans une gamme de pressions entre 10^{-11} et 10^{-5} bar pour permettre les conditions d'impact d'électron.
Pour appréhender autant que possible les plages de mesure de la composition des gaz par spectrométrie de masse, nous essayons d'imaginer l'impact des réactions que l'on cherche à observer par rapport au dispositif expérimental.
L'étude des écoulements gazeux dans un système de tubulures/enceintes liées en série est le thème principal de cette partie. Pour cela, il est essentiel de passer en revue les concepts théoriques de base employés dans les calculs réalisés dans ce travail. En effet, avant d'effectuer des mesures par spectrométrie de masse, le calcul des écoulements nous permettra d'atteindre les objectifs suivants :

- dimensionnement du dispositif expérimental. Si nous comparons avec les dispositifs commerciaux, leur compacité et ajustement facilitent l'adaptation à n'importe quelle système d'introduction mais ils présentent des inconvénients de ne pas être reproductible ni de permettre des mesures quantitatives. De ce fait le montage d'un dispositif avec des sections multiples nous permettra la possibilité d'adapter les divers aspects de la théorie de calcul à des géométries appropriés.
- Obtention d'un écoulement de flux variable avec une commande de contrôle de pression dans l'ensemble du dispositif et selon les expériences spectrométriques. En outre, ceci permettra des possibilités de calibration aussi bien pour l'instrument que pour la gamme de pression accessible à l'expérience pour des mesures quantitatives en fonction de l'écoulement gazeux consommé ou produit pendant le broyage.

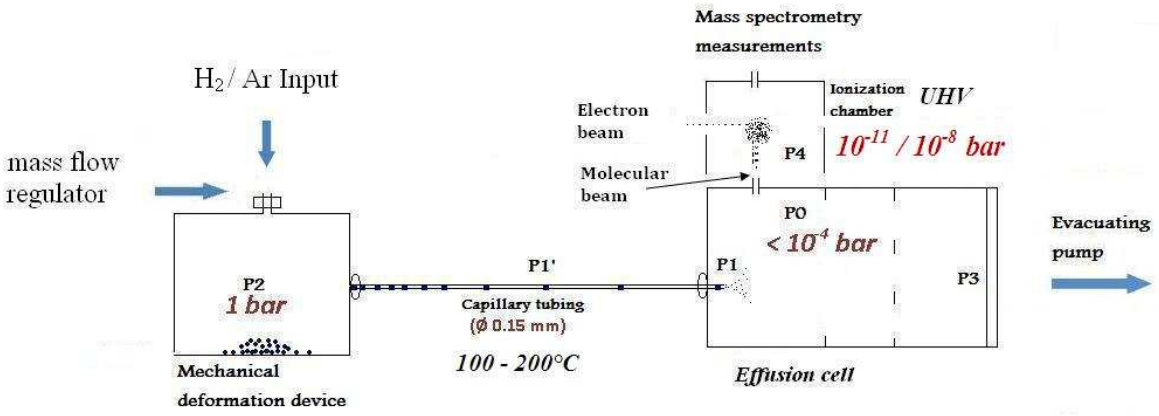

Figure 13. Schéma de répartition des pressions dans l'ensemble du dispositif expérimental : Cellule d'effusion connectée au broyeur à travers le tube capillaire et au système de régulation de pression pour des mesures du faisceau effusé par spectrométrie de masse.

La figure 13 présente les différentes régions de pression dans l'ensemble des appareillages à coupler. Dans ce qui suit, nous décrivons plus précisément l'architecture expérimentale sélectionnée. La détermination du flux gazeux dans chaque section est basée sur un calcul des écoulements en utilisant les équations appropriées. Différentes configurations ont été testées selon la géométrie.

4.1 Description du réacteur-broyeur et du système d'introduction

Pour l'introduction de gaz, deux systèmes peuvent être considérés : -(i) prélèvement par un tube capillaire et -(ii) par une buse micronique courte dite de détente supersonique déjà utilisée par Chatillon [13]. La buse est utilisée lorsque l'on veut éviter des gaz condensables. Un tube capillaire simple et moins onéreux est le système le plus adapté aux gaz non condensables et, en principe, non réactif vis-à-vis des espèces à détecter. Le tube capillaire présente aussi l'avantage de mettre une certaine distance entre le broyeur et le spectromètre qui sera mise à profit pour éviter la transmission des vibrations.

Le système de prélèvement de gaz du broyeur vers le spectromètre doit assurer un flux de gaz très faible correspondant à celui usuel d'une cellule d'effusion muni d'un pompage propre pour assurer une pression dans la gamme de 10^{-4} à 10^{-11} bar. Cette cellule d'effusion produit alors un faisceau moléculaire dirigé vers la chambre d'ionisation comme cela est usuel pour les montages de mesure de pression de vapeur avec cellule d'effusion [14,15]. Un obturateur mobile situé sur le trajet du faisceau moléculaire permet de distinguer à tout

instant les molécules du faisceau moléculaire provenant directement de la cellule d'effusion de celles identiques existantes à l'état stationnaire de pompage dans la source d'ions. Le faisceau moléculaire pourra être aussi perturbé par des phénomènes liés à des interactions physico-chimiques des espèces gazeuses avec le four et la cellule de Knudsen. Morland et al.[16] proposent le principe de la collimation restreinte pour optimiser le faisceau. Ce type de mesure permet de s'affranchir à tout moment de l'influence du fond spectral contrairement aux montages commerciaux qui ne prennent en compte ce fond spectral qu'en interpolant celui avant et après introduction sans savoir quel est en fait son évolution.

A partir de cette analyse et d'un calcul préliminaire, nous envisageons le couplage entre le broyeur et le spectromètre de masse par un tube capillaire long (1-3 m) avec un diamètre de l'ordre de 1,5 à 0,15 mm et une sortie dite choquée dans une cellule d'effusion. L'orifice de la cellule d'effusion est une dimension standard (h=2 x Ø=2 mm). Une pompe primaire annexe connectée directement à la cellule d'effusion est envisagée pour assurer les conditions de Knudsen dans le compartiment « cellule d'effusion ». L'ensemble du dispositif sera maintenu à une température supérieure à 100℃ pour éviter de s phénomènes de condensation et d'adsorption le long du tube capillaire. Vu que notre expérience nécessite un apport continu d'hydrogène vers le broyeur, un débimètre, doté d'un outil de control de flux et de pression, sera installé dans le système d'introduction du gaz (H_2 + Ar). Cet outil permettra également un étalonnage des pressions ou flux du gaz inerte utilisé comme gaz porteur.
Des mesures de pression totale seront également effectuées dans la cellule d'effusion à l'aide d'une jauge de pression «Baratron». Ce qui permettra d'ajuster, au fur et à mesure, le flux dans la cellule d'effusion.

4.1.1 Dispositif de broyeur à bille

Le réacteur-broyeur (type vibreur) peut être couplé à une cellule d'effusion d'un spectromètre de masse pour l'analyse de la phase gazeuse. Le broyeur à bille a été réalisé à partir d'un acier inoxydable. Ce matériel a été choisi pour la non-réactivité avec certain nombre d'hydrures. La connexion à la cellule d'effusion est établie par un tube flexible puis suivi d'un tube capillaire mince. Le broyeur à bille est constitué de cinq parties distinctes (Fig.14) : le bol, un couvercle étanche, une plaque support, un espace creux pour la circulation d'air chaud et une bille.

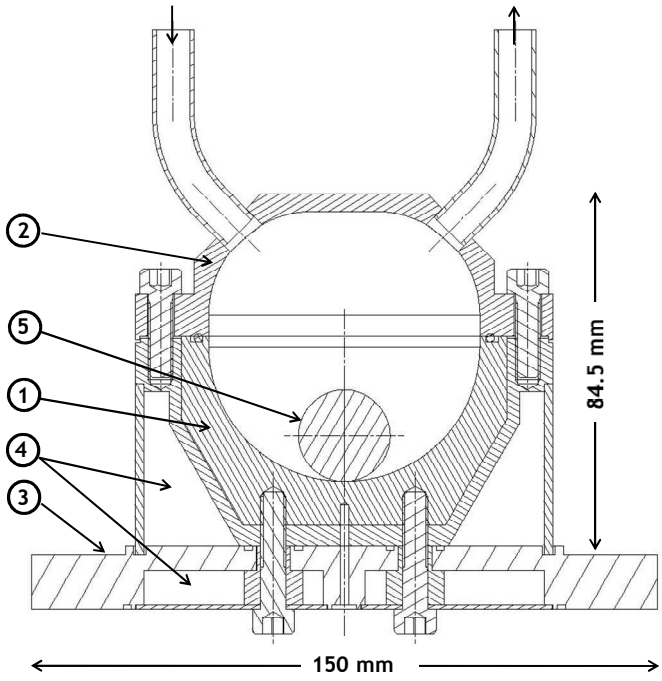

Figure 14. Coupe transversale du dispositif de broyage. (1) bol; (2) couvercle étanche muni d'un joint "Viton®"; (3) plaque support; (4) espace creux pour la circulation d'air chaud; (5) bille Ø 20-30 mm.

L'intérieure du broyeur est sous forme de cavité quasi-ellipsoïde. Le diamètre intérieur du bol est de 64 mm avec une hauteur de 35 mm. Toutes les parties du broyeur sont usinées à partir d'un acier inoxydable standard « 304 L », sauf la pièce principale du bol a été réalisée d'un acier inoxydable plus dure « 630 AISI ». En plus, ce dernier a été soumis à un traitement thermique à 1050℃ avec recuit à 480℃. Le pro cédé de traitement a été certifié par un fournisseur avec une dureté de 44 HRC (MPa 1472) sachant que pour un acier inoxydable standard cette valeur est autour de 500 MPa. Le couvercle étanche épouse la forme du bol et y est fixé par des vis et rondelles. L'étanchéité est assurée par un joint "Viton®" (2 mm d'épaisseur, FPM température -20℃ à +204℃) placé dans une rainure annulaire. Deux sorties (5 mm) ont été effectuées dans le couvercle. L'une d'entre eux sera employée pour le pompage ou l'arrivée de flux de gaz, alors que la seconde est destinée pour l'introduction de gaz vers la cellule d'effusion. Le bol est fixé sur une plaque cylindrique (h=15 x Ø=150 mm) par quatre vis. Un espace creux a été usiné dans la plaque et autour du bol pour un chauffage homogène (Fig.14). La bille est faite d'un acier. Différentes tailles de billes (Ø 20-30 mm) ont été testées selon l'énergie que nous voudrions transmettre au matériau à broyer. Un trou (Ø 3 mm) est foré au-dessous du broyeur pour l'insertion du thermocouple type K. La température peut être mesurée à 5 mm au-dessous de l'échantillon.

4.1.2 Système d'introduction de gaz

Le système d'introduction de gaz peut fournir de l'hydrogène et de l'argon (ou un mélange des deux). Le flux gazeux peut être ajusté dans les proportions désirées par un système de valves et de contrôleurs de débit. Le système est relié à une pompe primaire pour évacuation dans les tubulures ou dans le broyeur.

4.1.3 Tubulure de connexion du broyeur vers la cellule d'effusion

La connexion du broyeur à la cellule d'effusion sera établie par un tube flexible de 1 m de longueur (i.d. 1,5 mm) directement soudé au couvercle du broyeur visant l'absorption des vibrations pendant le broyage. Le tube est suivi d'un tube capillaire mince de longueur 1-3 m (i.d. 0,15 mm) pour assurer une diminution progressive de la pression (de la pression atmosphérique dans le broyeur au vide secondaire dans la cellule d'effusion du spectromètre de masse). Le raccordement entre les deux tubes est établi par un connecteur de vis de Swagelok®. Le capillaire est inséré dans un tube plus grand (o.d. 25 millimètres) après être enrouler en forme de spirales avant sa connexion à la cellule par un embout approprié.

4.2 Calculs de flux dans les lignes d'introduction du réacteur-broyeur

4.2.1 Régimes d'écoulement gazeux

Un flux de gaz en écoulement dans une canalisation est caractérisé par trois régimes d'écoulement :

- Le régime moléculaire
- Le régime de transition
- Le régime visqueux.

Le nombre de Knudsen K_n permet de déterminer dans quel régime d'écoulement se trouve un flux gazeux à travers une canalisation. Il est donné par la formule suivante :

$$Kn = \frac{d}{\lambda} \tag{4}$$

où d est le diamètre de l'orifice d'effusion et λ est le libre parcours moyen, donné par l'expression:

$$\lambda = \frac{RT}{\pi\sqrt{2}N_A\sigma^2 p} \tag{5}$$

R est la constante des gaz parfaits, p la pression, T la température, N_A le nombre d'Avogadro et σ le diamètre de Van Der Waals de la molécule considérée [17].

Les différents régimes d'écoulements des gaz dans des tubulures sont ainsi définis par rapport au nombre de Knudsen:

- Si Kn ≤ 3, l'écoulement est moléculaire, c'est-à-dire seules les collisions avec les parois sont prises en compte,
- Si Kn ≥ 80, l'écoulement est visqueux,
- Si 3 ≤ Kn ≤ 80, le régime est transitoire (intermédiaire entre moléculaire et visqueux).

4.2.2 Résolution informatique des différents régimes d'écoulement

Dans le but de quantifier les flux dans l'ensemble de l'installation, du broyeur au spectromètre de masse, nous décrivons les étapes suivies dans le calcul et donc les conditions de l'état stationnaire de flux dans les appareillages. Le calcul a été réalisé par programmation à l'aide de Visual Basic sous Excel.

Due à la complexité du calcul des flux, Santeler [18] a proposé une méthode pratique pour résoudre des systèmes à multiéléments interconnectés entre eux : il traite chaque tube et sa sortie comme deux éléments différents ce qui permet de définir un régime d'écoulement pour chaque élément.

La stratégie de calcul consiste à choisir une section du système avec une pression imposée à l'entrée et dont le flux sera calculé à partir des dimensions des tubulures. Ensuite chaque section sera résolue par itération afin d'obtenir la pression à l'entrée de la section suivante. Le raisonnement suivi est illustré dans la figure 15. Dans le système proposé, trois flux principaux seront distingués : le flux visqueux (celui du capillaire), le flux de pompage (celle connectée à la cellule d'effusion) et le flux d'effusion (vers le spectromètre), désignés respectivement par Q_{vis}, Q_{pompe} et Q_{eff}. Au niveau de la cellule d'effusion, le bilan des flux correspond à la condition de l'état stationnaire de flux :

$$Q_{eff} = Q_{vis} - Q_{pompe} \tag{6}$$

La résolution informatique va se baser sur le changement de signe de la valeur de l'expression $Q_{pompe} - Q_{vis} + Q_{eff}$ qui sera tantôt positif tantôt négatif.

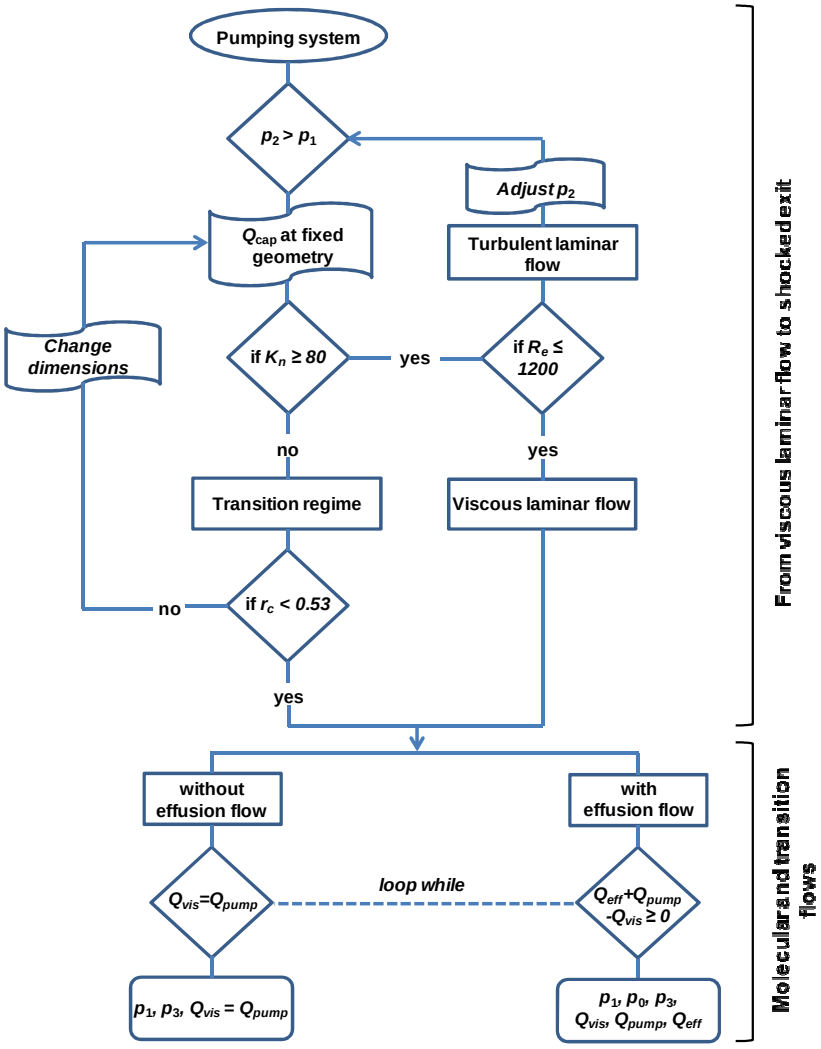

Figure 15. Algorithme simplifiant la méthode de résolution des équations de flux poursuivie

4.2.3 Résultats et discussion

L'exécution du programme informatique nous fournit une série de données brutes que nous exploitons dans ce paragraphe pour fixer les paramètres expérimentaux. Dans le cas de l'hydrogène gazeux, on constate qu'une augmentation de la longueur du capillaire (de 1 à 3 m) permet de travailler à des pressions p_0 plus basse au niveau de la cellule d'effusion ou des pressions amonts p_2 plus élevées qui vont jusqu'à 4 bar. Au niveau du diamètre du capillaire, le calcul montre qu'il faut un diamètre le plus petit possible. Un capillaire usuel et commercialement distribué de diamètre de 0,15 mm répond aux exigences fixées pour notre système d'introduction.

En effet, pour un flux adiabatique à la sortie de l'orifice, la vitesse de sortie est limitée à la vitesse locale du son. Pour cela, le flux sera dans son optimum et constant pendant que le

rapport de pression continuera de tendre vers des valeurs nulles. A ce stade de calcul, nous essayerons de maintenir le rapport des pressions inférieur au rapport critique (r_c = 0.53) afin d'éviter le régime de transition. Sachant que le régime choqué ne peut être établi que si la pression p_1 est en régime visqueux attesté par le nombre de Knudsen.

A ce propos, la figure ci-dessous (Fig.16a) montre d'une part l'état du flux le long du capillaire représenté par la variation du nombre de Knudsen dans différents endroits du capillaire avant la sortie choqué pour diverse pressions amonts. Ce qui montre qu'aux derniers millimètres avant la sortie du capillaire, le gaz subit une détente très rapide ce qui peut affecter le régime visqueux isentropique à la sortie de l'orifice. Ce changement de régime devient plus prononcé au-dessous de 0.5 bar. Ceci est en accord avec nos estimations du régime choqué basé sur le calcul du rapport critique.

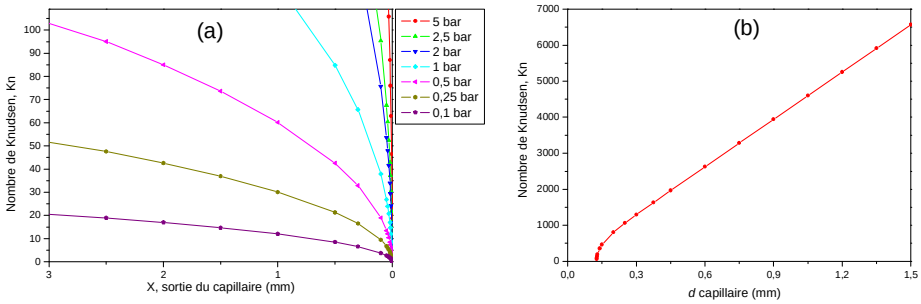

Figure 16. Variation du nombre de Knudsen en fonction : (a) de la pression le long du capillaire, (b) du diamètre du capillaire pour une pression amont de 1 bar.

D'autres parts, pour une pression amont de 1 bar, la figure 16b rapportent des données sur le choix du diamètre du capillaire. La pression dans le capillaire n'est pas une variation linéaire en fonction du déplacement du flux gazeux. Il en est de même pour le nombre de Knudsen. Pour cela nous considérons le milieu du capillaire comme point de référence. Un capillaire de petite taille est plus adapté à cette étude pour éviter un flux visqueux élevé de type turbulent. En effet, le régime dans le capillaire est en général visqueux-laminaire ; mais une fois la pression p_2 est au dessous de 250 mbar, on est dans le régime de transition correspondant à une pression p_1 de 0.07 mbar, valeur assez faible vu la longueur du capillaire choisit.

En comparant les différents régimes existants en fonction de la pression, dans la ligne de pompage entre la cellule d'effusion et la pompe qui contribuent au flux total calculé selon la formulation du flux de transition, on remarque que le débit doit être effectivement calculé à partir du régime de transition un peu avant que la pression se rapproche de la limite de fonc-

tionnement de la cellule d'effusion (≈ 10^{-4} bar). La figure 17 montre la répartition des différents flux au niveau du compartiment « cellule d'effusion » en fonction de la pression amont p_2 (par rapport au réacteur) ainsi que le flux de transition évacué par la pompe. On constate que pour des pressions amont inférieures à 0,4 bar le flux évacué par la pompe devient pratiquement nul selon les caractéristiques fonctionnelles de la pompe fournies.

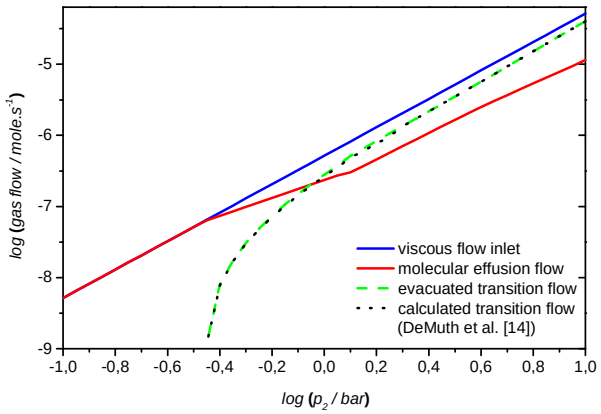

Figure 17. Relation entre les différents flux au niveau du compartiment de la cellule d'effusion

L'utilisation de l'équation du flux de transition dans le tube de pompage permet d'apporter une correction sur le bilan des flux dans la cellule d'effusion notamment pour des pressions amont supérieures à 2 bar. Pour des conditions de travail idéal par rapport au flux de transition entre la cellule et l'entrée de la pompe, nous choisissons de se situer à des pressions amont inférieures à 2,5 bar.

4.3 Construction du réacteur à coupler au spectromètre de masse

Comme on s'attend à ce que la cellule d'effusion contienne seulement des espèces gazeuses issues du tube capillaire, sa conception a été adaptée et consiste en enceinte cylindrique (h=68 mm, d=30 mm) avec un couvercle vissable muni d'un orifice (i.d. 2 mm). Dans le réacteur-cellule on distingue: la cellule principale d'effusion et son compartiment liée directement au système de pompage (Fig.18). Il sera également utile de mesurer la pression dans la cellule d'effusion afin de réguler l'écoulement de flux et calibrer le spectromètre de masse. La pression amont du capillaire sera fixée à l'aide d'un contrôleur de débit dans la gamme de pression 0,1 – 2,5 bar.

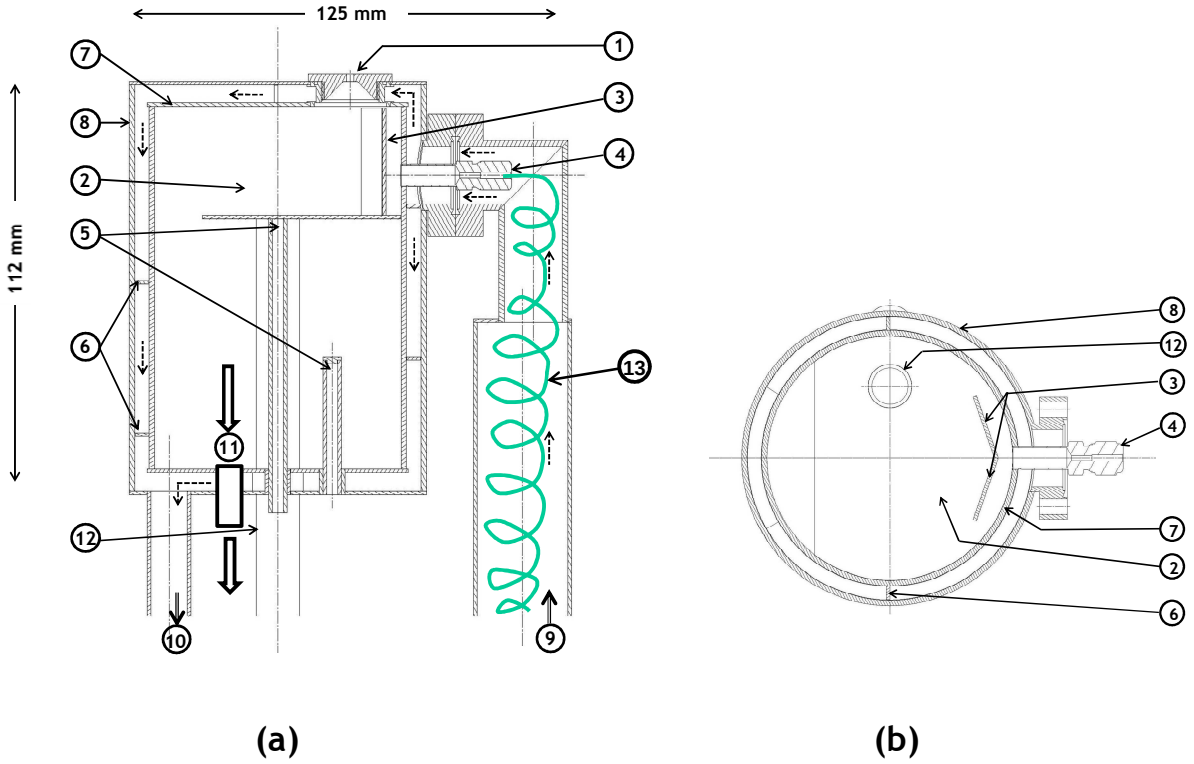

Figure 18. Schéma du réacteur-cellule d'effusion pour les hydrures : (a) coupe transversale; (b) Section transversale de la vue supérieure. (1) orifice d'effusion; (2) compartiment cellule; (3) deux barres réflectrices; (4) embout pour la connexion avec le capillaire; (5) deux tubes pour des thermocouples de types K; (6) cloisons; (7) paroi de la cellule; (8) enveloppe d'air chaud; (9) entrée d'air chaud; (10) sortie d'air chaud; (11) vers le système de pompage; (12) tube pour la jauge de pression; (13) tube capillaire.

Comme déterminé dans la partie calcul des écoulements, le flux excessif sera évacué par la pompe annexe tandis que seulement une faible quantité effusera vers la chambre d'ionisation pour son analyse par le spectromètre de masse. Le flux arrivant du capillaire avec la sortie dite « choquée » est dévié par deux barres réflectrices pour permettre une distribution dispersée de flux dans le compartiment cellule. La sortie d'évacuation de la cellule a été faite de manière à avoir la même section que le tube de pompage (Ø 25 mm). La mesure de la température est effectuée directement dans la cellule à deux niveaux au moyen de deux thermocouples par deux tubes, alors que la mesure de pression dans la cellule est faite par une jauge « Baratron » à travers un tube long (i.d. 10 mm).

La cellule est entourée par une enveloppe pour que la circulation d'air chaud permette des conditions isothermes. Des cloisons ont été soudées alternativement dans le circuit de chauffage à air (Fig.18) pour la transmission de la chaleur par convection. Toutes les parties de la cellule sont faite d'acier inoxydable, soudées et testées pour vérifier leur étanchéité. La

cellule est montée sur une bride de vide pour une incorporation aisé à l'installation du spectromètre de masse.

4.4 Conclusion

Dans les conditions expérimentales, le flux stationnaire dépendra principalement de la capacité réelle de la pompe et des conditions de pression optimale que nous pouvons atteindre dans la chambre d'ionisation. Néanmoins, toute fluctuation sera compensée par la pompe d'évacuation en minimisant le flux d'effusion à des jets moléculaires suffisants pour l'analyse par spectrométrie de masse. D'autres aspects pratiques pourront subsister lors de nos mesures, notamment la solubilité élevée de l'hydrogène dans les aciers, même si n'aura que peu d'effets à température de travail, ce qui pourrait contribuer à des chutes de flux calculé dans l'enceinte de la cellule d'effusion. La raison pour la quelle nous effectuerons des mesures préliminaires avec des gaz dont les effets de fluctuation seront faibles afin d'approuver les résultats de nos calcul.

CONCLUSION GENERALE ET PERSPECTIVES

Le présent travail s'inscrivant dans le cadre du projet européen "COSY-Project", correspond à une étude multidisciplinaire pour subvenir à des besoins énergétiques industriels et gouvernementaux basés sur l'utilisation des hydrures en tant que matériaux pour le stockage d'hydrogène en phase solide. Les matériaux hydrures étudiés possèdent des capacités gravimétriques en hydrogène entre 7 et 14 %, correspondant respectivement aux limites maximales de MgH_2 et $LiBH_4$ purs. De telles densités constituent la motivation majeure de l'émergence de ce projet pour une éventuelle application aux engins et appareils mobiles. En comparant ces hydrures à H_2 pressurisé, ce dernier comporte un réservoir de poids important et volume très encombrant. En effet le composé $LiBH_4$ possède des atouts vis-à-vis de sa capacité élevée en hydrogène : - 3 atomes en considérant la réaction de décomposition principale, - et du fait de la présence du Li, le matériau le plus léger par comparaison aux autres hydroborates. Néanmoins, en vue de son application, des données thermodynamiques caractérisant son comportement, et cinétiques caractérisant la réversibilité des opérations restent insuffisamment connues pour maîtriser le stockage.

Le composé $LiBH_4$ peut exister en deux structures: ortho-$LiBH_4$ et hexa-$LiBH_4$ avec T_{trs} = 113℃. Les données thermodynamiques actuelles (stoc kée notamment dans la banque de données thermodynamique SGTE) considèrent le composé $LiBH_4$ comme une seule phase sans tenir compte de la phase hexagonale, et ne décrivent pas la phase liquide. Ainsi ce manque de données, nous a amené d'une part à revoir la description thermodynamique de ce composé (c.à.d. C_p, $\Delta_f H$ et ΔH_{trs}), et d'autres part à entreprendre des mesures calorimétriques et de pression de vapeur par spectromètre de masse avec cellule de Knudsen.
Afin de minimiser ou réduire l'influence des paramètres cinétiques sur les étapes de désorption (et d'adsorption), nous avons testé les mélanges de ce composé avec un autre hydrure MgH_2. Les poudres d'hydrures étaient réactivées en augmentant leur surface spécifique par broyage à bille de haute énergie. Nous avons également testé l'influence de quelques additifs, à base de Ti et de Ni pour faciliter la réaction de désorption.

Le chapitre 3 était consacré au système d'hydrures MgH_2-x$LiBH_4$ avec analyse microstructurale des différentes compositions ($0<x<3,5$), identification de phases formées lors du broyage et analyse du comportement thermique à la désorption. Les résultats obtenus montrent :

- Pour des tailles de cristallites des composés purs réduites jusqu'à des valeurs de l'ordre de 10 nm pour MgH_2 et 20 nm pour $LiBH_4$, l'analyse thermique différentielle (ATD) a montré clairement une diminution de la température de désorption de H_2 qui peut atteindre 70°C.
- L'analyse par calorimétrie différentielle à balayage (DSC) du mélange MgH_2-$2LiBH_4$, montre l'existence de 4 événements thermiques dont le dernier présente deux étapes consécutives :

$$2LiBH_4(l) \xrightarrow{endo} 2LiH(s) + 2B(s) + 3H_2(g)$$
$$Mg(s) + 2B(s) \xrightarrow{exo} MgB_2(s)$$

  L'apparition de MgB_2 a été mise en évidence par microscopie électronique à balayage, et par caractérisation DRX après traitement thermique à 500°C, le mélange étant alors complètement déshydruré avec formation de LiH et d'une solution solide Li-Mg. Ce résultat suggère une présence du B probablement sous forme amorphe puisque non détecté.
- L'étude de la désorption par ATD des mélanges de différentes compositions ($0 < x$ ($LiBH_4/MgH_2$) $< 3,5$) met en évidence que le point de fusion de $LiBH_4$ et les températures de désorption de MgH_2 et de $LiBH_4$ diminuent pour des teneurs en MgH_2 de plus en plus importantes. La formation de certaines phases, solutions solides Li-Mg et composé MgB_2, semble dépendre de la composition. La composition x= 2 reste la plus favorable et elle constitue un bon compromis entre la capacité d'hydrogène du mélange et la valeur de la température de désorption.
- Dans le cas de la composition x = 2, nous avons testé quelques additifs pour étudier l'amélioration des conditions de désorption de H_2. L'ajout d'isopropoxyde de titane (Tiso) a un effet cinétique considérable. Cet additif a permis de réduire les températures de désorption de MgH_2 et $LiBH_4$ d'environ 70°C en intervenant par ses deux composa ntes : oxyde de titane et hydrocarbure. Un autre additif retenu montrant une amélioration comparable à celle du Tiso est à base de nickel (mélange Ni-NiF_2).

Sur le plan des données thermodynamiques, le chapitre 4 a porté sur deux aspects, - (i) celui relatif au manque de données, - (ii) et à leur fiabilité dans les bases de données déjà compilées pour le composé $LiBH_4$.

- De nouvelles expériences en calorimétrie différentielle à balayage ont été réalisées, et ont permis d'établir une description plus complète de la capacité calorifique, C_p, de la phase orthorhombique (basse température) du $LiBH_4$. Une fonction pour le C_p de la phase hexagonale (haute température) de ce composé a été proposée. L'anomalie dans l'évolution du C_p observée avant la transition de phase a été considérée comme

indépendante de cette transition polymorphique principale et attribuée à une forte augmentation de la concentration de défauts (déformation du réseau non-cubique).

- Certaines fonctions thermodynamiques étant complètement absentes dans la littérature et les tables thermochimiques, à la lumière de ces nouvelles données, une évaluation critique a été réalisée. De nouvelles enthalpies de la transition et de la fusion du composé ont été proposées. Une fonction de Gibbs a été dérivée selon l'approche CALPHAD pour chacune des phases incluant la phase liquide. On note l'importance de ces données car, dans le cas du $LiBH_4$ solide, ils correspondent à une diminution relative en pression de H_2 qui peut atteindre 20% par rapport aux données actuelles.

La stabilité des phases en équilibre avec le composé $LiBH_4$ ainsi que la décomposition du composé ont été étudié dans le système Li-B-H. Des mesures de « pression de vapeur » de $LiBH_4$ en utilisant la spectrométrie de masse de haute *T* associée à la méthode d'évaporation de Knudsen ont été effectuées. Dans ce chapitre 5 nous sommes concentrés sur la recherche des espèces nouvelles qui pourrait être présente durant la « cyclabilité » de ces hydrures.

- Dans le diagramme de phase du système Li-B-H, nous nous sommes d'abord focalisés sur l'étude du système triphasé $LiBH_4$-LiH-B, d'une part pour vérifier que la réaction principale de décomposition correspondait à l'équilibre et d'autre part pour détecter la présence éventuelle de toute autre phase. Le triphasé est stable dans le domaine de *T* jusqu'à 250℃ (identification des phases par DRX) et rien n'indique la présence d'état fondu. Un déplacement systématique des pics de Bragg de $LiBH_4$ a été observé indiquant une augmentation de défauts liés à une probable sous-stœchiométrie et en accord avec les observations faîtes lors de nos mesures de C_p. La transformation du $B_{cry} \rightarrow B_{am}$ a probablement lieu, suite à une disparition partielle du B_{cry} après recuit. Au-dessus de la *T* de fusion de $LiBH_4$, il y a la formation d'un état fondu de plus en plus important en volume pour des échantillons riche en bore. Deux pics de Bragg ont été également indexés pour la phase $LiBH_2$ « boryle de lithium » dont la structure cristalline est issue de calcul *ab-initio*.
- Un travail expérimental par spectrométrie de masse a été entrepris pour confirmer et/ou infirmer la présence de nouvelles espèces gazeuses en évaporant le composé $LiBH_4$. Dans le domaine de *T* jusqu'à 205℃, H_2 est l'espèce majoritaire avec présence mineure de H, BH_3 et B_2H_5. L'espèce BH_3 a été détectée uniquement en utilisant un échantillon broyé à 205℃. Le dimère B_2H_6 est une espèce plus stable thermodynamiquement que BH_3, avec des pressions de vapeur plus élevés, mais sa présence dans notre cas est difficile à confirmer en raison d'un chevauchement avec la masse mo-

laire de N_2, très présent dans l'atmosphère du spectromètre de masse. L'ion $B_2H_5^+$ proviendrait de cette espèce par ionisation dissociative. Aucune perte de masse significative pour ces échantillons n'a été observée.

- Avec une cellule de Knudsen conventionnelle installée dans un four haute température (chauffage par rayonnement), nous avons obtenu des données de pression totale pour la phase solide jusqu'à 255°C. La fusion de $LiBH_4$ sous ce vide dynamique est accompagnée d'une effervescence et d'un « débordement », probablement lié à l'apparition d'une phase gazeuse suite à une décomposition. La présence soudaine d'une plus haute pression par rapport au solide, indique une évaporation en phase solide limitée par un processus cinétique. Le coefficient d'évaporation calculé par la relation de Motzfeldt a été trouvé très faible suggérant qu'il ne s'agissait pas d'un phénomène de désorption à la surface mais probablement d'une diffusion de H_2 au travers des couches superficielles de composition différente telle que LiH et/ou B, formés par décomposition de $LiBH_4$.

Le chapitre 6 présente un travail de conception en vue de la construction d'un réacteur-broyeur mécano-chimique couplé au spectromètre de masse via une cellule d'effusion pour mieux maîtriser les flux de gaz désorbés. Ce couplage a comme but d'effectuer des mesures directes de pression sous l'effet du broyage à la fois lors de la désorption ou de l'absorption d'hydrogène pour des matériaux d'hydrures. La difficulté majeure était d'assurer le couplage entre le tube de sortie du broyeur qui est à la pression atmosphérique vers une cellule d'effusion fonctionnant sous vide et spécialement adaptée à l'enceinte du spectromètre de masse. Le dimensionnement de l'architecture expérimentale est basé sur le calcul des écoulements gazeux (régimes visqueux à moléculaire). Le broyeur construit permettra d'établir des pressions amont de 0,1 à 2,5 bar sur le broyeur, avec un capillaire standard de 3m de longueur et 0,15mm de diamètre. Le broyeur est entouré d'un compartiment pour la circulation d'air chaud qui permet des *T* de travail de 100-250°C. La cellule d'effusion com porte également une enveloppe externe pour la circulation d'air chaud pour des *T* jusqu'à 150°C. Le réacteur nécessite des mises au point techniques avec la mise en place de jauges de pression en aval et en amont du capillaire. La calibration de flux stationnaire permettra – en présence d'un système de pompage additionnel sur la cellule d'effusion pour l'évacuation de l'excès de flux – de calibrer le spectromètre de masse et de suivre en direct (temps de transit court) les effets du broyage.

Références

[1] J.J. Vajo, S.L. Skeith, F. Mertens, The Journal of Physical Chemistry B 109 (2005) 3719-3722.
[2] U. Bösenberg, S. Doppiu, L. Mosegaard, G. Barkhordarian, N. Eigen, A. Borgschulte, T.R. Jensen, Y. Cerenius, O. Gutfleisch, T. Klassen, M. Dornheim, R. Bormann, Acta Materialia 55 (2007) 3951-3958.
[3] F.E. Pinkerton, M.S. Meyer, G.P. Meisner, M.P. Balogh, J.J. Vajo, The Journal of Physical Chemistry C 111 (2007) 12881-12885.
[4] AIST, Chemical Abstract, Integrated Spectral Database System of Organic Compounds, Japan.
[5] P.-J. Wang, Z.-Z. Fang, L.-P. Ma, X.-D. Kang, P. Wang, International Journal of Hydrogen Energy 33 (2008) 5611-5616.
[6] A. El kharbachi, I. Nuta, F. Hodaj, M. Baricco, Thermochimica Acta (2011) 10.1016/j.tca.2011.1002.1043.
[7] A. El kharbachi, I. Nuta, C. Chatillon, E. Pinatel, M. Baricco, (2011) *To be published soon.*
[8] A. Züttel, S. Rentsch, P. Fischer, P. Wenger, P. Sudan, P. Mauron, C. Emmenegger, Journal of Alloys and Compounds 356-357 (2003) 515-520.
[9] A. Züttel, P. Wenger, S. Rentsch, P. Sudan, P. Mauron, C. Emmenegger, Journal of Power Sources 118 (2003) 1-7.
[10] H.I. Schlesinger, H.C. Brown, Journal of the American Chemical Society 62 (1940) 3429-3435.
[11] R.P. Mitrofanova, Y.I. Mikhailov, N.N. Mal'tseva, Zh. Neorg. Khim. 34 (1989) 2207-2211.
[12] Y.N. Shevchenko, N.N. Mal'tseva, V.A. Nazarenko, N.S. Kedrova, N.T. Kuznetsov, Journal Name: Dokl. Phys. Chem. (Engl. Transl.); (United States); Journal Volume: 290:4-6; Other Information: Translated from Dokl. Akad. Nauk SSSR; 290: No. 4-6, 1426-1430(Oct 1986) (1987) Medium: X; Size: Pages: 968-970.
[13] C. Chatillon, La Revue de Métallurgie 95 (1998) 1077-1099.
[14] J. Drowart, C. Chatillon, J. Hastie, D. Bonnell, Pure and Applied Chemistry 77 (2005) 683-737.
[15] C. Chatillon, M. Heyrman, Journal of Physics and Chemistry of Solids 66 (2005) 488-493.
[16] P. Morland, C. Chatillon, P. Rocabois, High Temperature and Materials Science 37 (1997) 167-187.
[17] D. Bianchi, J.-P. Joly, A. Perrard, Le Vide, Science,Technique et Applications 286 (1997) 533-555.
[18] D.J. Santeler, Journal of Vacuum Science & Technology A: Vacuum, Surfaces, and Films 4 (1986) 348-352.

GENERAL CONTEXT

The global warming and climate changes with non-predictable consequences imposed to national and intergovernmental policies, mandatory reductions of emission of polluting gases from industrial and transport activities. This supposes that classical energy carriers have to be replaced by alternative energies. A part from the duty of mankind is to soften the above mentioned ecological consequences and develop new scientific and technological knowledge for setting up of a basis of our future economy.

One of the promising future scenarios is the hydrogen economy. Hydrogen, from clean-energy concept point of view, is the ideal way for energy storage, transportation and conversion. Its combustion generates water and hence it is non-polluting system in particular in the future "zero-emission vehicle". It is abundant and can be produced from a variety of conventional and renewable energy resources. These are the main reasons why there is now widespread agreement that hydrogen will play a key role in the actual European Union's energy policy. However, the storage of hydrogen is still a big issue.

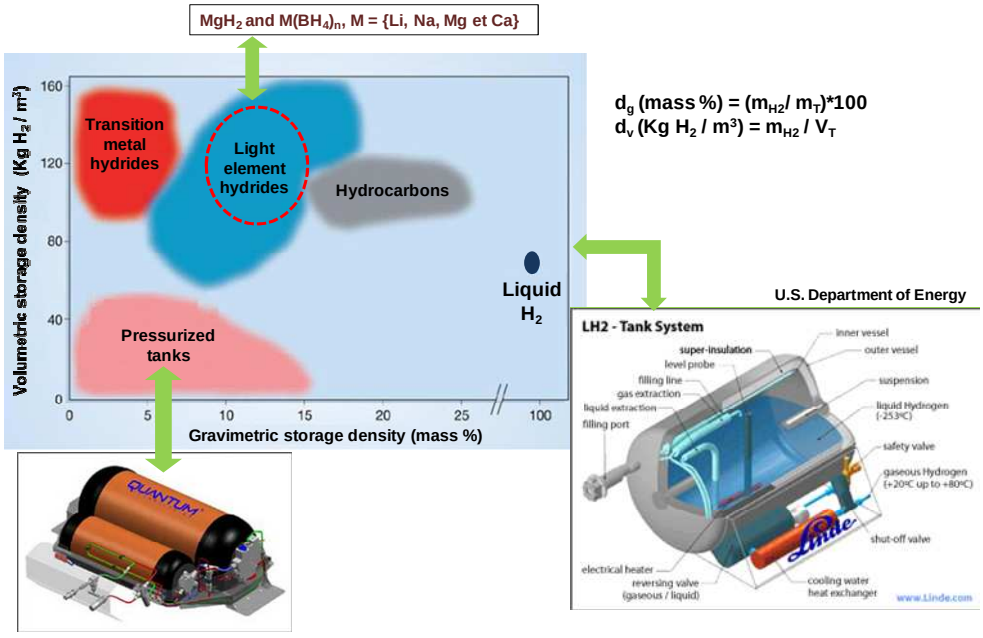

Figure 0.1. Hydrogen storage capacity. Volumetric (mass of H_2 per unit volume of storage medium) versus gravimetric (% H_2 storage density) values for different hydrogen storage systems[1,2]

[1] Schüth, Nature ***434*** (2005) 712-3

[2] www.energy.gov

The very low boiling point of liquid hydrogen, around -250℃, makes its storage in liquid form inefficient. Its low density in the gaseous state requires storage in high-pressure vessels, a disadvantage for safety problems and its storage in mobile applications.

The figure 0.1 shows the different kinds of hydrogen storage styles. Tanks were developed by the US-DOE (for US-Department of Energy) either for gaseous or liquid hydrogen. Hydrocarbons need re-forming and liquid hydrogen needs a refrigeration system. Weights and volumes of pressure tanks for pressurized storage are included. Thus the storage densities depend on tank type. The hydrides are in the upper field of the diagram which makes them advantageous regarding their important storage capacities.

A safe alternative for transportation and storage of hydrogen can be the storage as a hydride form. Among systems under discussion, hydrogen absorbed in metal hydrides (transition metal based hydrides, complex hydrides) is a promising idea. These light-weight complex hydrides have the required high storage capacity (Fig.0.2). For instance, the partial decomposition of $LiBH_4$ to LiH + B + $1.5H_2$ could yield 13.6 mass % hydrogen. Use of complex hydrides for hydrogen storage is challenging because of both kinetic and thermodynamic limitations. Strong improvements in kinetics are possible with suitable catalysts. The second problem is the heat released during hydride formation. The standard enthalpy for the above given reaction is around -67 $kJ.mol^{-1}$ of H_2 and thus, if reversible, an equilibrium pressure of 1 bar would require a temperature of >400 ℃.

Figure 0.2. Volume of 4 kg of hydrogen compacted in different ways, with size relative to the real size of a car. (Adapted from Toyota press information, 33rd Tokyo Motor Show, 1999) [3]

[3] Schlapbach and Züttel, Nature ***414*** (2001) 353-8

The high desorption temperature bears two problems: (i) the energy loss during desorption reduces the efficiency of the total storage process. (ii) The same amount of energy is released as heat during absorption, which causes enormous technical problems during filling of the tank (ca. 1 MW heat has to be dissipated in a typical car tank).
The mentioned problems are typical for complex hydrides and clearly demonstrate the need to find materials with suitable thermodynamic properties for technical needs. European Union is aware of the importance of this research and, consequently, has supported "Complex Solid State Reactions for Energy Efficient Hydrogen Storage" (COSY) Project proposed by seven European countries: Germany, Spain, Italy, France, Netherlands, Switzerland and United Kingdom. The main objective of this network will be to reach a fundamental understanding of the sorption kinetics in hydride composites and their related systems using three different strategies: empirical studies, model systems and a theoretical/modeling approach. The addition of a suitable catalyst, which might affect one of the various elementary steps of solid state reactions (e.g. formation of nucleation centers, intermediate structure with a lower activation barrier, lowering interface and surface energies or forming gateways for hydrogen), is also explored. (See in appendices part the specific research task of each partner of COSY network).

This work in the frame of COSY project is focused on MgH_2-$LiBH_4$ hydride composite system. In this thesis is presented, at the beginning, phases characterization and thermodynamic data of Mg-B-H-Li system. Each raised point will be thorough in the continuation of the manuscript which is framed in six chapters. Their respective contents are summarized below.

This section of general context constitutes the first part of the thesis ***"Chapter 0"***.
Chapter 1 presents the bibliographical part on the hydride system to be studied. It gives a progressive report on the characterization of the involved materials, their structural and thermodynamic properties. The mechanisms of sorption reactions are also approached in this chapter with specificities related to the use of catalysts.
Chapter 2 details the experimental techniques and practical methods used during the present work of thesis with focus on mass spectrometry and thermal techniques.
Chapter 3 provides a detail about thermal treatment which was applied to the hydride at variables compositions and describes the microstructural and structural characteristics of the phases.

Chapter 4 reports heat capacity measurements and a critical assessment of the thermodynamics of $LiBH_4$ compound.

Chapter 5 deals with the decomposition reactions and phases stability in the Li-B-H system where mass spectrometry, closely to Knudsen effusion method, is used to study the decomposition of the $LiBH_4$ compound. In this chapter, are also presented experiments related to the stability of the three phase system $LiBH_4$-LiH-B.

Chapter 6 is devoted to the building of the milling reactor coupled to a mass spectrometer. First, it will present an essential flow calculation for the conception of the entire instrumentation and feasibility of the connection between the two devices (milling reactor and the cell of the mass spectrometer through a capillary tubing).

General conclusions are presented as the last ***chapter*** of this manuscript.

Finally, the ***references*** and ***appendices*** containing additional complements are given at the end of each chapter.

CHAPTER 1. BIBLIOGRAPHY OF THE STUDIED HYDRIDES

The enhancement of the yield of hydrogen cycle in hydride composites for solid state hydrogen storage could not be done without knowledge of the control parameters of this mechanism. These parameters could be directly derived from thermodynamic functions namely the Gibbs energy function of the compounds and the driving forces of the reactions. Though kinetic and reversibility of the reactions are compromise phenomena which could depend on many factors. These factors could be of different natures, such as particles agglomeration and sintering, diffusion of elements in powder-solid phase and impurities forming protective layers. Besides, comparing to liquids, the absence of the displacements by migration and convection phenomena makes of the solids as kinetically poor reactants. Nevertheless, their low diffusivity could be improved depending on the matrix content. In this part we present the preceding studies in the field of the hydride systems of interest. Firstly, we describe their atomic structures then we summarize the existing thermodynamic and kinetic data of the directly involved substances or that may be formed in the powders. This part will also deal with the steps followed in our approach for the study of the complex hydrides.

1 Crystalline structure

1.1 $LiBH_4$

The crystal structure of $LiBH_4$ compound has been studied in different publications [1-4]. The structure at room temperature, as identified firstly by Harris and Meibohm [1], is orthorhombic with the space group *Pcmn* equivalent to *Pnma*. By thermal analysis method, Fedneva et al.[5] detected the presence of a polymorphous transition in the temperature range 381 – 385K. The high temperature phase (386-554 K), originally indexed to be tetragonal [2,6], was later identified to be hexagonal with new lattice parameters and space group $P6_3mc$ [3,4]. As showed in the figure 1.1, the new phase exhibits less compact structure as shown by the cell volume with reorientation of the $[BH_4^-]$ group. Thus $LiBH_4$ could exist in three phases: orthorhombic low temperature phase, hexagonal phase with a short temperature range and liquid phase since the compound melts at around 553 K.

The calculation of the lattice parameters was also reviewed many times [2-4]. This reflects the complex structure of $LiBH_4$ mostly for the high temperature short range phase. In fact, this subject is still under discussions due to disagreements between theoretical and experimental methods. Indeed, this quantity could affect directly the entropy of the transition of

$LiBH_4$. This point will be discussed in the thermodynamic assessment of $LiBH_4$ compound. Table 1.1 presents the unit cell volume of the two solid phases given in literature. For both solid phases, the unit cell volume increase with temperature. By means of X-ray reflections, Only Filinchuk et al.[4] reported the negative volume change at the phase transition in agreement with Pistorius's high pressure phase diagram [2].

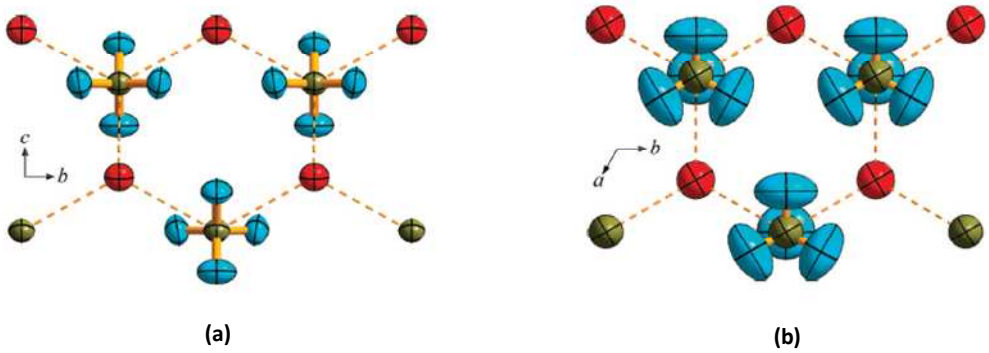

Figure 1.1. Crystal structure of $LiBH_4$. Li (red spheres) coupled to the BH_4 units : (a) low temperature orthorhombic phase at 225 K and (b) high-temperature hexagonal phase at 535 K [4]

Soulié et al.[3] suggested a first-order polymorphous transition involving a discontinuity in the enthalpy during which the tetrahedral $[BH_4^-]$ anions are reoriented. The transition has a hysteresis of about 2 to 8 K [2,7,8]. The data for the high-temperature structure are consistent with a rotational disorder of the tetrahedral $[BH_4^-]$ anions around their trigonal axis.

The compressibility of the MBH_4 compounds (M = Li, Na, K, Rb, Cs) was predicted by Vajeeston et al.[9] using DFT calculations by calculating the bulk modulus. Strong covalent interaction between B and H in the $[BH_4^-]$ anionic complex and ionic bonding character between $[BH_4^-]$ and M^+ were deduced. The compounds MBH_4 were classified as wide band-gap insulators. Kang et al.[10] calculated the structure $P6_3mc$ to be less stable then *Pnma*. Filinchuk et al.[4] attributed the disagreement between theoretical predictions and experiment to the disorder phenomena and lattice anharmonicity.

Recently, Tekin et al.[11] using first principle calculations, on the basis of Soulié and coworkers XRD study, optimized the two structures. In addition, new high-temperature monoclinic *P2/c* structure, which was found more stable than the observed one, is proposed.

Consequently, the calculation methods predict a tetrahedral $[BH_4^-]$ configuration [9,12], while experiments found a distorted $[BH_4^-]$ anionic complex [3,7]. Boron atom constructs a sp^3 hybridation and forms covalent bonds with four surrounded H atoms [12]. All the hydrogen atoms present a hydride character different from those of proton entities due to their high electron affinity compared to boron.

Table 1.1. Unit cell volume of the $LiBH_4$ phases

Authors and ref.	Method	Measured/ calculated quantity	Purity %	Unit cell volume / Å^3				Observations
				T / K	Low T (Z=4)	T / K	High T (Z=4)	
Harris and Meibohm [1]	Volumetry/XRD	ρ = 0.66 g.cm^{-1}	--	--	217.62	--	--	Recal. ρ = 0.666 g.cm^{-1}
Davis el al. [13]	Volumetry	ρ = 0.681 g.cm^{-1}	99.23	298	212.47	--	--	Liquid toluene displacement
Semenko et al.[6]	XRD	Lattice parameters	98.7	293	219.2	423	275.13	Identified tetragonal
Pistorius [2]	High pressure piston cylinder/XRD	Volume change /Lattice parameters	--	298	217.4	413	210.4	Identified tetragonal
Soulié et al.[3]	Synchrotron powder diffraction	Lattice parameters	95	293	216.68	408	220.08	Identified hexagonal. [BH_4^-] distorted
Zuttel et al.[14]	Synchrotron powder diffraction	Lattice parameters	95	298	216.2	--	--	Slight H_2 release at T_{trans}
Miwa et al.[12]	DFT calculation	Lattice parameters	--	--	212.8	--	--	High T structure far from expt.
Vajeeston et al.[9]	DFT calculation (VASP)	Lattice parameters	--	0	213.64	--	201.27	Variant $KGaH_4$-type. [BH_4^-] Tetrahedral
Kang et al.[10]	DFT calculation	Lattice parameters	--	--	209.82	--	--	Cutoff energy 270 eV
Zarkevich and Johnson [15]	DFT/MD calculations	Lattice parameters	--	0	212.1	--	202.03	Li and B fixation from expt.
Filinchuk et al.[4]	Single crystals diffraction	Lattice parameters	95	225	213.5	535	227.76	Dynamic disorder at T_{trans}
Tekin et al.[11]	First-principles	Lattice parameters	--	--	207.61 212.11	--	234.9 --	Optimized [3] Proposed

1.2 MgH_2

Magnesium hydride has a tetragonal lattice unit cell (rutile type). Meanwhile, pure Mg has an hexagonal crystal structure. The most stable phase is labelled as β-MgH_2 in order to distinguish it from the other phases γ-MgH_2 and α-MgH_2 which can be formed during the milling process or under high pressure constraint respectively [16]. MgH_2 phases will be discussed in the sample preparation part using high energy ball milling. Figure 1.2 shows the structure of β-MgH_2 phase where Mg is located at the tops and the center of the tetrahedron and hydrogen has well defined coordinate system.

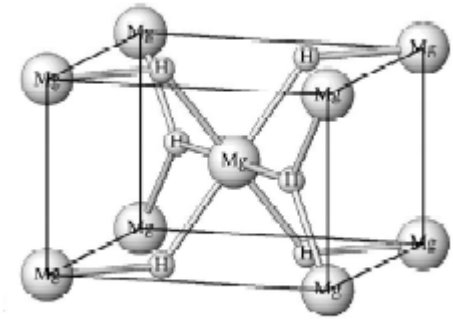

Figure 1.2. Crystal structure of β-MgH_2 (rutile type)

As stated by Noritake et al.[17] , there are significant weak covalent bonds between Mg and H as well as between H and H. The weak bonding constitutes an advantage for hydrogen storage yield in term of reversibility and heat of the reactions.

2 Thermodynamic data for Mg-Li-B-H systems

2.1 Li-B-H system

We started the bibliography study of Li-B-H system mainly with the $LiBH_4$ compound in order to obtain thermodynamic parameters and to be able to plan mass spectrometric measurements. Thermodynamic assessment including thermodynamic data collection is reported in chapter 4 particularly dealing with heat of formation and the specific heat of $LiBH_4$.

For $LiBH_4$ compound, earlier mass spectrometric measurements have been performed with special cell coupled to a mass spectrometer by a short capillary tubing [18]. B_nH_m molecules including polymers in the gas phase have been proposed from the observed ions. For this system, the H_2 main species and some B_nH_m species are observed but some minor species could also exist as pollutants. Collected data with details about how the experiments were conducted for Li-B-H system are given in the table 1.2.

The calculated Li-B-H phase diagram at $T < T_{melt}$ of $LiBH_4$ using FactSage software and its available data bank (SGTE) is illustrated in the figure 1.3. Following H_2 loss, the phases in equilibrium should correspond to the stable three-phase system $LiBH_4$-LiH-B. The phase diagram at $T > T_{melt}$ could not be calculated due to lack of data for the liquid phase.

Table 1.2. collected data for Li-B-H system: Method and mechanism

Authors and references	Studied system	Methods	Experimental conditions	p / bar	T / K	Proposed reactions	Observations	
							Detected ions by mass spectrometry	Other conditions
Shevchenko et al.[18], (1986)	$LiBH_4$ (for gas phase evolving)	mass spectrometry (MS)	Quartz holder soldered to a connecting tube (Fe-Co-Ni alloy)	vacuum	293-673	$nLiBH_4 = Li_nH(BH_4)_{n-1} + BH_3$ and $BH_3 \rightarrow B + 3/2H_2$ $2BH_3 = B_2H_6$	H_2, B, BH_3, Li, B_2H_6, BH_5, BH_7, B_2H_8, B_2H_{10}	Connection to the ion source through 2 dosing valves. Heating rate:5Kmin^{-1}. Detection of 3 masses simultaneously. Holding samples at isothermal cond. for 30min with closed valve after pumping, then the valve is opened and mass spectra recorded in 1-100m/z.
Ihle and Wu [19], (1974)	Li - H	MS-Knudsen effusion method	UHV and Quadrupole mass filter		700-873	LiH (s. sat. Li) = Li (l. sat. LiH) + 1/2 H_2 (g)		Knudsen cell in Mo with 0.2mm orifice Ø. Use of a shutter to distinguish atoms / molecules effusing from residual gas. PtRh/Pt thermocouple.
Smith and Bass [20], (1963)	$LiBH_4$				>673	$LiBH_4 = LiH + B + 3/2H_2$		
Züttel et al. [14], (2003)	$LiBH_4$	XRD - Synchrotron (SLS)/Mass flow controller				H_2 desorption in different reaction steps and T regimes		Use of additives such as SiO_2
Orimo et al.[21], (2005)	$LiBH_4$/ LiH + B	DSC/XRD	100 mg in Mo crucible then sealed		298-550	$LiBH_4 = LiH + B + 3/2H_2$		Structural differences before and after the melting. Substitution (or mixing) of $LiBH_4$ (10 at.% of Li) with Mg : T_{des} reduced to 30 K. comparable behaviors with $LiNH_2$.
Fedneva et al.[5], (1964)	$LiBH_4$	ATG / ATD	Chemical synthesis		298-873	$LiBH_4.C_4H_8O_2$		Losses of dioxan at 85℃ with simultaneous evolution of hydrogen content

Table 1.2 (continued): Collected data for Li-B-H system: thermodynamic parameters

Ref.	Studied system	Other indications	Conditions	p / bar		T / K			ΔG / kJ.mol^{-1} H_2	ΔH dec. kJ.mol^{-1} H_2	Other informations
				Des.	Abs.	Dec.	Des.	Abs.			
[18]	$LiBH_4$	recrystallised from diethyl-alcohol	If the valve is totally open and with too few products only H_2 is detected (vice versa). At high m/z, presence of complexes								Main H_2 peaks at temperature increase. BH_5 species is reported to be more stable than $BH_3.H_2$ adduct.
[19]	Li - H			log p / Torr = f(1/T)					(-70,16±2,1)	(-91,21±2,1)	Δ_fH from 2nd and 3d Law. H_2 activities calculated as: $\Delta_fG = f(pH_2)$
[20]	$LiBH_4$				100	>673		<623		68,6	
[14]	$LiBH_4$	Mark-tubes ID 1mm and sealed. 200-300mg sample	use of SiO_2 additive				473				Low T desorption from orthorhombic phase: small amount of H_2.
[21]	$LiBH_4$		synthesized from elements at moderate conditions	10	350		873	873			Hydriding the mixture LiH and B during 12h. In this case the effect of Mg is not investigated.
[5]	$LiBH_4$	Chem. Synthesis	554 K fusion, 385 K polymorphic trans.								

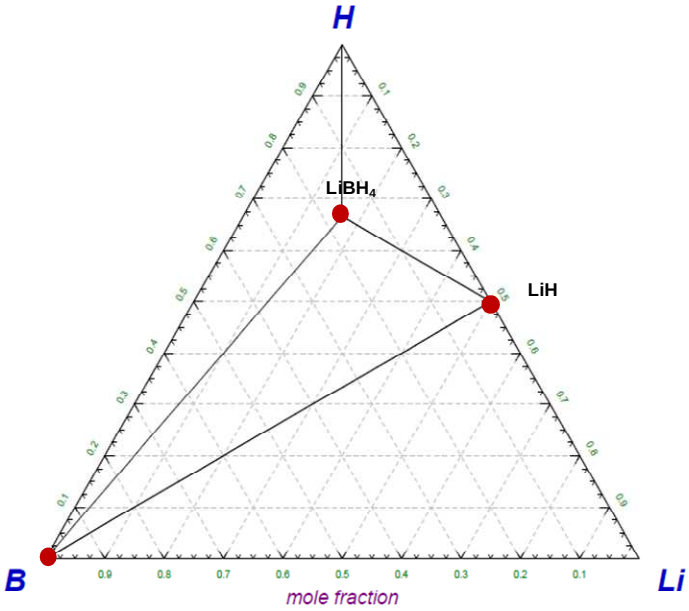

Figure 1.3. Ternary Li-B-H phase diagram

To our knowledge the Li-B system is not well known (no optimization available), meanwhile the system Li-H is well assessed which could serve to the study of the upper part of the ternary phase diagram. The presence of oxygen impurities at high temperature leads to consider also the B-H-O system. In that case under various conditions, the gaseous species H, H_2, B, O, O_2, B_2O_3, B_2O_2 and BO could exist. B_2O_3 was thought to be the most important boron species, with minor amounts of BO and B_2O_2. Reversely, some authors suggest that HBO_2 is the most important boron species [22].

2.2 Mg-H system

The standard enthalpy of formation of MgH_2 was optimized by Bohmhammel et al.[23] when using several experimental data ($\Delta_fH°_{298}$ = – 74.70±1.3 kJ.mol^{-1}). The retained value agree with the reported one by Stampfer et al.[24]. For MgH_2, it was observed that H_2 gaseous species is the only gas detected at moderate temperature and pressures.

From their experiment and existing data, the authors calculated the Gibbs energy, enthalpy and entropy of formation for the β-phase, while the heat capacity was measured until 360 K [23]. Up to now there is no study devoted to the high temperature heat capacity of MgH_2. The previous existing data were estimated from MgF_2 [25].

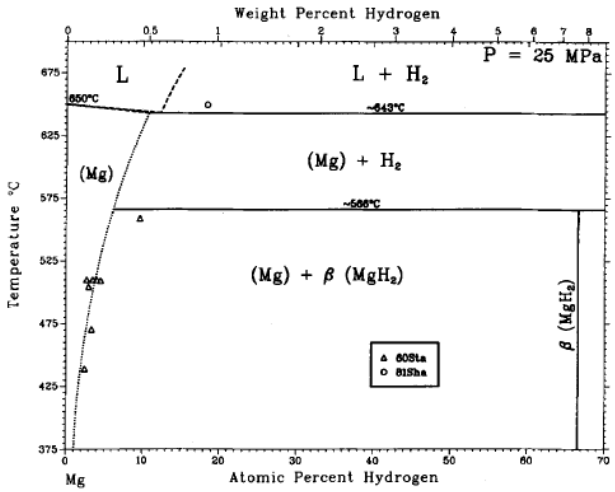

Figure 1.4. Assessed Mg-H phase diagram [26]

Figure 1.4 presents the assessed Mg-H phase diagram. At moderate hydrogen pressure, the only hydride phase existing in equilibrium with Mg is MgH_2 with a solubility in Mg solid that could reach 10 at.% of H_2. At high pressure (250 bar), a peritectic-type phase diagram is determined at 839 K. Rummel [27] studied the Mg-H_2 system in the temperature range 560-800 K. The system was used as a heat protector due to its endothermicity. The author found that MgH_2 decompose at 560 K and the heat of formation of the hydride is a third of the heat of combustion of hydrogen i.e. $\Delta_f H°(MgH_2) \approx 1/3 \bullet \Delta_f H°(H_2O) = -39.2 \cdot 10^3$ kJ.Kg^{-1} H_2 = -79.03 kJ.mol^{-1} H_2.

Stampfer et al.[24] measured by a static method the decomposition pressure of MgH_2 and calculated the solid phase composition. The solubility of H_2 in magnesium was deduced as 2 at.% at 440℃ and 10 at.% at 560℃. In this study [24], they reported the thermodynamic functions of formation of MgH_2. The experiment was carried out in steel container with thick walls (to prevent from H diffusion) surrounded by a furnace. The device allowed measurements of pressure p_{max} = 350 atm and temperature up to 600℃. The measure ments took account of the solubility and the diffusion of hydrogen through the walls container. For measurements of the pressure of decomposition, the container is loaded with the desired amount of Mg (fine turnings) then welded with the tube of pressure measurement. After vacuum evacuation, hydrogen is introduced at the same temperature and pressure (200-300 atm) to convert the major part of magnesium into magnesium hydride. The studied equilibrium in the case of the system Mg-H, corresponds to the reaction,

$$Mg\ (s, \text{std with } H_2) + H_2\ (g) \leftrightarrow MgH_2\ (s) \qquad (1.1)$$

MgH_2 being considered as stoichiometric.

The volumetric measurements along isotherms allowed the determination of the compositions. The hypo-stoichiometric composition at the high extreme is $MgH_{1.99\pm0.01}$ in the studied temperature range. The pressure of decomposition was converted into fugacity by using the equation of state of Beattie-Bridgeman for real gases. In the case of hydrogen the least square regression leads to the equation:

$$R\ln f(H_2) = \frac{(-17785 \pm 76)}{T} + 32.28 \pm 0.45 \quad (1.2)$$

The authors [24] described the difficulty to reach the equilibrium state due to the competitive diffusion of hydrogen through the walls. Thus, quantitative conversion of magnesium into hydride is not complete. The best yield which was determined contains: 93.1% MgH_2, 3.0% MgO and 3.9% Mg. In general, the MgH_2 content is slightly variable and Mg is always present.

2.3 Mg-Li-B-H system

For Mg-Li-B-H system few data exist in literature. The reported data in table 1.3 contain data for the quaternary system. Unfortunately, the thermodynamics of the compounds are not well known. The existing studies of the quaternary system are only comparative kinetic purposes in presence or not of additives for catalytic effect, but are not aimed at the quantification of thermodynamic properties.

Table 1.3 summarizes most studies of the quaternary system using mass spectrometry, calorimetry and other techniques of characterization of the phases.

Table 1.3. collected data for Mg-Li-B-H system: Method and mechanism

Authors and references	Studied system	Methods	Experience conditions	p / bar	T / K	Mechanism and processes	Observations
Bösenberg et al.[28], (2007)	RHCs : MgH_2-$2LiBH_4$ / MgB_2-2LiH	HP-DSC/TG/MS and In situ synchrotron XRD (Sievert-type apparatus)	Sapphire capillaries. Heated with W wire and T controlled with a regulator / thermocouple inserted in the powder-bed	1-150	298-738	$MgH_2 + 2LiBH_4 = Mg + 2LiBH_4 + H_2 = MgB_2 + 2LiH + 4H_2$	The samples are premilled in spex (mixer mill) for 5h before milling the mixture in Fritsch 5 (planetary ball mill). H_2/Ar recorded by MS.
Kubaschewski et al.[29], (1993)	MgH_2-$2LiBH_4$	Thermodynamic data compilation				$MgH_2 + 2LiBH_4 = MgB_2 + 2LiH + 4H_2$	
Vajo et al.[30], (2005)	MgH_2-$2LiBH_4$ / MgB_2-2LiH	Isothermal measurements / PCT/XRD/MS/FTIR(not shown)	Sievert apparatus. XRD analysis with sample sealed in glassy capillaries			$MgH_2 + 2LiBH_4 = MgB_2 + 2LiH + 4H_2$	Including 2-3 mol.% $TiCl_3$ additive.
Barkhordarian et al. [31], (2007)	LiH + MgB_2/LiH + B/CaH_2 + MgB_2		Spex mill. Exposed to 2 differents H_2 p/bar:T/K; 200:573(48h) and 350:673(24h).	150	298-923	$LiH + B + 1/2H_2 = LiBH_4$, $MgB_2 + 2LiH + 4H_2 = MgH_2 + 2LiBH_4$, $MgB_2 + CaH_2 + 4H_2 = MgH_2 + Ca(BH_4)_2$.	Systematic study of the effect of reactants on the kinetic barriers. $Ca(BH_4)_2$ is synthesized, for the 1st time by solid-gas reaction.

Table 1.3 (continued). Collected data for Mg-Li-B-H system: thermodynamic parameters

Ref.	Studied system	Other indications	Conditions	p / bar		T / K				ΔG / kJ.mol^{-1} H_2	ΔH		Other informations
				Des.	Abs.	Equ.	Dec.	Des.	Abs.		decomp. kJ.mol^{-1} H_2	Reaction kJ.mol^{-1} H_2	
[28]	MgH_2-2 $LiBH_4$ / MgB_2-2LiH	average cristallite size:10-15nm	Add of dopants (VCl, Ti-isopropoxide, SiO_2). H_2 flow 20 ml.min^{-1}	3	50			673-723	523-573				Desorption in two-step reaction. If suitable additives, kinetic could be improved. T_{dec} (MgH_2) = 538 K. 5 K.min^{-1}.
[29]	MgH_2-2$LiBH_4$				1	442 (1bar)						-46	
[30]	MgH_2-2$LiBH_4$ / MgB_2-2LiH	1,2g of mixture milled for 1h.	for the 1st hydrogenation: slow kinetic. Under dynamic vacuum, dehydro. Formation of Mg metal instead of MgB_2.	5 to 6	100	498 (1bar)		723	503-623		-40,5		Mass spectra analysis of the desorbed gas using a residual gas analyzer (RGA), only H_2 detected. Low conc. of B_2H_6 and HCl can't be ruled out.
[31]	LiH + MgB2 / LiH + B / CaH2 + MgB_2					442 (1bar, LiH+MgB_2), 402 calcul. (1bar, LiH+B), <159 ($Ca(BH_4)_2$)	> 593			(-7 for LiH+MgB_2) and (-19 for LiH+B), no therm. data exist for $Ca(BH_4)_2$		(-23 for LiH+MgB_2) and (-33 for LiH+B)	Δ_fH is reduced (10 kJ.mol^{-1} H) when using MgB_2 instead of B. The effect of MgB_2 is not clear. Formation of [BH_4^-] complexes. $Ca(BH_4)_2$ is the most promising.

3 Hydrogen storage: kinetics, reversibility and catalysts

3.1 MgH_2

Magnesium hydride is able to release and absorb hydrogen without deterioration. It offers high weight and volume capacity at low costs because it could contain 7.6 wt.% of H_2 (Table 1.4) in a reversible way compared to many other metal hydrides [32]. But this threshold is hard to reach due to rough dispersion and sintering of the particles. However, the MgH_2 hydride conversion into hydrogen molecule accompanied by electron transfer ($2H^- \leftrightarrow H_2 + 2e^-$) is still slow due to the formation of Mg agglomerations surrounding the MgH_2 matrix (formation of a diffusion layer) and vice-versa i.e. from H_2 into H^-.

Table 1.4. Hydrogen content of simple binary hydrides in comparison with gaseous and liquid hydrogen. T_{dec} and kinetic reversibility of the hydrides are also given [33-35]

Compound	Wt% H_2	Volumetric density N_H (atoms H/ml $\times 10^{-22}$)	T_{dec} (°C)	Kinetic reversibility
H_2, liquid	100	4.2	—	—
H_2, gas (100 atm)	100	0.49	—	—
LiH	12.6	5.3	720	Poor
NaH	4.2	2.3	425	Good
CaH_2	4.8	5.1	600	Good
MgH_2	7.6	6.7	330	Very poor
AlH_3	10.0	8.84	150	Irreversible
TiH_2	4.0	9.1	380	—[a]

[a] No literature data available.

Magnesium and magnesium hydride equilibrium binary system has been reported previously in many publications which show that the absorption and desorption reactions require activation of such material due to the low kinetic rates [24,36,37]. However, the milling of magnesium hydride at high energy improves considerably the performances of the material regarding the cycling of hydrogen by decreasing the activation energy [37]. Mechanical grinding by solid phase ball-milling has been shown as promising method not only due to the particle size reduction, but also to morphological structure changing. The tetragonal β-MgH_2 phase is the compound the most present. A small fraction of the orthorhombic γ-MgH_2 phase was observed as reported previously by Schulz et al.[37], when pure MgH_2 is milled. In fact, the γ-MgH_2 phase formed through the milling process by restructuration in the crystal lattice of β-MgH_2 phase is not enough abundant [36-38]. This structure considered as a metastable phase was also observed [37,39] in the stressed β-MgH_2 under high pressure effect.

Similarly to MgH_2, the hydrogenation of Mg is dependent on the size of the particles. By reducing the specific surface area, this interfacial phenomenon is illustrated in the figure 1.5 where fast kinetics was observed for grain size less than 25 µm.

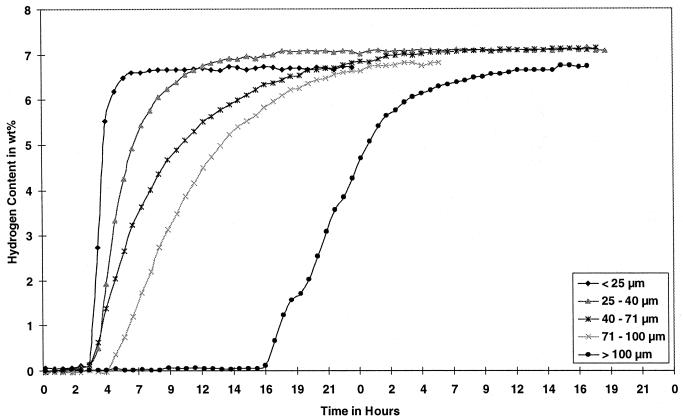

Figure 1.5. Progress of the hydrogenation of the Mg powder samples with different particle sizes at temperature 350℃ and pressure up to 30 bar [40]

The effect of magnesium, as both catalyst and reactant, concerning the (de)-hydrogenation kinetic is low and poor. In the aim to induce the formation and the dissociation of hydrogen molecule then to allow a bonding with magnesium at low energy, many researchers advice the use of metals with particular affinity toward hydrogen, likely noble metals as well as transition metals (in oxide or saline forms), some of them being already applied in electrocatalysis and electrochemical reactions [41,42]. Hence, the introduction of small amounts of transition metal nanoparticles can improve the H-sorption in the nanostructured metal hydride. Indeed, MgH_2 is constrained during milling when they are mixed with transition metals. The activation energy of hydrogen desorption is reduced drastically while the thermodynamic properties (enthalpy and entropy of formation) of MgH_2 are not changed [43]. Moreover, the role of transition metals in catalysis is to chemisorb hydrogen molecules and split into hydrogen atoms for bonding with magnesium sites with a lower energy barrier, consequently reducing nucleation and growth phenomena.

The addition of elemental transition metal catalysts such as Ni, Ti, V, Cr, Nb enhance the kinetic process during hydrogen-sorption and desorption [41,43,44]. Meanwhile, under hydrogen pressure of 10 bars, Ti and V have shown the best catalytic effect compared to Fe, Ni and Mn in both cases (absorption and desorption) [43]. The fluorine transition metals have showed to decrease the decomposition temperature of MgH_2 (Fig.1.6) namely Ti, Ni, V and Nb are more effective than Fe, Zr and Cr fluorides [45]. Oelerich et al.[41] have studied the influence of abundant metal oxides on the sorption behavior of Mg-based system. The Mg_2NiH_4 phase was synthesized by mixing MgH_2 with elemental nickel. In the Mg_2Ni alloy powder, the addition of catalyst such as Mn_2O_3 has a negative effect during absorption and positive one during desorption which explain that different behaviors of the catalysts could

appear toward mono(di)atomic hydrogen. Nevertheless, the milling process of metal-based hydride, mainly when many metallic elements are present, can induce the formation of new structures [32,36,37,43,46]. The resulting products of the milling depend on the relative affinity of each metal to the other elements and with hydrogen. Furthermore, intermetallic compounds such as $LaNi_5$, $FeTi_{1.2}$, $ZrFe_{1.4}Cr_{0.6}$ have been reported to improve the kinetic of reaction of magnesium at high temperature by activating hydrogen reactions (> 300℃) [47,48].

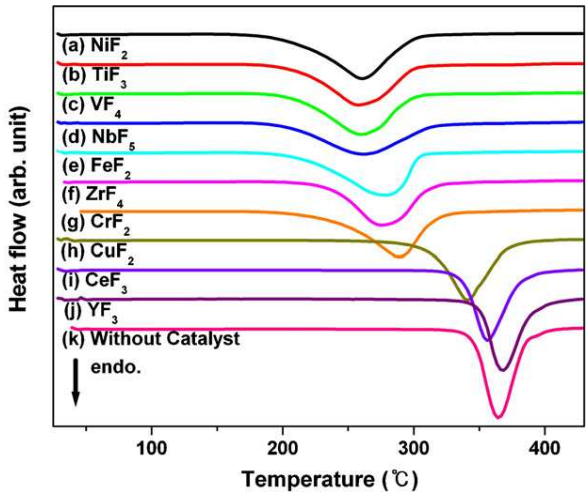

Figure 1.6. DSC curves of MgH_2 with 1 mol% transition metal fluorides [45].

It was proved that the catalytic effect of Ti exhibits the most rapid absorption kinetics followed by V, Fe, Mn and Ni [43,49] in decreasing order. Nickel is not as good catalyst as Ti and V, even though it was commonly used in Mg and its alloys [36]. Moreover, TiNi-based alloys have been tested as hydrogen storage electrodes where Ti has showed an effective improving of the electrode cycling life. Unlikely, dissimilar results have been found due to different structures for the same elemental compositions [50,51]. Nickel oxides can be readily reduced by hydrogen to form nickel clusters on the surface [43]. For that, the introduction of nickel could protect the oxidation of titanium and its catalytic effects toward hydrogen. Moreover, the incorporation of Ni increases the surface area and creates interfaces in the crystal lattices.

The formation of the stable phase TiH_2 was described in the literature during mixing MgH_2 and Ti. Idem in the case of V, the phase $VH_{0.81}$ was also formed when Ti is substituted to V. Mg_2NiH_4 structure is also formed when milling MgH_2 with single Ni as described elsewhere by observing the dehydrogenated phase Mg_2Ni by XRD [43].

The present bibliographic analysis of MgH_2 system and its additives used before will help us for the choice of suitable catalysts in our improvements of the kinetics of MgH_2 reactions.

3.2 $LiBH_4$

In contrast to magnesium hydride, lithium borohydride has been less studied. This is because it is thermodynamically reversible under rigorous conditions of pressures (350 bar) and temperature (873 K) and presents unfavorable kinetics. The decomposition of $LiBH_4$, in the temperature range 300-873 K of interest, is presented usually as occurring with two steps where the second step is probably faster:

$$LiBH_4(s,l) \rightarrow LiH(s,l) + BH_3(g) \rightarrow LiH(s,l) + B(s) + 3/2H_2(g) \quad (1.3)$$

This reaction in the first step is an exchange of hydride H^- then H_2 is released in the second step. Knowing that H^- and H_2 have different chemical potentials, these two reactions will likely express different affinities toward catalysts. Due to its instability, BH_3 will be hardly formed during the absorption process of hydrogen. Probably, it would necessitate the intervention of two types of catalyst with two different natures. We consider that the choice of catalyst must be done on these two criteria; nickel based catalyst is known to be suitable for the case of solids and for liquids which have solubility properties of hydrogen close to those of amorphous phases. A second choice would be an amorphous like vitreous carbon and silica, or a metal of transition less electronegative than nickel or nickel salt.

$LiBH_4$ compound can release ca. 14 wt. % of hydrogen at elevated temperature (T > 400℃) if reaction (1.3) is considered. The thermal desorption spectra of $LiBH_4$ mixed with SiO_2 show three peaks corresponding to the probable compositions $LiBH_{3.6}$, $LiBH_3$ and $LiBH_2$ [52]. The compounds LiB_3H_8 and $Li_2B_nH_n$ (n = 5-12) are also proposed in the literature as intermediate compounds of decomposition of $LiBH_4$ [53].

3.3 MgH_2 – $LiBH_4$

Complex borohydrides of light metals are promising hydrogen storage materials due to their high hydrogen capacity. The hydride system $LiBH_4$ – MgH_2 has shown interesting functionalities for hydrogen storage, as reported by Vajo et al.[30] by reacting the complex hydride $LiBH_4$ with another compound of metal hydride such as MgH_2. Indeed, this has allowed a considerable lowering of the pressure and the temperature of the equilibrium reaction. The total reaction of the system in the case of the ratio x = 2 under heating is supposed as follows:

$$MgH_2 + 2LiBH_4 \leftrightarrow MgB_2 + 2LiH + 4H_2 \quad (1.4)$$

Bösenberg et al.[28] report the best improvement of the kinetic and the temperature of the hydride composite when Ti-isopropoxide and VCl_3 was added as catalysts (Fig.1.7). The

mass spectrum of Ti-isopropoxide heated at 180℃, s hows the presence of several possible fragments with or without titanium [54].

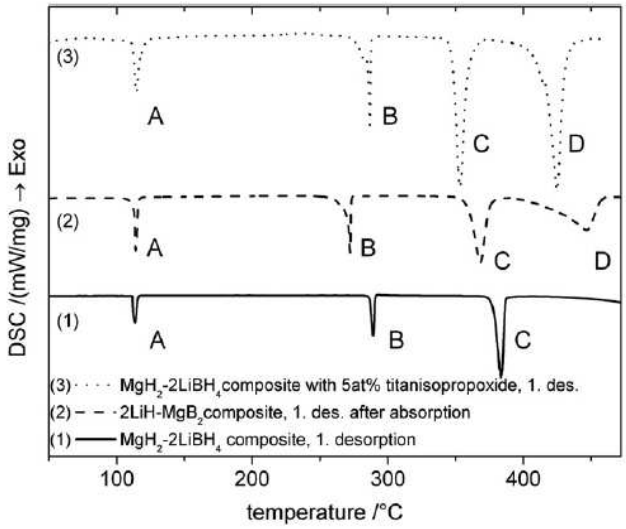

Figure 1.7. High Pressure-DSC of MgH_2+2$LiBH_4$ after (1) milling, (2)initial hydrogenation (3) Ti-isopropoxide addition (5 K.min^{-1}, 20 ml.min^{-1}and 3 bar H_2) [28]

Comparable behavior is obtained when carbon nanotubes were added as shown in the figure 1.8.

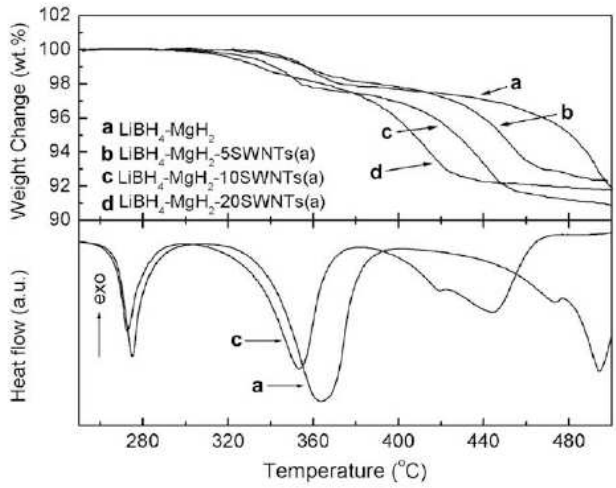

Figure 1.8. DSC of MgH_2+2$LiBH_4$ with addition of carbon nanotubes (SWNTs) under Ar gas flow at 10 K.min^{-1}

Single-walled carbon nanotubes (SWNTs) were mechanically milled with MgH_2/2$LiBH_4$ mixture. As reported by the authors, SWNTs exert influences by “micro-confinement” effect, by prohibiting particle agglomerations and the spreading of the product phases. Thus the material facilitates subsequent hydrides restoration [55].

The kinetic barrier for the formation of $LiBH_4$, $NaBH_4$ and $Ca(BH_4)_2$ are drastically reduced when MgB_2 is used instead of B as starting material (reduction of the activation enthalpy by about 10 $kJ.mol^{-1}$ H). The observed effect is attributed to the higher reactivity of B in MgB_2 to form $[BH_4^-]$ complexes. $NaAlH_4$ is the only complex hydride reversible at moderate pressures and temperatures. It exhibits a temperature of the desorption of about 130℃ (capacity < 5 wt.%). Other complex hydrides $LiAlH_4$ of analates are considered thermodynamically instable. Some authors report that complex borohydrides have high desorption temperatures and cannot be formed at moderate temperature and pressures [31].

These authors have followed several approaches:

- The first is to substitute specific atoms in the structure of the hydride by dopant atoms.
- The second is to modify the reaction by choosing suitable reactants (as MgB_2 instead of B) that present another thermodynamic path.

The formation of B_4C or CaB_6 instead of MgB_2, in the case of carbon and calcium based materials, does not show any hydrogenation. Unlikely, kinetic effect of MgB_2 is not clearly identified. The majority of the works involves the implication of carbon (in various forms) in magnesium hydride. Concerning the complex hydride ($LiBH_4$), it exist very little applications at the moment. The form most used in the literature is Mg_2C and Mg_2C_3. These two materials can be synthesized by mechanical milling starting from pure Mg and carbon (graphite) after its amorphization [56].

Simple carbon nanotubes showed an interest for their use as catalysts in complex hydrides such as in the $MgH_2/LiBH_4$ system. Indeed these materials were used in various forms (10 wt. %, entangled with amorphous carbon, carbon nanoparticules, nanoparticules of Ni/Co/Fe (20 wt. %)). They were prepared mechanically by milling with $LiBH_4/MgH_2$ during 1h using planetary mill under argon atmosphere. The first motivation which brought back to the study of these materials is that carbon nanotubes improve the exchange of hydrogen and kinetics of formation of the hydrides materials MgH_2 and $LiBH_4$. After dehydrogenation (450℃) and hydrogenation (400℃ / 75 bars), the presence of th e phase $MgNi_{2,5}B_2$ is detected in the case of entangled Ni into nanotubes. On the other hand, it was shown that elemental Ni has a negative kinetic effect [55].

Among interpretations, carbon nanotubes can act as milling assistant while, graphite exerts an effect kinetically limited. Consequently, carbon nanotubes exert influences by microconfinement effect as the authors said, to inhibit particles agglomerations, thus to facilitate the diffusion of the solid phases during the hydrogenation reactions [55]. So this will allow a

more effective restoration i.e. return to the initial conditions of the starting hydrides after recycling. Probably, the carbon nanotubes create a micro-confined environment which supports the solid-liquid reaction. It was also noticed that the materials prepared starting from the dehydrogenated state are more stable with regard to the capacity of the exchange of hydrogen.

This is in agreement with previous work which reported that the addition of carbon plays a mechanical role by facilitating the process of milling due to the creation of finer particles while improving the absorption of hydrogen. It was also noted that the addition of carbon nanotubes, called dispersive medium, to magnesium hydride increases the effectiveness of milling because fine particles and uniform powders were obtained. On the other hand, doping with carbon has only one minor role in the dissociation of hydrogen on the surface but a rather remarkable role by facilitating hydrogen diffusion through the interfacial layers and so contributes to the improvements of the re-organization of MgH_2 by increasing the real storage capacity of hydrogen. Consequently, this additive improves the yield of the process of dehydrogenation of MgH_2 (300℃) [57].

Another study [58], shows that carbon in various forms entangled nickel, improves the kinetics of decomposition of MgH_2 in comparison to nickel mixed with carbon or nickel alone in agreement with reference [55]. The effect of these various types of carbon containing nickel (1-2 wt.%) seems to appear quasi similar. It was also reported that carbon improves the kinetics of decomposition of MgH_2 even in the form of mixture with another catalyst.

This improvement is probably due to the reduction of the size of the particles and of thermal conductivity of the prepared materials. Contrary to samples containing only nickel, carbon supported catalysts do not show any change in the kinetics of decomposition nor the quantity of hydrogen involved after five cycles of (dis)charge [58].

The Mg-B-C system was much studied in the last years after the discovery of the superconductivity of MgB_2 at the beginning of the century. For that, it was important to know the optimal conditions of preparation and the effect of addition of doping agent (carbon) for the improvement of the superconductivity.

For MgB_2 synthesis, chemical doping is an effective approach to improve its superconductivity properties. As carbon has one more electron than boron, it is expected that electrons move in the system by the substitution of carbon. In a study where the samples are prepared by mechanical milling and then compressed in pellets, the majority of the $Mg(B_{1-x}C_x)_2$ phases, are formed after the fusion of Mg (650℃) when star ting from amorphous compounds for boron and carbon [59].

The experiment had shown that the reaction between Mg and B to form MgB_2 is done by the diffusion of Mg through boron. The diffusion and evaporation of Mg induce the formation of porous products. Note that the formation of MgB_x phases starting from Mg and B depends on the temperature. For that, it could be distinguished:

- solid – solid reaction: the onset temperature of reaction is 495.6℃ for the sample Mg:B = 3:2.
- solid – liquid reaction: the onset temperature of reaction is between 650 and 660℃ for the most samples [60].

In the case of the system Mg-B-C, the dominant phase remains MgB_2. But small amounts of MgB_4 and Mg_2C_3 are also formed and boron remains in excess at this stage of reaction. Moreover, MgB_4 reacts with Mg to form MgB_2. The elemental Mg is also present. The substitution of the boron sites by carbon in the MgB_2 lattice increases the stability of the MgB_2 phase. Indeed, the analysis by DSC and XRD indicate that the temperature of reaction of Mg with B and the stability of MgB_2 phase increase for the samples doped with carbon. On the other hand, the reaction kinetic rate of Mg with B decreases with the increase of the carbon content [59].

4 Conclusion

The present bibliographic study of the hydrides allows detecting the discrepancies which prevent the reactions to proceed as intended. Indeed, thermodynamic assessment seems necessary in order to establish the thermodynamic control parameters for the compounds before being applied to the hydride mixtures and built assumptions about kinetic limitations.

Spectrometric measurements with Knudsen cell or a similar vaporization reactor are very few in the literature, and this method will enable us to determine the enthalpy of the reactions of decomposition and to deduce the enthalpy of formation of $LiBH_4$. We plan measurements of specific heat of $LiBH_4$ due to its lack in the literature in particular above room temperature.

At that time, thermodynamic calculations, will give us information about phases which could exist in our chemical reactor in particular in the case of mixtures. Indeed, the use of the hydrides in mixtures allows the lowering of the conditions of cycling of hydrogen.

Also we could conclude on the following points:

- The milling process is effective for the reactivation of the hydride powders.
- The addition of additive is as important as the reactivation by milling to accelerate the reactions with slow kinetics. We plan to test some additives in particular Ni and C-based additives.

- Carbon showed interesting properties which confer to powders a remarkable dispersive effect by preventing the agglomerations and local nucleation phenomena. The important heat absorbent effect of carbon will be able to also play a role in the homogeneous thermal process inside these materials.

Also we started constructing an assembly by coupling a milling device to a mass spectrometer for measurements of the gaseous phase presents at the moment of milling.

References

[1] P.M. Harris, E.P. Meibohm, Journal of the American Chemical Society 69 (1947) 1231-1232.
[2] C.W.F.T. Pistorius, Zeitschrift fuer Physikalische Chemie 88 (1974) 253-263.
[3] J.P. Soulié, G. Renaudin, R. Cerný, K. Yvon, Journal of Alloys and Compounds 346 (2002) 200-205.
[4] Y. Filinchuk, D. Chernyshov, R. Cerny, J. Phys. Chem. C 112 (2008) 10579-10584.
[5] E.M. Fedneva, V.I. Alpatova, V.I. Mikheeva, Russian J. Inorg. Chem. 9 (1964) 826-827.
[6] K.N. Semenenko, A.P. Chavgun, V.N. Surov, Russian J. Inorg. Chem. 16 (1971) 271-273.
[7] S. Gomes, H. Hagemann, K. Yvon, Journal of Alloys and Compounds 346 (2002) 206-210.
[8] V.E. Gorbunov, K.S. Gavrichev, V.L. Zalukaev, G.A. Sharpataya, M.S.I. Baku, Zhurnal Neorganicheskoi Khimii 29 (1984) 2333-2337.
[9] P. Vajeeston, P. Ravindran, A. Kjekshus, H. Fjellvåg, Journal of Alloys and Compounds 387 (2005) 97-104.
[10] J.K. Kang, S.Y. Kim, Y.S. Han, R.P. Muller, W.A. Goddard, Iii, Applied Physics Letters 87 (2005) 111904-111903.
[11] A. Tekin, R. Caputo, A. Züttel, Physical Review Letters 104 (2010) 215501.
[12] K. Miwa, N. Ohba, S.-i. Towata, Y. Nakamori, S.-i. Orimo, Phys. Rev. B 69 (2004) 245120.
[13] W.D. Davis, L.S. Mason, G. Stegeman, Journal of the American Chemical Society 71 (1949) 2775-2781.
[14] A. Züttel, S. Rentsch, P. Fischer, P. Wenger, P. Sudan, P. Mauron, C. Emmenegger, Journal of Alloys and Compounds 356-357 (2003) 515-520.
[15] N.A. Zarkevich, D.D. Johnson, Physical Review Letters 100 (2008) 040602.
[16] J.-P. Bastide, B. Bonnetot, J.-M. Létoffé, P. Claudy, Materials Research Bulletin 15 (1980) 1779-1787.
[17] T. Noritake, S. Towata, M. Aoki, Y. Seno, Y. Hirose, E. Nishibori, M. Takata, M. Sakata, Journal of Alloys and Compounds 356-357 (2003) 84-86.
[18] Y.N. Shevchenko, N.N. Mal'tseva, V.A. Nazarenko, N.S. Kedrova, N.T. Kuznetsov, Journal Name: Dokl. Phys. Chem. (Engl. Transl.); (United States); Journal Volume: 290:4-6; Other Information: Translated from Dokl. Akad. Nauk SSSR; 290: No. 4-6, 1426-1430(Oct 1986) (1987) Medium: X; Size: Pages: 968-970.
[19] H.R. Ihle, C.H. Wu, Journal of Inorganic and Nuclear Chemistry 36 (1974) 2167-2170.
[20] M.B. Smith, G.E. Bass, Journal of Chemical and Engineering Data 8 (1963) 342-346.
[21] S. Orimo, Y. Nakamori, G. Kitahara, K. Miwa, N. Ohba, S. Towata, A. Züttel, Journal of Alloys and Compounds 404-406 (2005) 427-430.
[22] R.L. Wilkins, R.L. Altman, The Journal of Chemical Physics 31 (1959) 337-340.
[23] K. Bohmhammel, U. Wolf, G. Wolf, E. Königsberger, Thermochimica Acta 337 (1999) 195-199.
[24] J.F.J. Stampfer, C.E.J. Holley, J.F. Suttle, Journal of the American Chemical Society, vol. 82 (1960) 3504-3508.
[25] M.W. Chase, Jr., C.A. Davies, J.R. Downey, Jr., D.J. Frurip, R.A. McDonald, A.N. Syverud, J. Phys. Chem. Ref. Data, Suppl. 9 (1998) 959-1951.
[26] A. San-Martin, F. Manchester, Journal of Phase Equilibria 8 (1987) 431-437.
[27] W. Rummel, Siemens Forsch.- Entwicklungsber. 7 (1978) 44-50.
[28] U. Bösenberg, S. Doppiu, L. Mosegaard, G. Barkhordarian, N. Eigen, A. Borgschulte, T.R. Jensen, Y. Cerenius, O. Gutfleisch, T. Klassen, M. Dornheim, R. Bormann, Acta Materialia 55 (2007) 3951-3958.
[29] O. Kubaschewski, C.B. Alcock, P.J. Spencer, Materials and thermochemistry, Oxford 1993.
[30] J.J. Vajo, S.L. Skeith, F. Mertens, The Journal of Physical Chemistry B 109 (2005) 3719-3722.
[31] G. Barkhordarian, T. Klassen, M. Dornheim, R. Bormann, Journal of Alloys and Compounds 440 (2007) L18-L21.
[32] L. Schlapbach, A. Zuttel, Nature 414 (2001) 353-358.
[33] W. Grochala, P.P. Edwards, Chemical Reviews 104 (2004) 1283-1316.
[34] B. Sakintuna, F. Lamari-Darkrim, M. Hirscher, International Journal of Hydrogen Energy 32 (2007) 1121-1140.
[35] K.C. Hoffman, J.J. Reilly, F.J. Salzano, C.H. Waide, R.H. Wiswall, W.E. Winsche, International Journal of Hydrogen Energy 1 (1976) 133-151.

[36] P. Selvam, B. Viswanathan, C.S. Swamy, V. Srinivasan, International Journal of Hydrogen Energy 11 (1986) 169-192.
[37] R. Schulz, J. Huot, G. Liang, S. Boily, G. Lalande, M.C. Denis, J.P. Dodelet, Materials Science and Engineering A 267 (1999) 240-245.
[38] A.R. Yavari, J.F.R. de Castro, G. Vaughan, G. Heunen, Journal of Alloys and Compounds 353 (2003) 246-251.
[39] J.-P. Bastide, B. Bonnetot, J.-M. Létoffé, P. Claudy, Materials Research Bulletin 15 (1980) 1215-1224.
[40] B. Bogdanovic, K. Bohmhammel, B. Christ, A. Reiser, K. Schlichte, R. Vehlen, U. Wolf, Journal of Alloys and Compounds 282 (1999) 84-92.
[41] W. Oelerich, T. Klassen, R. Bormann, Journal of Alloys and Compounds 315 (2001) 237-242.
[42] J.F.R.d. Castro, A.R. Yavari, A. LeMoulec, T.T. Ishikawa, W.J.B. F, Journal of Alloys and Compounds 389 (2005) 270-274.
[43] G. Liang, J. Huot, S. Boily, A. Van Neste, R. Schulz, Journal of Alloys and Compounds 292 (1999) 247-252.
[44] J.F.R. de Castro, S.F. Santos, A.L.M. Costa, A.R. Yavari, W.J. Botta F, T.T. Ishikawa, Journal of Alloys and Compounds 376 (2004) 251-256.
[45] S.-A. Jin, J.-H. Shim, Y.W. Cho, K.-W. Yi, Journal of Power Sources 172 (2007) 859-862.
[46] D.L. Douglass, Pergamon (1977).
[47] K. Yamamoto, S. Tanioka, Y. Tsushio, T. Shimizu, T. Morishita, S. Orimo, H. Fujii, J. Alloy Compd. 243 (1996) 144.
[48] E. Ivanov, I. Konstanchuk, A. Stepanov, V. Boldyrev, J. Less-Common Metals 131 (1987) 25.
[49] C.X. Shang, M. Bououdina, Y. Song, Z.X. Guo, International Journal of Hydrogen Energy 29 (2004) 73-80.
[50] C. Iwakura, W.-K. Choi, R. Miyauchi, H. Inoue, Journal of the Electrochemical Society 147 (2000) 2503-2506.
[51] S. Ruggeri, L. Roué, J. Huot, R. Schulz, L. Aymard, J.-M. Tarascon, Journal of Power Sources 112 (2002) 547-556.
[52] A. Züttel, A. Borgschulte, S.-I. Orimo, Scripta Materialia 56 (2007) 823-828.
[53] L. Mosegaard, B. Møller, J.-E. Jørgensen, U. Bösenberg, M. Dornheim, J.C. Hanson, Y. Cerenius, G. Walker, H.J. Jakobsen, F. Besenbacher, T.R. Jensen, Journal of Alloys and Compounds 446-447 (2007) 301-305.
[54] AIST, Chemical Abstract, Integrated Spectral Database System of Organic Compounds, Japan.
[55] P.-J. Wang, Z.-Z. Fang, L.-P. Ma, X.-D. Kang, P. Wang, International Journal of Hydrogen Energy 33 (2008) 5611-5616.
[56] Wang, Chang-chun, Zhang, Qing-an, Anhui Gongye Daxue Xuebao, Ziran Kexueban 22 (2005) 355-357.
[57] X. Yao, C. Wu, A. Du, G.Q. Lu, H. Cheng, S.C. Smith, J. Zou, Y. He, The Journal of Physical Chemistry B 110 (2006) 11697-11703.
[58] M.A. Lillo-Rodenas, K.F. Aguey-Zinsou, D. Cazorla-Amoros, A. Linares-Solano, Z.X. Guo, The Journal of Physical Chemistry C 112 (2008) 5984-5992.
[59] S.C. Yan, L. Zhou, G. Yan, Q.Y. Wang, Y.F. Lu, Journal of Alloys and Compounds 459 (2008) 452-456.
[60] S.C. Yan, G. Yan, C.F. Liu, Y.F. Lu, L. Zhou, Journal of Alloys and Compounds 437 (2007) 298-301.

CHAPTER 2. EXPERIMENTAL METHODS

1 Samples preparation by ball-milling

During this work we have used two types of ball-mills, planetary and vibrating ball-mills, which differ by their form and operating conditions. Indeed different results could be obtained depending on the milling modes. After describing the difference between the two types of mills, we will present the method of preparation of the samples.

1.1 Milling devices

1.1.1 Planetary mill

Planetary mill works with four balls of 1 cm diameter and an amount of powder placed in the two vials, interdependent of a disc which turns in opposite direction to theirs (Fig.2.1a). Milling acts either by impact shocks or friction. Without external heating, the average temperature of the vial is between 50℃ and 90℃, dependin g on the speed of the balls [1]. To prevent heating, milling is carried out in several cycles with periods at rest. An ultimate state (steady-state) of milling process is generally attended in 24 hours.

1.1.2 Vibrating mill

Vibrating mill is a device with a single ball of 50 mm diameter placed in the vial. The ball comes to strike the powder in vertical movements. (Fig.2.1b). The ball oscillations are induced by an electromagnet. The average temperature of the vial is about 30℃ and temperature rise does not exceed 10℃. The total duration of milling is of about one week.
The used balls and vials are made of steel. During milling, it is unavoidable that small contaminations come from the mill, which is more or less important according to the mill type used. Indeed during our experiments, we have observed a contamination using the first model of mills, notably by nickel. In the case of the vibrating mill, contaminations were very low.

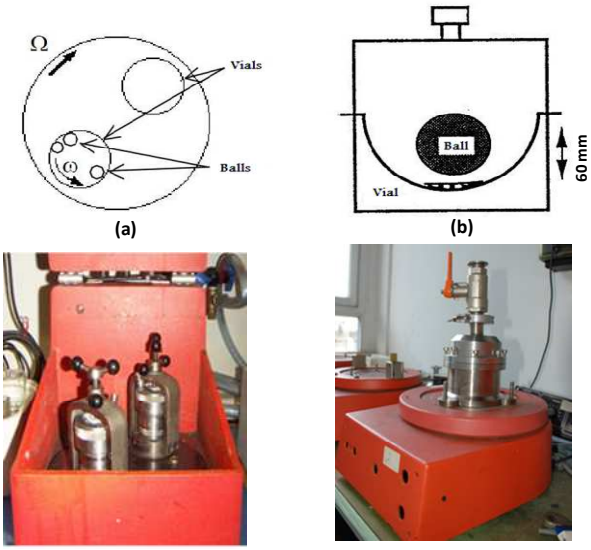

Figure 2.1. Milling devices, (a) planetary mill and (b) vibrating mill with vertical vibrations

1.2 Milling procedure

In spite of the fairly long duration of millings, vibrating mill had shown its effectiveness in the *SIMaP* laboratory, with regard to the powder particles size reduction [2]. An increase in the specific surface of the powders is induced in the case of hydrides composites. This kind of milling was chosen primordially for the treatment of the powders in this work. Consequently, the planetary mill was used only as a mixer of the pre-milled powders for short times (1-2 hours).

The steady-state of milling could be determined by two parameters: temperature and intensity of milling. At first approximation when the temperature should not change too much, the milling process is controlled by the intensity of milling transmitted by the balls to the powder.

At the beginning of this work, we tried to quantify the energy of milling. For the vibrating mill, it seems that this could not be determined directly because of the dependence of the milling on many parameters such as the vial material, the height of the ball jump during milling and the powder nature and its amount. The vibrating mill is constituted of two parts, the ball-mill (top) and the vibrating device (lower part). Figure 2.2a shows the components of the lower part. As there is no commercial information about the mill working, we have measured tentatively the magnitude and vibrations frequency of the vibrator plate using a dial indicator (Fig.2.2b).

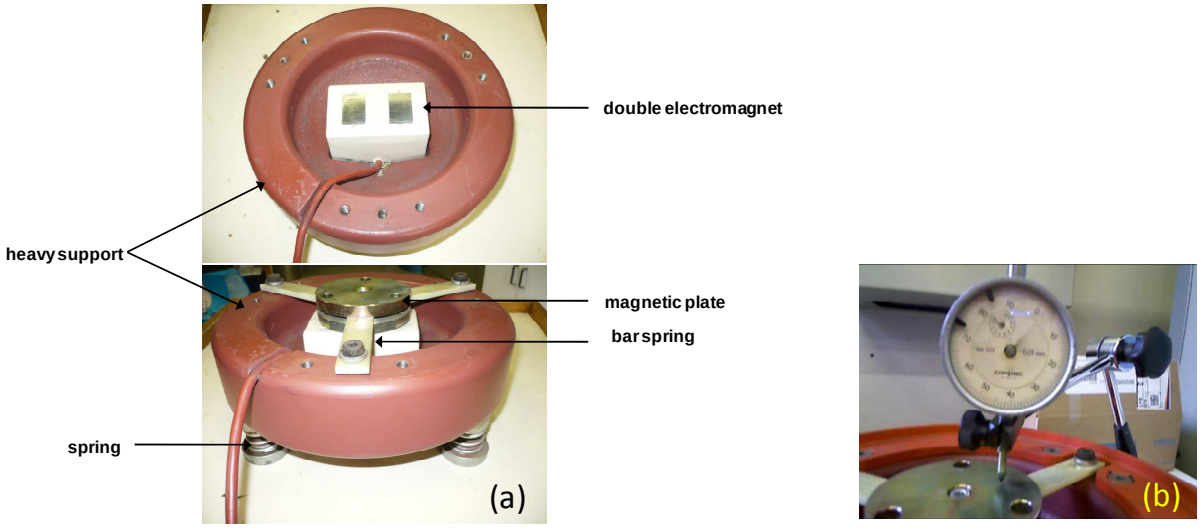

Figure 2.2. Exploring the milling device: (a) components of the vibrating mill, (b) characterization of the plate vibrations

The vibrations frequency is found almost constant and near to 50 Hz (Table 2.1), whereas the magnitude increase upon the milling intensity. The variations and counts were observed using a precision camera.

Table 2.1. Measured frequencies using a dial indicator and precision camera

Exp.	Frequency	Exp.	Frequency
1	48	*4*	46
2	53	*5*	45
3	47	*6*	51

The vibrations are created by reversing the magnetic field in the two electromagnets. In this way, the plate movements are symmetric. Likely, the fixation of the plate by three bar-springs gives a quasi random movement, also affected by the springs supports at the bottom of the vibrating device. By observing the ball action as a function of milling intensity both contributions, friction and shock impact, were observed to be significant for hydride powders milling. Accordingly, the movement of the ball becomes complex and thus difficult to simulate. However, the only quantity which could be quantified is the electromagnets current intensity and this will be only significant for the same amount of powder and vial material.

1.3 Sample preparation

MgH_2 (purity 98%), $LiBH_4$ (95%, assay 98.1 %) and LiH (99.4%) crystal powders were purchased from Alfa-Aesar. The filling in the mill with powders was made in protective atmosphere (Ar) in a glove box. After introduction of the desired amount of powder, the mill is drained off by a pump and filled again with a pressure of about 200 mbar of argon (99.9999%) to prevent the return of air inside the mill. This procedure is made so that the reactions such as oxidation or hydrolysis of the moisture sensitive powders as $LiBH_4$, could be avoided. The pressure after the end of milling is also checked using pressure manometer. The cleaning of the vials consists on the reaction of the residue with water or diluted acid then washed with acetone.

Annealed powders, containing either $LiBH_4$ alone or with B and LiH additions, were hand-mixed, milled and prepared using quartz tubes sealed under vacuum better than 5.10^{-3} mbar. The resulting products were observed using XRD technique without air contact in a special sample-holder (see XRD technique). For mass spectrometry measurements, the effusion cell-reactor with tight closing is filled with the milled powders in the glove box.

2 Vapor pressure measurements

2.1 Mass spectrometry

Knudsen cell mass spectrometry technique was chosen because it is particularly well adapted for the study of the vapor phases in order to determine their composition, i.e. atoms and molecules. This technique has also the advantage that it could be coupled to other techniques of analysis or to different types of effusion reactors, depending on the studied reactions.

2.1.1 Principle

In 1954 the effusion method (used since 1904) was coupled to a mass spectrometer in order to analyze the vapor composition and to enlarge pressure determinations to the high temperature field of complex gaseous phase reactions for partial pressures determination [3,4]. Thereby, mass spectrometry is a powerful technique for the analysis of the vapors at high temperatures with low vapor pressure range (< 10^{-4} bar). The gas analysis is made in the molecular flow regime and the technique is more generally called molecular beam or effusion cell mass spectrometry.

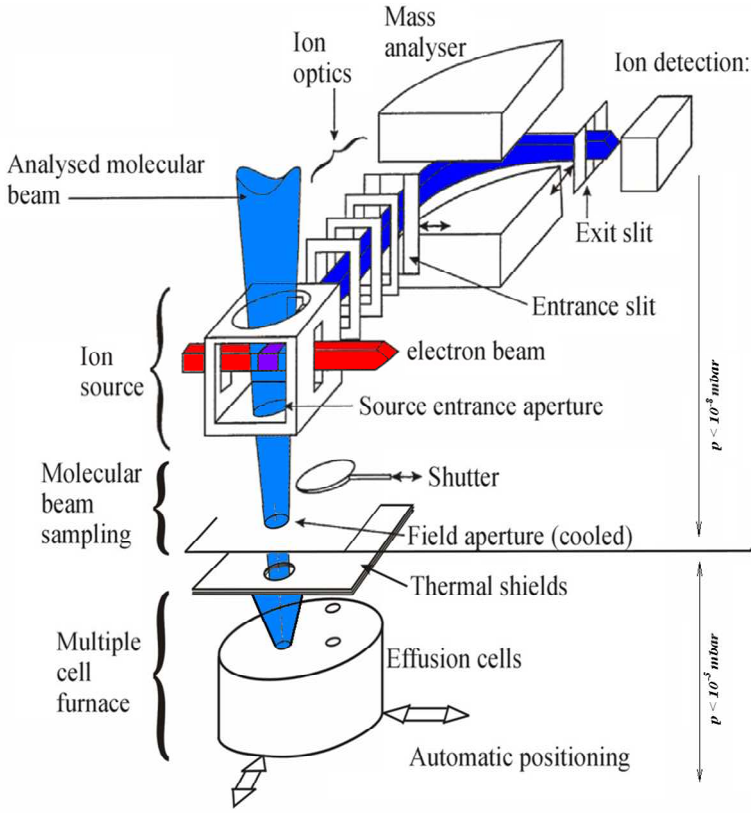

Figure 2.3. General view on the machinery of the mass spectrometer of SIMaP laboratory

High temperature mass spectrometry consists in associating a chemical reactor operating under vacuum whose up-level is effusive for mass spectrometer detection. The reactor is generally equipped with an adequate heating system. The vapor is studied after gas ionization by electron impact conditions (figure 2.3). The flow of rarefied gas or molecular beam (internal pressure < 10^{-5} bar) issued from the Knudsen cell orifice is introduced through a sampling aperture to the ionization chamber of a mass spectrometer that is maintained under ultra-high vacuum (*UHV*).

Molecular beam molecules and atoms are ionized by an electron beam at the level of the ion source and produces positive ions from the neutral molecules according to the simple adiabatic ionization process:

$$M + e^- \rightarrow M^+ + 2e^- \qquad (2.1)$$

The produced ions are accelerated and then separated according to their mass/charge ratios by a magnetic field (Mass analyzer in our case). Finally, they are collected in a Faraday cup or with a secondary electron multiplier. From ionic intensities and isotopic abundance of each ion, it is possible to give the atomic composition of each ion.

The identification is based on the isotopic distribution of the expected ion. Indeed the a priori calculated distribution starting from the mass of the atoms constituting the ion and its stoichiometry is compared with the recorded mass spectra. For example, the formed ion $A_nB_m^+$ from the atoms A and B will thus be identified perfectly. Now, to go up to the identification of the molecules starting from the detected ions, it is necessary to discriminate between an ion formed by direct ionization (adiabatic process) of a neutral molecule, i.e. a “parent” molecular ion (reaction 2.2), and an ion obtained by dissociative ionization from a molecule having a larger molecular weight, i.e. a fragment ion (reaction 2.3):

$$A_nB_m + e^- \rightarrow A_nB_m^+ + 2e^- \text{ (Molecular ion)} \quad (2.2)$$

$$A_nB_m + e^- \rightarrow A_nB_{m-1}^+ + B + 2e^- \text{ (Fragment ion)} \quad (2.3)$$

These different ionization patterns can be identified using two main physical ways: -(i) the determination of ionization threshold, -(ii) the relative amounts of the ions as a function of the ionization energy (above the threshold up to 100 eV). A third way is chemical, i.e. the study of relative ionic amounts as a function of the sample chemistry.

After identification, the measured intensity of the ion related to one gaseous species makes it possible to go back to its partial pressure in the effusion cell as we will see it in the vapor pressure analysis part.

2.1.2 Vapor pressure analysis

The produced ions are extracted from the ionization chamber and accelerated by an electric field and then separated according to their mass/charge ratios - in our case by a magnetic field – before their detection. As the molecular beam of gaseous atoms or molecules produced at low pressure travels without any collision from the effusion orifice to the ionization chamber, the detected ions reflect the gas composition at the vaporization equilibrium, i.e. the sample surface.

The partial pressure p_i of a gaseous species in the effusion cell is directly related to the measured intensity I_i for the species i, to the temperature T of the neutral species in the cell and to the sensitivity of the spectrometer S_i within the basic mass spectrometric relation issued from the Beer-Lambert law applied to electrons absorption in a rarefied medium [4]:

$$p_i.S_i = I_i.T \quad (2.4)$$

The sensitivity S_i is often written in the following way:

$$S_i = G\eta\sigma_i(E)\gamma_i f_i \quad (2.5)$$

where G is an instrument factor which depends on the solid angle between the ionization chamber and the molecular beam source (effusion orifice), η is the extraction coefficient of the ions from the ionization source toward the spectrometer analyzer (in our magnetic analyzer, η = cste), $\sigma(E)$ is the ionization cross section at the ionizing electrons potential E, γ is the detector yield (for our pulse counter, γ = 1) and f_i is the isotopic abundance fraction of the ion i as calculated. Hence the expression 2.5 in our case is simplified to:

$$S_i = G\sigma_i(E)f_i \tag{2.6}$$

The sensitivity cannot be calculated a priori because a certain number of parameters are not quantified as observed in the previous formula. It is thus necessary to determine the sensitivity experimentally, at least for a given species and in each experiment.

2.1.3 Knudsen effusion method and sensitivity determination

Total vapor pressure measurements using Knudsen effusion method are based on vaporizing a substance in a closed container (Knudsen or effusion cell, Fig.2.4) with an orifice drilled in the lid which is small compared to the vaporizing surface of the loaded sample. The molecular flow in mole per unit time (t) which effuses from an orifice of surface s is written using the Herz-Knudsen relation [5]:

$$\frac{dN}{dt} = \frac{psC}{\sqrt{2\pi MRT}} \tag{2.7}$$

where p is the pressure, C the Clausing coefficient (total transmission probability referred to the ideal thin wall orifice), M the molecular mass of the effused gas species, R the gas constant, and T the absolute temperature of the cell.

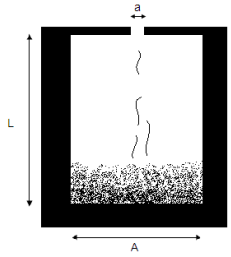

Figure 2.4. Simple Knudsen effusion cell

The flow of molecules or atoms vaporized from a surface s is the same as the effusion flow of a rarefied gas resulting from a sufficiently large container by an orifice with an ideal thin wall and of the same surface s. The essential condition is that the mean free path λ of the molecules in the gas should be higher than the diameter of the orifice. More detail devoted to the

flows calculations is presented in the *chapter 6* about ball-mill coupled to the mass spectrometer.

Knowing the Knudsen pressure upper limit (10^{-4} bar) - threshold of the molecular flow regime for an orifice with 1 mm diameter-, the expression (2.7) is used to calculate the vaporization rate of a substance. The mass-loss rate is then given by the expression:

$$\frac{\Delta m}{\Delta t} = \frac{psC\sqrt{M}}{\sqrt{2\pi RT}} \tag{2.8}$$

The obtained mass-loss rates at different temperatures will serve to calibrate the pressures measured by the mass spectrometer. This could be done by combining the spectrometric relation (2.4) with the total mass loss Δm of the sample according to the Hertz-Knudsen relation, to obtain the sensitivity S:

$$S = \frac{sC\sqrt{M}}{\Delta m\sqrt{2\pi R}} \sum_{i=1}^{n} \left(I\sqrt{T}\right)_i \delta t_i \tag{2.9}$$

The quantity $I\sqrt{T}\delta t$ is obtained by mass spectrometric observation for all the temperature plateaus and intermediate regimes. We have to emphasize that the underlying assumption for using such relation is that the ratio between the detected portion of the molecular beam and the total effused flow from the cell orifice remains constant throughout the experiment. This constant is consequently included in the sensitivity S. For several species in the same vapor phase, the equation (2.9) becomes [4]:

$$S_1 = \frac{sC\sqrt{M_1}}{\Delta m\sqrt{2\pi R}} \sum_{j=1}^{p} \left(\sum_{i=1}^{n} \frac{S_1}{S_j} \sqrt{\frac{M_j}{M_1}} \left(I_j\sqrt{T}\right)_i \delta t_i \right) \tag{2.10}$$

where the summation over *i*=1 to *n* corresponds to the various temperature plateaus of the experiment, and *j* enumerates the species. This last relationship requires the knowledge or estimates of the ratios S_1/S_j.

In our case this ratio is directly deduced from the ratio σ_1/σ_j according to the following equation:

$$S_j = \frac{\sigma_j f_j}{\sigma_1 f_1} S_1 \tag{2.11}$$

The ratio σ_1/σ_j is obtained with the additivity rule for total ionization cross section using tabulated values reported by Drowart et al.[4]. This rule is to be applied to the whole ionization process of a molecule and takes into account the total ionic current (parent and fragment ions). The ionization cross sections of the atoms were calculated according to the working ionization energy (in eV). In the case of a dimmer, the additivity rule leads to dimmer/monomer ionization cross-section ratio equal to 2.

2.1.4 Description of the mass spectrometer equipment

A picture of the present MS device with the associated cell-reactor is presented in figure 2.5. The spectrometer is composed of three principal parts: ion source, mass analyzer and the detection system.

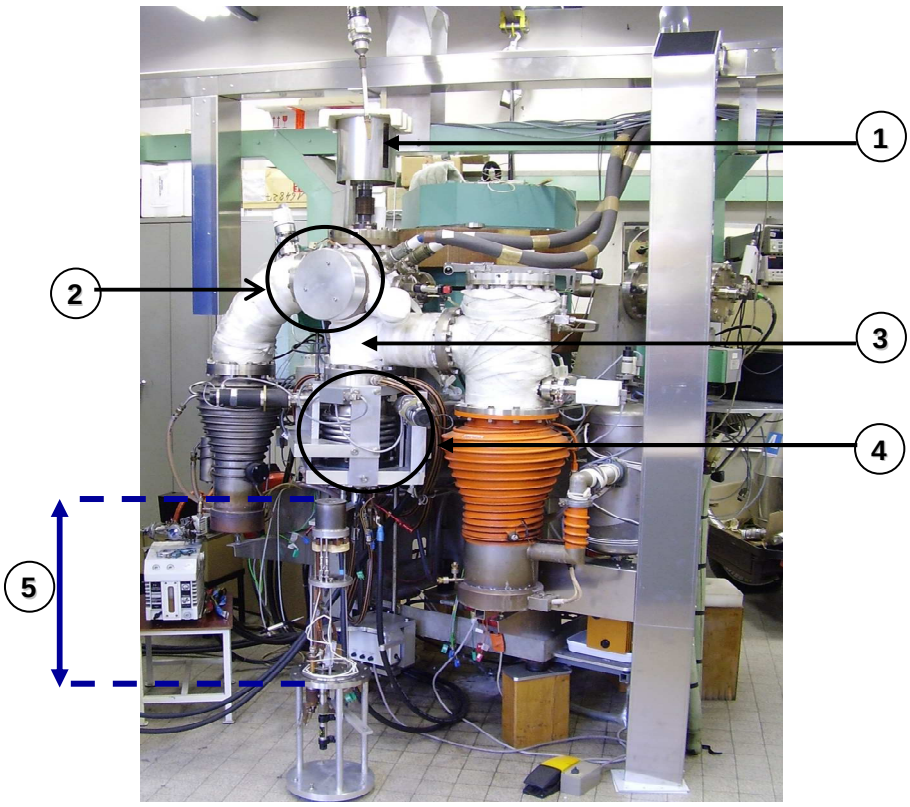

Figure 2.5. Picture of MS (SIMaP device). 1: N_2 liquid dewar linked to the ionization chamber. 2: Ion source housings. 3: Oven housings. 4: Mechanical positioning system for any Knudsen cell reactor. 5: Knudsen cell reactor (total height H=53cm)

- **Ion source**

The ionization chamber is made of μ-metal (screening-protection against parasitic magnetic fields) and ensures the extraction of the ions by the combined effects of the “immersion” lens and a “repeller voltage” of ions. The extracted ions are then accelerated and focused by an electrostatic lens functioning between 5000 V and the mass at 0 V before entering in the mass analyzer. The ionization chamber is provided with an aperture in order to collimate the beam coming from the effusion cell.

Two tungsten filaments ensure a regulated emission current of electrons while maintaining them at a fixed potential - ionization potential – in the range -4 to -100 V regarding the ionization chamber. The system with 2 filaments is preferred because it allows a better homogeni-

zation of the density of the electrons in the chamber and a two-fold increase of the ionic current. These filaments are responsible of the heating of the walls of the ionization chamber (temperature close to 600 K) what could causes reactions of the deposited products during experiment. In our case there is no secondary evaporation since the walls are cooled *in situ* with liquid nitrogen cooling system.

The ionization source is welded to a nitrogen-trap made of glass located above the chamber. This makes it possible to avoid the re-evaporation of the molecular beam species which would have condensed on the upper part of the ionization chamber. The nitrogen trap allows also the improvement of the local vacuum (reduction of the residual spectrum).

The acceleration potential of the ions is obtained by a power supply *FUG-0-6500V* of stability lower than 10^{-4} controlled by an *IEEE* interface.

The ions source is also provided with a fixed focusing slit of ions and with an aperture slit (manual adjustment) which makes it possible to improve the peaks resolution by eliminating a part of the aberrations, meanwhile the sensitivity decreases.

- **Mass analyzer**

The mass analyzer is a magnetic prism of 30.5 cm radius and $\theta = 90°$ angle ("Nuclide Corporation" origin - 1967). The magnetic field can vary between 0 and 1 T. Winding was modified by the *Drusch* company to work with low voltage and the magnetic field is controlled by a solid-state-power supply *Drusch/Bouhnik* (0-60 V, 0-10 A) of 2.10^{-5} stability, provided with an *IEEE* interface.

As mentioned before, the ion source and magnetic prism assembly ensure a constant transmission η of the ions whatever is the measured mass. It is an advantageous characteristic (compared to the quadrupoles) of the magnetic prisms when the ion sources are purely electrostatic and correctly protected from the magnetic fields.

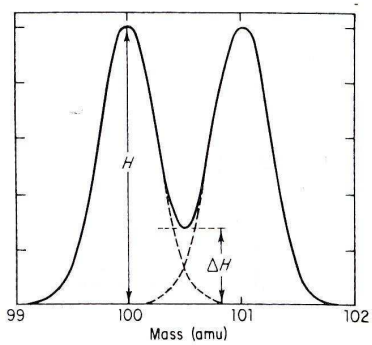

Figure 2.6. Resolution between two adjacent peaks of intensity H and height of valley ΔH

The spectrometer resolution, which depends on the characteristics of the magnetic prism, is in general defined by the greatest mass for which a preliminary criterion established is respected. For our spectrometer, we retained as a criterion the height of the valley which expresses the resolution as the greatest mass to which two adjacent peaks of equivalent intensity, separated by a unit of atomic mass, has a height of valley between the two peaks lower than a certain percentage of the peak intensity. The selected percentage is 10% and thus *ΔH/H* must be lower or equal to 0.1 (Fig.2.6). This criterion allows us to ensure that during the measurement at the maximum peak intensity, there is no peak interference. In our case, the spectrometer has routinely a resolution ≥ 600.

- **Detection system**

The detection can be done in two modes:

- Faraday cup equipped with an electrometer *KEITHLEY model 6517A* for the detection of the ions current > 10^{-15} A.
- Secondary electron multiplier *ETP* 1000 (Ag/Mg dynodes) of reduced size conceived for pulse counting (transit times and pulses of 2-3 ns). The background noise is lower than 0.1 count.s^{-1} for a gain from 10^7 to 10^8 electrons per incident ion. A fast preamplifier *ORTEC 9327* formates the signal. The counting chain of pulses is a Universal *Counter Hewlett Packard model 53132 A.*

- **Mass spectra recording**

The remote control of the interfaces and data acquisition is done with a *HP Kayak XM 600 (Ets BOURBAKY, Tournon, France)* work station on which is implemented a program realized at *SIMaP* in *HT-BASIC* language. The program is developed not in view of carrying out entirely automated experiments but to be suitable for each experiment. The program consists of several elementary commands such as the adjustment of the high voltage, the repeller voltage of ions, the magnetic field and scientific tasks like a scanning on a given peak with or without shuttering, monitoring any ionization efficiency curve or simply measurements of the intensity and temperature. These elementary controls are managed at the request of the experimenter during experiments. Additional modules are regularly programmed according to the type of experiment.

2.1.5 Mass spectrometer improvements

- **Sampling of the molecular beam by conventional or restricted collimation devices**

The molecules that collide on the walls of the ionization chamber are scarce (10 to 50 times less compared to a conventional assembly) because the molecular beam is formatted by a collimating system known as “restricted collimation”. Indeed, the absence of collisions between the molecular beam and any wall guarantee representative properties of the studied molecules in term of the effusion cell temperature and pressure.

Coupling the effusion cell to the ion source of the mass spectrometer is achieved by interposing a cooled separation, i.e. a water jacket in order to protect the ion source from heat flow of the furnace and from molecular deposits from outer parts of the whole effused beam. In a conventional device (Fig.2.7i), the different apertures (shields, cooled jacket and ion source entrance) allow molecules to enter the ionization chamber from a quite large solid angle. Thus, the ion source observes at the level of the effusion orifice a large area defined by the umbra and penumbra zones (Fig.2.7): parasitic surface vaporizations are thus detected in addition to the useful (equilibrium) molecular beam issued directly from the effusion orifice. Restricted collimation (Fig.2.7ii) involves the introduction of a fixed aperture (field aperture) located in the cooled jacket separating the furnace and ion source housings [6]. Together with the source aperture, the field aperture fully defines the molecular beam [7]. The size of the field and source apertures defines the size of the useful molecular beam in such a manner that at the effusion orifice level the penumbra zone (diameter D_p) is less than the effusion diameter D_e.

The restricted collimation method with regards to the conventional collimation presents the advantage to discard any external surface contributions (from the orifice neighbours) of the useful molecular beam from the cell. The second advantage is that the solid angle of detection as defined by both apertures remains fixed and independent of the effusion cell (in contrast with a conventional collimation), that is only dependent on the MS. This advantage can be used in the evaluation of surface diffusion flow contributions as it was shown by Roki et al.[8] when applied to the CsOH system.

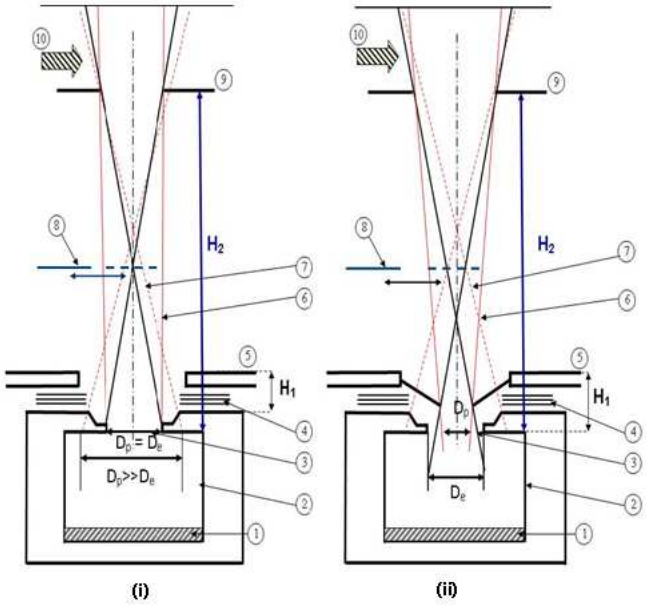

Figure 2.7. Conventional collimation (i) and restricted collimation (ii) of the effused molecular beam showing the various molecular emitting surfaces seen in each method by the ionization chamber: (1) sample; (2) Knudsen cell; (3) effusion orifice; (4) thermal shields; (5) cooled field aperture; (6) solid angle corresponding to effusion orifice alone; (7) the supplementary surface viewed by the detector; (8) shutter; (9) source aperture; (10) ionizing electron beam. D_p is the diameter of the penumbra zone for detection of molecules and D_e the effusion diameter

The use of restricted collimation device imposes that the distance between the effusion orifice (from the inner face of the lid, *i.e.* the entrance of the effusing molecules in the effusion orifice) and the first (field) aperture must be short and systematically checked for any new cell geometry and associated furnace device to be certain to detect molecules coming directly only from the inner gas phase of the effusion cell.

Besides, the mechanical positioning of the effusion cells orifice must be performed with the best accuracy (± 0.025mm). The overall molecular transmission of the restricted collimation has been previously optimized by the correct choice of the two source and field apertures in relation with different distances according to the earlier work performed by Morland and al.[6].

- **Free floating shutter**

A shutter is a disk or a blade which can be moved mechanically to cut off perpendicularly the direct molecular beam and by this way we are able to distinguish the background molecular flow (from source background pressure) from the useful molecular beam. This is particularly important when the gaseous species existing in the background are the same as those de-

tected from the cell (H_2 or H_2O for instance) or appearing at the same non resolved masses (CO and N_2 for instance). This shutter is located at the mid-way between the two apertures and its movement is “free” from any mechanical part linked to the water jacket in order to avoid any partial closing of the field aperture that can disturb the vacuum pumped permanent flow between the furnace and source housings which are rarely at the same background pressure due to the heating of the furnace as well as to effusing species. The version used in this work was developed by the laboratory in last years and equipped with the mechanics of positioning [7].

2.2 Description of the cell-reactors

The effusion cell-reactors are developed most of the time in laboratories because there is no satisfactory commercial version. The material of the effusion cell must be inert with respect to the studied systems. For the study of the Li-B-H system, the difficulty is to find materials inert as well as with the gas and with the liquid phase to avoid any reaction. We thus thought of materials such as nickel and stainless steel for the classical and special reactor with tight closing respectively, that we employed in this work. In our experiments with other materials such as alumina and silica as well as borosilicate, $LiBH_4$ already had shown a strong reactivity which render doubtful our experiments. This was the case for DSC experiments and heat annealing of samples. During this thesis, we have used two types of cell-reactors: classical and cell-reactor with tight closing. The difference between the two types is detailed as following.

2.2.1 Classical cell-reactor

The classical cell-reactor is made of a combination of a furnace and an effusion cell. The furnace is a radiation heating system made with a tungsten sheet resistance [8] and fitted with Ta/W thermal slides. The temperature of the cell is measured either with a thermocouple *K-type* or an optical pyrometer in a sighting hole (Fig.2.8). The entire device is cooled by water and maintained under high vacuum. In the cell wall an opening (orifice) is bored whose dimensions (section s) are small regarding the surface of the sample (S). One generally uses the condition $s/S \leq 10^{-2}$ (Fig.2.8).

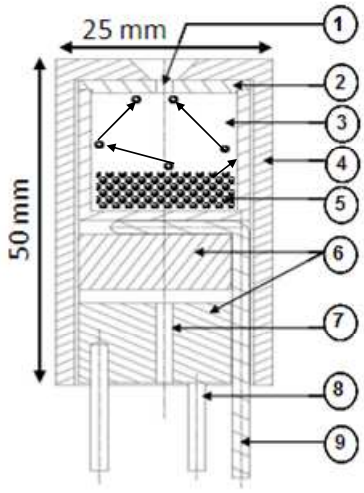

Figure 2.8. Drawing of the simple effusion cell inserted in the classical cell-reactor. (1) effusion orifice; (2) lid; (3) crucible; (4) external envelope; (5) sample; (6) holder; (7) hole for pyrometric sighting; (8) three thin tungsten poles; (9) thermocouple K-type.

2.2.2 Special cell-reactor with tight closing

This reactor designed originally for organometallic compounds [9], was convenient for the vaporization of borohydride compounds. The effusion cell has a screwed lid fitted with a gasket and with an effusion orifice of 2 mm diameter and 4 mm height. In spite of its poor thermal conductivity, stainless steel has been chosen for its mechanical and chemical properties. The cell interior has a quasi-orthocylindrical shape with 40 mm *i.d*. and 43mm height: suitable thermal conditions and pressure equilibrium conditions are assured when the cell height above sample is equal to the cell *i.d*. (orthocylindrical volume for the gas phase) and the ratio *sC/S* (s orifice section, *C* Clausing coefficient and *S* cell section) is low enough [10].

Knowing the highly hygroscopic nature of metal borohydride compounds, a special cell opening/closing system preserves the original chemical purity of the sample (Fig.2.9). First, the screwed lid allows the cell to be opened for filling with the sample: the cell was loaded with a large amount of metal borohydride powder (3 g) in a glove box. Second the effusion orifice can be locked with a long-stemmed valve, tightened with a *Viton*® gasket. The valve has a groove with a 0.1 mm tapering wall in order to retain the gasket.

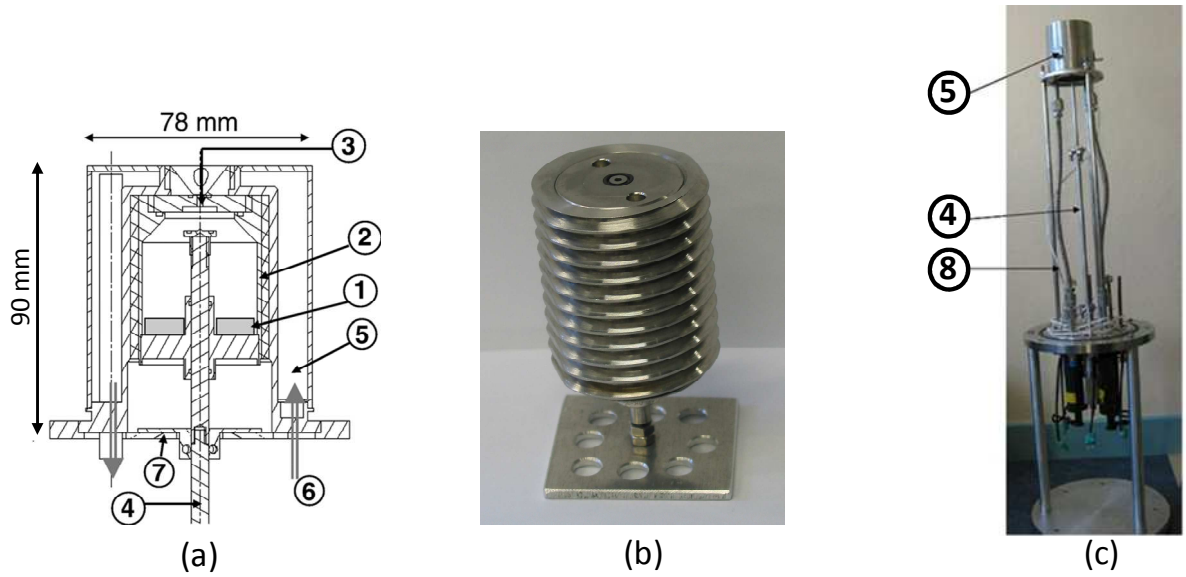

Figure 2.9. Special Knudsen cell-reactor with tight closing: (a) Schema and (b) its picture and (c) the whole cell-reactor. (1) sample; (2) screwed tight Knudsen cell; (3) effusion orifice; (4) valve and rod actioning device; (5) thermoregulation envelope; (6) input of thermostatic fluid; (7) screwed protecting copper shields; (8) heating circuit by the carrier liquid.

Once loaded in the mass spectrometer housings, the total stem translation movement, from top to bottom, is 8 mm and the stem can be moved under vacuum from outside the spectrometer to open the effusion orifice. Two *Viton*® gaskets guarantee the tightness of the stem to the cell during the movement. Locking of the translation movement in the closed cell position is made by a nut: this nut is essential to guarantee permanent tightness during the cell transport inside-outside the glove box and the cell mounting into the reactor. The nut is removed after locking the stem translation movement in the closed cell position.

The cell is screwed in an envelope. Heating of the effusion cell occurs by conduction from an envelope in which there is a continuous circulation of silicone-oil fluid from an external thermostatic bath. The temperature of the bath is controlled via a K-type thermocouple located inside the thermostatic envelope at the cell level. This heating system allows to reach temperatures around 473 K. There are copper shields tight to the bottom part of the valve stem in order to ensure thermal equilibrium of the valve stem with the effusion cell when the valve is open for measurements. Between different temperature plateaus (≈30 degrees difference) there was a stabilization time of 1½ h in order to reach thermal equilibrium. The temperature was monitored within ± 3 degrees uncertainty on a temperature plateau.

3 Thermal analysis and scanning calorimetry

Calorimetry is a technique for thermodynamic studies that use widely heat flow measurements at fixed conditions. It's based on two different notions: isothermal and adiabatic. Calorimeters are devices for determining the heat input by measuring the temperature rise of a system under fixed conditions. In the isothermal method, an outer jacket is maintained at a constant temperature and the inner container of high thermal conductivity (copper or aluminum block), where the heat of reactions is produced, maintains a relatively uniform temperature. A metal shield between the two compartments serves mainly to decrease convection heat transfer. The heat flow is measured between the container and the outer jacket. In the adiabatic method, the outer jacket is maintained at the same temperature as the inner container so that there is no temperature difference and no heat exchange between the chamber and the surrounding jacket. Physically, it is the same principle as for the isothermal calorimeter except that the jacket is maintained at the same temperature as in the reaction vessel in order to warranty adiabatic conditions. Then the measured temperature increase is used directly to determine the heat effect [11]. In differential thermal analysis two samples (one is a reference) are heated or cooled together in a furnace so that, as nearly as possible, the heat received is identical and the temperature difference between them measured.
We have used two different techniques for the thermal analysis of the samples: Differential thermal analysis (DTA) and Differential scanning calorimetry (DSC). The main difference between the two methods is that DTA characterizes by the thermal effect essentially the temperature at which the event is taking place while the DSC, additionally, can provide the corresponding amount of heat.

3.1 Differential thermal analysis

The apparatus used is from NETZSCH firm (model 2920A). The sample and the reference in the same crucibles are heated in the same enclosure. The difference in the temperature (ΔT) of the sample and the reference is measured by means of two thermocouples located just below the two crucibles. We have used this technique for the characterization of the thermal events of the hydrides using alumina crucibles. Thermogravimetric analysis is also coupled to this instrument. A microbalance is associated to the DTA instrument, which provides additional information about the weight loss of the sample after correction for the empty crucible.

3.2 Differential scanning calorimetry

3.2.1 Description

DSC is a method to evaluate the heat capacity of a compound by measuring the amount of heat that is provided to the sample. We have used two types of apparatus, power compensation DSC (TA 2900A Instrument, Fig.2.10a) for heat capacity measurements and heat flow DSC (Setaram Apparatus, Fig.2.10b) for the characterization of the thermal events. In this last device, the sample and the reference are located in the same furnace which is controlled by a temperature regulator program. Furnace, holder and crucibles are made of alumina. The first device uses two independent furnaces with separate crucibles in which are placed the sample and the reference. The crucibles are built as Al or Cu crimped pans.

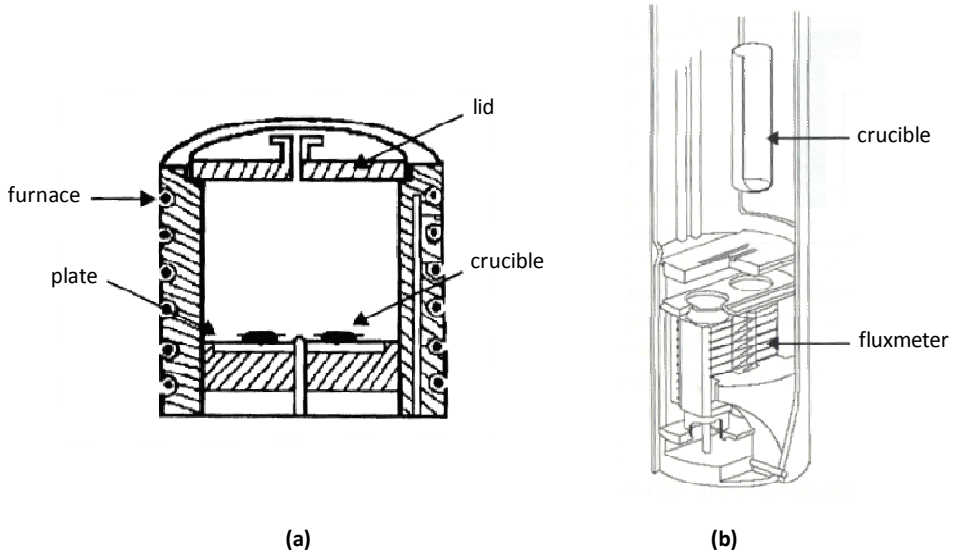

Figure 2.10. DSC types: (a) TA Instrument and (b) Setaram models

Generally for DSC measurements, a heating rate is programmed and acquisition of the thermograms is presented as heating flow transfer (ΔQ) versus time or temperature of the furnace ramp. This quantity corresponds to the heat required to increase the temperature of a sample and its reference which are maintained at the same temperature surrounded by a furnace. For heat capacity measurements, the reference sample (monocrystalline alumina) has a well known heat capacity over the range of the scanned temperature. For the study of phase transitions standard samples (Sn and In melting) are used as reference for the extraction of the enthalpy of transition.

3.2.2 Heat capacity determination

For the determination of the heat capacity of $LiBH_4$, the samples were encapsulated in aluminum crimped pans then weighed carefully in the glove box. Since the signal obtained from the DSC gives the power ($J.s^{-1}$), it can be divided by the programmed scan rate to yield heat capacity directly ($J.K^{-1}$). Several scanning methods are developed for an accurate heat capacity. In our measurements, we have used a scanning method consisting on a linear ramp of the temperature. Isothermal regimes are imposed at the beginning and after the end of the scan (Fig.2.11).

The first run involves a scan with an empty pan (ΔY_0). The second one is a scan of a pan containing a material whose heat capacity is well known (ΔY_{std}). In addition the pans should be as similar as possible, although the small mass differences can be corrected.

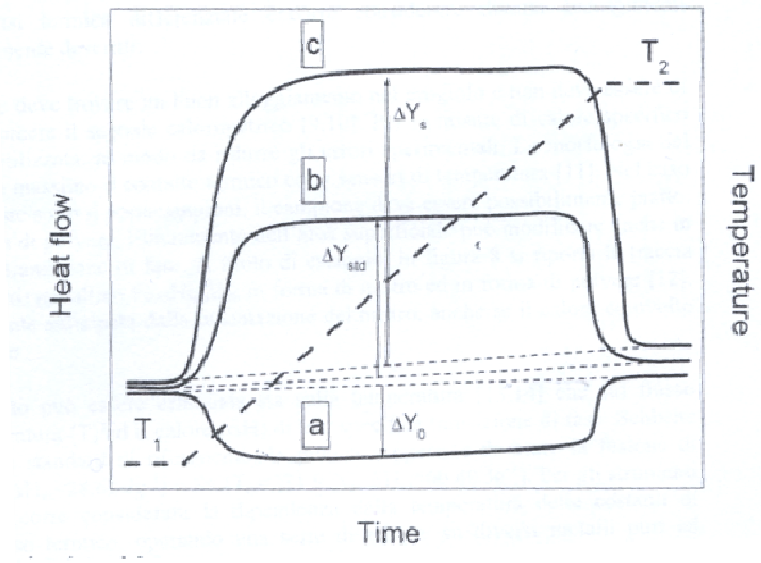

Figure 2.11. Specific heat determination by the method of the heights

For all the scans and in the same day, we worked with heating rates of 5 $K.min^{-1}$ for an interval of 230 K between 293 and 523 K. The following formula is used for the determination of the heat capacity of the sample:

$$C_p^s = C_p^{std} \frac{\Delta Y_0 + \Delta Y_s}{\Delta Y_0 + \Delta Y_{std}} \cdot \frac{m_{std}}{m_s} \qquad (2.12)$$

Quantitative calibration of the heat flow has been carried out using monocrystalline alumina as reference, (α-Al_2O_3, *Sapphire*) prealably dried at 1173 K. The calibration of the thermocouple temperature was made by observation of tin and indium ingot (99.99%) melting. For

heat capacity measurements of $LiBH_4$ and after several cycles, the measurements were found to deviate for each cycle by a constant factor, the mean value of which was considered in the correction of the final recorded heat flow.

4 Characterization techniques

In the previous part we have presented the methods used for the analysis of the vapor phases and for the thermal analysis of solids. In this part, we will see the different techniques for samples characterization.

4.1 X-ray diffraction technique

4.1.1 Diffractometer

The characterization by X-ray diffraction in the reflexion mode was carried out using a classical diffractometer (PANalytical X'Pert Pro MPD) located at the "Consortium des Moyens Technologiques Communs" (CMTC) of Grenoble-INP. The diffractometer is equipped with copper lamp of 1800 W associated to a Ni filter which allows the selection of the K_α radiation (λ = 1.5418 Å). The detector is the X'Celerator which uses a RTMS (Real Time Mulitple Strip) detection technology. This diffractometer has $\theta/2\theta$ reflection geometry mode (Fig.2.12).

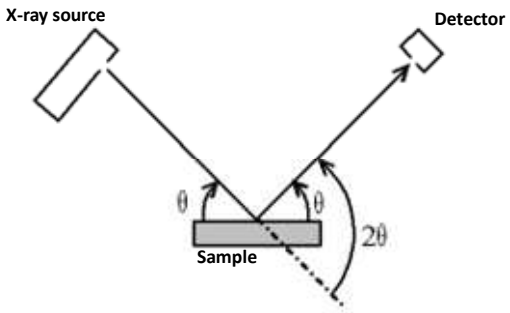

Figure 2.12. Principle of the diffractometer ("Bragg-Brentano" assembly)

An angular scanning at room temperature from 10 to 90 (in 2θ) are made with a step varying from 0.017° to 0.034° and time count of 100 to 210 seconds per step, depending on each powder to be analyzed. Hence, the recording time could vary from 1800 to 3600 s to carry out the entire diffractogram. The diffraction data processing are made with "EVA" software which allows the identification of the crystalline phases with comparison to the PDF4+ database (ICDD).

4.1.2 Sample holder

Due to the high reactivity of the hydride powders mainly $LiBH_4$, a sample holder was especially designed in the laboratory for that purpose to avoid air contact. The home-made sample-holder (Fig.2.13) consists on duplicating the commercial version as to be adaptable to the main holder in the diffractometer.

Figure 2.13. XRD sample-holder with Kapton® film cover avoiding air contact

The main part is made of aluminium. At the sample location, a Plexiglas® disk of 14 mm diameter and 2 mm thickness is placed to avoid Al signal. While the diffractomer has a magnetic response for its rotation movement, a steel ring is added to insure more representative measurements. After filling with the sample, the holder is covered with a Kapton® film (25 µm thickness) which is tightened with a ring in the groove machined in the aluminium main part. The tightness of the holder system was improved by silicone lubricant at the groove edge. The prepared samples have less than 1 mm thickness.

4.2 Scanning electron microscopy

Scanning electron microscopy (SEM) is a technique based on the principle of the interactions electron-matter, able to produce high-resolution images of the sample surface. The operation of the microscope is based on the emission of electrons produced by the electron gun and the detection of signals coming from the interaction of these electrons with the sample.
In the interaction volume, the electrons of the beam will lose their energy by multiple collisions with the atoms of material generating many phenomena. From those events, there is an emission of the secondary electrons with energy of 5 eV coming from the surface and backscattered electrons from the inside of the material with an energy of 20 KeV. X-ray radiations are also emitted. Secondary electrons mode is used to observed micrographs with topological contrast. Whereas, backscattered mode is applied for chemical dispersion of the

microstructure. In this mode, enhancement of the micrographs could be optionally obtained on the basis of the signals combination. The microscope is also equipped with X-ray detector for elemental chemical analysis (EDAX). Depending on the atomic number, the emitted X photons from the interaction have different energies. The EDAX use allows us to determine approximately the local composition of the sample. Nevertheless, light elements as Li could not be detected by this technique.

During this work, scanning electron micrographs were obtained with LEO S440 microscope (tungsten filament) equipped with X digital analyzer fit with silicon-lithium diode (EDAX) for chemical analysis. After training in SEM, this equipment is used to examine the microstructure and morphology of the hydride powders. In our case, this technique was useful when additives are added. The large depth field yield a characteristic relief appearance useful for understanding the surface structure of the particles. The SEM experiments were carried out under vacuum and the contact with air couldn't be avoided for few seconds during the transfer of the samples.

Reference

[1] E. Gaffet, A. Köhler, Matériaux (2002) 1-4.
[2] A.R. Yavari, J.F.R. de Castro, G. Vaughan, G. Heunen, Journal of Alloys and Compounds 353 (2003) 246-251.
[3] M.G. Inghram, J. Drowart, In "High Temperature Technology", McGraw-Hill, New York (1959) 219-281.
[4] J. Drowart, C. Chatillon, J. Hastie, D. Bonnell, Pure and Applied Chemistry 77 (2005) 683-737.
[5] D.J. Santeler, Journal of Vacuum Science & Technology A: Vacuum, Surfaces, and Films 4 (1986) 338-343.
[6] P. Morland, C. Chatillon, P. Rocabois, High Temperature and Materials Science 37 (1997) 167-187.
[7] M. Heyrman, C. Chatillon, H. Collas, J.-L. Chemin, Rapid Communications in Mass Spectrometry 18 (2004) 163-174.
[8] F.Z. Roki, C. Chatillon, M.N. Ohnet, D. Jacquemain, The Journal of Chemical Thermodynamics 40 (2008) 401-416.
[9] P. Violet, I. Nuta, L. Artaud, H. Collas, E. Blanquet, C. Chatillon, Rapid Communications in Mass Spectrometry 23 (2009) 793-800.
[10] K. Motzfeldt, The Journal of Physical Chemistry 59 (1955) 139-147.
[11] W.D. Kingery, Property measurements at high temperatures, John Wiley & Sons, Inc. (1959).

CHAPTER 3. MICROSTRUCTURAL BEHAVIOUR OF HYDRIDE COMPOUNDS

In the aim to study the storage behaviour of the complex hydride system (MgH_2-$LiBH_4$), preliminary experiments were carried out with MgH_2 compound alone then with $LiBH_4$ compound additions. Indeed, $LiBH_4$ compound was chosen for its high gravimetric capacity to uptake hydrogen. For that, MgH_2 is used as a destabilizing agent of $LiBH_4$ at different stoichiometries.

In this part we have studied the thermal interaction between the two hydrides in the temperatures range until 500℃. This study allows the choi ce of the suitable amounts of hydrides in the future storage mixtures. The addition of some additives for catalytic purposes will also be presented.

Firstly, we discuss about the mechanical activation by milling of magnesium hydride alone or mixed with lithium borohydride. The aim is to decrease as small as possible the size of the particles in order to increase the specific surface area of the powders. In a second time, the powders are characterized by thermal analysis, XRD and XPS techniques. The purpose is to study the change in the temperature of hydrogen desorption and the appearance of any new phases particularly in the case of hydride mixtures. For that, three consecutive steps are made for this study:

- Reactivation of the pure powders by high energy ball-milling for particles size reduction; at this step, we have determined the size of the particles at the end of a few hundred hours of milling for each compound.
- Desorption reaction of hydrogen from MgH_2 alone and with $LiBH_4$ addition; during this step, we have determined the temperature of desorption of hydrogen from magnesium hydride at different size of the particles and with different compositions of lithium borohydride to form the hydride mixture MgH_2-$xLiBH_4$ (x vary from 0 to 3.5, where x is the number of moles of $LiBH_4$ for one mole of MgH_2).
- Finally, we have tested some additives for catalytic goal in the mixture with the nominal composition x = 2. This last composition is chosen for the study of the hydride mixture as it gives the best hydrogen yield during decomposition with MgB_2 formation.

1 Reactivation of the pure compounds

1.1 MgH_2

The average size of MgH_2 crystallites is evaluated first using the Scherrer formula[1], and then estimated by statistical observations in the SEM micrographs. The average size of the particles depends on the milling time. Vibrating mill seems to be the suitable technique to enhance the specific surface area of the powders.

Around 4 g of MgH_2 is introduced in the mill in the glove box. The milling is performed for 5 hours, and then a sample is taken to be analyzed by XRD. The sampling method was described in the experimental part. It was also observed that there was an increase in pressure of about 40 mbar after 5 hours of milling using a pressure manometer owing to temperature increase by ball-milling. This increase in pressure is attributed to hydrogen release according to the chemical reaction:

$$MgH_2 \rightarrow Mg + H_2 \qquad (3.1)$$

The milling of the same powder for hundred hours does not lead to farther significant hydrogen release. For each powder, the milling is interfered by stop cycles and scrapping of the ball-mill walls to avoid powders agglomerates. Doing so, efficiency of the milling process becomes better. Upon milling, it was observed that the powders have different aspects. The color change from light gray to dark brown and the particles size of the powders decrease.

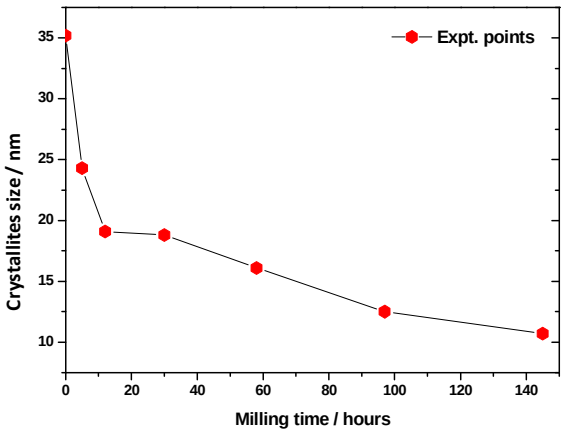

Figure 3.1. Average crystallites size evolution according to the milling time for MgH_2

[1] *Scherrer formula: crystallites size = (0.89 x 1.5418)/(cos(2θ) x FWHM) ; where 2θ in radian and FWHM (radian) is the full width at half maximum of the x-ray reflection in the diffractogram.*

On the basis of the XRD for each powder, we calculated the size of the particles with the Scherrer formula by considering the four intense Bragg peaks of MgH_2 in the diffraction patterns. An average particles size value was obtained for each powder milled at various milling durations. The obtained results are illustrated in the figure 3.1.

The size of the crystallites decreases upon milling time and reaches quasi-stationary state after 145 hours of milling. The calculated diameter of the crystallites for the commercial powder is 35 nm and about 10 nm at the end of milling for 145h using ball-milling device. It should be retained that the tenth first hours are the most important for the decrease of the crystallites size. As indicated, farther milling does not contribute too much to the enhancement of the specific surface of MgH_2 particles.

The size of the grains is also observed on the surface by SEM. The samples are deposited on carbon substrate then introduced in the SEM for analysis in SE mode. The following figure presents the SEM micrograph of commercial MgH_2 and its corresponding statistical distribution of the particles size.

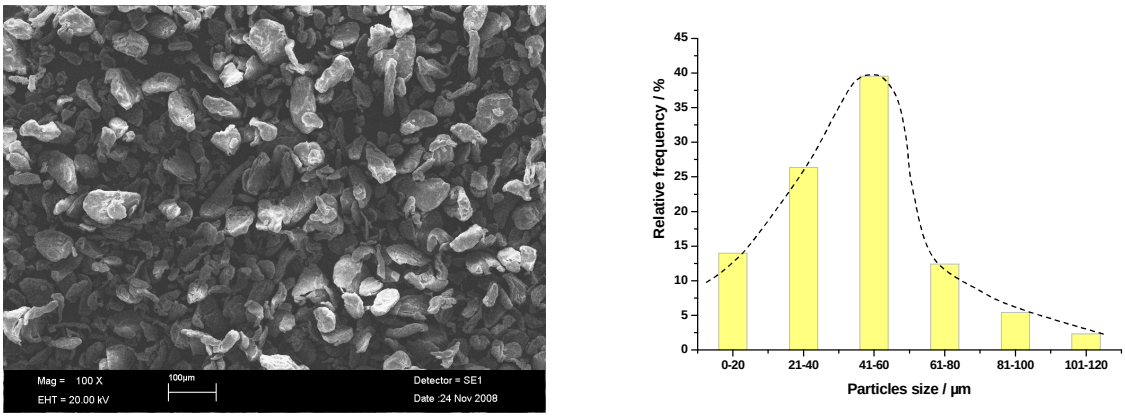

Figure 3.2. (a) SEM micrograph for commercial MgH_2 powder (as received) and (b) powder particle size distribution

A priori, the obtained SEM micrograph with a magnification of 100 fold shows that the size of the particles could vary from 20 µm for the small particles to 100 µm for the big ones (Fig.3.2). The statistical distribution follows a normal distribution with an average of the particles size of 45 µm. The estimated standard deviation (e.s.d) is of about 21 µm which is quite high due to the irregular geometry of the particles.

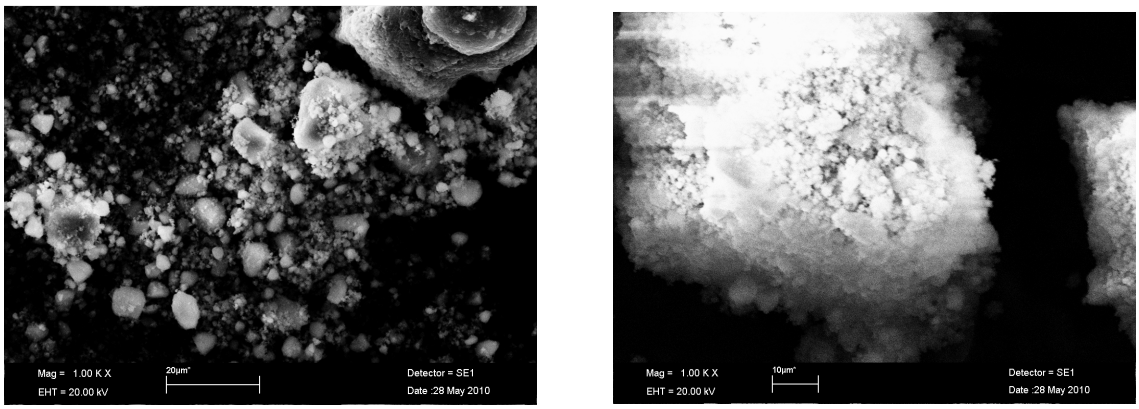

(a) *(b)*

Figure 3.3. SEM micrograph of MgH_2 powder after several milling times (Magnification x 1000): (a) 12 h, (b) 145 h

It should be mentioned that the particles size differs from crystallites size calculated by the Scherrer formula. The observed particles by SEM correspond to an assembly of agglomeration of several nanograins. The figure 3.3 illustrates the milling effect on the grain size and the formation of small agglomerates. At 12 h milling, the size of the particles is decreased with the formation of small agglomeration. The value corresponds to an average of 1 µm. After 145 hours of milling, particles size continues to decrease. The agglomeration increases and the coarse grains are constituted of submicronic particles.

As observed in the SEM micrographs, we could conclude that the commercial powder contains particles of few tens of microns. For the powder with 12 h milling, the particles have a submicronic size. After 145 hours of milling, the particles are even smaller but it is difficult to estimate their size due to agglomeration. In that case, distinguishing the particles is not possible.

After 20 hours milling the decrease in the grain size becomes weak. For that, MgH_2 powders will be pre-milled for about twenty hours before its use in mixture with $LiBH_4$. The XRD pattern of MgH_2 is showed in the figure 3.4 before and after milling. The same specific phases are present before and after milling. Only tetragonal phase (β-MgH_2) is observed without any presence of the orthorhombic phase. Some amounts of Mg and MgO are also present in the analyzed powders. The Miller indices (h,k,l) are indexed for each phase.

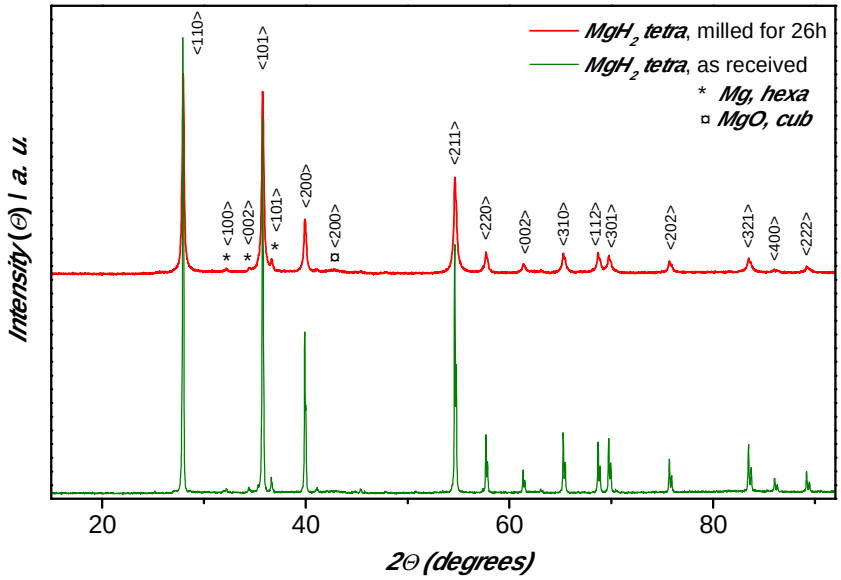

Figure 3.4. XRD pattern of MgH_2 as received and milled for 26 h

To elucidate the milling effect on the hydrogen desorption of MgH_2, we have analyzed the as-received commercial MgH_2, milled for 12 h and 145 h by DTA/TGA thermal analysis. 30 mg of the MgH_2 was filled in the alumina crucible then introduced in the DTA/TGA sample holder. The temperature of heating is regulated from RT to 450℃ with a rate of 5℃.min $^{-1}$. We don't heat higher in order to avoid the formation of Li-Mg alloys. Formation of new phases will be discussed in the next part which concerns the stability of the system $LiBH_4$-MgH_2. All measurements were corrected to the empty crucible cleaned with acid (see experimental part).

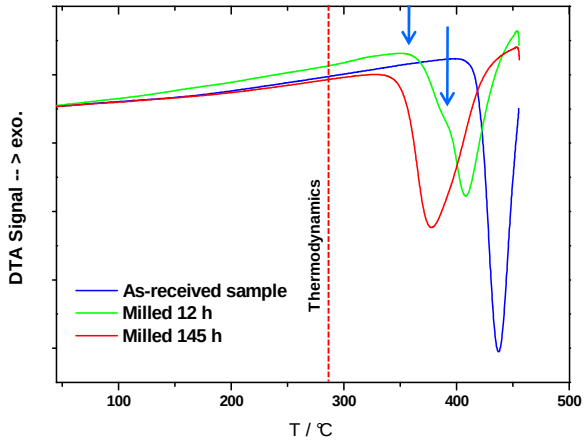

Figure 3.5. Thermal analysis (DTA) of MgH_2 milled at various milling times

The figure 3.5 presents the desorption of hydrogen from MgH_2 as a thermal event upon powder milling times. As expected, the temperature of desorption of hydrogen decreases according to the reduction of the particles size.

The milled powders seems to contain two steps at the desorption event and this point is under discussion in the literature [1], where the thermal splitting might be attributed to the nucleation of Mg for the first event and growth for the second. This behavior could also depend either on metastable phase formed during milling or probably on the particles size which is locally not homogeneous in the powder sample. The width of the events could be related to the low thermal conductivity of the powders with more fine particles.

The desorption temperature obtained by DTA are summarized in the following table where T_{des} corresponds to the onset of the thermal event.

Table 3.1. Dependence of the temperature of desorption (T_{des}) of hydrogen upon the particles size of MgH_2 milled powders

Sample	Average crystallites size / nm	T_{des} / ℃	wt.% H_2
MgH_2 As-received	35	413	7.1
MgH_2 Milled 12 h	19	362	6.9
MgH_2 Milled 145 h	11	341	6.5

From thermodynamic data, the desorption of MgH_2 is around 250℃ at 1 bar (value computed using FactSage software and SGTE-database). Note that, we could not reach this temperature due to kinetic limitations, although the gap could be reduced by decreasing the particle size or increasing the powder specific surface area. After this analysis by DTA/TGA, the temperature of desorption of hydrogen was reduced by milling of about 70℃ without any catalyst addition, a feature which is interesting for hydrogen storage applications. The weight loss obtained by TGA for “as-received” MgH_2 has showed a composition of 7.1 wt.% of hydrogen which is less than the theoretical value (7.5 wt.% corrected to 98 % purity of the commercial product). The decrease in hydrogen content upon milling agrees with the pressure measurements during milling. The hydrogen desorption of the “as-received” powder at 450℃ seems to still contain amounts of MgH_2 or probable contaminations of oxygen during the ball-milling process. The explanation of this feature, is the formation of protective layers either of oxide or elemental Mg around the un-desorbed MgH_2. Maybe the temperature is not high enough to favour the hydrogen loss through the formed layers. As the chemical environment of MgH_2 has an intermediate character between ionic and polarized covalent bond, a minimum of energy is needed to break the Mg-H bonding. In case of kinetic restriction as

discussed above, hydrogen requires more energy to diffuse thoroughly across Mg and MgH_2 layers. Thus, this energy which is dependent on the diffusivity of hydrogen in the studied bulk is the most responsible of the rise of the activation energy of the reaction.

1.2 $LiBH_4$

As in the case of MgH_2, approximately 4 g of $LiBH_4$ was introduced in the mill operating in the glove box, and thus milled for 7 hours. For each specified period, a sample is taken in order to be analyzed by thermal and XRD analysis. Contrary to MgH_2, $LiBH_4$ has shown stability during milling without any release of hydrogen. In the same way, no gaseous release was observed after 25, 53, 92 and 140 hours of milling using pressure manometer. As for MgH_2 milling procedure, for each time interval the $LiBH_4$ powders are removed and the mill's wall scrapped off.

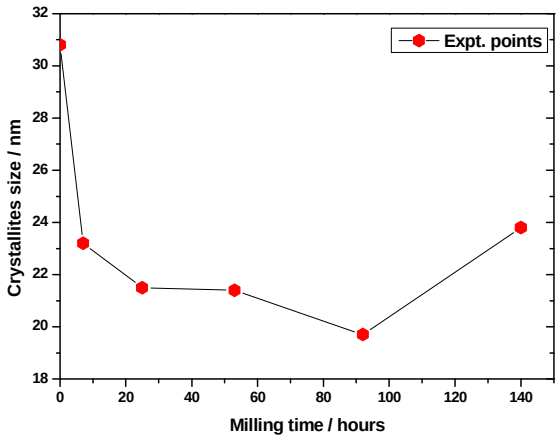

Figure 3.6. $LiBH_4$ crystallites size evolution according to the milling time

The figure 3.6 shows that the size of the crystallites decreases up to 92 hours of milling. At the end of 140 h of milling, the calculated size has increased. This can be explained by a strong agglomeration formed in the mill. Thus the ball-milling becomes inefficient due to the accumulation of $LiBH_4$ layers. Contrary to MgH_2, $LiBH_4$ needs short time of milling due to its easier tendency to agglomerate.

As $LiBH_4$ is constituted of light elements, the electronic density is low. Thus the surface of $LiBH_4$ is difficult to detect by SEM due to its low electrical conductivity and high reactivity compared to MgH_2.

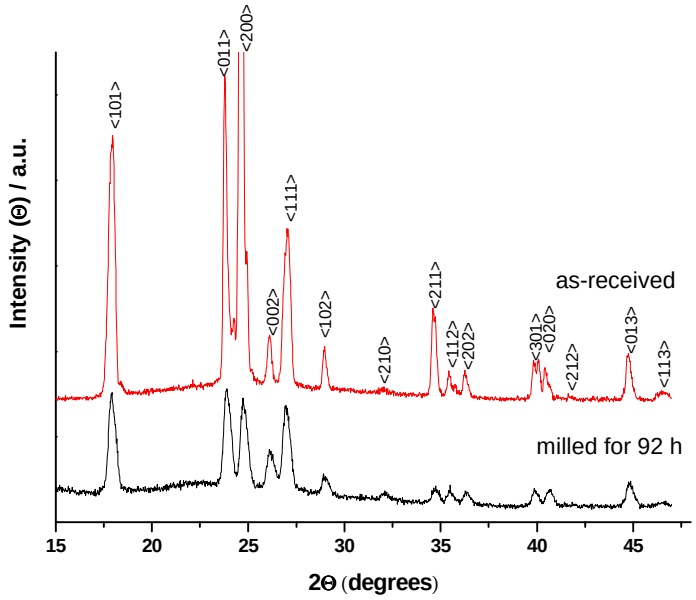

Figure 3.7. XRD patterns of $LiBH_4$ "as-received" and milled for 92 h

The milled $LiBH_4$ powders were analyzed by XRD (Fig.3.7). At room temperature $LiBH_4$ is constituted from single orthorhombic phase. The indexation of this phase is obtained from recent lattice parameters [2] using Poudrix software developed at LMGP laboratory from Grenoble-INP. The milling process does not affect the lattice planes reflection. The width of the peaks is well noticed due to crystallites size decrease by ball-milling effect.

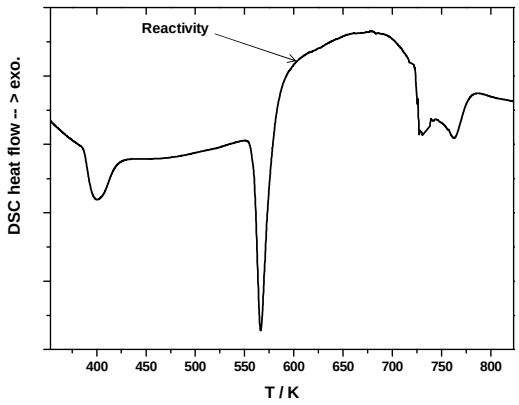

Figure 3.8. DSC curve of pure $LiBH_4$

The figure 3.8 shows a heat flow curve upon heating the $LiBH_4$ compound until 823 K using DSC instrument. The analysis was performed in order to extract enthalpies of the transformations. Unfortunately the compound has shown reactivity with alumina crucible. The decom-

position reaction of the milled $LiBH_4$ powder occurs at around 710 K = 437℃. For that, the thermal analysis of "as-received" $LiBH_4$ in the same instruments as for MgH_2 was avoided due to the reactivity with the crucible and air at the moment of the sample inlet. Despite of this inconvenient, the analysis of mixtures with MgH_2 was realized in these conditions.

2 Reactivation of the mixture MgH_2-x$LiBH_4$

2.1 Phases stability

The hydride mixture MgH_2-x$LiBH_4$ with the stoichiometric ratio x = 2 is predicted in the literature to be the most reliable for hydrogen storage. So we started with this composition in our study of the phases stability under thermal treatment until 500℃ then by varying the relative composition above and below x = 2. Experiments were made by preparing amounts of mixtures in different ratios x = 0.5, 1, 2 and 2.5. From pre-milled compounds prepared previously by ball-milling, the two powders were mixed manually until a quite homogeneous mixture in the glove box is observed before to start the ball-milling for 24 hours. The synthesized hydride mixtures are studied by thermal analysis and XRD for the identification of the phases. For the mixture x = 2, the identification is also supplemented by XPS technique.

- **MgH_2 : x$LiBH_4$ (x = 2)**

The DSC curve of the prepared sample is shown in the figure 3.9 that shows the different transformations taking place during heating. This calorimetric analysis reveals four distinct thermal events. The last shows two steps. The two first peaks correspond, respectively, to the solid phase transition and the melting of $LiBH_4$. The following events are the complete desorption of the hydride mixture, the first for MgH_2 then the second for $LiBH_4$.
The four thermal events observed in the figure 3.9 are summarized:

A. Polymorphic transition of $LiBH_4$ (sol+sol) [3]
B. Melting of $LiBH_4$ (liq+sol) [4]
C. Hydrogen desorption of MgH_2 (liq+sol+gas) [5]
D. Hydrogen desorption of $LiBH_4$ (liq+sol+gas) [6].

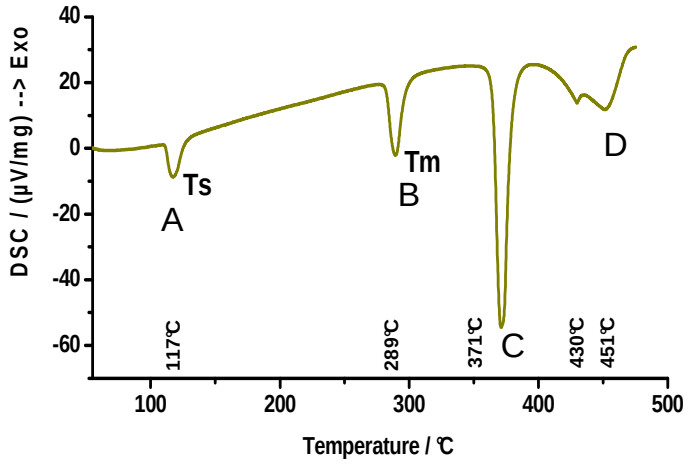

Figure 3.9. DSC curve of MgH_2-$2LiBH_4$ hydride mixture (Ar flow 100 ml.min^{-1}, 5 K.min^{-1} heating rate)

For the desorption of MgH_2, the isotherm shows a steep slope indicating fast desorption of hydrogen in this powder according to the reaction (3.1). The desorption from $LiBH_4$ followed by the formation of MgB_2 occurs in closely two steps according to the following reactions [7-9]:

$$2LiBH_4 \rightarrow 2LiH + B_2H_6 \rightarrow 2LiH + 2B + 3H_2 \quad (3.2)$$

$$Mg + 2B \rightarrow MgB_2 \quad (3.3)$$

where the total reaction, the most favorable thermodynamically, is [7,8]:

$$2LiBH_4+MgH_2 \rightarrow MgB_2+2LiH+4H_2 \quad (3.4)$$

As the formation of boron is globally endothermic, the exothermic formation of MgB_2, produced simultaneously, explains the appearance of rapid recovery in the DSC curve. However, the heat flow compensation effect depends on the enthalpies of decomposition of $LiBH_4$ and of the formation of MgB_2 which is more stable compared to Mg or B alone. If we consider these reactions, we have found at 437℃ - where the enthalpy does not change too much upon temperature - the enthalpic relationship deduced from JANAF tables:

$$\Delta H \text{ (reaction 3.2)} \approx -2 \cdot \Delta H \text{ (reaction 3.3)} \quad (3.5)$$

Pinkerton et al.[10] found that the desorption reaction of the hydride mixture occurs in two steps, unlike the absorption which occurs in one step starting from MgB_2 and LiH under 100 bar of H_2. The authors [10] assume the formation of the amorphous boron during $LiBH_4$ decomposition and report that the recombination of LiH with boron has a very poor kinetics. The presence of Mg was found to assist the decomposition of $LiBH_4$ at low temperature. Mg extract B from $LiBH_4$ leading to H_2 release. The formation of MgB_2 in place of B favours the hydrogenation reaction. They also found that samples dehydrogenated under He gives rise to

only Mg, LiH and probable amorphous boron. The authors [10] showed that MgB_2 could form only under H_2, but not He atmospheres [10]. May be this is dependent on the reducing properties of hydrogen. The presence of oxygen could also restrain the reactions occurring in normal conditions.

Considering the importance of the formation of MgB_2, we looked further the presence of this phase by XRD and XPS. Using both techniques, the synthesized hydride mixture is analyzed before and after thermal treatment. Other probable species which could form in the presence of moisture and oxygen traces will be also considered. This concerns oxides and hydroxides entities such as MgO, B_2O_3 and LiOH which could co-exist intuitively with the condensed phase.

The figure 3.10 shows the XRD pattern of the hydride mixture prepared by ball-milling during 70 h. The XRD of the only ball-milled sample presents the initial phases without any interaction. A peak at 37° is attributed to the γ-MgH_2 phase which is in agreement with previous studies reporting its formation during ball-milling.

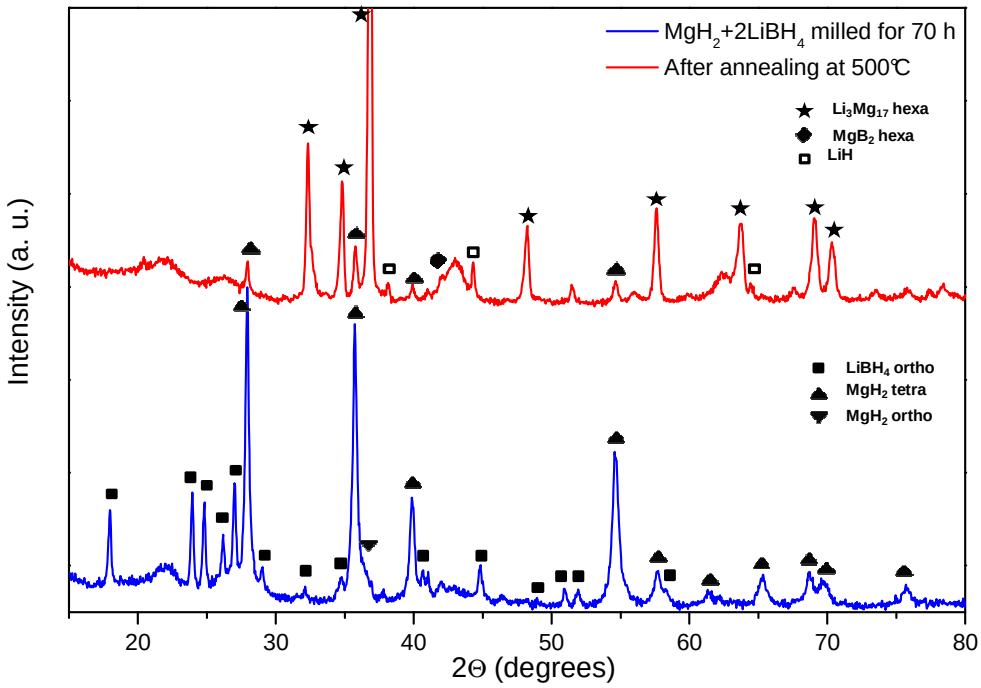

Figure 3.10. XRD pattern of the hydride mixture, milled and after thermal treatment at 500℃

After thermal treatment at 500℃ under Ar, the hydr ide mixture is totally dehydrided. Elemental products, Mg and B combine to form MgB_2 compound. The only hydride still present at such high temperature is LiH generated from subsequent decomposition of $LiBH_4$. Its detec-

tion is well identified by XRD. Nevertheless, the formation of the Li_3Mg_{17} alloy, at such composition is related to the presence of elemental Li during heating process but presumably at low contents. The Li origin could only issue from the decomposition of $LiBH_4$ directly to elemental compounds as follows:

$$LiBH_4 \rightarrow Li + B + 2H_2 \quad (3.6)$$

A non negligible amount of Mg has been alloyed to Li to form Li_3Mg_{17}. In this direction, the bulk should contain quantities of pure boron. As there is no reflection from crystalline phase, boron can be in amorphous state. Some amounts could disappear in B_2H_6 or BH_3 gaseous species even though thermodynamics provide very low pressures for these species.

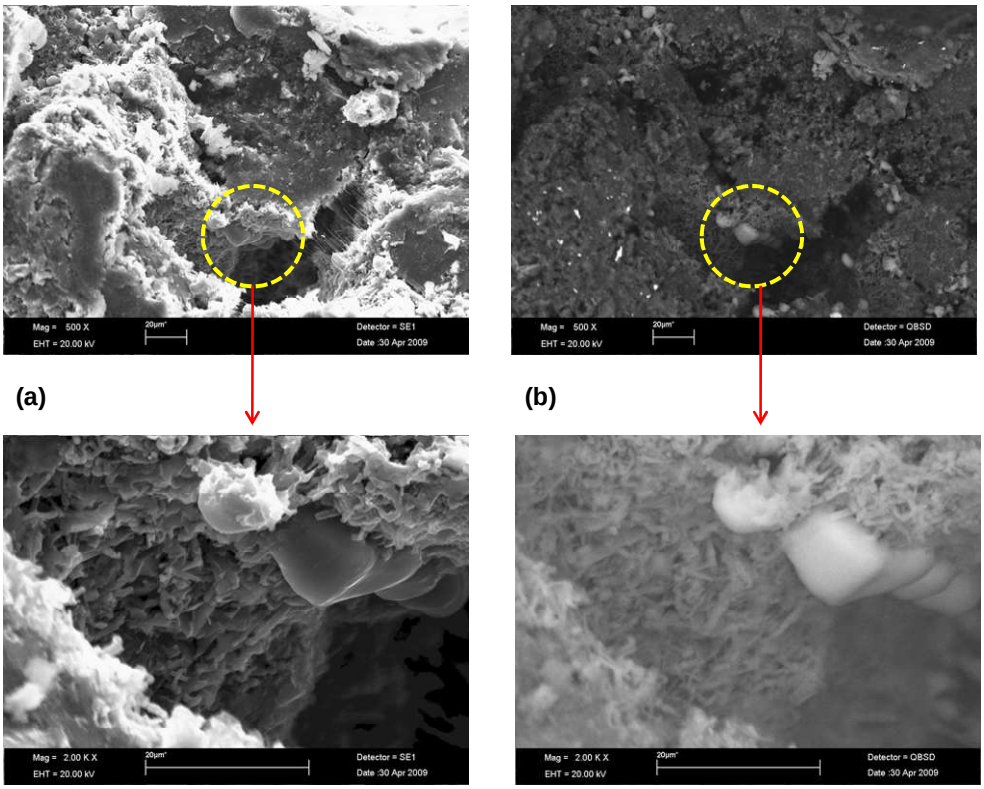

Figure 3.11. SEM micrographs of the hydride mixture after thermal treatment at 500℃ in DSC: (a) SE and (b) BSE modes (Mag. x500 and x2.10^3)

For additional information, the sample heated at 500℃ in the DSC was also observed by SEM (Fig.3.11). By analyzing the pictures, a solid sample was obtained after heating and presents different morphologies. It contains cracks and “seed-corns” resulting from nucleation phenomena. The EDAX analysis proves that the formed germs are enriched in Mg and contained amounts of boron. From our opinion, we think that the germs correspond to the

growth of MgB_2 grains during heating. It should be mentioned that relaxation aspects owing to cooling are also seen in the micrographs. This is probably due to the solidification of the material after the formation of the melt.

To understand the complex formation of the phases during desorption and about the chemical environment of each element, we have carried out the analysis by XPS of the hydride mixture. The figure 3.12 reports the entire recorded photoelectron spectra before and after DSC thermal treatment of the hydride mixture prepared in the same conditions as for XRD analysis. The signal to noise ratio is important because of the disordered powder-sample shape. The calibration of the spectra energy is done by reporting to the referential value of C1s (285 eV).

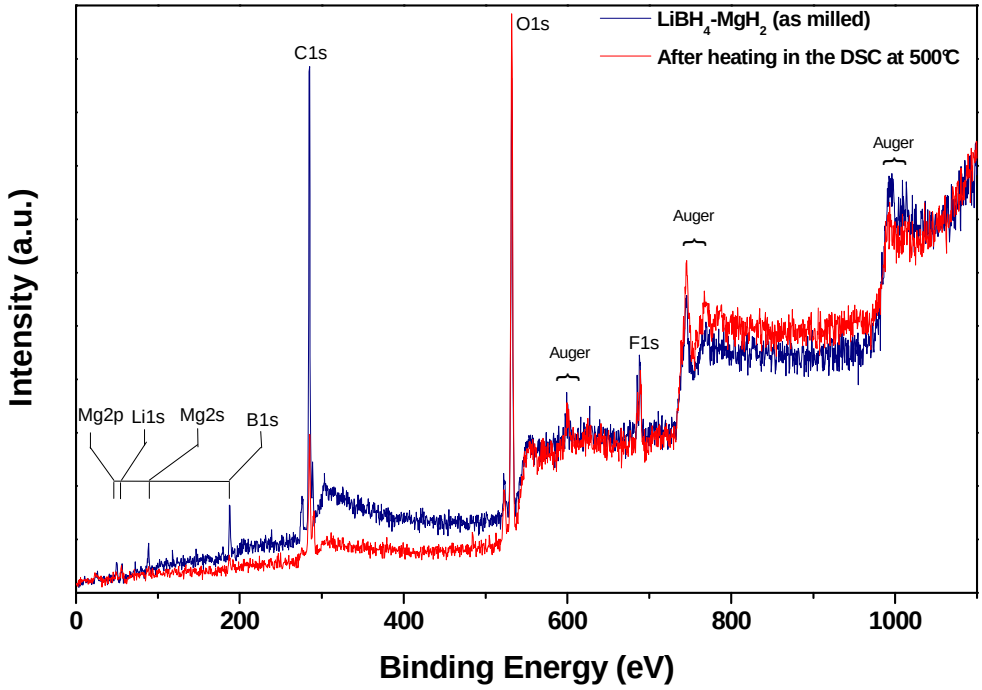

Figure 3.12. XPS analysis of the hydride mixture

Contamination with oxygen could not be avoided. We did not found any explanation for the fluorine F1s existence. All the expected elements are well assigned, except for hydrogen because XPS does not detect H1s. O1s peak intensity is very strong in the heated sample.

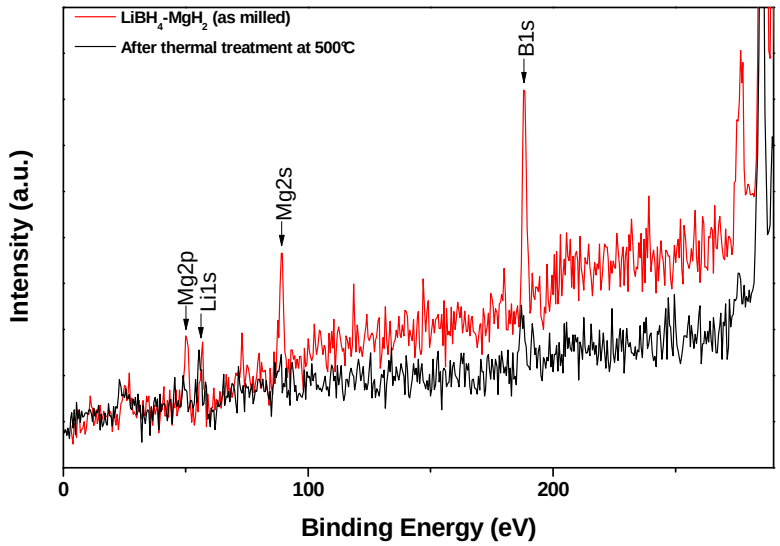

Elementary identification	
Before	After thermal treatement
C	C
O	O
Mg	few Mg
Li	Li
B	few B

Figure 3.13. XPS analysis of the hydride mixture and elementary identification summary

For the hydride mixture without thermal treatment, convenient intensities were observed. Unlikely to the first analysis, the heated sample at 500℃ shows a decrease or almost disappearing of the intensities of the elements. Only Li1s has kept roughly the same intensity with a shift in binding energy of about 1 eV which could be an indication of chemical environment changing. However few Mg and B elements are observed (Fig.3.13).

Air ratio	Milled	After treatment
B1s/Mg2p	2,23	2,58
B1s/Li1s	1,02	0,2
Li1s/Mg2p	2,18	12,6

Figure 3.14. Identified elements and their ratio for milled and thermal treated hydride mixture

The calculation of the peaks area ratios (Fig.3.14) between the elements for the milled hydride mixture indicates a good agreement with the starting composition ratios. However, the analysis of the thermally treated samples shows acceptable stoichiometric ratio between B1s and Mg2p, but their presence remains weak. As the Mg contribution is very weak, the shift in energy for Li1s is attributed to the high reactivity of Li with the moisture to form LiOH on the surface. The few Mg and B elements observed is due to the resolution of this technique to analyze the surface which is about 10 nm. Boron could also be justified by probable B_2H_6 or BH_3 gas loss.

As the presence of MgB_2 is well emphasized in the case of the hydride mixture x = 2, we were interested to other ratios which could enhance the production of more MgB_2 content.

- **MgH_2 : x$LiBH_4$ (x < 2)**

For ratios lower than 2, two powders were prepared with the same procedure as described for x = 2. At the end of ball-milling, the powder x = 1 presents some coarse grains. The reactivity with liquid water was also observed after the end of milling. The powder x = 0.5 has shown high reactivity compared to x = 1. These two powders were submitted to thermal treatment under argon atmosphere at 500℃. The XRD patterns of the resulting phases are indicated in the figure 3.15.

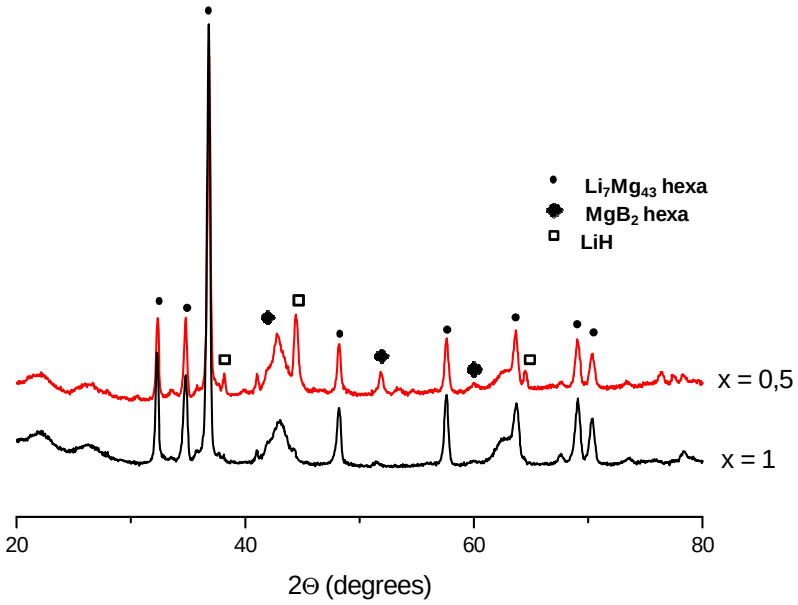

Figure 3.15. XRD patterns of the hydride mixtures (x = 0.5 and 1) after thermal treatment at 500℃

The production of LiH and MgB_2 is better identified for x = 0.5 than for x = 1. Yu et al.[11] have also reported the formation of Li-Mg compounds for Mg-enriched compositions such as for the ratio x = 0.3. MgB_2 was shown to form at temperature above 500℃ but n ot at 405℃. In addition, photoelectrons spectroscopy of MgB_2 shows that the Mg valence is lower than (2^+) [12], that could provide from several $MgB_{2-\varepsilon}$ phases ($0 < \varepsilon < 0.5$) with variable stoichiometries. It is also reported elsewhere by XPS that the atomic ratio x, according to the

surface enhancement, could vary such as: 1.17 < x < 2.21 [13]. For that, when x = 2-ε we can consider the total reaction:

$$MgH_2 + xLiBH_4 \rightarrow MgB_x + xLiH + (2+3x)/2H_2 \quad (3.7)$$

Starting with MgH_2 rich mixtures (x = 0.5 and 1), the resulting phase is more enriched with Mg. This is the reason for which the alloy Li_7Mg_{43} has been formed instead of Li_3Mg_{17} as in the case of the hydride mixture x = 2. The two alloys compositions are close in the Li-Mg phase diagram (framed region in figure 3.16) corresponding to the molar compositions 0.86 and 0.85. The presence of Li-Mg alloys in the bulk is not trivial. In fact, it has been reported recently that Mg-enriched mixtures increase the kinetic of the hydrogen sorption reactions compared to pure magnesium [14].

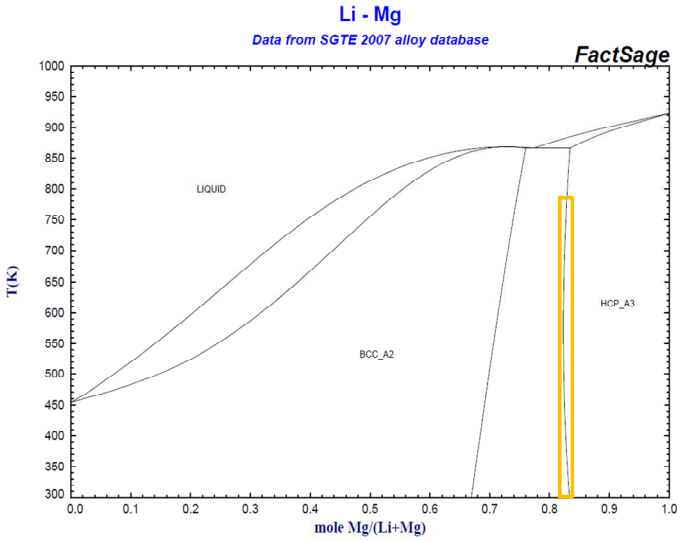

Figure 3.16. Li-Mg assessed phase diagram (computed with FactSage software)

- **MgH_2 : $xLiBH_4$ (x > 2)**

For higher content of $LiBH_4$, a sample of the hydride mixture with x = 2.5 was prepared. The product of the reactions after thermal treatment was analyzed by XRD for identification of the existing phases.

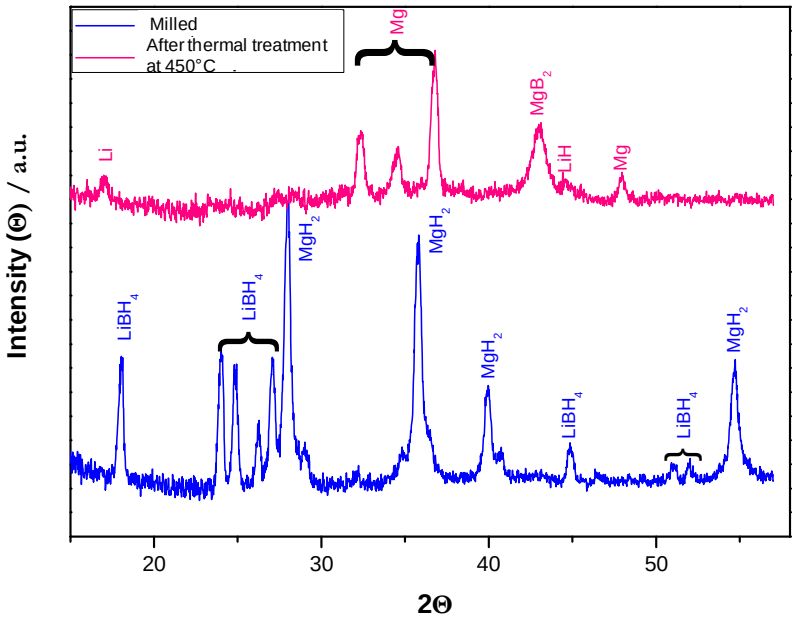

Figure 3.17. XRD patterns for the milled hydride mixture x = 2.5 before and after thermal treatment

The figure 3.17 shows that before thermal treatment (i.e. only milled sample), all the original phases are identified meaning no reaction occurs. After thermal treatment at 450℃ the Bragg peaks of $LiBH_4$ and MgH_2 disappear. As a result, there is a formation of Li and Mg elements. However, the Mg Bragg peaks present a slight shift which could be related to the formation of a solid solution with Li, as observed for $x \leq 2$, but in very weak alloying composition. For this hydride mixture with x = 2.5, the indexing of MgB_2 and LiH phases is difficult and not clear. This is probably due to low kinetic and weak diffusion of boron in the Li and Mg layers. This observation is proved by the presence of elemental Mg and Li. We did not observe boron by XRD because it is very probable that it exists as an amorphous phase. The presence of Li in addition to LiH suggests the decomposition of $LiBH_4$ in two paths (Equ.3.2 and 3.6) as predicted by Stasinevich et al.[4] when studying hydrogen pressure dependence of $LiBH_4$ thermal decomposition.

Until now, the phase diagram of the B-Mg system is not clearly established, although the identification of phases is still appearing since 1890 [15]. The existence of intermediate phases of the formula Mg_xB_y is confused [16]. Ariya et al.[17] have studied the Boron-Magnesium system by calorimetric and spectrometric techniques and he found that there are many individual compounds MgB_x in the B-Mg system for $x > 2$. The best known are MgB_2, MgB_4, and MgB_7, which have been synthesized directly from magnesium and boron powders.

The thermodynamic studies of the MgB_x phases show an increase in the heat of formation in the order as follows: $MgB_2 < MgB_4 < MgB_6$ ($\Delta_f H$ is given in $kJ.mol^{-1}$ of atoms).

2.2 Thermal analysis of the desorption reactions

The aim of this part is the determination of the temperature of the thermal events in MgH_2-$xLiBH_4$ mixtures. The "as-received" compounds (MgH_2 and $LiBH_4$) were pre-milled individually for approximately one week then mixed in the desired stoichiometric ratio x = {0, 0.1, 0.5, 1, 2, 2.5, 3.5} and milled again for 24 hours. The mixtures were analyzed by DTA/TGA up to 450℃.

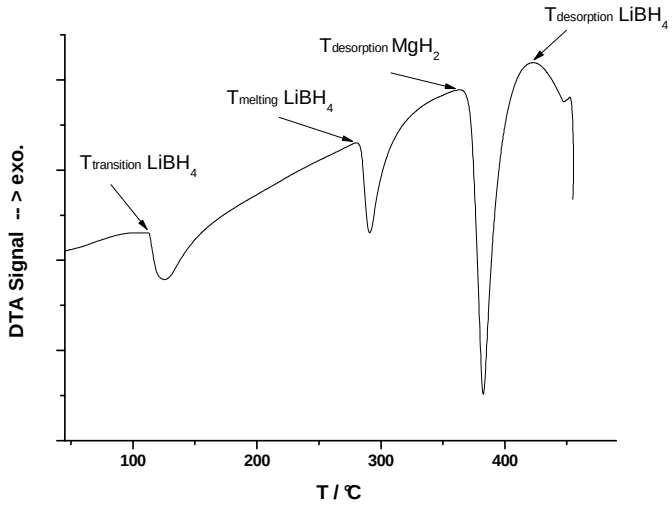

Figure 3.18. Thermal analysis of the hydride mixture (x = 2) by DTA

For x = 2 composition, the thermal analysis by DTA is reported in the figure 3.18. All the thermal events are identified and they agree with the previous DSC measurements for this composition.

The results of the analysis by DTA are summarized in the table 3.2. The temperatures correspond to the onset of the thermal events determined by the tangent method at ± 0.5℃.

Table 3.2. Thermal analysis of the hydride mixtures by DTA at different molar fractions

Ratio x	Molar fraction Li/(Li+Mg)	T_{trs} $LiBH_4$ / ℃	T_{melt} $LiBH_4$ / ℃	T_{des} MgH_2 / ℃	T_{des} $LiBH_4$ / ℃
0.00	0.000	--	--	352	--
0,10	0.091	117	--	355	--
0,50	0.333	116	277	366	--
1.00	0.500	115	282	362	423
2.00	0.667	113	284	372	429
2,50	0.714	119	283	371	435
3,50	0.778	122	285	378	>450

The MgH_2 desorption temperature increases with $LiBH_4$ addition with an anomaly for x = 2.5 which could be related to an experimental error. Two steps were identified for the desorption of $LiBH_4$ for x = 2. While for the other compositions the second step seems to appear at higher temperature. From table 3.2 and additional DSC analysis at higher temperature (500℃), it can be concluded that the two consecuti ve events depend on the composition. Indeed, T_{des} of $LiBH_4$ decreases by increasing MgH_2 content. The temperature of the transition of $LiBH_4$ shows a dependence on the composition with an eutectoid at around 66.7 mol.% of Li composition (x = 2). The melting of $LiBH_4$ has a tendency to decrease for Mg-enriched powders. For x < 0.5 the melting event is practically not well identified.

3 MgH_2-2$LiBH_4$ system for hydrogen storage

3.1 Without additives

MgH_2- 2$LiBH_4$ is prepared by milling under argon as described before. All samples were analyzed by XRD in order to confirm the presence of the initial phases and to detect any formation of oxides or any other compound.

The prepared samples using planetary and vibrating mill was analysed by SEM. The figure 3.19 illustrates the obtained micrographs in both SE and BSE modes. For the same duration of milling, the two powders present a little different morphology. The micrographs in SE mode show that the milled powders with the planetary mill present a uniform particles size, whereas the vibrating mill contains some fine particles.

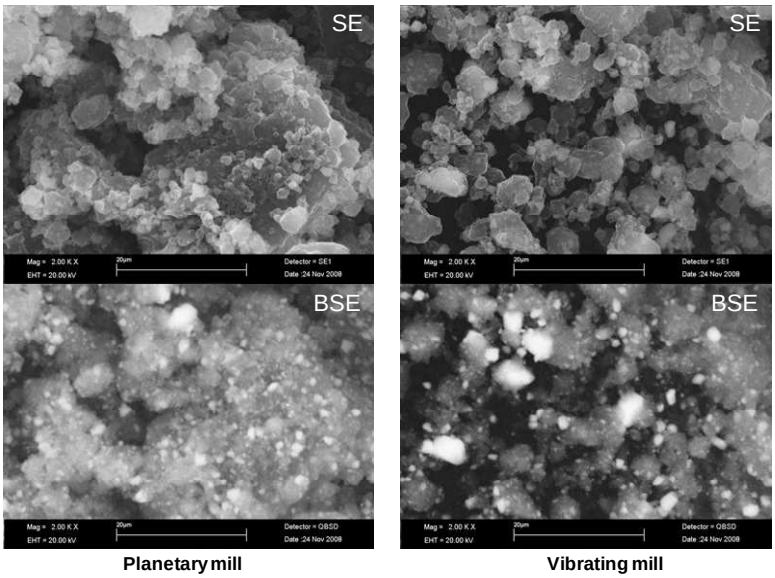

Figure 3.19. SEM Micrograph of MgH_2-2$LiBH_4$ prepared by planetary and vibrating mill in SE and BSE modes (Mag. x 2.10^3)

We have compared our samples with those received from GKSS by XRD, SEM and DSC analysis because the milling devices used for the preparation of the powders are not similar. The received MgH_2-2$LiBH_4$ hydride mixture from GKSS Research Center was stored in the glove box (Synthesis procedure is given in the experimental part).

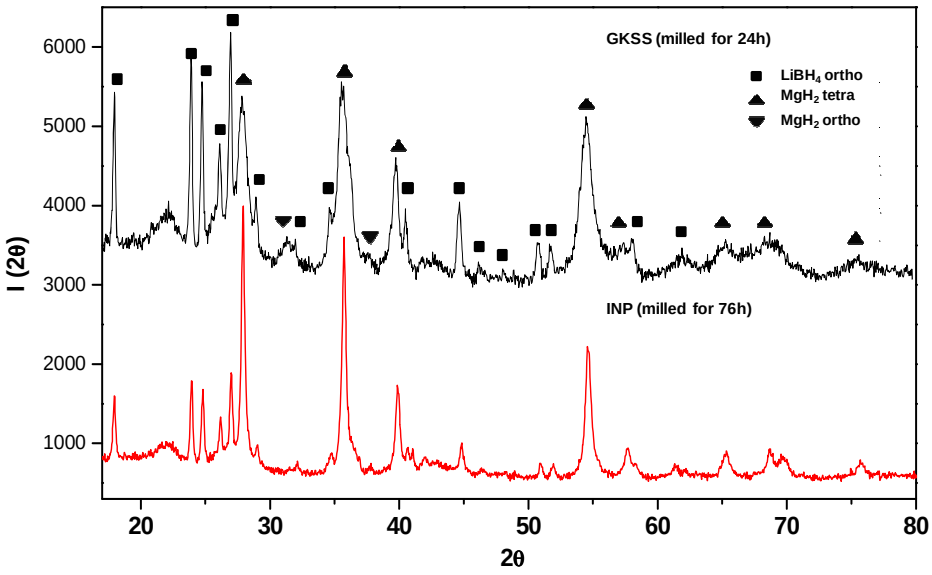

Figure 3.20. XRD patterns of received powder from GKSS Research Center compared to our own

After analysis in the DSC and SEM, we have observed the importance to mill the compounds before their mixing. Thereafter, the samples were prepared from pre-milled amounts of each compound (MgH_2 and $LiBH_4$). In order to avoid overheating of the mill and, consequently, the modification of the powders properties, a water cooling system was used during the milling. It was observed that this does not change the resulting powders. Finally, the milling procedures were carried out without water cooling.

The XRD patterns (Fig.3.20) show the presence of the same phases but with different widths of the peaks. It was concluded that, the preparation procedure could affect the resulting powders. Indeed by calculating the crystallites size using Scherrer formula the GKSS powder present more fine powder regarding MgH_2 and less fine one for $LiBH_4$. This result agrees with the fact that $LiBH_4$ from GKSS is used without pre-milling.

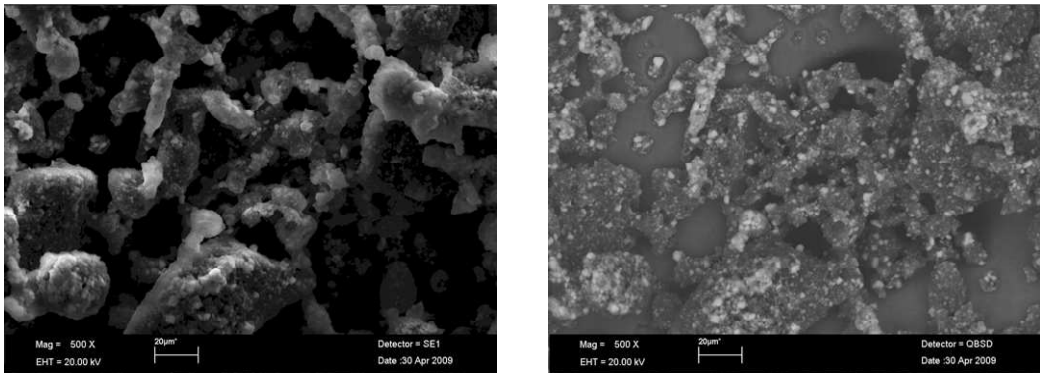

(a) **(b)**

Figure 3.21. SEM micrographs of received powder from GKSS Research Center: (a) SE and (b) BSE modes (Mag. x500)

The above figure 3.21 presents the SEM micrographs of the GKSS received powder. It shows a uniform distribution of the particles and good dispersion of Mg in the form of MgH_2 inside the bulk. This case appears to correspond more to our sample when planetary mill is used (Fig.3.19). The DSC analyses of the powders are reported in the figure 3.22.

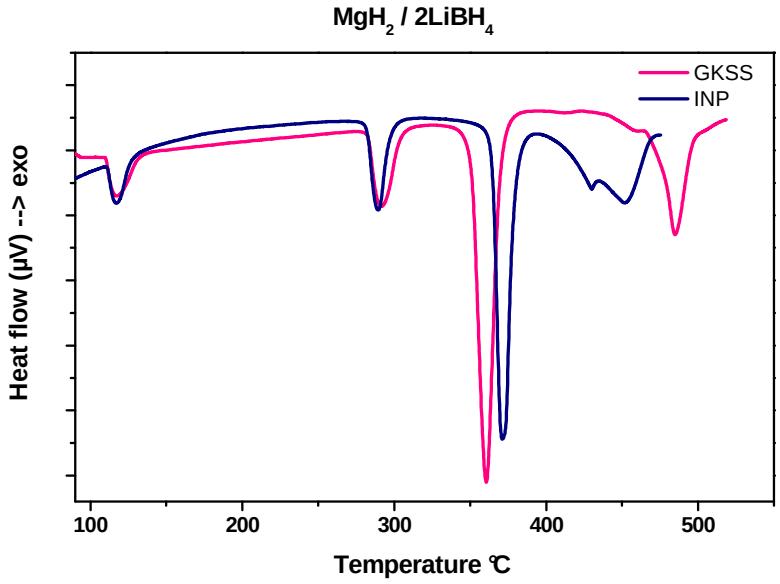

Figure 3.22. DSC analysis comparison of the hydride mixture at x = 2

As only MgH_2 is pre-milled for the samples received from GKSS, we have observed in the thermal analysis using DSC different behaviors for the two powders. The pre-milling of $LiBH_4$ allows a considerable decrease - about 40℃ - of th e temperature. It is clearly shown that the preparation method influences the temperature of the desorption isotherms.

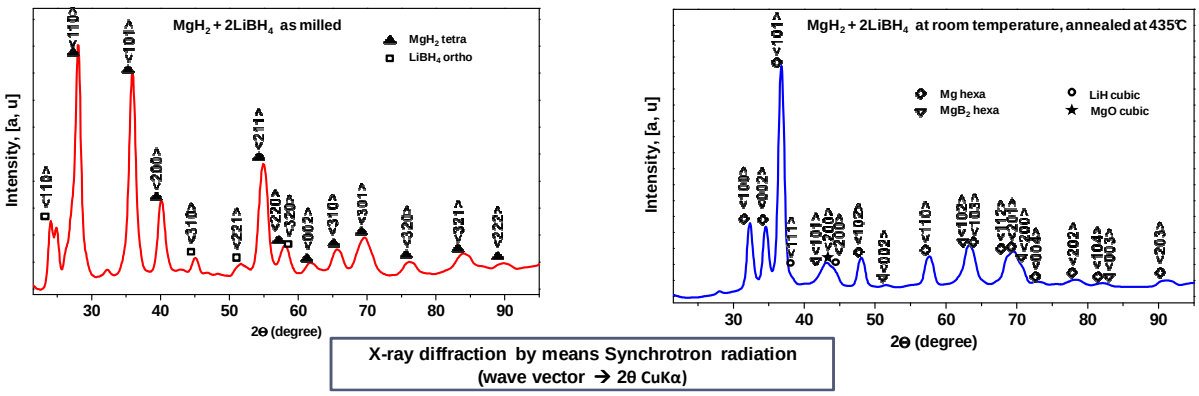

Figure 3.23. Room temperature X-ray reflections using synchrotron beam of the MgH_2-$2LiBH_4$ hydride mixture before and after annealing

From observation of the thermal behaviour of the hydride mixture, a sample was heated and stopped just after the decomposition of $LiBH_4$. The sample is introduced in a sealed glassy-tube for its analysis by means of x-ray reflection using synchrotron radiation in transmission mode. Experiments were performed at the ESRF (European Synchrotron Radiation Facili-

ties). The figure 3.23 shows the obtained results of the sample before and after annealing. At 435℃ we observe a complete desorption of the hydri de mixture. Weak escarpments are attributed to the presence of LiH and MgB_2. It is difficult to distinguish elemental Mg and its Li-alloys. In fact, the widths of the peaks can be due also to the thickness of glassy-tube walls which is about 1 mm.

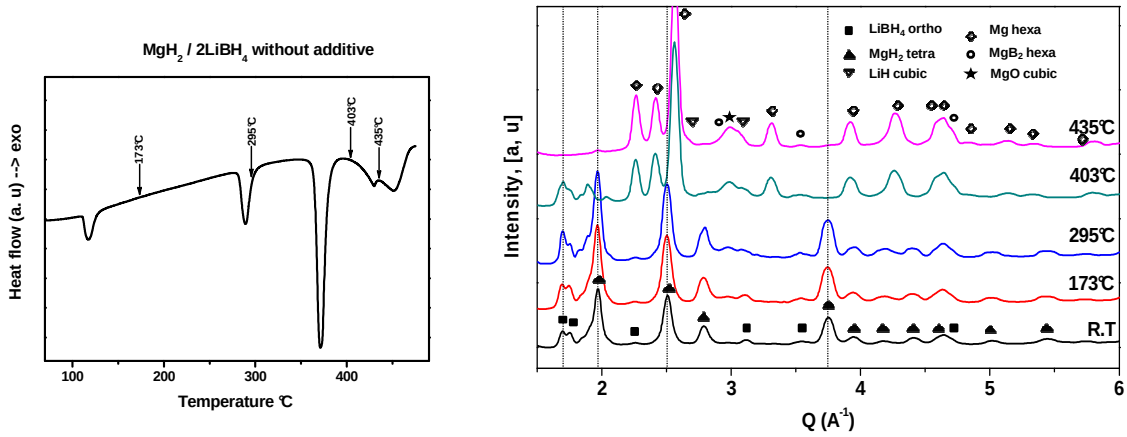

Figure 3.24. Room temperature X-ray reflections using synchrotron beam of the MgH_2-$2LiBH_4$ hydride mixture upon temperature of annealing in DSC

To understand the formation of the phases during heating in the DSC, the experiment is cooled at different step and the sample taken in sealed ampoules for analysis. The above figure shows the obtained x-ray patterns at each stage of heating. A good agreement between DSC and XR patterns was observed. This confirms the complete desorption of the MgH_2 at around 400℃. The phase transition (ortho → hexa) of $LiBH_4$ is confirmed to be reversible. At 435℃ $LiBH_4$ is already desorbed against the onset of the desorption temperature ~437℃ of pure compound analysed by DSC.

3.2 With additives

After having studied the desorption of the hydride mixture, we have also studied the mixture by adding additives for catalytic purposes. In general, the choice is based on the existing data about the affinity of these materials to catalyze hydrogen exchange reactions and also their stability during the thermal treatment. The used additives were Ti, Ni, Cu, B, C and Na-based additives.

- **Ti-isopropoxide (Tiso), Ti-$(OCH(CH_3)_2)_4$**

This additive was proposed by GKSS team. They found that the best improvement of the kinetic and the temperature of the hydride mixture was obtained when Ti-isopropoxide and VCl_3 were added as catalysts [8]. We have also tested in our laboratory the effect of this additive on the hydride mixture. Doing so, we think that this could clarify the following points:

- confirm the preparation of our samples since the addition of this additive should interact in the same manner in case of similar rheological and chemical aspects
- verify the catalytic effect of the additive
- and if the last point is valid, look for the catalytic mechanism.

Ti-isopropoxide (10 mol.%) additive which is liquid at room temperature is added to the hydride mixtures then milled again for 24 h. After milling, the powders present dry aspects which suppose the decomposition of the additive during milling. By addition of Tiso as additive to the two powders (our and received from GKSS), we have obtained comparable behaviours regarding the thermal events using DSC (Fig.3.25).

The identified isotherms show a good agreement between the two powders. The desorption of MgH_2 is closer to the melting event of $LiBH_4$ for the case of GKSS powder. This is in agreement with the observed DSC curves for the powders without additives in figure 3.22. Two consecutive exothermic events are also identified in both cases.

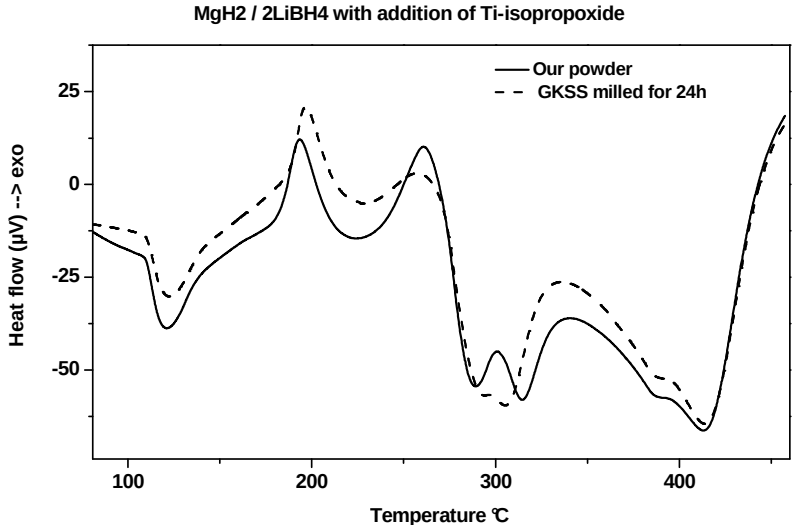

Figure 3.25. DSC thermograms of our MgH_2-$2LiBH_4$ and from GKSS when it is added Ti-isopropoxide as additive (under Ar flow, 10 $K.min^{-1}$)

Looking at the physical and chemical data upon heating of Tiso, several hydrocarbons could be concerned. In fact, mass spectrum of Tiso heated at 180℃, shows the presence of several possible fragments with or without titanium [18]. To explain the observed exothermic events-transformations, we have carried out the XRD of the samples heated and stopped after each event in the DSC as shown in figure 3.26. The as milled powder does not indicate clearly the presence of any Ti-based crystal. At 208℃ the diffractogram remains almost the same, unless some changes in $LiBH_4$ intensities ratio. Tow Bragg peaks of MgO are already observed at 262℃, resulting from the beginning of the desorption of MgH_2. Only after complete desorption of the MgH_2-$2LiBH_4$ hydride mixture at 530℃, a Ti_3O residue could be observed. As a result, that at such heating temperature Ti act in the powder in oxide form and remaining hydrocarbons transform into elemental carbon. Therefore, the effect of this catalyst could act by two separate components. As transition metals have been shown to improve the H-sorption of hydrides, the introduction of Ti has a considerable effect in relation with the presence of carbon compounds. Moreover, the obtained result for $LiBH_4$ desorption is comparable when carbon nanotubes were added as cited before [19].

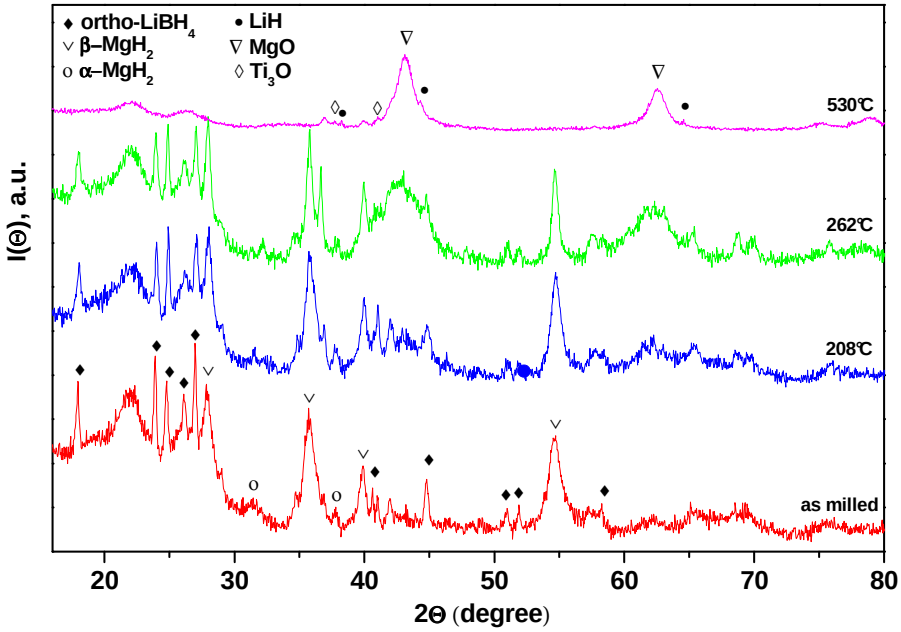

Figure 3.26. XRD patterns of MgH_2-$2LiBH_4$ with Tiso as a function of the temperature

From previous bibliographic study, the role of transition metals is to facilitate the break of hydrogen bonding and the chemisorption of hydrogen molecules. Likely, the role of carbon is to enhance the diffusivity of elements by avoiding bulk sintering. Indeed, local nucleation and growth phenomena are observed more clearly for mixture without additives.

■ Carbon-based additives

The Mg+C mixture was ball-milled at room temperature for 120h to synthesize the Mg_2C_3 compound but it does not form at the temperature of milling. [2Mg+3C] was used as a part of two elements Mg and $C_{graphite}$. This additive is then compared with $C_{graphite}$ alone and Tiso. C-based additives show different behaviors in the DSC (Fig.3.27) when metals are included.

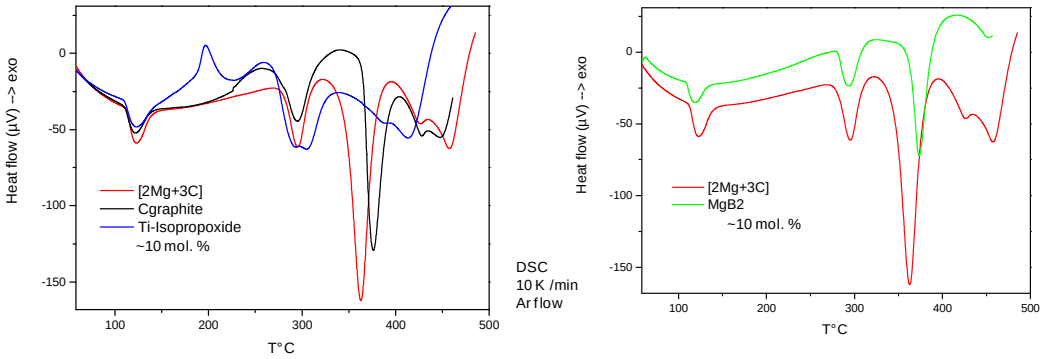

Figure 3.27. DSC curves of the hydride mixture with carbon-based additives (Ar flow, 10 K.min^{-1})

The mixture [2Mg+3C] shows a decrease in the temperature of desorption of MgH_2 when compared to $C_{graphite}$ alone. Whereas, the desorption of $LiBH_4$ appears at the same temperature. Despite its decomposition, Tiso is still the most interesting additive comparing to the two other additives. The addition of MgB_2 seems less efficient when compared to [2Mg+3C].

■ Boron-based additives

Boron additions, in the two condensed states B_{am} and B_{cry}, were tested and compared to MgB_2. The following figure 3.28 shows the desorption reactions of the hydride mixture with additives using DSC.

The temperature of MgH_2 desorption increases in this order, $MgB_2 < B_{cry} < B_{am}$, whereas the temperature of $LiBH_4$ desorption decreases in the opposite order. Thus, the additives MgB_2, B_{cry} and B_{am}, induce contrary effects regarding the MgH_2 and $LiBH_4$ desorption. Note that for $LiBH_4$, the effect agrees with as predicted by the equilibrium constant of the main decomposition reaction.

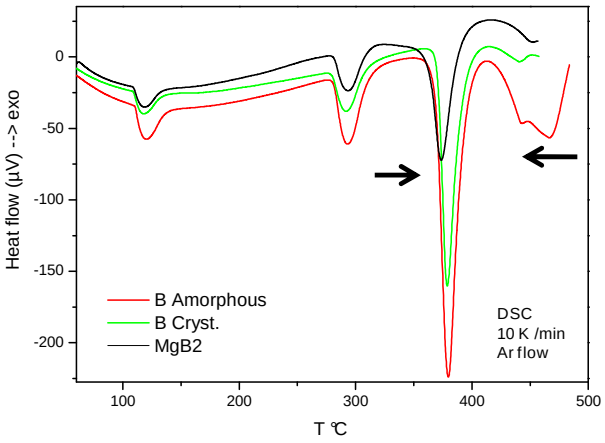

Figure 3.28. DSC curves of the hydride mixture with boron-based additives (Ar flow, 10 K.min^{-1})

Na-based additives

Additives are based on Na such as Na-pyrophosphate (Na-pyro, $Na_4P_2O_7$), Na-peroxide (Na-pero, Na_2O_2). The later was shown to react spontaneously with the hydride mixture, thus its use was dismissed. Na-pyro additive (10 mol.%) is carefully mixed and then milled with the hydride mixture. XRD patterns are reported in the figure 3.29 for the two cases.

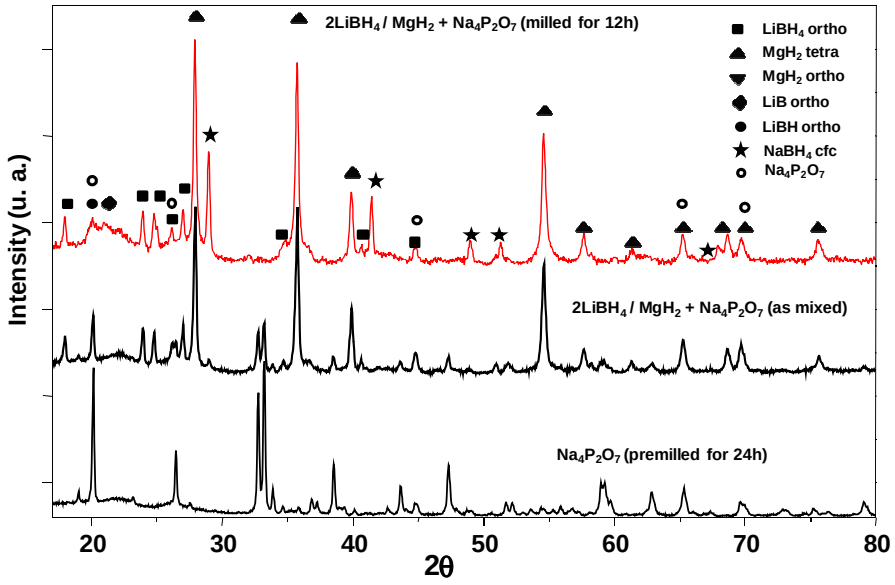

Figure 3.29. XRD patterns of the as-mixed and then milled hydride mixture with Na-pyro addition. The pre-milled Na-pyro additive is also reported as reference

After milling of the powder with additive, it was observed the formation of $NaBH_4$ compound. Until the mixing of the hydride and the additive, there were no significant contents of this compound. The reaction involving the formation of $NaBH_4$ compound would be:

$$4LiBH_4 + Na_4P_2O_7 \rightarrow 4NaBH_4 + Li_4P_2O_7 \quad (3.8)$$

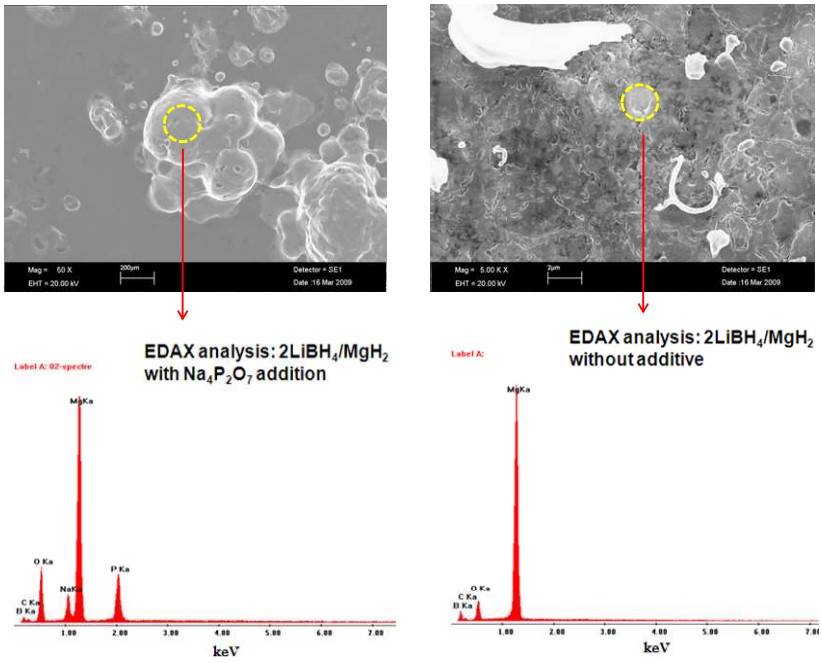

Figure 3.30. SEM micrographs and chemical analysis (EDAX) of the hydride mixture without and with Na-pyro addition (Mag. x5.10^3 and x50 respectively)

For the sample without additive, the elemental chemical analysis using EDAX probe shows the presence of Mg and B. C is related to the substrate and O to the contamination at least at the moment of the introduction of the sample in the SEM. Li and H could not be detected due to their low electronic density. The sample with Na-pyro additive presents amounts of P and Na in acceptable proportions.

For studying the thermal behaviour of the hydride mixture, samples were heated and stopped at different stages of heating in the DSC (Fig.3.31). The samples were treated in the same way as for the hydride mixture without additive.

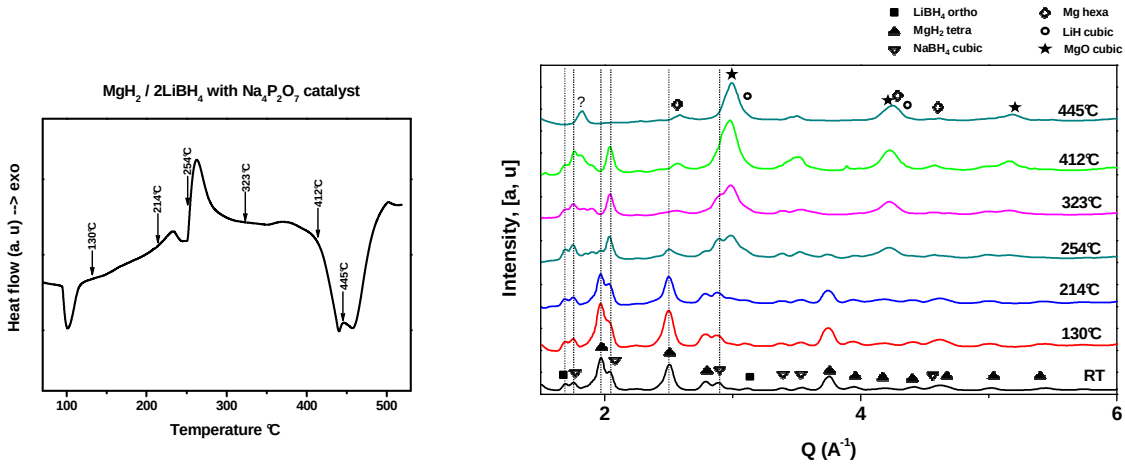

Figure 3.31. Room temperature x-ray reflections using synchrotron beam of the hydride mixture with Na-pyro addition upon temperature of annealing in DSC

The DSC curve of the hydride mixture with Na-pyro addition shows different behavior compared to the hydride mixture alone. It reveals also the presence of two exothermic events. From both X-ray and DSC data, MgH_2 desorption is almost over at 254℃. If the reactio n 3.8 is a complete reaction, 14 mol.% of $LiBH_4$ is being involved in the formation of $NaBH_4$. The last event in the DSC seems include respectively $LiBH_4$ and $NaBH_4$ desorptions assisted by x-ray reflections. The disappearance of the melting event of $LiBH_4$ may be related to a heat compensation effect due to the presence of an exothermal effect in the range 300 to 400℃ that reveals the existence of a compound or mixture (solid solution) formation. The hypothesis of the presence of an eutectic joined to $LiBH_4$ - $Li_4P_2O_7$ system is also probable at around 350℃. The additive Na-pyro seems to act as a catal yst only regarding MgH_2 desorption.

- **Nickel and Copper-based additives**

Using nickel-based additives, it is observed considerable reduction in the temperature of the desorption of hydrogen. Nickel was used in single and saline form. The best temperature yields were obtained with a mixture of the two compounds. With Ni, the reduction in the temperature of the desorption of MgH_2 is 40℃ and 16℃ for $LiBH_4$.

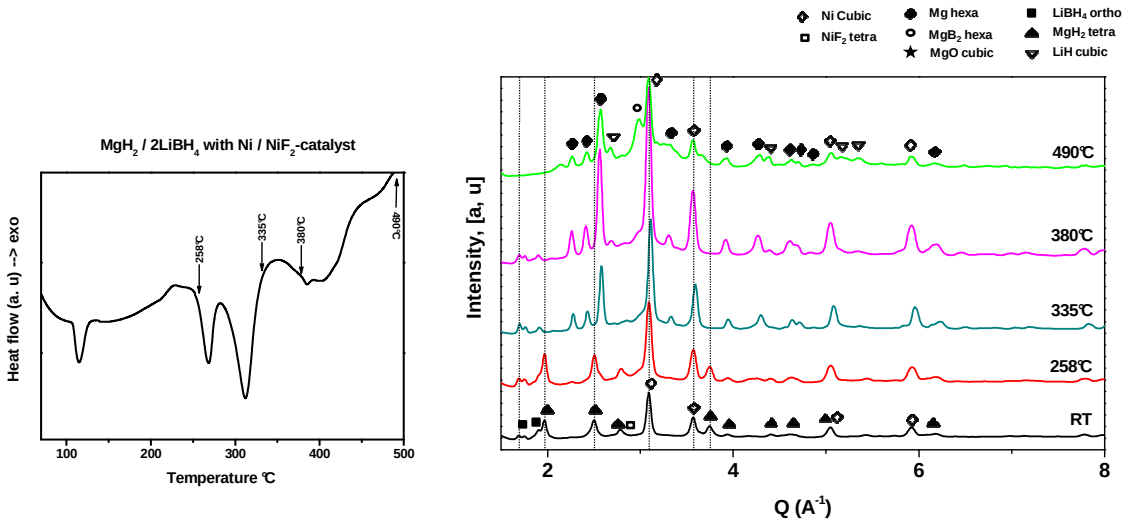

Figure 3.32. Room temperature X-ray reflections using synchrotron beam of the MgH_2-2$LiBH_4$ hydride mixture with Ni-based additive upon temperature of annealing in the DSC

From the above experimental data when Ni-NiF_2 (5-5 mol.%) is added, there is a decrease of the desorption temperature of MgH_2 of about ~60℃ and considerable effect on $LiBH_4$ melting and desorption temperatures. In contrast to Na-pyro additive, at 258℃ the desorption of MgH_2 is not yet occurring. The obtained results are very similar to Tiso addition. The presence of MgB_2 and LiH products are well identified. Ni is still present at the temperature of heating. Only few NiF_2 was observed. Probably, fluorine reacts to form a more stable phase which could be MgF_2.

Copper based additive was also tested with the addition of Si to ensure the stiffness of the material in view of facilitating the milling of powder samples. $Cu_{90}Si_{10}$ alloy was synthesized by rolling-mill and ball-milled for several days to obtain the powder. The effect of the temperature reduction with the $Cu_{90}Si_{10}$ additive is weak, about a few degrees.

4 Conclusion

- **Reactivation of the pure compounds**

In this chapter, firstly we have studied reactivation of the MgH_2 and $LiBH_4$ pure compounds using ball-milling. The calculated size of the crystallites using Scherrer formula could reach 10 nm for MgH_2 and 20 nm for $LiBH_4$, after approximately one week of milling. In a second time, we have studied the reaction of desorption of hydrogen from MgH_2 by DTA/TGA. It has shown a decrease in the temperature of desorption when the specific surface area of the

powder is increased. Indeed, the temperature was reduced with about 70℃ without any catalyst addition which is interesting for hydrogen storage applications. Contrary to MgH_2, $LiBH_4$ needs short time of milling due to its tendency to agglomeration for long time of milling.

- **Hydride mixture : phase stability**

By discussing the identified products of the hydride mixture MgH_2-$xLiBH_4$ desorption ($0.5 < x < 2.5$), the existence of other phases than given by the reaction 3.4 is probably due to low diffusion kinetic of boron in solids. After thermal treatment at 500℃, it was observed the formation of Li_3Mg_{17} alloy for the hydride mixture $x = 2$. For MgH_2 rich mixtures (i.e. $x = 0.5$ and 1), the resulting alloy is enriched with Mg. Consequently, the alloy Li_7Mg_{43} is formed instead of Li_3Mg_{17}. In all cases, the presence of LiH and MgB_2 phases are well identified. The XPS analysis indicate a valence of Mg in MgB_2 slightly higher than 2 in a reasonable agreement with what was reported in the literature about the existence of MgB_x phases ($1.2 < x < 2.2$).

- **Hydride mixture : thermal analysis**

By varying composition, the temperature of desorption of $LiBH_4$ is reduced when increasing MgH_2 content. The temperature of the transition of $LiBH_4$ shows a dependence on the composition with an eutectoid at around 66.7 mol.% of Li composition ($x = 2$). The melting of $LiBH_4$ has a tendency to decrease for Mg-enriched powders.

- **Hydrogen storage and hydride additives**

We have studied the reaction of the hydride mixture $x = 2$ without or with additives. It was observed that there can be a reduction of the temperature of desorption of MgH_2 and $LiBH_4$. Ti-isopropoxide additive has shown to act with two components: metallic and hydrocarbon based components. A considerable lowering of the temperature of desorption of $LiBH_4$ is observed whereas MgH_2 desorption is showed to be close to that is with the melting of $LiBH_4$. In our case, the best behavior was obtained with Ni-NiF_2 additive two components: pure metal and saline forms. This additive has a behaviour comparable to Ti-isopropoxide additive. Other additives were tested such as B amorphous, B crystalline and MgB_2. B amorphous has shown the most favorable kinetic behavior compared to B crystalline and MgB_2.

References

[1] R. Schulz, J. Huot, G. Liang, S. Boily, G. Lalande, M.C. Denis, J.P. Dodelet, Materials Science and Engineering A 267 (1999) 240-245.

[2] J.P. Soulié, G. Renaudin, R. Cerný, K. Yvon, Journal of Alloys and Compounds 346 (2002) 200-205.

[3] K.N. Semenenko, A.P. Chavgun, V.N. Surov, Russian J. Inorg. Chem. 16 (1971) 271-273.

[4] D.S. Stasinevich, G.A. Egorenko, Russian J. Inorg. Chem. 13 (1968) 341-343.

[5] P. Selvam, B. Viswanathan, C.S. Swamy, V. Srinivasan, International Journal of Hydrogen Energy 11 (1986) 169-192.

[6] A. Züttel, S. Rentsch, P. Fischer, P. Wenger, P. Sudan, P. Mauron, C. Emmenegger, Journal of Alloys and Compounds 356-357 (2003) 515-520.

[7] J.J. Vajo, S.L. Skeith, F. Mertens, The Journal of Physical Chemistry B 109 (2005) 3719-3722.

[8] U. Bösenberg, S. Doppiu, L. Mosegaard, G. Barkhordarian, N. Eigen, A. Borgschulte, T.R. Jensen, Y. Cerenius, O. Gutfleisch, T. Klassen, M. Dornheim, R. Bormann, Acta Materialia 55 (2007) 3951-3958.

[9] A. Züttel, A. Borgschulte, S.-I. Orimo, Scripta Materialia 56 (2007) 823-828.

[10] F.E. Pinkerton, M.S. Meyer, G.P. Meisner, M.P. Balogh, J.J. Vajo, The Journal of Physical Chemistry C 111 (2007) 12881-12885.

[11] X.B. Yu, D.M. Grant, G.S. Walker, Chemical Communications (2006) 3906-3908.

[12] A. Talapatra, S.K. Bandyopadhyay, P. Sen, P. Barat, S. Mukherjee, M. Mukherjee, Physica C: Superconductivity 419 (2005) 141-147.

[13] K.B. Garg, T. Chatterji, S. Dalela, M. Heinonnen, J. Leiro, B. Dalela, R.K. Singhal, Solid State Communications 131 (2004) 343-347.

[14] J. Huot, S. Bouaricha, S. Boily, J.P. Dodelet, D. Guay, R. Schulz, Journal of Alloys and Compounds 266 (1998) 307-310.

[15] V. Russell, R. Hirst, F.A. Kanda, A.J. King, Acta Crystallographica 6 (1953) 870.

[16] S. Lee, Physica C: Superconductivity 385 (2003) 31-41.

[17] S.M. Ariya, M.P. Morozova, G.A. Semenov, G.A. Rybakova, Russian Journal of Physical Chemistry 45 (1971) 102-103.

[18] AIST, Chemical Abstract, Integrated Spectral Database System of Organic Compounds, Japan.

[19] P.-J. Wang, Z.-Z. Fang, L.-P. Ma, X.-D. Kang, P. Wang, International Journal of Hydrogen Energy 33 (2008) 5611-5616.

CHAPTER 4. THERMODYNAMICS OF $LiBH_4$ COMPOUND

1 Above room temperature heat capacity and phase transition of $LiBH_4$ (*Published in Thermochimica Acta 2011*)

Interest in lithium tetrahydroborate ($LiBH_4$) is increasing owing to its widespread technological use in laboratories, mainly as a stand matrix for solid-state hydrogen storage and many other applications as a catalyst due to its reducing property. The polymorphic phase transition of the alkali metal (Na, K, Rb and Cs) borohydrides occurs at lower temperature than room one's [1], meanwhile for $LiBH_4$ this transition proceeds above room temperature [2]. Indeed, it was shown by X-ray diffraction and thermal analysis that the compound undergoes a crystalline phase transition from orthorhombic to hexagonal at about T_{trs} = 386 K then it melts around T_{fus} = 553 K [3,4]. The high temperature hexagonal phase has been clarified with more recent X-ray indexing, although it was considered to be tetragonal for over 30 years. Symmetry group suggest a first-order transition during which the tetrahedral [BH_4] anions are reoriented [5].

The thermal stability of the compound has been extensively studied [2-4,6,7] after its discovery in 1940 by Schlesinger and Brown [8] when reacting diborane with ethyl-lithium. To our knowledge, only one published paper, by Gorbunov et al.[3], has reported the above room temperature molar heat capacity $C_{p,m}$ of the $LiBH_4$ compound up to T = 450 K. In addition, the above room temperature heat capacity was estimated in JANAF thermochemical tables [9] from the $NaBH_4$ compound and was considered as a single polymorphic solid-phase and in fact has not been reviewed since December 1964. Within the 300 to 450 K temperature range, Gorbunov et al.[3] found that their differential scanning calorimetry (DSC) measurements were 5% higher than the values obtained from their extended low temperature experiments using adiabatic calorimetry under vacuum. This shift was attributed by the authors to the thermal conductivity of $LiBH_4$ which was not the same (for the two calorimetric runs) due to sample preparation differences: probably the morphology of the powders was different. These authors distinguish two different behaviours of $C_{p,m}$ within the 225 to 395 K temperature range: - (i) an "abnormal" increase from T = 225 K up to T = 381 K and - (ii) an isothermal event corresponding to the phase transition of $LiBH_4$ that occurred at 386.4 ± 1 K. Thus, there is only one determination of $C_{p,m}$ for the hexagonal crystalline phase (high temperature polymorphic form) characterized by a short temperature range (about 170 K) and

limited at a maximum of 450 K [3]. Even though some studies were related to the liquid phase, none of them determined the heat capacity of the $LiBH_4$ liquid (above 553 K). Additional experimental calorimetric data to evaluate the reliability and supplement the previous determinations are highly desirable in terms of thermodynamic description of this compound. Moreover, by analyzing the above room temperature heat capacity reported by Gorbunov et al.[3], the cause for the increase in the $C_{p,m}$ observed at about 360 K before the polymorphous transition needs to be understood. In order to clarify this point, we carried out our own $C_{p,m}$ measurements above room temperature with the following aims: - (i) check the reality of this increase in $C_{p,m}$ before the transition, - (ii) determine a new value for the enthalpy of the transition, - (iii) define a complete $C_{p,m}$ function for the hexagonal phase up to its melting point. Finally, from the hexagonal phase heat capacity, the $C_{p,m}$ of the liquid phase can be estimated based on the behaviour of similar high temperature molten salts of known heat capacity.

1.1 Experimental

Single-phase $LiBH_4$ was purchased from Alfa Aesar (mass fraction 0.981 assay) and stored as the received flask in a glove box equipped with permanent argon flow regeneration (H_2O/O_2, volume fraction < 10^{-5}). The original impurities were not identified and it was only shown by X-ray diffraction that these impurities do not form any solid solutions with the main substance. Heat flow measurements were performed using differential scanning calorimeter (D.S.C, TA Instrument 2920) under argon flow (0.8334 $cm^3 \cdot s^{-1}$, 0.999999 purity). The standard pressure was p° = 1 bar. Aluminium containers with lid in the for m of hermitic crimped pans were used. Quantitative calorimetric calibration of the heat capacity has been carried out using monocrystalline alumina (sapphire) previously just dried at 1173 K. Temperature and enthalpy calibrations were made using tin and indium (0.9999 purity) standards by considering their melting temperature and enthalpy as compiled in literature [10]. The uncertainty of heat capacity measurements are thus within 2.5% at room temperature and decreases down to 0.2% when rising temperature.

The weighting and loading of the pans with the samples was operated in the glove box when minimizing the atmospheric exposure time. The pan/samples were loaded in a closed vessel in the glove box, then transported and loaded immediately in the DSC under argon reflux. Empty pans were also handled and conducted in the same way as for the samples to avoid any undesirable effect. Before scanning cycles, $LiBH_4$ samples were desorbed in the calorimeter during 4 hours under primary vacuum at 523 K. Pumping flow contaminations were

reduced using liquid nitrogen trap. For the molar heat capacity, $C_{p,\mathrm{m}}$, determinations, at least 3 scanning cycles were used for all samples and the measurements were found to be reproducible beyond 3 cycles. Hence only this third and last record was used for the determination of $C_{p,\mathrm{m}}$. The reference (sapphire) was found to deviate practically by a constant factor with some asymptotic behaviour at the end of the record. But this should not influence the results as the correction was made at the same time, step-by-step, when knowing the $C_{p,\mathrm{m}}$ of the reference.

The $C_{p,\mathrm{m}}$ determinations were performed using separately two different scanning methods: "linear temperature ramp" (Fig. 4.1) and "enthalpy method" (Fig. 4.2). Records of the reference (sapphire) and of the empty pan (baseline) were carried out before and after each experiment to warrantee reproducibility of the measurements. The weight of the samples – coming back to the glove box – was checked after each measurement and found to be constant within the balance precision limit.

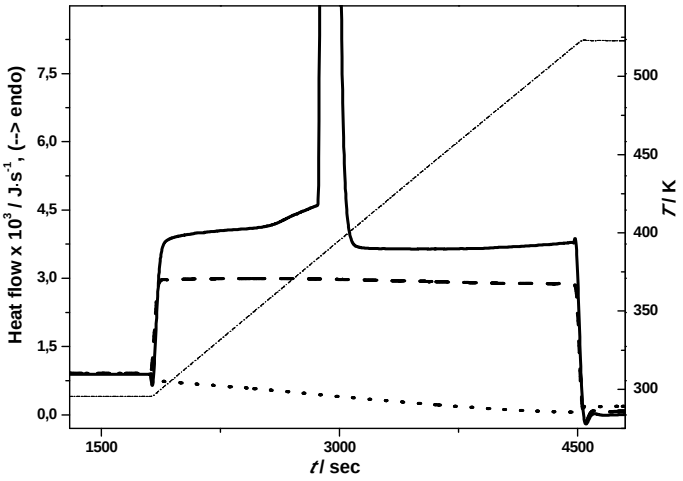

Figure 4.1. DSC heat flow measurements versus time t by the temperature T linear ramp method: ‾‾, $LiBH_4$ sample; ‾ ‾, sapphire reference; ··, baseline.

In the first case, transient isothermal periods at the start and end of each scan, are imposed to reach a steady-state dynamic equilibrium of the system. A scan rate of 0.08334 $K \cdot s^{-1}$ (5℃.min^{-1}) was chosen. The molar heat capacity of the sample $C_{p,\mathrm{m}}^{\mathrm{s}}$ was extracted using the following formula knowing the mole numbers of the sample (n_{s}) and of the reference (n_{ref}):

$$C_{p,\mathrm{m}}^{\mathrm{s}} = C_{p,\mathrm{m}}^{\mathrm{ref}} \cdot \frac{\Delta Y_{\mathrm{o}} + \Delta Y_{\mathrm{s}}}{\Delta Y_{\mathrm{o}} + \Delta Y_{\mathrm{ref}}} \frac{n_{\mathrm{ref}}}{n_{\mathrm{s}}} \tag{4.1}$$

Relation in which ΔY_s, ΔY_{ref}, ΔY_o, are the instantaneous heat flows for the sample, the reference and the empty pan respectively with the convention used in the reference [11]. $C_{p,m}^{ref}$ is the molar heat capacity of the reference taken from the thermochemical tables [12].

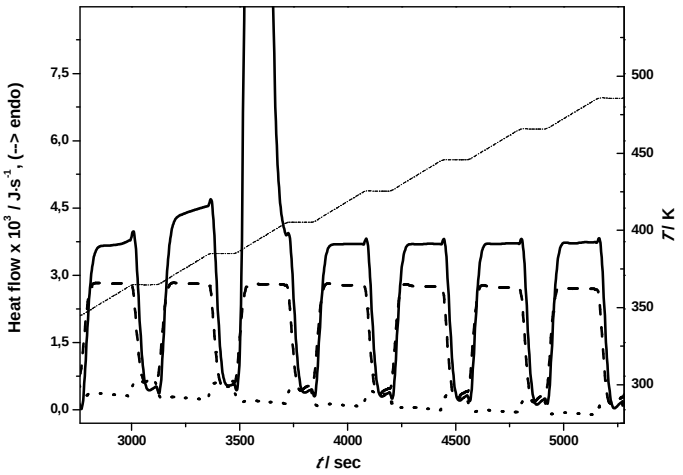

Figure 4.2. DSC heat flow measurements versus time t by the enthalpy method: ——, $LiBH_4$ sample; – –, sapphire reference; ··, baseline.

In the enthalpy method, the temperature is programmed as short ramps of 20 K with a scan rate of 0.08334 $K \cdot s^{-1}$(5℃.min^{-1}). The peak transition is managed to be inside this temperature interval. Between each ramps an isothermal stay of 120 s is imposed. By integrating the heat flow areas, the values are corrected to the baseline and reported to the reference for heat capacity data as measured for a mean temperature. This method is used mainly to check the previous continuous dynamic method since it allows the calculation of the average molar heat capacity of the sample, $\overline{C_{p,m}^{s}}$, in a temperature interval ΔT = 20 K, using the formula:

$$\overline{C_{p,m}^{s}} = \overline{C_{p,m}^{ref}} \cdot \frac{\Delta Q_o + \Delta Q_s}{\Delta Q_o + \Delta Q_{ref}} \frac{n_{ref}}{n_s} \tag{4.2}$$

where ΔQ_s, ΔQ_{ref}, ΔQ_o, are the amounts of heat required to increase the temperature by a 20 K step for the sample, reference and empty pan respectively as described elsewhere [11].

1.2 Results and discussion

1.2.1 $LiBH_4$ solid phase

The obtained above room temperature heat capacities of $LiBH_4$ compound using the two methods are presented in figure 4.3. Twelve experimental $C_{p,m}$ values were determined using the enthalpy method. The obtained experimental $C_{p,m}$ values using linear ramp method are in close agreement with the values obtained by enthalpy method within 1% standard deviation. As there is a very good agreement between the two methods, only results obtained by the linear ramp method are retained for the following analysis. The apparent $C_{p,m}$ increase has the value of 853.6 $J \cdot K^{-1} \cdot mol^{-1}$ at the apex with a hysteresis of about 12 K, a value which is higher than the previously reported thermal analysis and heat capacity data using lower heating rates (0.05 and 0.01667 $K \cdot s^{-1}$ respectively) [2,3].

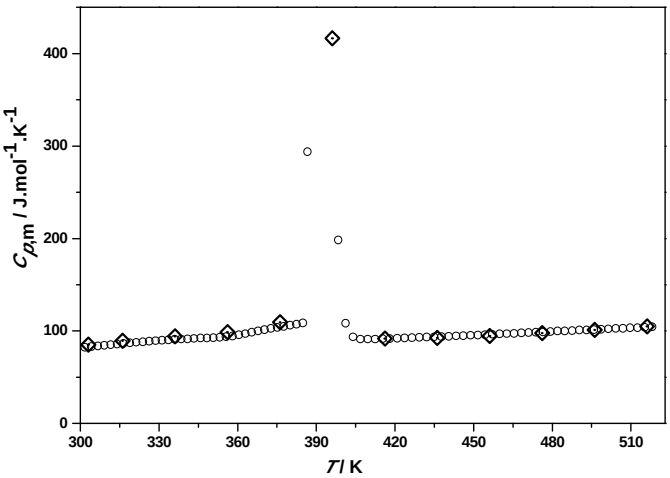

Figure 4.3. High-T experimental molar heat capacity of $LiBH_4$ compound: ◦, linear ramp and ◇, enthalpy methods.

Figure 4.4 presents a comparison between our results and those previously obtained in literature. It shows a good agreement between our determinations of $C_{p,m}$ and results obtained by Gorbunov et al.[3] and Hallett and Johnston [6] slightly extended from low temperature data. Above room temperature, the $C_{p,m}$ curve seems to present an inflexion point around 354 K then undergoes an increase which is independent on the main transition (Fig. 4.3). In agreement with Gorbunov et al.[3] results, the presence of an “abnormal” part in the $C_{p,m}$ curve is also observed in our own measurements (Fig. 4.4) but it is less pronounced and, consequently, presents a smaller heat capacity decreasing step at the phase transition (about 8 $J \cdot K^{-1} \cdot mol^{-1}$) between the two allotropic crystals. The larger increase of the abnormal part in the previous study, compared to our observations, is probably due to larger residual

desorption – water or some kind of hydroxide –, overlapping with the phase transition thermal effect. Probably the Gorbunov et al.[3] sample lost some mass in vacuum. Unfortunately, the authors did not discuss neither about this phenomenon nor on the possibility of performing cyclic measurements. Therefore this feature could not be totally attributed to the impurities in the compound since the samples in our case were desorbed at 523 K under vacuum before the measurements. As this increase was observed to be reproducible after several cycles, the present “abnormal” behaviour should be attributed to another phenomenon, unless some new re-adsorption occurred cyclically after introducing the sample in the calorimeter. Indeed we cannot discard the fact that in case of high purity prepared samples, the vacuum or flow gas quality in the calorimeter may be insufficient to prevent also some re-adsorption reactions after the desorbed stage when cycling, any cycle duration being about 4 hours. The heat flow signal became distorted beyond 6 cycles.

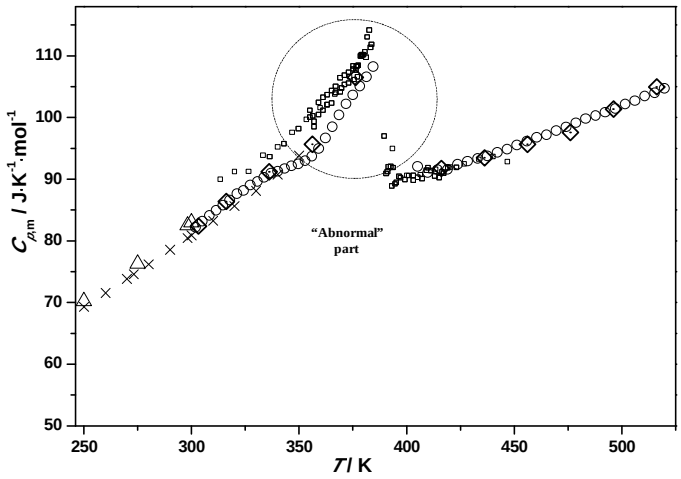

Figure 4.4. Experimental heat capacity data of $LiBH_4$ compound. - Low-T : △, Nernst calorimetry [6]; ×, Adiabatic calorimetry [3]. - High-T : ▫, DSC [3]; ○, linear ramp and ◇, enthalpy methods [this work].

From recent crystallographic data of Filinchuk et al.[13], the observed increase of the $C_{p,\mathrm{m}}$ before the main transition could be also attributed to the rearrangement of the crystal lattice, accompanied by structural compacting at the transition. This is a priori in agreement with the negative slope at the transition line obtained from Pistorius’ high pressure phase diagram [12] but in contradiction with his X-ray indexing. Another cause of heat capacity increase could be the increase of defects due to the existence of a non stoichiometric composition domain. Whatever are the causes for this phenomenon, the abnormal increase of the $C_{p,\mathrm{m}}$ could not be attributed as a part of the main allotropic transition as proposed by Gorbunov et al.[3]. This anomaly could influence drastically the way the transition temperature and enthalpy are determined. Indeed, the onset position and the area under peak which could be

integrated will be strongly affected by this anomaly. Above the transition temperature, the heat capacity of the hexagonal crystal follows again a regular trend.

Table 4.1 presents some experimental and corresponding fitted values of $C_{p,\mathrm{m}}$ with an average fractional deviation, $10^2 \cdot |C_{p,\mathrm{expt}} - C_{p,\mathrm{fit}}|/C_{p,\mathrm{fit}}$, of about 0.12. Standard deviations as well as relative error of the experimental values are presented in figure 4.5.

Table 4.1. Experimental and fitted molar heat capacities, $C_{p,m}/J \cdot K^{-1} \cdot mol^{-1}$

T / K	experimental	fitted
298	81.51 [a]	81.34
310	84.51	84.77
320	87.33	87.32
330	89.53	89.52
340	91.21	91.29
350	92.47	92.60
360	95.46	95.34
370	101.20	100.77
380	106.02	105.99
386.6	Transition, $\Delta_{tr}H$ = 5.069 ± 0.076 kJ·mol^{-1}	
410	91.06	91.19
420	91.83	91.99
430	93.09	92.97
440	94.12	94.08
450	95.43	95.29
460	96.70	96.57
470	97.95	97.90
480	99.14	99.26
490	100.69	100.63
500	101.90	101.97
510	103.30	103.30
520	104.78	104.57
530		105.79
540		106.94
550		108.01
553	Melting, $\Delta_m H$ = 8.18 ± 0.3 kJ·mol^{-1} [b]	

[a] average value from low-T heat capacity data [3,6]
[b] assessed literature value [14,15]

Hence, the proposed heat capacity of $LiBH_4$ is a non-linear least squares fit using a second order polynomial with a T^{-2} term from room temperature until the approach of the melting point of the compound. According to the equation 4.3, the $C_{p,\mathrm{m}}$ analytic expression is defined in three T ranges: above room T orthorhombic-phase, “abnormal” orthorhombic-phase and short T range hexagonal-phase. The obtained results are summarized in table 4.2. The calculated average value of $C_{p,\mathrm{m}}$ at 298 K from low temperature data is found to agree with the interpolated value in our measurements within 0.2%.

$$C_{p,\mathrm{m}}(T) = \mathrm{a} + \mathrm{b}T + \mathrm{c}T^2 + \mathrm{d}T^{-2} \tag{4.3}$$

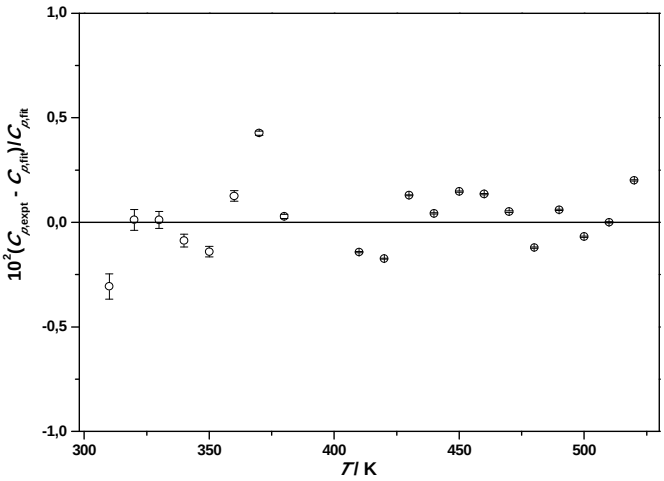

Figure 4.5. Relative deviations of some experimental heat capacity $C_{p,expt}$ from fitted values $C_{p,fit}$ as a function of temperature.

The integrated enthalpy for the allotropic transition is $\Delta_{tr}H$ = 5069 ± 76 J·mol^{-1} at the measured temperature of the transition 386.6 ± 0.1 K. As thermocouples and their electrical chain in this temperature range cannot be calibrated with an accuracy less than 1 K, we propose an uncertainty equal to ± 1 K (T_{tr} = 386.6 ± 1 K). The calculated entropy of the transition is $\Delta_{tr}S$ = 13.11 ± 0.23 J·K^{-1}·mol^{-1}. This value is lower than the determined value by Pistorius [12], *i.e.* 16.5 J·K^{-1}·mol^{-1}.

Table 4.2. Fitted molar heat capacities of the $LiBH_4$ phases as a function of temperature, $C_{p,m}$/J·K^{-1}·mol^{-1}, according to Eq. 4.3

Phase	*T*/K range	a	b	cx10^{3}	dx10^{-6}
ortho-phase	298-354	-732.302	3.717	-4.52	9.563
	354-386.6	-29738.586	107.620	-108.78	672.460
hexa-phase	386.6-553	-494.068	1.594	-1.13	20.500

1.2.2 $LiBH_4$ liquid phase

The $LiBH_4$ compound is a salt-like compound due to the hydride character of the [BH_4^-] anionic component. Available models for the estimation of the heat capacity of liquid phases, taking into account the anionic and cationic contributions, are not affordable for our system. In spite of the "apparent" instability of the hydrides after melting due to hydrogen gas release [2], we consider the $C_{p,\mathrm{m}}$ of the liquid as being stable under standard equilibrium conditions (at p° of H_2 in equilibrium with H dissolved in the liquid) as observed in related experiments under H_2 increasing pressures from 1 bar [4]. By analogy, $C_{p,\mathrm{m}}$ of the liquid was estimated by

considering the increase from that of the solid with the one observed in the two high-*T* molten salts LiF (T_m = 1122 K) and $LiBF_4$ (T_m = 583 K), the $C_{p,m}$ of which being determined experimentally [16,17]. This assumption is based on the comparison of the physical and chemical properties (structure close to $LiBF_4$ and ionic radius of the anion BH_4^- close to F^-). A mean value is adopted from the barycentric formula referred to the different compounds:

$$C_{p,m}(LiBH_4,l) = C_{p,m}(LiBH_4,s) x \Gamma \quad (4.4)$$

where Γ is an average factor assuming the increase of the $C_{p,m}$ from the solid to the liquid of the two salts $LiBF_4$ and LiF, according to the formula:

$$\Gamma=\{(C_{p,m}(LiBF_4,l)/C_{p,m}(LiBF_4,s))+(C_{p,m}(LiF,l)/C_{p,m}(LiF,s))\}/2 \quad (4.5)$$

Table 4.3. Molar heat capacity $C_{p,m}$/ $J \cdot K^{-1} \cdot mol^{-1}$ values of the solid and liquid salts $LiBF_4$ and LiF [16,17] used as reference in the calculations and the estimated value for liquid $LiBH_4$. Values are given at melting temperature of corresponding compounds.

Phase boundary	$LiBF_4$	LiF	$LiBH_4$
solid	131.5	63.2	108.3
liquid	167.8	64.9	124.7

From the reference values of $C_{p,m}$(liquid) and $C_{p,m}$(solid) used in this calculation (see table 4.3), Eq. 4.5 leads to Γ = 1.1515. Following the above assumption and knowing the $C_{p,m}$ of the hexagonal phase for temperatures close to its melting point (108.3 $J \cdot K^{-1} \cdot mol^{-1}$), a value of 124.7 $J \cdot K^{-1} \cdot mol^{-1}$ is found for the molar heat capacity of $LiBH_4$ molten salt which is supposed to be constant versus temperature.

2 Critical evaluation of the thermodynamic properties of lithium tetrahydroborate (*To be submitted for publication*)

The present thermodynamic critical assessment study follows the precedent heat capacity re- determination [18] and is aimed to propose new thermodynamic properties of the $LiBH_4$ compound. This compound has been chosen, primarily, as the first candidate for hydrogen storage by reference to its high “hydrogen” gravimetric density *i.e.* storage capacity. Nevertheless, the existing experimental data available up to now show that the compound is thermodynamically too stable to present available reversible hydrogen storage at moderate temperatures and pressures. Much attention was paid to the examination of thermodynamic and kinetic properties for which only specific parameters related to the instance experiment are determined. However, some thermodynamic data about this compound are still unknown and discrepancies between experimental and theoretical calculations data are quite large. Therefore, the reason for which we plan to re-examine the thermodynamic data of this compound is that new experimental data exist since the original compilations (JANAF tables, 1964) and new Gibbs energy function for the phases can be obtained in order to be able to calculate a priori the optimum yield of reactions where low thermal conductivity of this compound and reaction kinetic limitations, if they exist, can be reported to equilibrium conditions.

Thermodynamic properties of the solid $LiBH_4$ have been studied in a limited set of publications [3,4,6,19]. From those studies it appeared that three factors are important – (i) the purity of the compound, – (ii) the method used for thermodynamic determinations, – (iii) and the calculation method for the extraction of the main parameters. All these factors could influence the reliability of the results. Besides, solid $LiBH_4$ presented many difficulties during experiments due to its highly hygroscopic character that may affect the purity of the sample under study. Moreover, there is no thermodynamic study devoted up to now to the liquid $LiBH_4$ phase due to its decomposition and difficulties to get a suitable and chemically inert container. Due to such difficult working conditions, the critical assessment of thermodynamic parameters of this compound appeared to us necessary at first to evaluate the optimum yield for hydrogen storage as well as for sorption and desorption cycles. .

Irrespective of any direct sublimation or vapour pressure data, it is important to select available data for the condensed phases of $LiBH_4$ compound in order to take into account of the whole thermodynamic properties in the calculation of the compound behaviour during any hydrogen cycling process. In case of important lack of data, some new determinations [18]

as well as estimates were undertaken. Besides the system MgH_2-$LiBH_4$ [20] was recently discovered to be thermodynamically suitable for hydrogen exchange reactions, and consequently the data concerning $LiBH_4$ will be of an important usefulness for solid state hydrogen storage prospects, meanwhile MgH_2 compound has been already assessed [21].
The present thermodynamic study has been undertaken according to perform critical assessment of thermodynamic data including recent $LiBH_4$ experimental data and the phase transition (orthorhombic → hexagonal) since the data previously reported in JANAF tables were reviewed in December 1964. The ultimate aim is to establish the Gibbs energy function of the two solids and the liquid phase for storage in a thermodynamic data bank.

2.1 Thermodynamic data critical assessment of $LiBH_4$ compound

Establishment of the Gibbs energy function $G(T)$ for the condensed phases of $LiBH_4$ requires the knowledge of heat capacity, absolute entropy at 298 K, heat of formation and enthalpies and temperatures of the transformations (solid-solid, and melting). Both transformations are reversible as reported by Fedneva et al.[2], so that the entropy change could be calculated. Besides, experimental data critical assessments of heat capacity and heat of formation is also provided. Tables 4.4 and 4.5 summarize the data collected for the crystalline phase transition, melting transformation and available thermodynamic functions. The methods and experimental techniques are presented with their conditions of measurements, as well as the purity of the samples which may be different according to the sample preparations. Some additional useful observations that characterize the behaviour of the compound under study are also presented in these tables.

2.1.1 Low temperature heat capacity determinations

Hallett and Johnston [6] measured the heat capacity of $LiBH_4$ at low temperatures within the 15–303 K range (Fig.4.6) by adiabatic calorimetry and proposed the following values for the molar heat capacity and standard entropy at 298.15 K:
$C_{p,m}(298.15\ K) = 82.563\ J \cdot K^{-1} \cdot mol^{-1}$
$S°(298.15\ K) = 75.860 \pm 0.125\ J \cdot K^{-1} \cdot mol^{-1}$.

Table 4.4. Literature thermodynamic data of $LiBH_4$ compound: Experimental methods, conditions of measurements and theoretical calculations.

Authors and ref.	Method	*T* / K range	Conditions	Sample and purity	Observations
Davis et al.[19], (1949)	Dissolution in hydrochloric acid and Drop calorimetry	273-298	Ni crucible under dry N_2	Purified up to 0.9872	Instability of the stored compound
Hallett and Johnston [6], (1953)	Nernst Vacuum Calorimetry	15-303	Sample filled in the calorimeter container and sealed under He pressure	Purified under N_2 up to 0.997	Purification process according to ref. [19]
Fedneva et al.[2], (1964)	Differential Thermal Analysis (DTA)	298-873	Under dry H_2 at 0.05 $K \cdot s^{-1}$ flow rate (1 bar)	0.97-0.98	Synthesized from LiH and BF_3-ether
Stasinevich and Egorenko [4], (1968)	DTA	300-983	Under various H_2 pressures / $p°$ (1.0133 to 10.133 bar)	0.98	Four endothermic events were observed
Semenenko et al.[22], (1971)	Thermal analysis / XRD Phase diagram determination	300-620	Samples in sealed ampoules under vacuum ($0.2 \cdot 10^{-5}$ bar / $p°$); 0.08334 $K \cdot s^{-1}$ rate	Re-crystallized from DE: 0.987	Annealed mixtures ($LiBH_4$-$NaBH_4$) at varying compositions: eutectic observed
Pistorius [23], (1974)	High pressure/ DTA	298-823	Under high pressure piston in dry box up to 5 GPa	Powder	Thermodynamic parameters deduced using the slope or by extrapolation to zero pressure
Gorbunov et al.[3], (1984)	Adiabatic and Differential Scanning Calorimetry (DSC)	10-450	Under vacuum and measurements referred to $C°_p$ of Al_2O_3	Powder 0.993	DSC data were 5% higher than their adiabatic measurements
Züttel et al.[14], (2007)	DSC/Mass Spectrometry	298-773	No reference	0.95	No more detail
Zarkevich and Johnson [24], (2008)	Ab initio and Molecular Dynamics calculations	298-800	With fixed or relaxed B		Difficulty to assess H positions
Filinchuk et al.[13], (2008)	HR-XRD	80-500	Sample in thin glass capillaries under protective oil	0.95	Sample frozen using cryogenic system
Price et al.[15], (2009)	DSC/DTA	298-873	Under Ar at 0.08334 $K \cdot s^{-1}$ rate in Al hermetically sealed pans	0.95	No more detail about the extraction of the parameters
Pendolino et al.[25], (2009)	DSC/TGA	298-873	Under H_2 pressure at 0.1834 $K \cdot s^{-1}$ rate in Al crucible	0.95	Variable heating rates for kinetic activation energy measurements

Table 4.5. Thermodynamic parameters: T_{trs}, T_m, $\Delta_{trs}H$, Δ_mH are respectively the temperatures of the phase transition and melting, and their corresponding enthalpies.

Authors and ref.	T / K range	T_{trs} / K	$\Delta_{trs}H$ / kJ·mol^{-1}	T_m / K	Δ_mH / kJ·mol^{-1}	Other functions
Davis et al.[19], (1949)	273-298					$C_p°_{285.6}$ = 76.56 J·K^{-1}·mol^{-1}
Hallett and Johnston [6], (1953)	15-303					$S°_{298}$ = 75.86 J·K^{-1}·mol^{-1}; $C_p°_{298}$ = 82.56 J·K^{-1}·mol^{-1}
Fedneva et al.[2], (1964)	298-873	381-385		541-558		
Stasinevich and Egorenko [4], (1968)	300-983	383±3		551-555		
Semenenko et al.[22], (1971)	300-620	381		555		
Pistorius [23], (1974)	298-823	382±5	6.303 [a]	588 [b]		
Gorbunov et al.[3], (1984)	10-450	385.6	6.229±0.084			$S°_{298}$ = 73.70 J·K^{-1}·mol^{-1}; $C_p°_{298}$ = 80.46 J·K^{-1}·mol^{-1}
Züttel et al.[14], (2007)	298-773	391	4.18	560	7.56	
Zarkevich and Johnson [24], (2008)	298-800	381	4.6	553	6.3 / 6.9 [c]	
Filinchuk et al.[13], (2008)	80-500	381				
Price et al.[15], (2009)	298-873	383	4.38±0.04	552	8.03±0.07	
Pendolino et al.[25], (2009)	298-873	384		563		
This work [18]	298-600	386.6±1	5.069±0.076	554±1		$C_p°_{298}$ = 81.34 J·K^{-1}·mol^{-1}

[a] deduced from the entropy of transition obtained by high pressure volume change
[b] extrapolated from the phases boundary slope in the *p*–*T* diagram
[c] private communication in ref. [24]

Gorbunov et al.[3] reported the heat capacity measurements of the compound using both adiabatic and differential scanning calorimetry under vacuum between 10 and 450 K. In the low temperature range between 10 K and 350 K, their values agree with the previous measurements of Hallett and Johnston [6] (Fig.4.6) but their heat capacity is lower by 2.5% at 298 K. Consequently the deduced standard entropy should be also lower (Table 4.5). In this temperature range, low temperature heat capacity profile was found to follow the Debye model for solids.

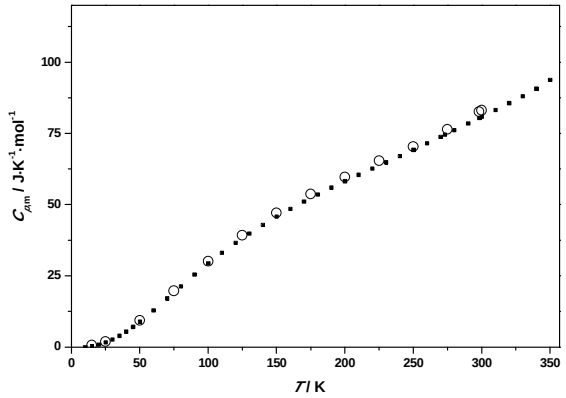

Figure 4.6. Experimental low temperature heat capacity of $LiBH_4$ reported in literature : ○, Hallett and Johnston [6] (1953); ▪, Gorbunov et al.[3] (1984).

From low-T data, the standard heat capacity and entropy at 298 K which can be retained are the average value given in table 4.5, as the two authors [3,6] got close values at least within a reasonable total uncertainty range in calorimetric experiments (± 2.5%):

$C_{p,m}$ = 81.51 J·K^{-1}·mol^{-1}

$S°_{298}$ = 74.78 J·K^{-1}·mol^{-1}.

Davis et al.[19] using drop calorimetry measured the enthalpy increment between T = 273.15 K and T = 298.15 K. The average value can be deduced as

$C_{p,m} = \Delta Q/\Delta T$ = 76.56 ± 0.91 J·K^{-1}·mol^{-1}

(for an average temperature of 285.6 K), and this value, is located by 1.4% lower than the adiabatic measurements [3] and confirms the preceding calorimetric data as discussed first.

In the course of the $LiBH_4$ thermodynamic study, we determined [first part] the heat capacity in the 298 – 553K range. The present retained average value $C_{p,m}$ at 298 K from low temperature data is found to agree within 0.2% with the interpolated value in our preceding measurements. For this reason we have chosen to retain the value from our recent measurements as they are consistent with the retained thermodynamic functions at 298.15 K.

Above room temperature, the heat capacity has been discussed in the previous part for the orthorhombic and hexagonal phases and the proposed values are retained for these phases.

2.1.2 Heat of formation

The heat of formation of $LiBH_4$ ($\Delta_f H° = -184.72 \pm 1.25$ kJ·mol^{-1}) was determined by Davis et al.[19] when measuring by calorimetry the heat of the dissolution reaction of $LiBH_4$ in hydrochloric acid at 298.15 K. The reported heat of hydrolysis was measured by considering the following reaction cycles:

$$LiBH_4 + 1.25(HCl.200\ H_2O) + [3H_2O] \rightarrow (LiCl + H_3BO_3 + 0.25HCl).247H_2O + 4H_2, \quad (4.6)$$

$$LiCl.60H_2O + H_3BO_3.60H_2O + 0.25(HCl.508H_2O) \rightarrow (LiCl + H_3BO_3 + 0.25HCl).247H_2O, \quad (4.7)$$

$$H_3BO_3.60H_2O + \infty H_2O \rightarrow H_3BO_3.\infty H_2O. \quad (4.8)$$

Summarizing the above reactions, the whole reaction associated to the thermal effect in the calorimeter is assumed as:

$$LiBH_4 + 1.25(HCl.200H_2O) + [3H_2O] + \infty H_2O \rightarrow LiCl.60H_2O + H_3BO_3.\infty H_2O + 0.25(HCl.508H_2O) + 4H_2 \quad (4.9)$$

In order to calculate the dissolution enthalpy at 298.15 K, the authors measured the heat capacity of the reactants and products using drop calorimetry. The enthalpy of reaction (4.6) at 298.15 K is thus determined to be -301.83 kJ·mol^{-1}. Different dissolution calorimetry experiments – either coming from literature or performed by the authors - provided the heat contribution of each compound during mixing. Nevertheless, the heat of reaction uncertainty was found to be much larger than the heat of mixing. The heat of reaction (4.7) was assumed to be zero since there is an equivalent amount of H_2O (no dilution). The heat of dilution of boric acid was determined to be 0.293 kJ·mol^{-1} for reaction (4.8). The total heat effects were measured with a precision of 0.35%, which is in fact the reproducibility of the experiments. As the $\Delta_f H°$ for $H_3BO_3 \cdot \infty H_2O$ has been calculated from $\Delta_f H°$ of B_2O_3 known within 1% i.e. ± 12 kJ, the authors report that the accuracy of the obtained value depends on the heat of formation of the latest. The uncertainty on the heat of formation of H_3BO_3 acid remains large and the value of the heat of formation is more uncertain than proposed - i.e. equal to -184.7 ± 7.6 kJ·mol^{-1} - as $\Delta_f H°$ of B_2O_3 contributes by half of the heat of formation of H_3BO_3 acid. In addition, the reference state of boron was at that time chosen as amorphous boron.

From this only experimental determination, many assessments of the heat of formation were reported in literature. A compilation made by Wagman [26], adopted by the "National Bureau of Standards" (to day NIST), proposed the value -194.31 ± 0.21 kJ·mol^{-1}. This value has been retained by Jeffes and McKerrell [27] in their thermodynamic tables that report several hydrides known at that time. From the above experimental value, Smith and Bass [28] recalculated a value equal to -194.01 kJ·mol^{-1}. The only reported experimental data have been also reviewed by JANAF in December 1964 and calculated with auxiliary data to be -190.46 ± 0.21 kJ.mol^{-1} [9]. Table 4.6 summarizes the heat of formation of the whole set of compounds involved in the calorimetric determination as used in the compilations made by all authors.

Table 4.6. Heat of formation of the involved compounds in the dissolution calorimetry made by Davis et al.[19]

Authors and ref.	$\Delta_f H°$ / kJ·mol^{-1}						
	H_3BO_3	B_2O_3 (c)	B_2O_3 (am)	$HCl.200H_2O$	$HCl.508H_2O$	$LiCl.60H_2O$	$H_3BO_3.\infty H_2O$
Davis el al. [19], (1949)		-1267.75		-166.51	-166.84	-444.13	-1066.92
Smisko and Mason [29], (1950)		-1267.75					-1069.26
Rossini et al.[30] , (1952)	-1088.68	-1263.57	-1245.16	-166.51	-166.84	-444.43	-1067.76
Wagman [26], (1962)	-1096.88	-1277.54					-1074.11
NIST-JANAF [9], (1964)	-1094.00	-1271.9		-166.09	-166.59	-443.60	-1071.31
Wagman et al.[31], (1982)	-1080.78	-1272.77	-1254.53	-166.27	-166.57	-444.42	-1072.36

From table 4.6, it seems indeed that the most important differences come from the boric acid H_3BO_3 heat of formation i.e. during its dissolution in water or indirectly from its basic products B_2O_3 and elemental boron. Likely, the reference state of boron in JANAF is boron crystalline whereas there is no indication in the NBS report made by Wagman in 1962.

First principle calculations were used to calculate the "cohesion" energy of $LiBH_4$ at 0K. Miwa et al.[32] calculated the heat of formation to be first equal to -194 kJ·mol^{-1} and second -160 kJ·mol^{-1} when zero-point energies were included. Nakamori et al.[33] studied theoretically the stability of metal-borohydrides and they found a correlation between the heat of formation and the Pauling electronegativity scale of the cation. The value pointed out for $LiBH_4$ is -146 kJ·mol^{-1}. Züttel et al.[14] provided a value of -194.15 kJ·mol^{-1} but without explanation, this value being probably issued from calculations. Siegel et al.[34] using the VASP ab-initio calculation package provided a value of 179.4 kJ·mol^{-1} for the heat of decomposition to the elemental compounds (B + Li + $2H_2$) at 300 K. Table 4.7 summarizes the most significant values of heat of formation compiled by different authors.

Table 4.7. Obtained heat of formation of $LiBH_4$

Authors and ref.	Method used	$\Delta_f H°$ / kJ·mol^{-1}	Observations
Davis el al. [19], (1949)	Calorimetric measurements	-184.72±1.25	Uncertainty on H_3BO_3 acid
Rossini et al.[30] , (1952)	Compilation	-186.61	B_{am} stated at 1.67 kJ·mol^{-1}
Wagman [26], (1962)	Compilation with additional data	-194.31±0.21	No more detail
Smith and Bass [28], (1963)	Recalculation [19]	-194.01	No detail
NIST-JANAF [9], (1964)	Compilation with auxiliary data	-190.46±0.21	No indication to reference state of boron
Wagman et al.[31], (1982)	Compilation	-190.8	No detail
Miwa et al.[32], (2004)	First -Principle calculations	-194	-160 when zero-point energies included
Siegel et al.[34], (2007)	VASP calculations	-179.4	decomposition to B + Li + $2H_2$

Unfortunately, there were no more explanations of the authors about their compilations and which reference state of boron they have considered. It is worth to mention that the heat of formation of boron amorphous from its crystalline structure is positive and equal to 4.4 kJ·mol^{-1} [12]. Hence, the main difference between the two referential bases, JANAF and NBS, is probably due to the nature of boron, which has led to different values for the heat of formation of $LiBH_4$. Indeed, this value has been corrected in 1982 by Wagman et al. as shown in table 4.7.

The heat of formation of the compound is crucial for thermodynamic functions determination. In the present assessment we propose to retain the compilation performed by JANAF ($\Delta_f H°_{298}$ = -190.46 ± 0.21 kJ·mol^{-1}) [26], which is also close to the corrected value by Wagman et al.[31] in their more recent thermodynamic tables. The ab-initio calculated value (-194 kJ·mol^{-1}) by Miwa et al.[32] considering the total energies seems to be fortuitously in agreement with the present retained value regarding the value obtained when zero-point energies are included, and because largely scattered values have been obtained for the LiH compound.

2.1.3 Crystalline phase transition and melting of the compound

2.1.3.1 Published works

In the published paper by Schlesinger and Brown [35] in 1940 when they synthesized the compound, the authors identified the melting point (under static vacuum) in the temperature range 548-553 K accompanied with a slight H_2 release (identified by volumetry). The synthesized compound had the chemical formula $Li_{0.98}B_{1.02}H_{3.8}$ which could suggest some "instability" of the compound by hydrogen compositional evolution. The assumed reaction of decomposition was at that time:

$$LiBH_4(s) \rightarrow LiB(s) + 2H_2(g) \tag{4.10}$$

when the sample is maintained at 553 K for 10 hours under primary vacuum with an observed 62.5% H_2 release.

Fedneva et al.[2] reported DTA observations under hydrogen flow of the $LiBH_4$ compound. They detected the presence of the polymorphic transition within the temperature 381-385 K and tentatively measured the temperature of the melting and it occurred in the range 541-559 K, the variation been probably related to composition evolution due to the loss of H_2. An additional thermal event is detected at 756-765 K attributed to the decomposition of the compound.

Stasinevich and Egorenko [4] observed by DTA analysis at different hydrogen applied pressures (1.0133 to 10.133 bar) the thermal decomposition of $LiBH_4$ compound according to the proposed process pathways :

$$LiBH_4(s \text{ or } l) \rightarrow LiH(s) + B(s) + \tfrac{3}{2}H_2(g) \tag{4.11}$$

$$LiH(s) \rightarrow Li(s \text{ or } l) + \tfrac{1}{2}H_2(g) \tag{4.12}$$

The phase transition and the events in the temperature range 380-555 K were reported to be not sensitive to the hydrogen pressure. The given average temperature of the allotropic transition is 383.3 ± 3 K. The melting point increased slightly with the pressure but not significantly when compared to the temperature accuracy. The obtained average melting temperature is 553 ± 3 K [4].

Pistorius [23] studied the compound (handled in dry box) behaviour in the high pressure range generated by a piston-cylinder apparatus. High-pressure phase transitions were observed by means of DTA under piston applied pressure. An oven was constructed with Teflon which allowed strong and sharp DTA signal at low heating/cooling rate. Only two volumetric transitions measurements were studied by means of the piston-rotation technique. The observed transition orthorhombic to tetragonal was determined at 381.6 ± 0.5 K by ex-

trapolating to 0 GPa pressure (Fig.4.7). The author reported that the decomposition at the melting did not occur due to the high pressure (more exactly by confinement of the gas volume). Extrapolation at 0 GPa from the last value at 0.5 GPa in the diagram gave the melting value T_m = 588 K but this non-linear extrapolation remains uncertain due to the lack of a suitable relation. At the triple point (p = 0.9 GPa), the volume change was deduced to be ΔV = -0.4 $cm^3 \cdot mol^{-1}$ and the slope dT/dp = -24 $K \cdot GPa^{-1}$. The deduced entropy of the transition is $\Delta_{trs}S$ = 16.5 $J \cdot K^{-1} \cdot mol^{-1}$. With the assumption that $\Delta_{trs}S$ is approximately constant along the transition line, the author found $(\Delta V)_{p=0}$ = -0.36 $cm^3 \cdot mol^{-1}$ a value the author said "in fair agreement" with the value -0.9 ± 0.5 $cm^3 . \cdot mol^{-1}$ obtained by XRD pattern indexing.

The enthalpy of the transition, accordingly the entropy, was also determined by Gorbunov et al.[3] graphically by integrating independently the two areas under – (i) the abnormal increase of the heat capacity (1174 ± 69 $J \cdot mol^{-1}$) before the transition peak, and – (ii) the main transition peak (5055 ± 15 $J \cdot mol^{-1}$). The enthalpy and entropy values were given as a sum of two values: $\Delta_{trs}H$ = (1174 ± 69) + (5055 ± 15) = 6229 ± 84 $J \cdot mol^{-1}$ and $\Delta_{trs}S$ = (3.54 ± 0.20) + (13.11 ± 0.04) = 16.65 ± 0.24 $J \cdot K^{-1} \cdot mol^{-1}$. This last value seems *a priori* in better agreement with the reported value by Pistorius [23].

Zarkevich et al.[24] using ab initio calculations by molecular dynamics approach, provide a value of 4.6 $kJ \cdot mol^{-1}$ for the enthalpy of the transition by considering boron relaxation (9.3 $kJ \cdot mol^{-1}$ was first obtained with fixed boron position). More recent values for enthalpies and temperatures of the transformations are shown in table 4.5 as measured by Zuttel et al.[14] and Price et al.[15] using DSC.

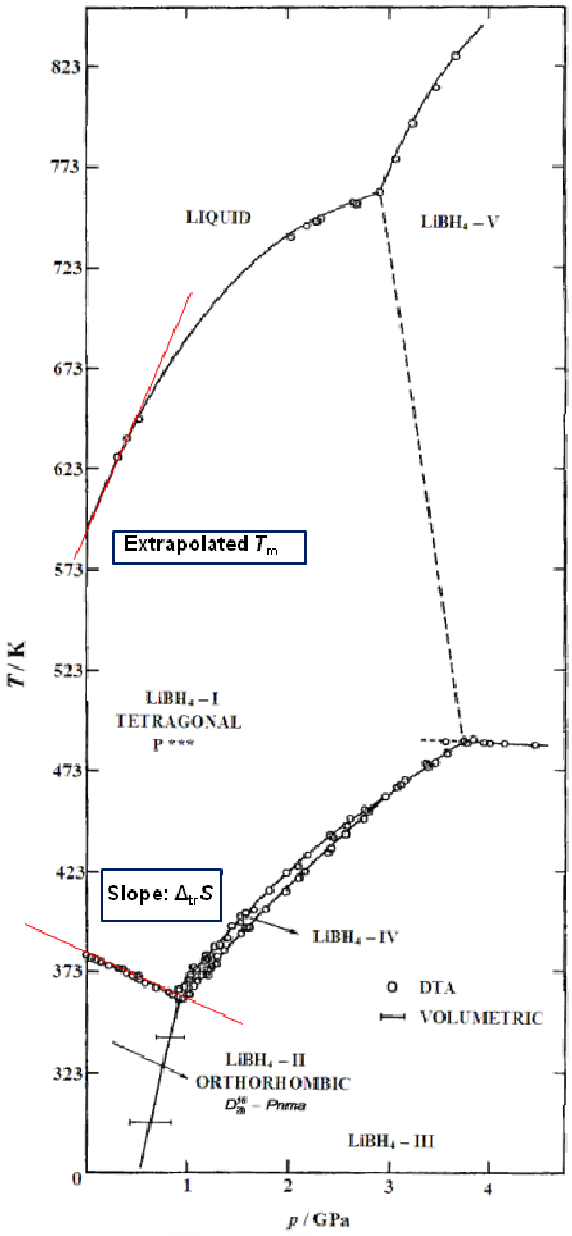

Figure 4.7. $LiBH_4$ high pressure p-T phase diagram deduced from Pistorius [23] data (the axes are transformed to the appropriate units): determination of the transition and melting temperatures by extrapolating at 0 GPa and extraction of the entropy of the phase transition from the slope of the boundary line.

Boron additives effect on the activation energy of the decomposition reaction of $LiBH_4$ compound was investigated by Pendolino et al.[25] using DSC. They give the temperatures of the transformations and a finally decomposition temperature at 773 K. The transition and melting temperatures have been observed to be identical to "pure" $LiBH_4$ when boron was added to $LiBH_4$ in the weight ratio B:$LiBH_4$ = 1:6. However, the enthalpy of reaction (4.11) was determined to be higher when B was added. They explain the increase of the enthalpy (proportionally the entropy) by dissolution of B in the melt, although they did not observe any tem-

perature effect on the transitions. More details about the experimental conditions and given values are presented in tables 4.4 and 4.5.

2.1.3.2 Crystalline phase transition

- Temperature of the phase transition

For temperatures reported in table 4.5, few authors pointed out problems associated to the measurement of this temperature. Fedneva et al.[2] detected the presence of the polymorphic transition in the temperature range 381 – 385 K. This 4 K range may be due to the effect of the "abnormal" increase of the heat capacity at the base of the peak apparition as discussed in our calorimetric study. The average temperature of the transition measured under different H_2 pressures by Stasinevich and Egorenko [4] was 383.3 ± 3 K. As the onset of the thermal event was not clear due to the presence of the abnormal increase, attributed by many authors as a part of the main transition, we decided to retain the transition temperature of our measurements 386.6 ± 1 K by considering the only main transition peak, independently of the abnormal increase. This value is in agreement with the values proposed by Gorbunov et al. and Stasinevich et al. [3,4]. Other values reported in table 4.5 are considered to be too low due to impurities that led either to a cryoscopic effect or to desorption thermal effects.

$$T_{trs}\ (\text{orthorhombic}\rightarrow\text{hexagonal}) = 386.6 \pm 1\ \text{K}$$

- Enthalpy of the phase allotropic transition

Pistorius [23] estimated the entropy of the transition, 16.5 $J\cdot K^{-1}\cdot mol^{-1}$, from the slope in the *p-T* diagram at the 382 K temperature (Fig.4.7). The deduced enthalpy is thus equal to 6.303 $kJ\cdot mol^{-1}$. In spite of the carefully established phase diagram, it seems that the volume change at the phase transition for entropy determination by Pistorius suffers from accumulation of approximations at the triple point and from disregarding a fourth phase. The only measured volume change at low temperature by high-pressure volumetry, from which the volume change at the phase transition of our interest was calculated, presents large hysteresis and has not been corrected for the piston friction. This transition has an uncertainty on the slope which could amounts to 50 $K\cdot GPa^{-1}$ for a value equal to 222 $K\cdot GPa^{-1}$ as used in the calculations. Maxwell's relation (4.13) is probably used by the author to derive approximate values of the entropy of the transition.

$$\left(\frac{\partial V}{\partial S}\right)_p = \left(\frac{\partial T}{\partial p}\right)_S \tag{4.13}$$

As there is no indication by the author for the purity and the ambient medium for handling the $LiBH_4$ compound, the assumption of the existence of an hypostoichiometric domain at such high pressure could not be discarded at the microscopic level. Besides, the volume change used from XRD indexing could not be considered as reliable since the structure was originally identified to be tetragonal in place of hexagonal. Indeed, more recent data from X-ray indexing [5,13], inform us that the hexagonal phase is denser than the orthorhombic phase near the transition. Then it follows a crystal density decrease upon temperature increase due to thermal expansion. This is only in agreement with the Pistorius [23] negative slope along the transition line. It seems that high pressure DTA analysis is not affected by the presence of the abnormal increase.

At the transition under standard pressure, the presence of impurities such as water should have an undesirable effect on the obtained value of enthalpy namely the desorption heat contribution of the impurities. For this reason, reading the explanations given by Gorbunov et al.[3] for the abnormal increase of the heat capacity far before the transition, we attribute this $C_{p,\mathrm{m}}$ increase either to desorption or to crystalline lattice structuring (due to non-stoichiometry) and finally to the two effects as explained in our calorimetric paper [ref] before the main transition and finally we decided to retain the only heat effect associated with the lone transition peak as mentioned for the temperature of the transition. Indeed, Filinchuk et al.[13] described the abnormal part by a highly anisotropic lattice expansion where the tetrahedral [BH_4] group was described as a rigid-undistorted component having very similar geometry in both crystalline phases and which is reoriented in a rotational disorder in agreement with Soulié et al.[5]. Zuttel et al.[14] give lower value for the enthalpy with a difference that amounts to 2 kJ·mol^{-1} comparing to the total value of Gorbunov et al.[3]. Zarkevich et al.[24] using ab-initio molecular dynamics, provide a value of 4.6 kJ·mol^{-1} by considering B relaxation in agreement with Zuttel et al.

Presently, there are two groups of authors who claim 2 different sets of values. In spite of the agreement between Gorbunov et al.[3] and Pistorius [23], the enthalpy seems to be too high and we decide to consider only the enthalpy corresponding to the only area under the peak for the main transition. Proceeding in such way, the retained enthalpy of transition is $\Delta_{trs}H$ = 5069 ± 76 J·mol^{-1} issued from our own measurements in agreement with the only “peak” value obtained by Gorbunov et al.

$$\Delta_{trs}H = 5069 \pm 76 \text{ J·mol}^{-1}$$

$$\Delta_{trs}S = 13.11 \pm 0.23 \text{ J·K}^{-1}\text{·mol}^{-1}$$

2.1.3.3 Melting of $LiBH_4$

- Temperature of melting

Schlesinger and Brown [35] identified the melting point to be in the 548-553K temperature range. Fedneva et al.[2] measured this temperature in the range 541-558 K. Stasinevich and Egorenko [4] found that the temperature of melting increase slightly (551-555 K) as a function of hydrogen pressure, but this temperature range is comparable to the measurement accuracy. The obtained average temperature was 553 ± 3 K. Semenenko et al.[22] give 555 K for the melting temperature. Price et al.[15] obtained 552 K and the value issued from our measurements was 554 K. The retained temperature of the melting is an average of the values given by Stasinevich and Egorenko for the following reasons: - (i) purity of the compound (98% compared to 95% for the commercial powder directly employed in almost studies), - (ii) measurements made under imposed H_2 pressure that avoid composition evolutions and found to be pressure independent and - (iii) even if Semenenko et al. worked with a high quality compound, the analysis under vacuum seems to affect the temperature of melting. The proposed melting temperature is,

$$T_m = 553 \pm 3 \text{ K}.$$

- Enthalpy of melting

Due to the high reactivity of the compound, a few data are available for the liquid phase. Up to day, for our knowledge only two measurements are reported in literature [14,15]. As the authors have got close values, 7.56 and 8.03 $kJ \cdot mol^{-1}$ [14,15], the retained enthalpy of melting is an average value. However, in the present thermodynamic critical assessment of the "pure" compound, a correction has been made for impurities content when assuming they are – (i) first chemically inert at the melting, – (ii) second that the measured heats may be only at least altered by an increment corresponding to the purity of the compound. Thus, correction was made taking into account the purity of the commercial compound (mass fraction 0.95). Consequently the melting enthalpy is,

$$\Delta_{melting} H° = 8.18 \pm 0.3 \text{ kJ} \cdot \text{mol}^{-1}$$

The uncertainty associated with the calculated value 6.3 $kJ \cdot mol^{-1}$ by Zarkevich et al.[24] using ab initio molecular dynamics approach, is difficult to estimate and we cannot check the reliability of this value against the retained experimental one.

On the other hand, the slope d*T*/d*p* at the melting in the diagram (Fig.4.7) given by Pistorius [23] could be used to calculate the volume change at the melting. Indeed by using the Clapeyron formula derived from relation (4.13) and the retained enthalpy of melting, we got the value $(\Delta V)_{p\rightarrow 0}$ = 1.93 ± 0.22 $cm^3 \cdot mol^{-1}$. Using the volume unit cell given by Filinchuk et al.[13] at 535 K and by neglecting the thermal expansion, the following liquid density is obtained near the melting temperature,

$$\rho_{liq} = 0.601 \pm 0.005\ g \cdot cm^{-3}$$

2.2 Gibbs energy function of the phases

The Gibbs energy function *G* of the compound is calculated from the reference phase enthalpy at 298 K; hence it is designed by *GHSER* (see appendix). The construction of the *GHSER* function for $LiBH_4$ condensed phases comes back to describe thermodynamically each phase with its own function in a wide temperature range even in temperature domains beyond the phase existence. The concerned phases for $LiBH_4$ compound are namely: orthorhombic-phase, hexagonal-phase and liquid-phase. Starting from the orthorhombic-phase where the heat of formation and absolute entropy at 298 K are known, the calculation of the *GHSER* function of each phase is deduced successively from the previous phase knowing the enthalpy and temperature of the transformations. The basic quantities used in the calculation of *GHSER* function for $LiBH_4$ are presented in table 4.8.

Table 4.8. Thermodynamic data used in the calculation of GHSER function of $LiBH_4$ compound

Phase / Transition	*T* / K range	Enthalpy / $kJ \cdot mol^{-1}$	Entropy / $J \cdot K^{-1} \cdot mol^{-1}$	Heat capacity / $J \cdot K^{-1} \cdot mol^{-1}$
ortho-phase	(298 to 386.6)	$\Delta_f H°_{298}$ = -190.46	$S°_{298}$ = 74.78	$C_{p,m}°_{298}$ = 81.34
ortho→hexa	(386.6 to 553)	$\Delta_{trs}H$ = 5.069	$\Delta_{trs}S$ = 13.11	$\Delta_{trs}C_{p,m}$ = -18.05
hexa→liquid	(553 to 756)	$\Delta_m H$ = 8.18	$\Delta_m S$ = 14.79	$\Delta_m C_{p,m}$ = 16.39

An integration of these quantities with specific software (available at Thermodata [36]) was used for the calculations of these phase functions. Therefore, the obtained *GHSER* functions are defined for four regions according to the CALPHAD formalism:

- above room temperature, the orthorhombic-phase from *T* = 298 K to *T* = 354 K,
- "abnormal" orthorhombic-phase from *T* = 354 K to *T* = 386.6 K,
- short-temperature range hexagonal-phase from *T* = 386.6 K to *T* = 553 K,
- and high-*T* liquid phase *T* > 553 K.

Table 6 shows the obtained *GHSER* functions for each phase with their *T* range of validity. The coefficients correspond to the relation:

$$GHSER(T) = \mathrm{A} + \mathrm{B}T + \mathrm{C}T\,lnT + \mathrm{D}T^{2} + \mathrm{E}T^{3} + \mathrm{F}T^{-1} \quad (4.14)$$

The coefficients C to F are deduced from the present polynomial fitting of the experimental $C_{p,\mathrm{m}}$ for the defined phase regions. A and B are the contribution of the enthalpy and entropy of the transformation.

Table 4.9 : *GHSER* function of the $LiBH_4$ condensed phases

$LiBH_4$ phases	*T* / K range	A	B	C	D	E x 10^4	F x 10^{-4}
ortho-phase	(298 to 354)	-65287.51443	-4126.12994	732.3021	-1.8583	7.53711	-478.1610
	(354 to 386.6)	7106856.76199	-175774.69894	29738.5861	-53.80984	181.30	-33623
hexa-phase	(386.6 to 553)	-30476.96149	-3086.14844	494.0684	-0.79716	1.88744	-1025
liquid-phase	(553 to 756)	-221605.59610	750.58939	-124.7			

3 Conclusion

The above room heat capacity of the $LiBH_4$ compound, containing less than 0.02 mass fraction impurities, have been measured. The present work proposes a new selected heat capacity set for the different condensed phases (orthorhombic, hexagonal and liquid) on the basis of existing data and from our own additional measurements. Improvement is clear for the hexagonal phase in the short temperature range of its existence from 386.6 K until the melting at 553 K. The observed anomaly before the allotropic phase transition at 386.6 K has been discussed and attributed to an “abnormal” trend independent of the main transition: this trend is either coming from the existence of an hypostoichiometric domain for the $LiBH_4$ compound or related to lattice rearrangements. Our results lead to modify the previous retained enthalpy increments by the integration method as well as the temperature of the transition. Consequently, a new enthalpy for the allotropic transition is proposed (5069 ± 76 $J{\cdot}mol^{-1}$) with a transition temperature 386.6 ± 1 K.

The assessment of the thermodynamic properties of the $LiBH_4$ compound has been performed taking into account of all available thermodynamic original data. This work is a sound complement to the NIST-JANAF thermochemical tables data of $LiBH_4$ which were not reviewed since December 1964, their above room temperature heat capacity being estimated at that time by analogy with the solid $NaBH_4$. The present work propose a selection of a new set of data for the different condensed phases (orthorhombic, hexagonal and liquid). The

observed anomaly before the allotropic phase transition at 386.6K discussed in a previous calorimetric part allowed the extraction of new parameters for the allotropic transition. Compilations of the different heats of formation of the compound reviewed in the literature and only obtained from a single original work were also reviewed. Finally, we report free energy functions of the phases with addition of the hexagonal and liquid phases observed until the decomposition of the compound around 756 K. The added new thermodynamic functions would provide relevant insights into the modelling of reactions involving the desorption and chemisorption of hydrogen from $LiBH_4$ for hydrogen storage purposes.

References

[1] C.C. Stephenson, D.W. Rice, W.H. Stockmayer, Journal of Chemical Physics 23 (1955) 1960.
[2] E.M. Fedneva, V.I. Alpatova, V.I. Mikheeva, Russian J. Inorg. Chem. 9 (1964) 826-827.
[3] V.E. Gorbunov, K.S. Gavrichev, V.L. Zalukaev, G.A. Sharpataya, M.S.I. Baku, Zhurnal Neorganicheskoi Khimii 29 (1984) 2333-2337.
[4] D.S. Stasinevich, G.A. Egorenko, Russian J. Inorg. Chem. 13 (1968) 341-343.
[5] J.P. Soulié, G. Renaudin, R. Cerný, K. Yvon, Journal of Alloys and Compounds 346 (2002) 200-205.
[6] N.C. Hallett, H.L. Johnston, Journal of the American Chemical Society 75 (2002) 1496-1497.
[7] A. Züttel, P. Wenger, S. Rentsch, P. Sudan, P. Mauron, C. Emmenegger, Journal of Power Sources 118 (2003) 1-7.
[8] H.I. Schlesinger, H.C. Brown, Journal of the American Chemical Society 62 (1940) 3429-3435.
[9] M.W. Chase, Jr., C.A. Davies, J.R. Downey, Jr., D.J. Frurip, R.A. McDonald, A.N. Syverud, JANAF Thermochemical Tables. Fourth Edition. Part I, Al-Co, J. Phys. Chem. Ref. Data, 1998.
[10] F. Grønvold, Journal of Chemical Thermodynamics 25 (1993) 1133-1144.
[11] R. Montanari, Tecniche sperimentali per la caratterizzazione dei materiali - dal laboratorio all produzione, Associazione Italian de Metallurgia, Milano, 2005.
[12] A.T. Dinsdale, Calphad - Computer Coupling of Phase Diagrams and Thermochemistry 15 (1991) 317-425.
[13] Y. Filinchuk, D. Chernyshov, R. Cerny, J. Phys. Chem. C 112 (2008) 10579-10584.
[14] A. Züttel, A. Borgschulte, S.-I. Orimo, Scripta Materialia 56 (2007) 823-828.
[15] T.E.C. Price, D.M. Grant, I. Telepeni, X.B. Yu, G.S. Walker, Journal of Alloys and Compounds 472 (2009) 559-564.
[16] T.B. Douglas, J.L. Dever, Journal of the American Chemical Society 76 (1954) 4826-4829.
[17] A.S. Dworkin, Journal of Chemical and Engineering Data 17 (1972) 284-285.
[18] A. El kharbachi, I. Nuta, F. Hodaj, M. Baricco, Thermochimica Acta, In press (2011) 10.1016/j.tca.2011.1002.1043.
[19] W.D. Davis, L.S. Mason, G. Stegeman, Journal of the American Chemical Society 71 (2002) 2775-2781.
[20] U. Bösenberg, S. Doppiu, L. Mosegaard, G. Barkhordarian, N. Eigen, A. Borgschulte, T.R. Jensen, Y. Cerenius, O. Gutfleisch, T. Klassen, M. Dornheim, R. Bormann, Acta Materialia 55 (2007) 3951-3958.
[21] K. Bohmhammel, U. Wolf, G. Wolf, E. Königsberger, Thermochimica Acta 337 (1999) 195-199.
[22] K.N. Semenenko, A.P. Chavgun, V.N. Surov, Russian J. Inorg. Chem. 16 (1971) 271-273.
[23] C.W.F.T. Pistorius, Zeitschrift fuer Physikalische Chemie 88 (1974) 253-263.
[24] N.A. Zarkevich, D.D. Johnson, Physical Review Letters 100 (2008) 040602.
[25] F. Pendolino, P. Mauron, A. Borgschulte, A. Zuttel, J. Phys. Chem. C 113 (2009) 17231-17234.
[26] D.D. Wagman, N.B.S. Report N°7437 (1962) 79-9 5.
[27] J.H.E. Jeffes, H. McKerrell, J. Iron Steel Inst., London 202 (1964) 666-676.
[28] M.B. Smith, G.E. Bass, Journal of Chemical and Engineering Data 8 (1963) 342-346.
[29] J. Smisko, L.S. Mason, J. Am. Chem. Soc. 72 (1950) 3679-3680.
[30] F.D. Rossini, D.D. Wagman, W.H. Evans, S. Levine, I. Jaffe, N.B.S. Circ. (U. S.) No. 500 (1952) 1266 pp.
[31] D.D. Wagman, W.H. Evans, V.B. Parker, R.H. Schumm, I. Halow, S.M. Bailey, K.L. Churney, R.L. Nuttall, J. Phys. Chem. Ref. Data, Vol. 11, Suppl. No. 2: The NBS Tables of Chemical Thermodynamic Properties, Am. Inst. Phys., 1982.
[32] K. Miwa, N. Ohba, S.-i. Towata, Y. Nakamori, S.-i. Orimo, Phys. Rev. B 69 (2004) 245120.
[33] Y. Nakamori, K. Miwa, A. Ninomiya, H. Li, N. Ohba, S.-i. Towata, A. Zuttel, S.-i. Orimo, Phys. Rev. B 74 (2006) 045126-045129.
[34] D.J. Siegel, C. Wolverton, V. Ozolins, Physical Review B 76 (2007) 134102.
[35] H.I. Schlesinger, H.C. Brown, Journal of the American Chemical Society 62 (2002) 3429-3435.

[36] http://www.thermodata.fr/.
[37] P.J. Spencer, Calphad - Computer Coupling of Phase Diagrams and Thermochemistry 32 (2008) 1-8.

Appendix. CALPHAD approach

In order to perform thermodynamic calculations using a computer for any chemical complex system, we need to provide the Gibbs energy functions for all existing phases as a function of temperature, pressure and composition [37]. The first step is to select thermodynamic functions of the known compounds. For the solid phase functions, we use a formalism proposed by SGTE [12] and also by the NIST-JANAF database in the CALPHAD method of calculations. The Gibbs energy function has the following expression:

$$G(T) = \mathrm{a} + \mathrm{b}T + \mathrm{c}T\ln T + \sum_{\mathrm{n}} \mathrm{d}_{\mathrm{n}} T^{\mathrm{n}} \ ; \ \mathrm{n} = 2, 3, -1 \tag{A.1}$$

usually written as:

$$G(T) = \mathrm{A} + \mathrm{B}T + \mathrm{C}T\ln T + \mathrm{D}T^2 + \mathrm{E}T^3 + \mathrm{F}T^{-1} \tag{A.2}$$

As the thermodynamic functions are related by the following expressions:

$$H = \int_0^T C_{p,\mathrm{m}} \mathrm{d}T \ , \quad S = \int_0^T \frac{C_{p,\mathrm{m}}}{T} \mathrm{d}T \quad \text{and} \quad G = H - TS \tag{A.3}$$

by integration of the heat capacity at constant pressure $C_{p,\mathrm{m}}$, one can deduce the other functions as following:

$$S(T) = -\mathrm{B} - \mathrm{C} - \mathrm{C}\ln T - 2\mathrm{D}T - 3\mathrm{E}T^2 + \mathrm{F}T^{-2} , \tag{A.4}$$

$$H(T) = \mathrm{A} - \mathrm{C}T - \mathrm{D}T^2 - 2\mathrm{E}T^3 + 2\mathrm{F}T^{-1} , \tag{A.5}$$

from $C_{p,\mathrm{m}}$ in that case having the following analytical form:

$$C_{p,\mathrm{m}}(T) = -\mathrm{C} - 2\mathrm{D}T - 6\mathrm{E}T^2 - 2\mathrm{F}T^{-2} . \tag{A.6}$$

GHSER (*H* for enthalpy of the SER *i.e.* Stable Element Reference at 298 K) is used in thermodynamic calculations using a computer because the reference state is well defined at 298.15K and 1bar applied pressure. As the solid $LiBH_4$ undergoes physical transformations (phase transition and melting), the compound *GHSER* function takes into account of all these transitions as a function of temperature.

If $298 < T < T_{\mathrm{tr}}$, we have to consider the formula:

$$GHSER^{\varphi_1}(T) = \Delta_{\mathrm{f}} H_{298} + \int_{298}^{T(<T_{\mathrm{tr}})} C_{p,\mathrm{m}}^{\varphi_1} \mathrm{d}T - T(S_T^{\varphi_1} - S_{298}^{\mathrm{o}}(\varphi_1)) \tag{A.7}$$

where $S_T^{\varphi_1} - S_{298}^{\mathrm{o}} = \int_{298}^{T(<T_{\mathrm{tr}})} \frac{C_{p,\mathrm{m}}^{\varphi_1}}{T} \mathrm{d}T$

Otherwise, i.e. $T \geq T_{\mathrm{tr}}$ the *GHSER* has the following expression:

$$GHSER^{\varphi_2}(T) = GHSER^{\varphi_1}(T = T_{\mathrm{tr}}) + \Delta_{\mathrm{tr}}H + \int_{T=T_{\mathrm{tr}}}^{T} C_{p,\mathrm{m}}^{\varphi_2} \mathrm{d}T - T(S_T^{\varphi_2} - S_{T_{\mathrm{tr}}}^{o}(\varphi_2) + \Delta_{\mathrm{tr}}S) \qquad \text{(A.8)}$$

where the quantity, $S_T^{\varphi_2} - S_{T_{\mathrm{tr}}}^{\mathrm{o}}(\varphi_2) = \int_{T_{\mathrm{tr}}}^{T} \frac{C_{p,\mathrm{m}}^{\varphi_2}}{T} \mathrm{d}T$, is the absolute entropy contribution of the phase φ_2 calculated from the standard entropy of the preceding phase at the temperature of the transition.

CHAPTER 5. PHASES STABILITY AND DECOMPOSITION REACTIONS

The main feature of hydrides behaviour is to present variable compositions due to hydrogen loss. As already observed, some transformations occur and new phases could appear. To understand the appearance of new products during hydrogen absorption or desorption in the case of $LiBH_4$ compound, we have to consider the ternary phase diagram Li-B-H, at least for compositions close to the $LiBH_4$ phase or for phases that can be in equilibrium with this compound. The hereafter figure (Fig.5.1) shows a schematic room temperature phase diagram of the ternary system drawn from known compounds as well as from the hypothetical compounds $LiBH_{4-x}$ (0<x<4). Indeed, the existence of the boryl-lithium compound "$LiBH_2$" is still under discussion in literature [1,2].

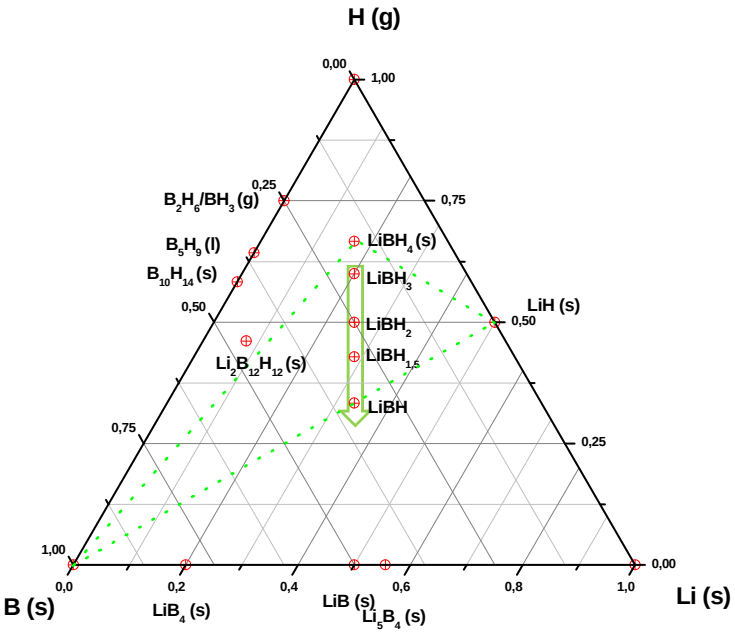

Figure 5.1. Schematics of the room temperature Li-B-H ternary phase diagram including $LiBH_{4-x}$ hypothetical compounds

This part of our study is aimed to investigate the different reactions during $LiBH_4$ decomposition. On the other hand, we present some experiments related to the stability of the Li-B-H system in the three phases triangle $LiBH_4$-LiH-B. The hypo-stoichiometric compound analyzed by XRD is also discussed in this part when only $LiBH_4$ pure compound samples are heat treated. Mass spectrometry qualitative analysis is also performed for the identification of

the various gaseous species which could be present in the gaseous phase. Finally, Knudsen evaporation was used to quantify the total vapour pressure.

1 Contribution to the study of the Li-B-H system

In this section on the basis of the assessed data in the previous chapter, we try to ascertain the existence of the most stable phases in equilibrium with $LiBH_4$ and consequently to check the predominant reaction of decomposition of the $LiBH_4$ compound in the Li-B-H system. The compositions as presented in the figure 5.1 concern condensed phases as well as gaseous phases when rising temperature. Indeed, for temperatures below the melting of LiH at 953 K (680℃), a temperature range suitable for hydrogen storage, the following reaction is expected to be the most probable:

$$LiBH_4(s,l) = LiH(s) + B(s) + 1.5H_2(g) \quad (5.1)$$

But another reaction could release single lithium (melting at 453 K) as follows [3]:

$$LiBH_4(s,l) = Li(s,l) + B(s) + 2H_2(g) \quad (5.2)$$

Different other reactions are also occurring simultaneously with the reaction (5.1) involving BH_3 and B_2H_6 species as the two following reactions:

$$LiBH_4(s,l) = LiH(s) + BH_3(g) \quad (5.3)$$

$$LiBH_4(s,l) = LiH(s) + 0.5B_2H_6(g) \quad (5.4)$$

An hypostoichiometric domain for the $LiBH_4$ (s) compound could also exist as it was systematically observed in our XRD indexing after heating in sealed ampoule under vacuum. This observation could be the result of a small hydrogen release:

$$LiBH_4(s,l)=LiBH_{4-x}(s) + x/2H_2(g) \quad (5.5)$$

The figure 5.2 presents the Gibbs energy difference for the different above reactions reported to the predominant one (5.1) in standard state. Note that the presented Gibbs energy increments (i.e. $\Delta(\Delta G)$) depend only on the reactions products.

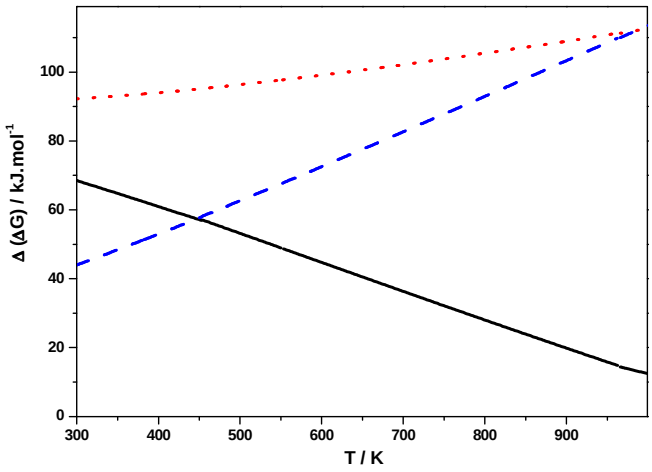

Figure 5.2. Gibbs energy of the different reactions reported to the more favourable reaction (5.1): ──, Eq.5.2; ···, Eq.5.3; - - -, Eq.5.4.

From this figure using SGTE database [4], the sign (>0) shows that reaction 5.1 remains more favourable than the other reactions. Reaction (5.2) has the tendency to become as favourable as the reference reaction at high temperatures after the melting and decomposition of LiH when the products of the reactions should be the same. In contrast, the formation of B_2H_6 (g) (Eq. 5.4) becomes less favourable at higher temperatures, which is an important indication for eventual mass spectrometric measurements. The reactions (5.2) and (5.4) seem to be energetically comparable at the intersection point 447 K (174℃). In addition to the products (LiH (s), B (s) and H_2 (g)) of the predominant reaction, the equilibrium at this temperature can be described thermodynamically by the vaporisation of minor B_2H_6 species meanwhile a few Li (s,l) quantity can growth on the $LiBH_4$ (s) grains. In reality this feature is probably difficult to occur due to some kinetic limitations in powder materials. On the other hand, the reaction 5.3 remains constantly not probable, i.e. the pressure of BH_3 (g) should remain very low.

1.1 Stability of the $LiBH_4$-LiH-B three-phase domain

1.1.1 Preparation method

In order to confirm the proposed decomposition reaction (5.1) up to the melting of $LiBH_4$, we have studied the stability of the three-phase system $LiBH_4$-LiH-B by thermal treatment in sealed ampoules (under vacuum $5x10^{-3}$ mbar). This study allows clarifying the presence of

intermediate phases if existing such as $LiBH_{4-\varepsilon}$ where ε is more or less small according to Eq.5.5. In the ternary phase diagram, our samples compositions are located in the $LiBH_4$-LiH-B three-phases triangle. We prepared the following hypothetical compound compositions: $LiBH_3$, $LiBH_2$, $LiBH_{1.5}$ LiB_2H_2 and $Li_7B_3H_{10}$ from suitable molar fraction of the needed amounts of each compound starting from only $LiBH_4$, LiH and B powders (Table 5.1). 5 samples were prepared by mixing the three phases, ball-milled and then filled in sealed ampoules (borosilicate for solids at low temperature and silica when melting could occur) (Fig.5.3).

Table 5.1. Corresponding ternary molar fraction of each sample

Molar fraction of components	Sample 1 ($LiBH_3$)	Sample 2 ($LiBH_2$)	Sample 3 ($LiBH_{1.5}$)	Sample 4 (LiB_2H_2)	Sample 5 ($Li_7B_3H_{10}$)
X_{Li}	1/5	1/4	2/7	1/5	7/20
X_B	1/5	1/4	2/7	2/5	3/20
X_H	3/5	1/2	3/7	2/5	10/20

The calculated amounts of each compound are based on the corresponding equations:

Sample 1: $3LiBH_3 = 2LiBH_4 + LiH + B$

Sample 2: $3LiBH_2 = LiBH_4 + 2LiH + 2B$

Sample 3: $6LiBH_{1.5} = LiBH_4 + 5LiH + 5B$

Sample 4: $LiB_2H_2 = LiBH_4 + 5LiH + 5B$

Sample 5: $Li_7B_3H_{10} = LiBH_4 + 5LiH + 5B$

Figure 5.3. Samples of the three-phase system sealed in ampoules under vacuum

The samples 1, 2 and 3 correspond to the direct hydrogen loss when started from $LiBH_4$. Samples 4 and 5 were prepared by considering that $LiBH_4$ is enriched with boron and lithium respectively and had lost H_2 (Fig.5.4). The boron used in this part of the study is crystalline

boron (rhombohedral). The phases that will be produced by reaction under heat treatment will inform us on the phases in equilibrium with $LiBH_4$, that would have lost H_2.

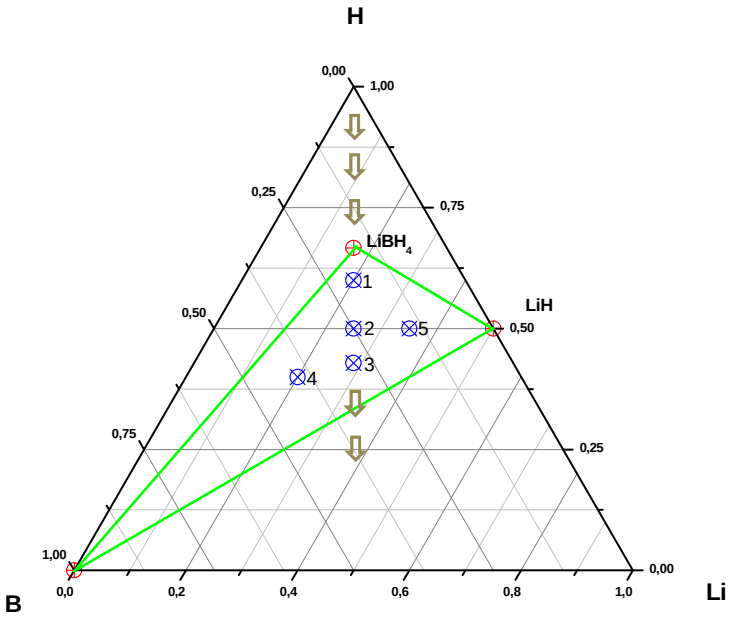

Figure 5.4. Li-B-H ternary phase diagram with the three-phase $LiBH_4$-LiH-B domain. The pointed compositions are indicated in blue circles. The arrows show the composition evolution by H_2 loss.

1.1.2 Results and discussion

The samples were heat treated at different temperatures until approaching the melting temperature of $LiBH_4$. Two series of samples were prepared. The first series was heated at 250 ± 2.5 ℃ for 4 hours. At this temperature no meltin g was visually observed. For those samples a slight gaseous release from the solid mixture was observed at the breaking of the ampoules in the glove box. The following figure shows the XRD patterns of the three-phase sample 1. By powder XRD indexing, the “as milled” sample presents all the starting phases without any modification. After heating in quartz sealed ampoule, the XRD pattern did not change anymore. Only slight change in relative intensities of the phases is observed (Fig.5.5).

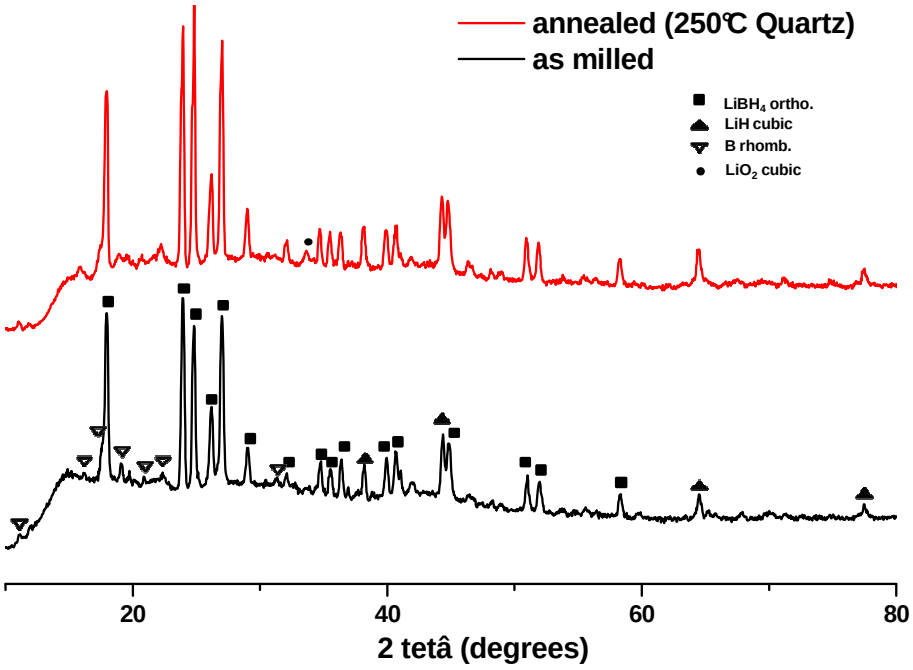

Figure 5.5. XRD patterns of sample1 after and before (as milled) annealing

For this first series, the independent observed phases before mixing are the same as after thermal treatment, but it was observed that $LiBH_4$ peaks undergo a shift in 2 tetâ axis. Similar observations are made for the other samples at this temperature. But in addition, the B-enriched sample shows a decrease in relative intensity of boron. This may be due to the transformation to amorphous boron peaks during heating.
We could conclude that the pseudo-ternary $LiBH_4$–LiH–B_{am} is stable in the temperature range below the melting temperature of $LiBH_4$.

In the second series, the samples were heated until 300 ± 5 ℃. All the samples, except sample 5, showed reactivity with the quartz tube (silica) revealed by the presence of Li_3BO_3 compound mainly in case of B-enriched sample (sample 4). After melting, the samples have formed a dark protective layer that prevents the melting of the totality of the powder. The Li-enriched sample (sample 5) has not melted at this temperature but it has formed a kind of sintered product.

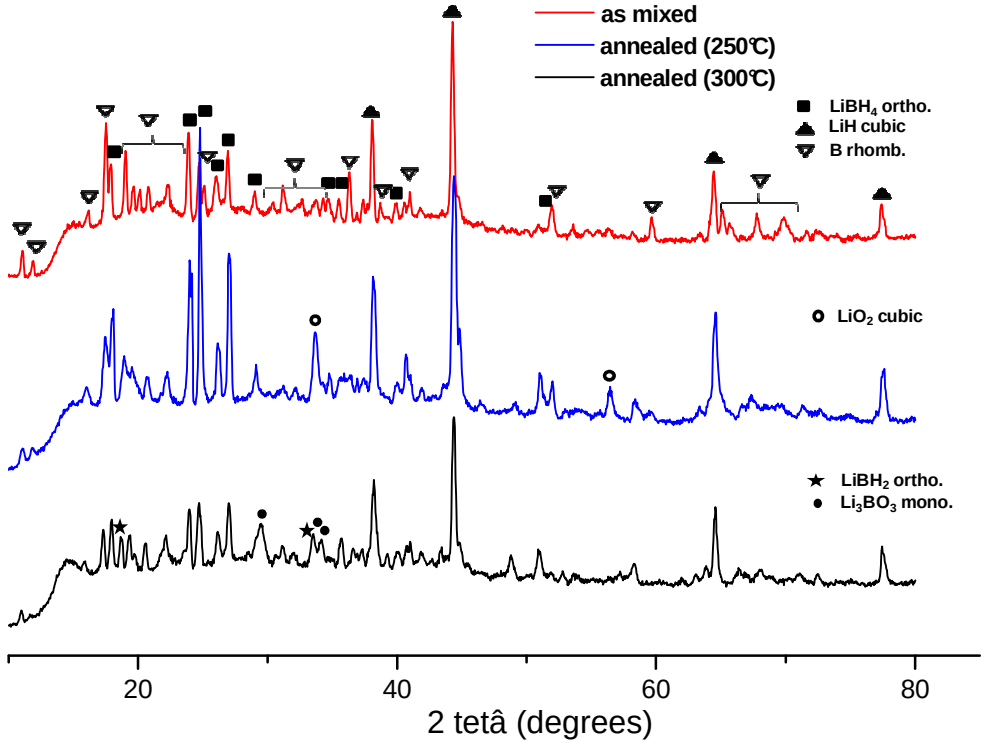

Figure 5.6. XRD patterns of sample 3 before and after annealing at 250 and 300℃

The sample 3 analyzed by XRD (Fig.5.6) showed the disappearance of some B peaks as mentioned for the first series. For sample heated at 300℃ the presence of $LiBH_2$ in the sample is probable because two Bragg peaks were indexed for this compound as shown in the above figure. $LiBH_4$ peak intensities are also reduced at this temperature.

1.2 $LiBH_{4-\varepsilon}$ hypostoichiometric compound

The thermal study of $LiBH_4$ pure samples at 270 ± 2.5 ℃ (just below the tempe rature of melting) for 3 days, did not show the presence of any new phase, although a shift in the peaks positions was well identified. For such a treatment, this shift can be attributed to the hypostoichiometry of the compound as already proposed in literature [5]. As mentioned for the three phase mixture, the presence of $LiBH_2$ composition is also probable for this sample annealed for longer time. In another temperature run, a liquid $LiBH_4$ was maintained under static vacuum (sealed ampoule) then frozen as it will be discussed in the next total pressure measurements part. In that case, a composition of $LiBH_{3.96}$ was calculated from final mass loss in accordance with XRD intensities shift but in that case without any signature of the $LiBH_2$ phase. This result highlights the good homogeneity of the formed phases in case of

liquid formation, where the hypo-stoichiometric compound is more favoured than the formation of any other phase, probably because the composition evolution is small due to small hydrogen loss. The $LiBH_{3.96}$ composition shows that the non- stoichiometric domain extends at least to this composition.

1.3 Vapour pressure measurements of $LiBH_4$

1.3.1 Mass spectrometry

The commercial $LiBH_4$ compound used in this part of study has an assay of 98.1% (certificate of analysis provided by the supplier, Alfa Aesar). $LiBH_4$ was synthesized by reaction between lithium hydride and boric acid trimethylester (MM. 103.91 $g.mol^{-1}$) at high temperature.

The $LiBH_4$ vaporisation was carried out using a magnet mass spectrometer coupled to an airtight Knudsen cell described in the experimental part. This special cell with a valve uses a heating system (silicon oil circuit) that allows working temperatures up to 473 K. In the glove box, the cell was loaded with 3 g of $LiBH_4$, “as received” or milled. The uncertainties in sample evaporation time, sample mass loss and cell temperature reading are estimated at 60 s, 0.2 mg and 3 K respectively. A high vacuum 10^{-8} mbar, is maintained in the mass spectrometer. The major gaseous species expected is H_2.

The first experiment was started at the temperature 105℃, in which H_2 vapor pressure should be of 0.1 mbar - pressure limit for applying the Hertz-Knudsen formula -. The calculated mass loss rate should be 18 mg/h. But no mass loss was observed experimentally at this temperature and the observed ionic intensity of H_2^+ is very low. Experiments were repeated for other $LiBH_4$ samples at higher temperatures: 156, 185 and 205℃. For the last temperature, milled powder was loaded in the cell instead of the “as received” sample in order to increase the specific surface and consequently the desorption rate. Even for this temperature, no significant mass loss were observed after 24 h of heating and only qualitative measurements could be obtained from low ionic intensities. Distinctively, the weighted mass loss for the samples at 185℃ and 205℃ were very l ow and within the precision limit ($\Delta m \leq 1$ mg) of the balance.

The following table (5.2) summarizes all the ions and their related masses detected using the shutter mode to ensure that the measured species are coming directly from the cell.

Table 5.2. Mass spectrometric analysis of $LiBH_4$ compound vaporisation gases at various temperatures (156, 185 and 205℃). The measured intensitie s are reported to the H_2 relative intensity.

Species	Mass (a.u.)	I/I(H_2) vs. T/℃		
		156	185	205
H	0.95	11.4	1.02	0.1
BH_3	13.9	--	--	0.14
?	19	--	--	0.1
?	25.7	0.05	0.1	--
B_2H_5	26.7	0.03	0.1	--
?	28.9	0.39	--	--
?	29.7	--	0.22	--
?	39.7	0.51	0.66	--
$Li_2B_2H_8$?	43.9	0.74	1.56	0.14

Eleven $LiBH_4$ vaporisation experiments were performed. In each experiment the cell was loaded with a new $LiBH_4$ powder. To facilitate the attribution of the observed ions by mass spectrometry to gaseous species, a list of masses of all probable species and their isotopes for the Li-B-H system with the corresponding calculated probabilities is prepared before experiments. Oxygen is also considered in the possible theoretical combinations of the basic components. The detected H_2 with very low ionic intensity (corresponding to $pH_2 < 10^{-7}$ bar) is observed to increase with the increase of the temperature. Nevertheless, H_2 species remains the most intense signal, except for single H species that was observed to be high compared to H_2 at low-T. But this species seems to come from the background vacuum. BH_3 is only observed for the milled sample heated at 205℃. As demonstrated by thermodynamics, the dimer B_2H_6 is more stable but its presence is difficult to confirm due to the abundant presence of N_2 (the main component of the background atmosphere) which is not resolved at almost the same mass. The observation of BH_3 seems to agree with the reported mass spectrometry measurements by Mitrofanova et al.[6] in the temperature range 110-200℃. Along the temperature range 25-450℃ they always observed the B_2H_6 species with some decomposition starting from 220℃ into the fragments BH_2, BH_3 and BH_4. Nevertheless their method of determination of the intensities by subtraction to the background without using a specific molecular beam “shutter” remains doubtful and since recombinations can be observed as coming from the walls. In addition, we observe that erroneous attributions were reported in

their previous work for BH_7 species instead of H_2O [7], a molecule existing at least in the background atmosphere (vacuum).

In contrast, the observed mass at 26.7 a.u. corresponds well to the B_2H_5 obtained by dissociative ionization process, B_2H_6 (g) + e^- → $B_2H_5^+$ + H + 2e^-. This ion becomes negligible at high temperatures a feature which is in agreement with our thermodynamic calculations at the beginning of this chapter. B_2H_6 species disappears at the same time when Li (s,l) precipitates. The presence of B_2H_6 is also proved by the fact that the masses 26.7 a.u. and 25.7 a.u. agree reasonably with the provided isotopic distribution of B_2H_5. The identification of the dimer $Li_2B_2H_8$ (43.9 a.u.) was doubtful because it is at the same mass as CO_2 species. But yet the absence of the other isotope let suppose that this species did not exist. The gaseous species such as BH_4 and $LiBH_4$ were not observed.

Ten experimental intensities for H_2 were obtained around the previous three temperatures and reported in the figure 5.7. Considering the reaction 5.1 and the present obtained slope, an enthalpy of the reaction is estimated to be 67.4 kJ.mol^{-1} H_2 at the average temperature of 455 K (182℃) according to the Van't Hoff relation. The calculated standard deviation is 0.4 kJ.mol^{-1}.

$$\Delta_r H = 67.4 \pm 0.4 \text{ kJ.mol}^{-1}\ H_2$$

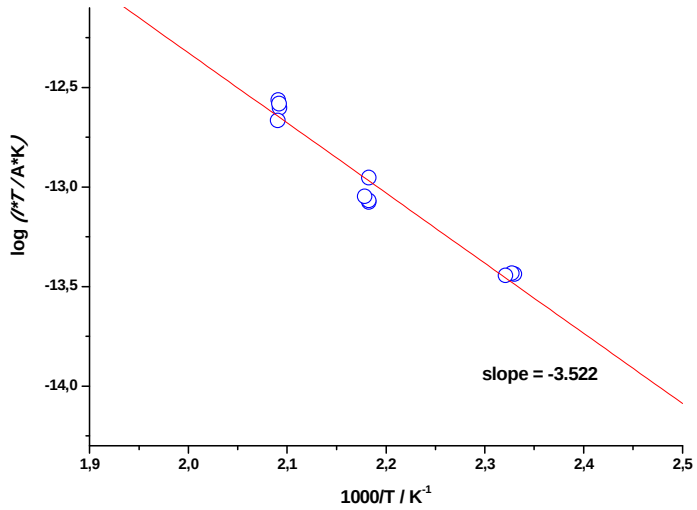

Figure 5.7. Logarithmic variation of the factor $I*T \propto$ pressure (for H_2) as a function of the inverse of the temperature.

This obtained value is in agreement with SGTE (Substance database) value [4], $\Delta_r H$ = 66.9 kJ.mol^{-1} H_2, calculated using Thermo-Calc software at the same temperature [8], whereas the assessed database in the previous chapter leads to the value 63.2 kJ.mol^{-1}.

1.3.2 Knudsen evaporation method

During the precedent mass spectrometric measurements no significant mass loss was observed at the reported temperatures. In this part only Knudsen method was performed using our simple cell device (conventional) for the quantification of any weight loss when rising temperature above 200℃. After loading with the sam ple and weighting every parts, the cell lid and its orifice were sealed by *paraffin wax* in the glove box to avoid any further atmospheric contact. Then introduced under vacuum in the high temperature furnace of the mass spectrometer. Once under vacuum, the first step of heating was dedicated to the vaporisation of the wax. For technical problem in this experiment, the mass spectrometric detection and ion source systems were disabled. At the end of each experiment, the mass spectrometer housing is filled with dried Ar, then the furnace taken off and the removing of the cell done under Ar flow before encapsulation and re-introduction in the glove box for weighting the different parts.

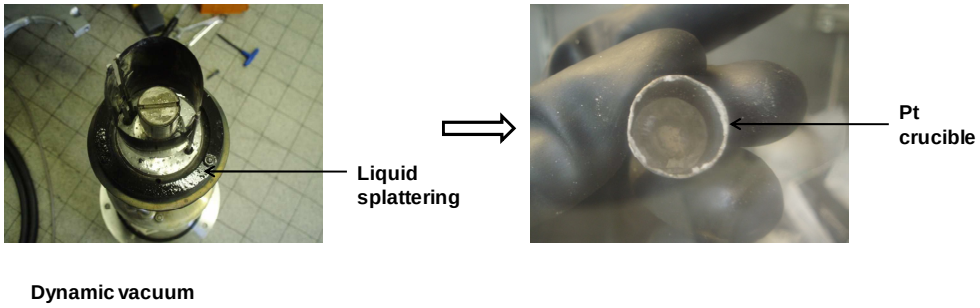

Figure 5.8. Liquid $LiBH_4$ evaporation tentative using high-T reactor under dynamic vacuum

For the “as received” solid $LiBH_4$, three experiments were performed at temperature plateaus 223, 245 and 255℃ after heating with a ramp 3-6℃/m in. The data at 185℃ deduced from the precedent experiment for the “as received” compound is also added to the log *p* vs. 1/T diagram in the figure 5.10 (arrow). The main component as discussed at the beginning of this chapter being H_2, the mass loss allows the calculation of the H_2 pressure using the Hertz-Knudsen relation. The experiment with the liquid phase under vacuum was not successful because the liquid undergoes a spontaneous overflowing at the melting which caused its

creeping on all the furnace-reactor parts as can be seen in the figure 5.8. After cooling only a very small $LiBH_4$ residue still remained in the crucible.

For the study of the liquid phase and in order to avoid the damage of the mass spectrometer furnace reactor, we melted the compound in a separate Pt crucible inserted in a glass ampoule as shown in the figure 5.9. The system is loaded carefully with the sample in the glove box and then sealed under vacuum outside with special valve. The ampoule is maintained vertically, placed in an alumina bath (container + powder) to ensure a homogenous temperature and then introduced in an oven. A low heating rate 0.4℃/min is chosen followed by an isotherm at 290℃ for 4 hours. After quenching the ampoule in liquid N_2 and introduction in the glove box, the sample is weighted and removed for XRD analysis (see 1.2).

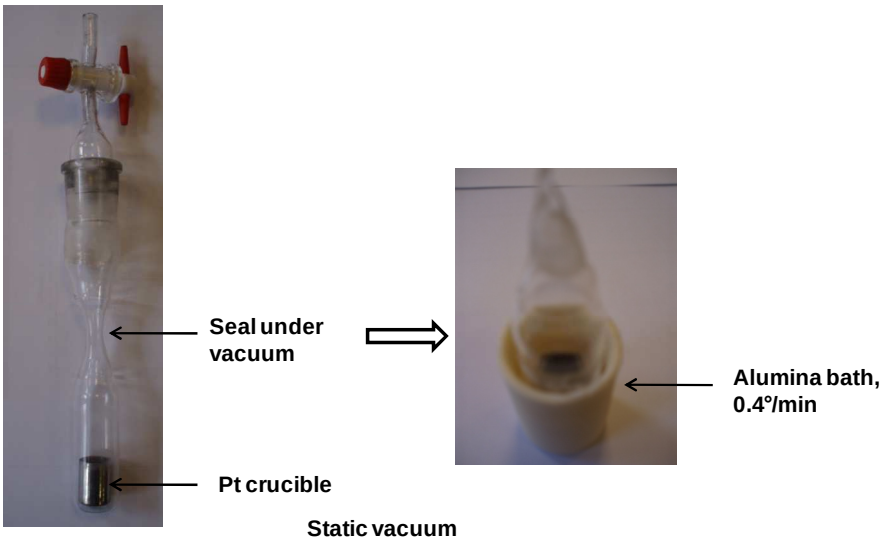

Figure 5.9. Liquid $LiBH_4$ formation under static vacuum in a sealed ampoule

All the obtained vapor pressure data using Knudsen vaporisation are presented in the following table.

Table 5.3 Calculated vapor pressures of $LiBH_4$ compound as a function of temperature according to mass loss.

$LiBH_4$ Phase	T / K	pH_2 / mbar
Solid (Knudsen)	458	$2{,}467 \cdot 10^{-4}$
	496	$5{,}241 \cdot 10^{-4}$
	518	$1{,}552 \cdot 10^{-3}$
	528	$1{,}397 \cdot 10^{-3}$
Liquid (Volumetry)	563	3.97

It was observed after cooling that the liquid had formed a concave meniscus at the bottom of the crucible without any notable projections as observed under dynamic vacuum. Nonetheless some brown deposits are formed on the glass ampoule which indicates the presence of boron. In such case the boron source is probably a gaseous species (B_nH_m type) which has deposited on the walls. As the vaporisation is different from the Knudsen conditions, H_2 pressure is calculated volumetrically by ideal gas law from the estimated ampoule volume and the mass loss of the crucible-sample (Table 5.3).

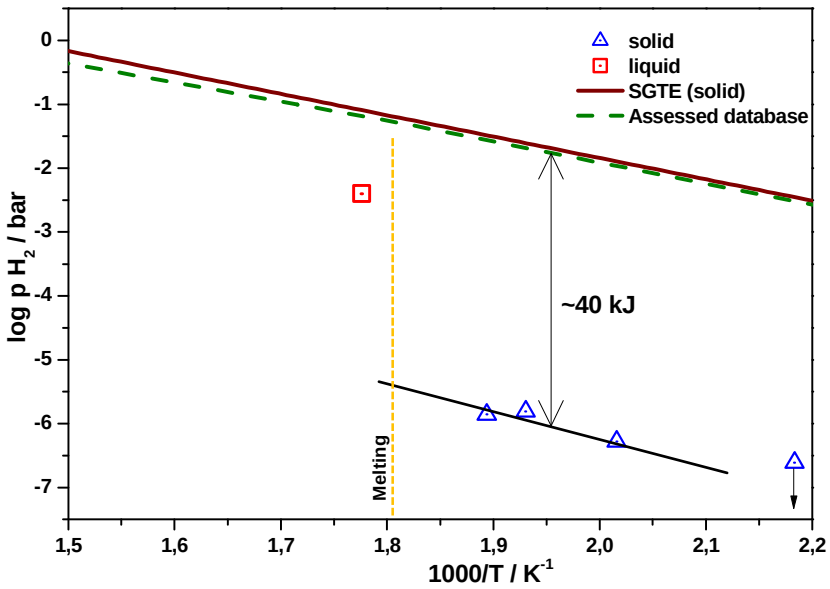

Figure 5.10. Measured total pressures over $LiBH_4$ using Knudsen method (solid) and volumetry (liquid) and comparison with thermodynamic prediction.

XRD does not provide any additional phase besides the $LiBH_4$ peaks, shifted as usually. A hypo-stoichiometric compound is probably formed during the melting with the nominal composition $LiBH_{3.96}$, calculated according to the observed mass loss. Finally one experimental pressure data is obtained over the liquid phase and is added in the figure 5.10.

The solid vapour pressures are far from the existing data given by SGTE and the assessed database in the previous chapter. Unlikely the logarithmic difference, converted to a Gibbs enthalpic increment (about 40 kJ), is huge. This difference is far from usual uncertainties and thus reveals that some kinetic phenomenon limits the vaporisation/desorption rate. Tentatively, we used the concept of “evaporation coefficient” to relate the two rates – desorption and equilibrium (maximum rate).

The vaporization coefficient α given by Motzfeldt relation [9] was used in that case to interpret the apparent phenomena. For orthocylindrical cells this relation is as following:

$$p_{equ} = p_{mes} (1 + f/\alpha) \tag{5.6}$$

where p_{equ} and p_{mes} are the equilibrium pressure and measured pressure by effusion respectively. f is the area ratio of the effusion orifice to the sample in the effusion cell (cross section). The calculated vaporization coefficient is of the order of 10^{-8} which shows a limited-step due to a very low kinetic rate. For such low coefficient, this kind of measurement is not significant because $\alpha << f$ as explained by Motzfeldt. But yet we can deduce as a first conclusion that the limitations is not due to reactions in the gaseous adsorbed mobile layer. The only explanation is that the $LiBH_4$ grains are coated with impurities (1.9 - 5%) or by the creation of a layer (LiH or B) due to the H_2 loss. This assumption is also justified by the sudden increase of the pressure for the liquid phase due to convective effects that probably break the surface layer.

2 Contribution to the study of the Mg-Li-B-H system

From the assessed thermodynamic properties of $LiBH_4$ compound, phases characterisation and gaseous identification carried out in the previous chapters, reactions can be tabulated for the MgH_2-x$LiBH_4$ mixture composite when exposed to thermal effect. As demonstrated and shown in the Mg-Li-B-H phase diagram (Fig.5.11), many products could be involved in the decomposition reaction of this mixture. Hence, different reaction pathways could be explored depending on the starting relative composition (ratio x), temperature (at *p*°) and assuming that impurities are stable without interaction with the main phases. In the figure 5.11, if one proceeds by H_2 evolving (green arrow), three main equilibrium could be considered: (1) with formation of MgB_2 and LiH (purple tetrahedron), (2) with Mg-Li alloy and B or MgB_2 (yellow tetrahedron) and (3) with Mg, B and LiH (sky blue).

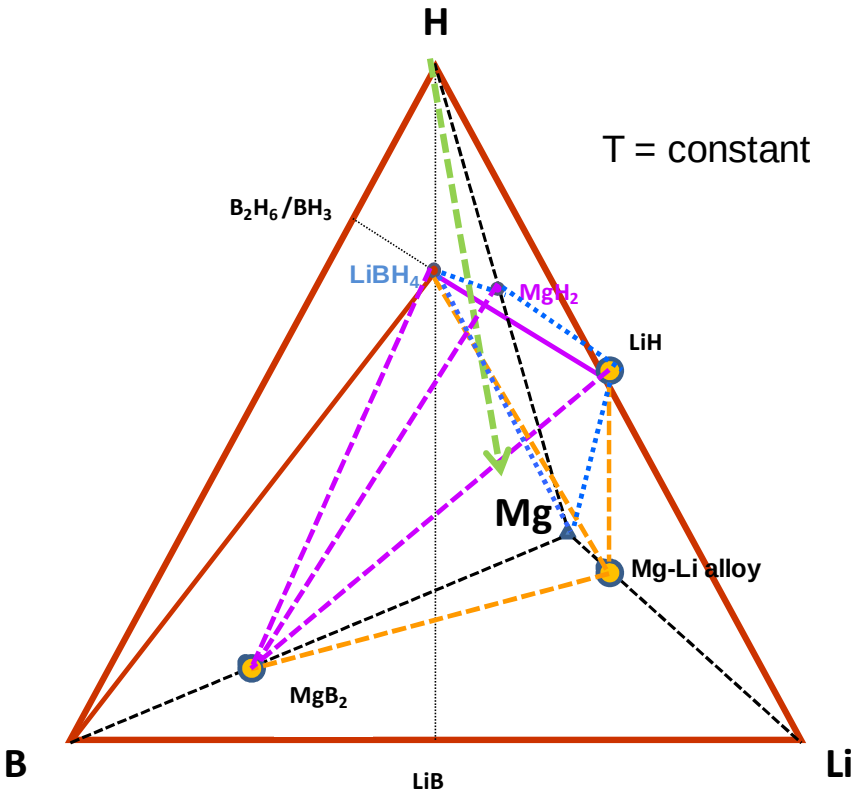

Figure 5.11. Phase diagram of the Mg-Li-B-H system

The following table summarizes the different possible decomposition reactions involving or not the MgB_2 compound. Low enthalpy of reaction is obtained for the stoichiometric decomposition of the mixture to MgB_2 and LiH with H_2 release.

Table 5.3. Enthalpy of the decomposition reaction of the mixture composite MgH_2-x$LiBH_4$

Ratio x	Reaction	$\Delta_r H$ (298.15 K) / kJ.mol^{-1} H_2
X = 1	$MgH_2+LiBH_4 \rightarrow 0.5MgB_2+LiH+0.5Mg+2.5H_2$	51.8
	$MgH_2+LiBH_4 \rightarrow Mg+LiH+B+2.5H_2$	70.2
X = 2	$MgH_2+2LiBH_4 \rightarrow MgB_2+2LiH+4H_2$	45.8
	$MgH_2+2LiBH_4 \rightarrow Mg+2LiH+2B+4H_2$	68.8
X = 3	$MgH_2+3LiBH_4 \rightarrow MgB_2+3LiH+B+5.5H_2$	51.5
	$MgH_2+3LiBH_4 \rightarrow Mg+3LiH+3B+5.5H_2$	68.2

The reported Van't Hoff plot in the following figure shows a fair agreement between our results and the obtained by Siegel et al.[10] obtained by first principle calculations, mainly at high temperature after the melting of $LiBH_4$. The experimental pressure plot of Vajo et al.[11] seems to be too low.

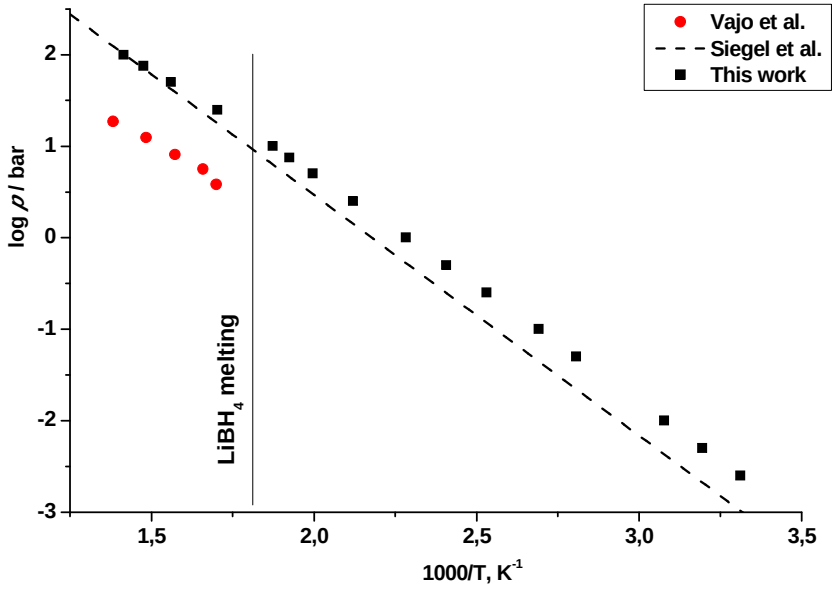

Figure 5.12. Van't Hoff plot of the stoichiometric reaction involving the formation of MgB_2 for the mixture MgH_2-2$LiBH_4$.

3 Conclusion

The thermodynamic study of the proposed decomposition reaction of $LiBH_4$ compound in literature certifies the following predominant process:

$$LiBH_4(s,l) = LiH(s) + B(s) + 1.5H_2(g)$$

The heat treated $LiBH_4$ compound, in both solid and liquid phases, is observed after cooling to be slightly hypo-stoichiometric by XRD and mass loss under vacuum.

The pseudo-ternary $LiBH_4$–LiH–B was concluded to be stable in the temperature range below the melting temperature of $LiBH_4$. After heating at 300℃, the Li-enriched sample has not melted and has formed a kind of sintered product. The B-enriched samples showed the disappearance of some B_{cr} peaks in favour of B_{am}. $LiBH_2$ is probably a phase existing along the $LiBH_4$ – LiB line as two Bragg peaks were indexed for this compound.

From mass spectrometry qualitative measurements up to 205℃, H_2 species is detected to be the main species but with very low ionic intensities ($pH_2 < 10^{-7}$ bar) which were observed to increase upon temperature. B_2H_6 species is more stable thermodynamically than BH_3 but its presence is difficult to confirm due to an overlapping with N_2, even if the presence of an isotopic abundance at mass 27 exists for this species.

Mass loss measurements using the Knudsen effusion method up to 255℃ for $LiBH_4$ solid vaporisation have shown very low pressures probably due to low desorption kinetics. Liquid $LiBH_4$ was observed to undergo a spontaneous effervescence at the melting point under dynamic vacuum. A volumetric method was used to estimate the total pressure over the liquid. A hypothesis is formulated that the $LiBH_4$ grains are coated with impurities (1.9 - 5%) or a thin layer due to H_2 loss with creation of the two LiH and B phases. This observation is also justified by the sudden increase of the pressure over the liquid phase when formed under static vacuum. Finally, the addition of Mg to the Li-B-H system has allowed the clarification of some of the possible reactions pathways of hydrogen cycle in the MgH_2-x$LiBH_4$ composite.

References

[1] A. Züttel, S. Rentsch, P. Fischer, P. Wenger, P. Sudan, P. Mauron, C. Emmenegger, Journal of Alloys and Compounds 356-357 (2003) 515-520.
[2] A. Züttel, P. Wenger, S. Rentsch, P. Sudan, P. Mauron, C. Emmenegger, Journal of Power Sources 118 (2003) 1-7.
[3] D.S. Stasinevich, G.A. Egorenko, Russian J. Inorg. Chem. 13 (1968) 341-343.
[4] A.T. Dinsdale, Calphad - Computer Coupling of Phase Diagrams and Thermochemistry 15 (1991) 317-425.
[5] H.I. Schlesinger, H.C. Brown, Journal of the American Chemical Society 62 (1940) 3429-3435.
[6] R.P. Mitrofanova, Y.I. Mikhailov, N.N. Mal'tseva, Zh. Neorg. Khim. 34 (1989) 2207-2211.
[7] Y.N. Shevchenko, N.N. Mal'tseva, V.A. Nazarenko, N.S. Kedrova, N.T. Kuznetsov, Journal Name: Dokl. Phys. Chem. (Engl. Transl.); (United States); Journal Volume: 290:4-6; Other Information: Translated from Dokl. Akad. Nauk SSSR; 290: No. 4-6, 1426-1430(Oct 1986) (1987) Medium: X; Size: Pages: 968-970.
[8] P.J. Spencer, Calphad - Computer Coupling of Phase Diagrams and Thermochemistry 32 (2008) 1-8.
[9] K. Motzfeldt, The Journal of Physical Chemistry 59 (1955) 139-147.
[10] D.J. Siegel, C. Wolverton, V. Ozolins, Physical Review B 76 (2007) 134102.
[11] J.J. Vajo, T.T. Salguero, A.F. Gross, S.L. Skeith, G.L. Olson, Journal of Alloys and Compounds 446-447 (2007) 409-414.

CHAPTER 6. PROJECT OF A MILLING REACTOR COUPLED TO A MASS SPECTROMETER

1 Introduction

The principal goal of this project is to study the chemical reactions of decomposition or re-combining of the complex hydrides. Our objective is to carry out measurements of vapor pressures for slow reactions (limited by the kinetics) and going until equilibrium by "mechanical activation" at standard pressure and temperatures until 250℃ in the milling reactor. In order to study the evolution of the gas phase – pressure and composition – emitted by the complex hydrides during ball-milling, we have planed the coupling of a mechanical reactor (ball-mill) with a mass spectrometer. This means that we would connect a device (ball-milling) working at atmospheric pressures to a mass spectrometer in which the ionization chamber usually works in vacuum, pressures as low as possible (UHV).

We expect to observe the different species resulting from milling - mainly H_2 and probably H_2O and HF (in the case of fluorinated doping agents). It is thus necessary to analyse very small gas flow issued continuously from the reactor, meanwhile the milling parameters will be moved. We describe here the choice of the inlet system to carry out such connection and to ensure precise and reliable measurements.

The milling reactor will have to be flexible in term of geometry, temperature as well as flow capabilities for different gaseous species. According to the set geometry, it would be interesting to carry out measurements close to equilibrium in addition to kinetic studies. The mass spectrometer was selected to be associated to the milling reactor, with an especially designed effusion cell, for the following main reasons:

- A great sensitivity of detection – dynamic range of 10^6 – 10^7 depending on the observed species nature
- A high resolution – about 800 at 10% valley – to separate almost completely all the observed species
- A shutter of the molecular beam which is reliable not only for condensable vapors but also for the detection of "permanent" gases (H_2, N_2, Ar..) and for high volatile vapors (HF, H_2O..).
- Effusion cell reactor and "ion source" housings well insulated and equipped with large pumping capacities, respectively 1300 and 800 l/s which correspond to 900 and 450 l/s at the level where the molecules are produced and ionized.

The study of the gaseous flows in a system of tubes and enclosures linked in series are the principal topics of this part. For that, it is essential to review the main theoretical concepts which are the base of the calculations carried out in this work. Indeed, before performing measurements by mass spectrometry, flow calculations will enable us to achieve the following goals:

- Dimensioning of the device. If we compare with the commercial devices, their compactness have intermediate adjustments which facilitate the adaptation to any enclosure but they present the disadvantages to be neither reproducible nor to allow quantitative measurements. Thus fixing the device with multiple sections will allow us the possibility to match the various aspects of the calculation theory on an adequate geometry.
- Obtaining a better flow and pressure control in the whole device according to the spectrometric experiments and in particular the possibilities of calibration of the instrument as well as the pressure range accessible to the experiment for quantitative measurements, in terms of gaseous flow consumed or produced during mechanical millings.

To make our flow calculations close to the planned experiments, we detail the relation with the hydrides mechanism commonly called “absorption/desorption”. As described in the literature [1], HP-DSC measurements coupled to Sievert apparatus – for kinetic study goal -, have allowed to observe the reaction of dehydriding of $LiBH_4$ destabilized by MgH_2 according to two following stages while heating at 465℃.

$$MgH_2(s) + 2LiBH_4(s) \longleftrightarrow Mg(s) + 2LiBH_4(s) + H_2(g) \longleftrightarrow MgB_2(s) + 2LiH(s) + 4H_2(g) \qquad (6.1)$$

The analysis by X-rays diffraction - after experiment - showed that this reaction is much more complex by revealing the existence of several other possible phases. These phases are probably formed during the process of reactivation of the powders by milling or when heating at such temperature.

The above reaction supposes the appearance of the unique gas, the hydrogen, whereas at the mentioned temperatures some other vapor pressures can be also important. However, magnesium could play a reactive role by transfer via the gaseous phase and then create layers at the surface which can have either a catalytic effect or an inhibition effect on the reac-

tions. The following equilibrium reaction (solid-gas) illustrates a case of a simple reaction of a metal hydride (MgH_2):

$$MgH_2(s) \longleftrightarrow Mg(s) + H_2(g) \tag{6.2}$$

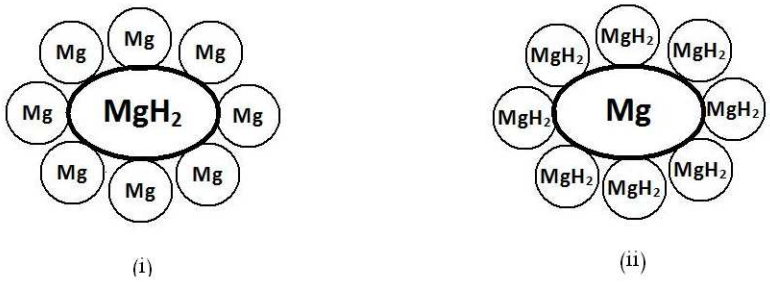

Figure 6.1. Model of rate-limiting steps, during hydrogen (i) desoption and (ii) absorption.

Among the possible rate-limiting steps, the two models presented in figure 6.1 where the desorption of MgH_2 could be limited by the formation of Mg layers all around and vice-versa for the absorption of hydrogen. For that, vapor pressure measurements will be made under different mechanical constraints during the milling process for the determination of their effects on the rate of formation of the gaseous species. During desorption /absorption processes, the expected behaviours for Mg-MgH_2 system are shown in the figure 6.2. The desorption kinetic should be improved by the start of the milling meanwhile the H_2 pressure will go toward equilibrium. Hence hydrogen release increase by creating new interfacial surfaces in the powders. Similar behaviour is to be predicted for absorption at low energy ball-milling but in reverse order of hydrogen intensities.

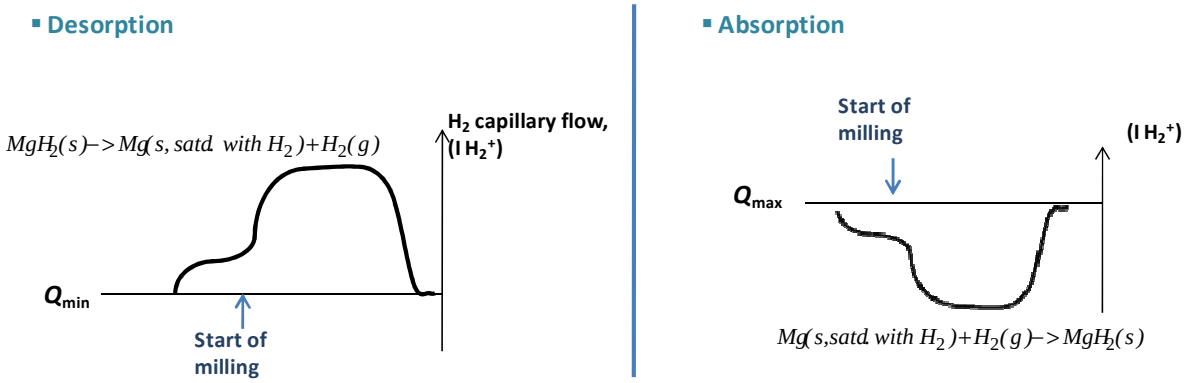

Figure 6.2. Expected milling effect on hydrogen intensities at set gas flow (Q) in case of the Mg-MgH_2 system (Eq.6.2).

We can expect also to observe the BH_3 (g) and LiH (g) gas molecules [2,3], as well as more complex hydrides B_nH_m(g) already observed by mass spectrometry [2] when heating this compound. In the milling device, a minimum amount of sample 2.5 g is necessary to protect the vial against its own degradation. For this quantity, magnesium hydride could release theoretically 0,095 mole of hydrogen while heating beyond 300℃ (2.1L under normal conditions). Knowing that under the further spectrometric conditions the release of hydrogen could be complete in approximately 26 hours, it is important to calculate the real conditions which will enable us to optimize this flow in the final effusive stage for spectrometric analysis. A solution for gas introduction device is the installation of an additional pump (primary) for the evacuation of the excess flow for measurements which is supposed to reduce the time for mass spectrometric observation. Figure 6.3 presents the various areas of steady-state pressures in the whole equipment to be coupled.

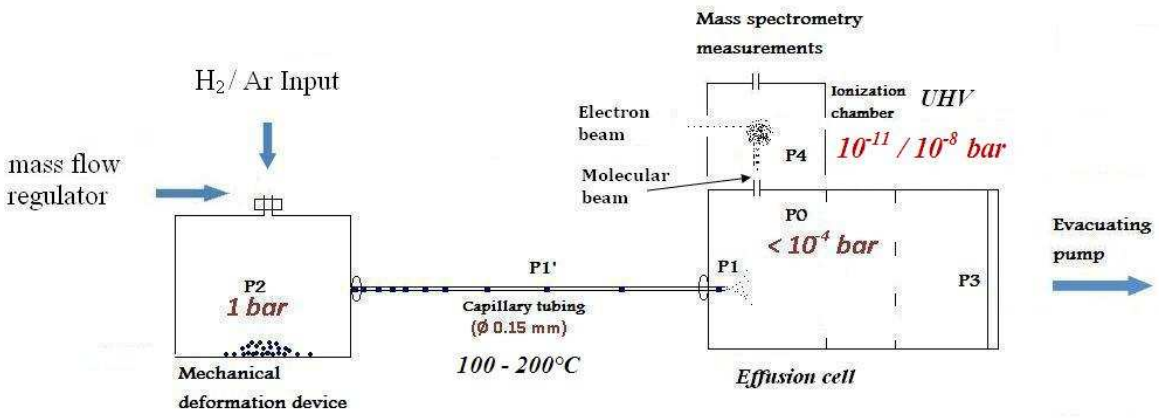

Figure 6.3. Distribution of the total pressures in the whole experimental device: effusion cell connected to the mill through the capillary tube and the system of regulation of pressure of the effused beam by mass spectrometry.

In the following part we describe more precisely the architecture of the experimental device which was selected. Gas flow determination in each section is based on calculation using appropriate flow equations depending on geometry.

2 Description of the milling reactor and inlet system

For gas introduction two systems can be considered: -(i) a capillary tube or –(ii) a micronic nozzle with supersonic beam already used by Chatillon [4]. The nozzle is used when one wants to avoid vapor condensations in the capillary tubes. A simple capillary tube is the system more convenient for non condensable gas when not reactive with the species to be detected. The capillary tube has also the advantage of allowing a certain distance between the milling device and the spectrometer to avoid the transmission of the milling vibrations.

The gas sampling system from the mill to the spectrometer must ensure a very small gas flow corresponding to that of an usual effusion cell. As the capillary flow is somewhat higher than the usual effusion flow, it was decided to provide the effusion cell with a vacuum pumping to ensure a suitable pressure in the range of 10^{-4} to 10^{-11} bar. The pressure in the effusion cell produces a molecular beam directed to the ionization chamber. A mobile shutter located on the way of the molecular beam allows at any moment to distinguish the molecules of the molecular beam coming directly from the effusion cell from those identical existing in flow steady state while pumping in the ion source. The molecular beam could be also disturbed by phenomena related to physicochemical interactions of the gas species with the different walls. Morland et al.[5] proposed the use of a restricted collimation device to optimize the molecular beam sampling. This type of measurement makes possible to monitor directly the pressure of a permanent gas contrary to the commercial assemblies which take into account the residual signal only by interpolating before and after introduction without knowing in fact its evolution of the real background during the measurements.

From this analysis and a preliminary calculation, we consider the coupling between the ball-mill and the effusion cell by a long capillary tube (1-3 m) with a diameter of about 1.5 to 0.15 mm and an orifice characterized by a shocked exit in the effusion cell. The orifice of the effusion cell has the standard size (2 X 2 mm) used in the present spectrometer with a continuous production of the molecular beam. A primary pump connected directly to the effusion cell is planned to ensure the Knudsen conditions at the cell orifice ($p_0 < 10^{-4}$ bar) (Fig.6.2). The whole device will be maintained at temperature higher than 100℃ to avoid condensation and adsorption phenomena especially for water along the capillary tube. Considering that the experiment requires a continuous contribution of hydrogen in the mill, a flow or pressure controller fitted with a dosing valve will be set up on the input line for the introduction of the gas (H_2 + Ar). This unit will also allow a calibration of the pressures or flows of gas used as carrier gas.

Total pressure measurements will be also monitored in the effusion cell using a capacitance gauge (Baratron). This will help to calibrate the mass spectrometer knowing the total pressure by applying the Knudsen formula displayed hereunder.

2.1 Ball-milling device

The milling reactor could be coupled to the effusion cell for mass spectrometric analysis of the gaseous flow. The ball-mill (vibrating type) is made of stainless steel. This material was chosen for non-reactivity with certain number of hydride compounds. The connection to the effusion cell is made using a flexible-tube then followed by a thin capillary-tube. The ball-mill is constituted from five distinct pieces (figure 6.4): a vial, air tight lid, plate holder, hollow space for hot air circulation and ball.

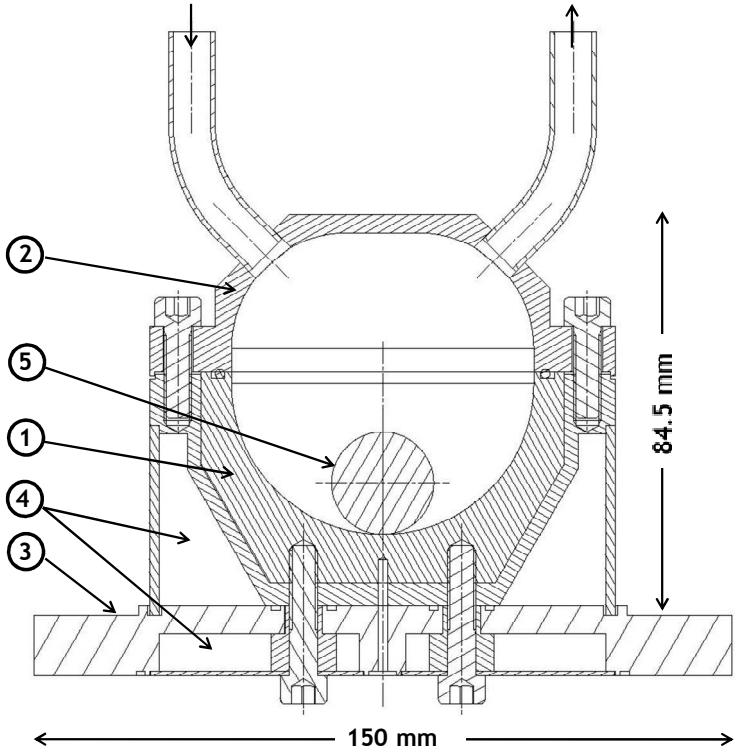

Figure 6.4. Cross section of ball-milling device. (1) vial; (2) airtight lid fitted with a "Viton®" gasket; (3) plate holder; (4) hollow space for hot air circulation; (5) ball of 20-30 mm diameter.

The inner shape of the vial has a quasi-ellipsoidal cavity wall. The shape allows the getting back of the ball at the right balance during milling. The inner diameter at the top of the vial is 64 mm with a height at middle of 35 mm. All the parts of the ball-mill are machined from standard stainless steel "304 L", except the main part of the vial has been built from stiffer stainless steel "630 AISI", heat treated at 1050℃ then re-heated at 480℃ for hardness increasing. The procedure was made and certified by a supplier who provides a hardness of

44 HRC (1472 MPa) compared to a standard stainless steel which is around 500 MPa. As for the other parts, the external part of the vial was made of stainless steel “304 L” without any treatment to ensure a good connection with the plate holder. The airtight lid is attached to the vial by screws. The tightness is ensured by a FPM O-ring (i.d. 2 mm, temperature range -20℃ to +204℃) placed in a groove. Two holes (i.d. 5 mm) were drilled in the lid and welded to stainless steel tubes. One of them will be used for pumping or gas flow inlet, while the second is the outlet for gaseous analysis. The vial is fixed to a cylindrical plate (15 x 150 mm) by four screws. A hollow space was machined in the plate for air heating system. A circular wall of 2 mm thickness encloses the vial for air heating with connection to the plate to allow homogeneous heating of the whole mill. The ball is made of a steel material. It has vertical movement range of 65 mm, which corresponds to the height from the bottom of the vial to the ceiling of the lid. Different ball sizes (20-30 mm diameter) were tested depending on the energy which would be transmitted to the material to be milled. A hole of 3 mm is drilled in the bottom wall of the mill for K-type thermocouple insertion; hence the temperature could be measured at 5 mm below the sample.

2.2 Gas inlet system

Gas inlet system supplies hydrogen and argon gases either in mixture or each alone. The gas flow can be adjusted in the desired proportions by a system of valves and mass flow controllers. The gas pipes are connected to a primary vacuum pump for evacuation either in the pipes system or in the milling-reactor as it’s illustrated in the synoptic schema of the pipes (Fig.6.5).

2.3 Connection tubing from the ball-mill to the effusion cell

The connection from the ball-mill to the effusion cell will be progressively made by flexible-tube of 1 m length (i.d. 1.5 mm) directly welded to the ball-mill aiming to the absorption of the vibrations during milling. The tube is followed by thin capillary-tube 1-3 m length (i.d. 0.15 mm) to ensure gradual decrease of the pressure from atmospheric pressure in the ball-mill to secondary vacuum in the effusion cell of the mass spectrometer. The connection between the two tubes is made by a Swagelok® screw connector. The capillary is inserted in a larger tube (o.d. 25 mm) after its coiling in spiral form before its connection to the cell by suitable nozzle.

3 Flow calculations in the input lines of the milling reactor

3.1 Gas flow theory

3.1.1 Flow regimes

When a gas flows inside a tube, there are 3 different configurations of flow regimes:

- The molecular regime
- The transition regime
- The viscous regime.

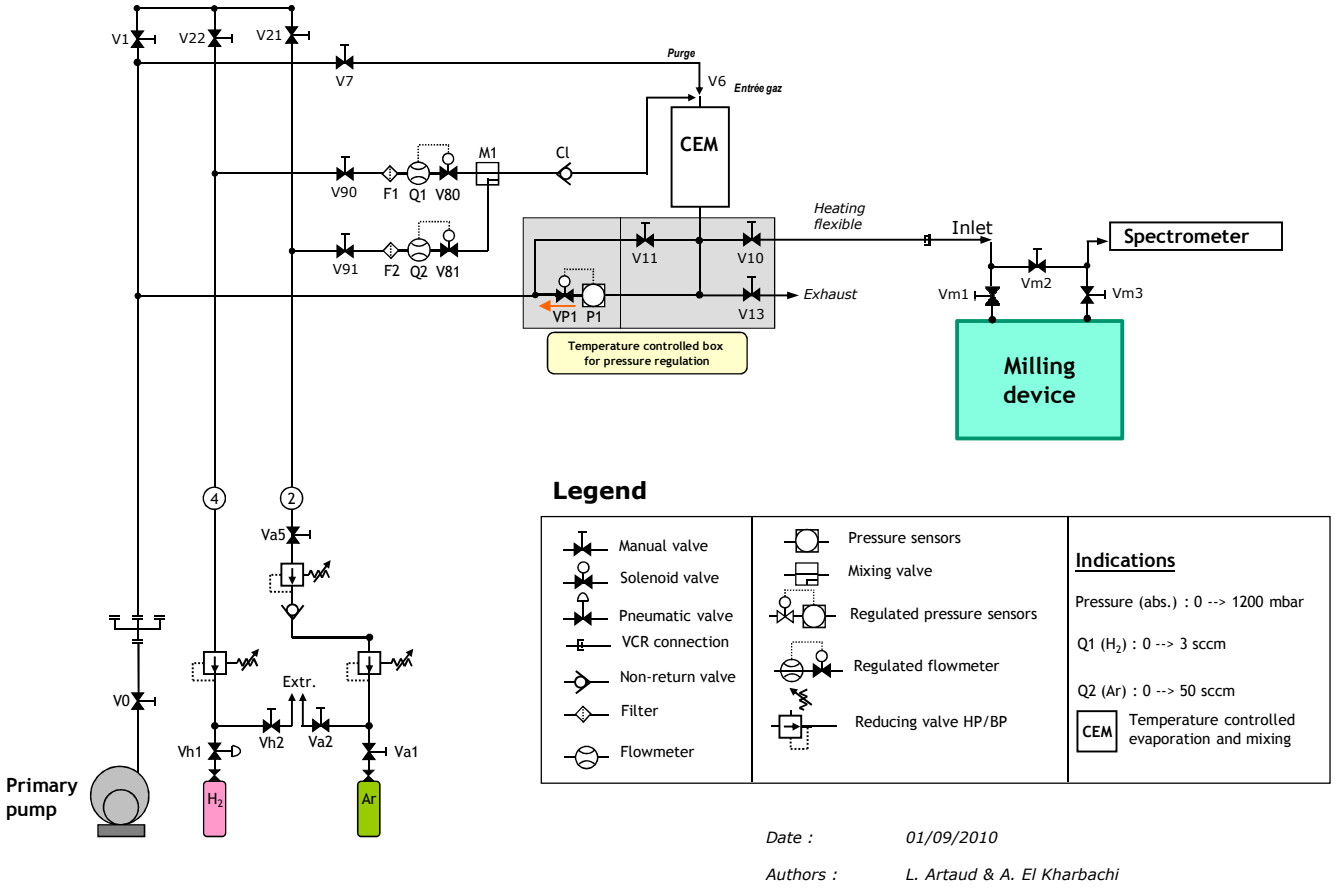

Figure 6.5. Synoptic of pipes for gas (H_2+Ar) supplying of the milling reactor

In the case of pressure gradient a cylindrical tube, the Knudsen number K_n, allows the determination of the gas flow regime through. It is given by the following formula:

$$K_n = \frac{d}{\lambda} \tag{6.3}$$

where d is the exit orifice diameter and λ is the mean free path of molecules in the gas, given by the expression:

$$\lambda = \frac{RT}{\pi\sqrt{2}N_A\sigma^2 p} \tag{6.4}$$

R is the ideal gas constant, p the pressure, T the temperature, N_A the Avogadro number and σ the *Van Der Waals* diameter of the considered molecule [6].

The various gas flow regimes in a tubing are thus defined according to the Knudsen number K_n:

- If $K_n \leq 3$, the flow is molecular, i.e. only the collisions with the walls are taken into account,
- If $K_n \geq 80$, the flow is viscous,
- If $3 \leq K_n \leq 80$, the flow corresponds to the transition regime (intermediate between molecular and viscous).

The viscous regime can be laminar or turbulent. The distinction between these two types of flows is done according to the Reynolds number (R_e):

$$R_e = \frac{4}{\pi}.\left(\frac{M}{\eta}\right).\left(\frac{Q}{d}\right) \tag{6.5}$$

where Q is the molar flow, M is the molar weight of the considered fluid, η its viscosity at the considered pressure and temperature T and d the diameter of the tubing.

- if $R_e \geq 2200$, the flow is turbulent ($Q \geq 1{,}73.10^3.\left(\frac{\eta}{M}\right).d$ in S.I. units)

- if $R_e \leq 1200$, the flow is laminar ($Q \leq 9{,}42.10^2.\left(\frac{\eta}{M}\right).d$ in S.I. units).

- **Viscous laminar regime**

In our case the choice of the pipes and orifices will be made so that the flow regime could not be turbulent. This feature is connected to the maximal flow which will depend on the size of the chosen capillary. According to Santeler [7], a pressure drop is stated in the presence of a system of pumping down to the vacuum - as in our case – and laminar viscous flow is the

predominant regime which can be fixed by the type of tubes and its orifices. He considers a static local pressure instead of a total pressure (Fig.6.6) for the evaluation of the gas behavior in systems with molecular and viscous flows. This enables him to avoid taking into account the mean velocity of the gas line in the pressure value and to consider that the pressure depends on the direction of the measurement related to that of the flow. Thus it allows to develop a series of simple equations for the calculation of the pressure drops in the systems with several compartments and through a large range of pressure from atmospheric pressure to ultrahigh vacuum [7].

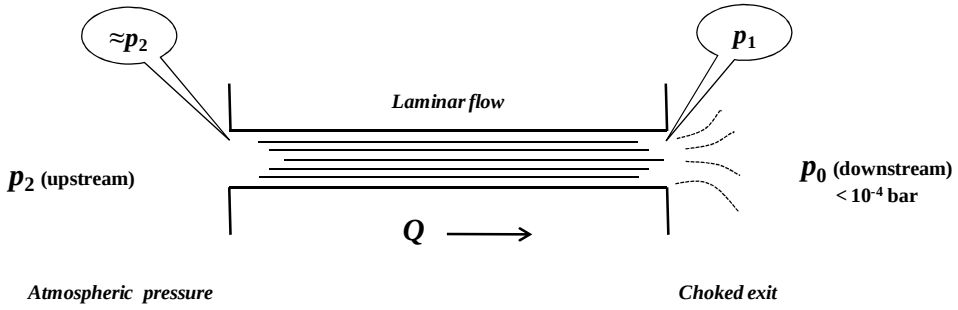

Figure 6.6. Macroscopic illustration of different regions of pressure through a tube with a chocked exit

If the length to the diameter ratio of the tube is sufficiently large, then the viscous-laminar flow is governed by the Hagen-Poiseuille law which is given by the following formula:

$$Q_{\text{vis}} = K_{\text{vis}}\left(p_2^2 - p_1^2\right) \tag{6.6}$$

where $K_{\text{vis}} = \dfrac{\pi a^4}{16\eta l R T}$

Q_{vis} is the molar viscous flow in mol.s^{-1}. l and a are respectively the length and the radius of the tube. η is the gas viscosity in poise.

Note that the Eq.6.6 is applied between the two pressures p_2 (ball-mill pressure) et p_1 (pressure at the capillary exit) corresponding at each ends of the tube and not between the two compartments p_2 and p_0 (effusion cell pressure). Thus, the Hagen-Poiseuille equation applies only for a tube, but not for its orifice.

- **Molecular regime**

In the case of a molecular effusion regime, where only the collisions with the walls are taken into account through an effusion orifice or a tube, the effused total flow (Q_{mol}) is obtained by

the Hertz-Knudsen relation [8] corrected by a factor known as the Clausing coefficient (Eq.6.7) which is the probability of transmission of the molecules through an orifice of specified form compared to an orifice ideally thin [9].

$$Q_{mol} = \frac{s.C.\Delta p}{\sqrt{2\pi MRT}} \tag{6.7}$$

where $s = \pi a^2$ is the section of the orifice, C is the Clausing coefficient and Δp the difference in pressure between the two sides of the orifice (the two compartments in this regime).

The Clausing coefficient was discussed by Santeler et al.[10] and confronted with more recent work of Cole [11]. By comparing the various published coefficients and their resulting errors (up to 12% for l/d = 2), we proposed to use the relation where the maximum error is only 0.6%:

$$C = \frac{1}{1 + \frac{3l'}{8a}} \tag{6.8}$$

where $l' = l\left(1 + \frac{1}{3 + \frac{3l}{7a}}\right)$ is the equivalent length which depends on l and a respectively the length and the radius of the orifice. Note that in Santeler's calculations the exit orifice of a tube is the only one which is considered.

- **Chocked flow for the laminar to molecular transition**

This sonic flow state has the role to restrain the passage from viscous laminar flow to molecular flow (i.e. between the capillary end orifice and the effusion cell i.e. lower pressure compartment) without loss of the operating vacuum. R.P. Henry [12] defines the conductance of an orifice in thin wall separating two tanks of pressures p_0 and p_1 ($p_0 < p_1$). He points out that gas flow through this orifice undergoes a contraction, then a succession of relaxations and compressions (shock waves). Afterwards, rearrangement of Wantzel-Zeuner formulas (Eq.6.9) and of the equation of the mass flow G of the gas (Eq.6.10), he proposes the formula (Eq. 6.11) of isentropic flow which travels through the orifice.

$$u_0^2 = \frac{2\gamma}{\gamma - 1}\frac{p_1}{\rho_1}\left(1 - \left(\frac{p_0}{p_1}\right)^{\frac{\gamma-1}{\gamma}}\right) \tag{6.9}$$

$$G = s u_0 \rho_0 \tag{6.10}$$

$$Q = s.p_1.\left(\frac{p_0}{p_1}\right)^{\frac{1}{\gamma}}\sqrt{\frac{2\gamma}{\gamma - 1}\frac{1}{RTM}\left(1 - \left(\frac{p_0}{p_1}\right)^{\frac{\gamma-1}{\gamma}}\right)} \tag{6.11}$$

where u_0 and ρ_0 being respectively the velocity and density of the gas at the pressure p_0.

$\gamma = \frac{C_p}{C_v}$ is the heat capacities ratio (5/3 = 1.67 for a monatomic gas and 7/5 = 1.4 for a diatomic or polyatomic gas) and Q is the flow in $\mathrm{mol.s^{-1}}$.

By considering the flow evolution when p_0/p_1 ratio decreases or pumping rate increases (Fig.6.7), a maximum is observed for a critical ratio:

$$\frac{p_0}{p_1} = \left(\frac{2}{\gamma + 1}\right)^{\frac{\gamma}{\gamma-1}} = r_c \tag{6.12}$$

The critical ratio r_c, defines the condition of sonic flow as the gas velocity at the exit is equal to the local velocity of the sound for the pressure p_1. In the sequence of pressure values going from the atmosphere (or more) to the vacuum in the system of introduction between the milling device and the spectrometer, it is important to correctly locate this phenomenon by an adequate geometry. Indeed the sonic regime has the following principal advantages:

• limit at least the maximal gas flow by only the diameter of the tube orifice

• ensure the proportionality between pressure and flow and thus to relate directly the flow value to that of the upstream pressure measurement

• obtain down to the orifice a molecular regime adapted to the effusion cell in a mass spectrometer.

The figure 6.7 represents the variation of the output flow of the gas as a function of the p_0/p_1 ratio through a tube. Flow is known as subsonic for pressure ratios close to unity which corresponds to an adiabatic pressure drop. For an optimal flow, the ratio r_c is known as sonic where the velocity of the particles is equal to the local velocity of the sound. Our computed values correspond well to the theoretical curve in the field of the supersonic flow attended for weak pressure ratios. In equation 6.11, the flow reduction is due to a fast reduction in the density compared to a slow increase in velocity [7]. According to the type of the sampling

system, the gas velocity through the exit orifice of the capillary towards the downstream vessel (the effusion cell) could not exceed a limiting threshold that corresponds to sonic regime. If the pressure p_0 decreases under this critical ratio, relation (6.11) is no more applicable (part in dotted lines in figure 6.6) because the only force able to push the molecules out of the orifice is then that contained in the gas, and the maximal flow corresponds at the own molecules velocity (cf. Kinetic theory of the gases) to escape the exit plan of the orifice toward the ideal vacuum (no molecule of the compartment of pressure p_0 comes back to shock the molecules leaving the orifice). For all values $p_0/p_1 < r_c$, the flow according to the Eq. (6.11) has a maximum and constant flow, called critical flow which corresponds to the shocked flow, such as:

$$Q_{\text{critical}} = p_1.C_{\text{choc}} \tag{6.13}$$

By considering the total pressures, if the difference in pressure between p_0 et p_1 is important, the molecules are ejected as “shocked” at the exit of the tube for a ratio p_0/p_1 < 0.53. According to the geometry of the orifice at the exit, made up of a cylindrical tube emerging freely in a rather large volume, this pressure ratio corresponds to a threshold limit after which a pressure decrease p_0 will not affect any more the value of the exit flow [13,14].

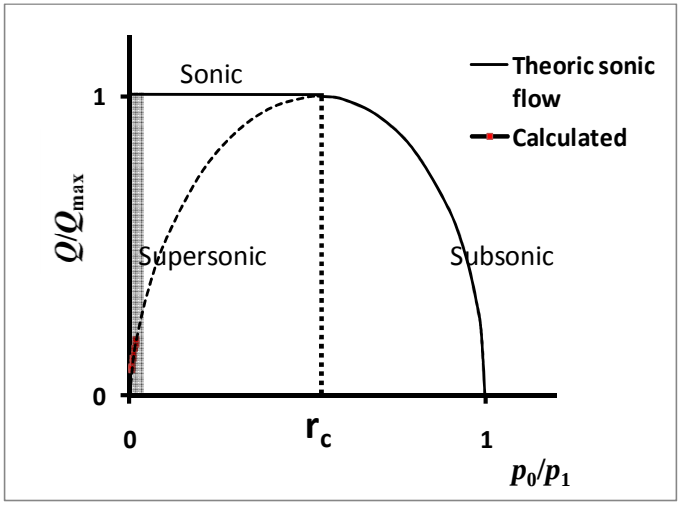

Figure 6.7. Flow – pressure ratio diagram (sonic flow)

The expression of the conductance C_{choc} can be simplified to:

$$C_{\text{choc}} = s.\sqrt{\gamma.\left(\frac{2}{\gamma+1}\right)^{\frac{\gamma+1}{\gamma-1}}.\frac{1}{RTM}} \tag{6.14}$$

C_{choc} depends only on the molecule type (its molar mass and monoatomic or polyatomic nature) and on the temperature. The flow $Q_{critical}$ at the orifice remains proportional to the pressure p_1 before its exit. It is the principle of proportionality which is used in the flow controllers in general. Note that for this shocked flow no molecules can come backwards in the tube.

The expression of the critical flow ($Q_{critical}$) in the orifice, imposed by the shock effect of the gas particles could be reduced to the Eq.6.15 by eliminating the pressure p_1 in relation (6.6) by substitution from the Eq.6.13. This formula was also included in the work of Santeler [7] for a tube with a shocked exit by considering the total pressure:

$$Q_{critical} = \frac{C_{choc}^2}{2K_{vis}}\left[\sqrt{1+\left(\frac{2K_{vis}\,p_2}{C_{choc}}\right)^2}-1\right] \tag{6.15}$$

- **Transition regime**

The transition regime is an intermediate regime between molecular and viscous-laminar and which corresponds to a Knudsen number between 80 and 3. For a compressible flow DeMuth et al.[15] developed a model which combines the expressions of the two flows, molecular (Q_{mol}) and viscous(Q_{vis}). They use the Knudsen number (K_n) to combine these flows, in particular for values between 2 and 45 according to the expression:

$$Q_{trans} = Q_{vis}\left(1-Ca^{-Kn}\right)+Q_{mol}Ca^{-Kn} \tag{6.16}$$

The experimental constant of DeMuth *Ca*= 1.05, represents the inverse of the probability that a molecule after collision with another molecule will not be hit against the walls of the orifice. The use of the Knudsen number in this relation has a physical significance where the molecular percentage of flow represents the number of molecules able to go upward the tube after collisions (molecular regime) on the walls. The remaining percentage is the contribution of viscous flow. This model considers an asymptotic regression of the molecular regime towards an isentropic regime, generally viscous-laminar, where the pressure ratio is maintained constant.

3.2 Computing the different flow modes

In order to quantify the flows in the whole device, from the mill to the mass spectrometer. Calculations were carried out using Visual Basic programming language in Excel software. All the units are in S.I. unit and flows Q are in molar flow ($\mathrm{mol.s^{-1}}$).

The viscosity of dihydrogene was obtained starting from a polynomial regression of $\eta = \mathrm{F}\ (T)$ obtained from the data of the CRC [18]:

$$\eta_{\mathrm{H_2}} = -1.0893 \cdot 10^{-11} \times T^2 + 2.7796 \cdot 10^{-8} \times T + 1.59 \cdot 10^{-6} \tag{6.17}$$

Note, the shock constant C_{choc} (Eq.6.14) depends on the nature of gas by its mass. The shock constant will be calculated for each type of gas. The shock becomes limiting when the ratio satisfies $p_0/p_1 < r_c$. We will be in this case when the pressure p_0 (effusion cell) will be always much lower than p_1.

Due to the complexity of the flow calculation, Santeler [7] proposed a practical method to solve systems with multielements inter-connected between them. He supposed that each tube and its exit are calculated as two different elements which allows to define a flow regime at each stage. For example the tube could work in laminar flow and its exit in “shocked” regime if the downward pressure corresponds to the molecular vacuum that is the case for our capillary connected to the effusion cell.

The strategy of calculation consists in choosing a section of the system with an imposed pressure at the entry. The flow will be calculated starting from the pipes dimensions. Then each section will be solved by iteration in order to obtain the pressure at the entry of the following section. A simplified schema is given in figure 6.8 illustrating the reasoning lines.

In the suggested system, three principal flows will be distinguished: the viscous flow in the capillary Q_{vis}, the pumping flow Q_{pump} that is connected to the effusion cell and the effusion flow Q_{eff} (towards the spectrometer). At the effusion cell level, the flows are described by the flow steady-state condition:

$$Q_{eff} = Q_{vis} - Q_{pump} \tag{6.18}$$

The computational resolution is based on the sign change of the relation $Q_{\mathrm{pump}} - Q_{\mathrm{vis}} + Q_{\mathrm{eff}}$.

Because the choice of primary pump is imposed by the offer of different suppliers, this condition must be the beginning of iteration calculation first without taking into account the effusion flow. For that we have proceeded by section approach as discussed above.

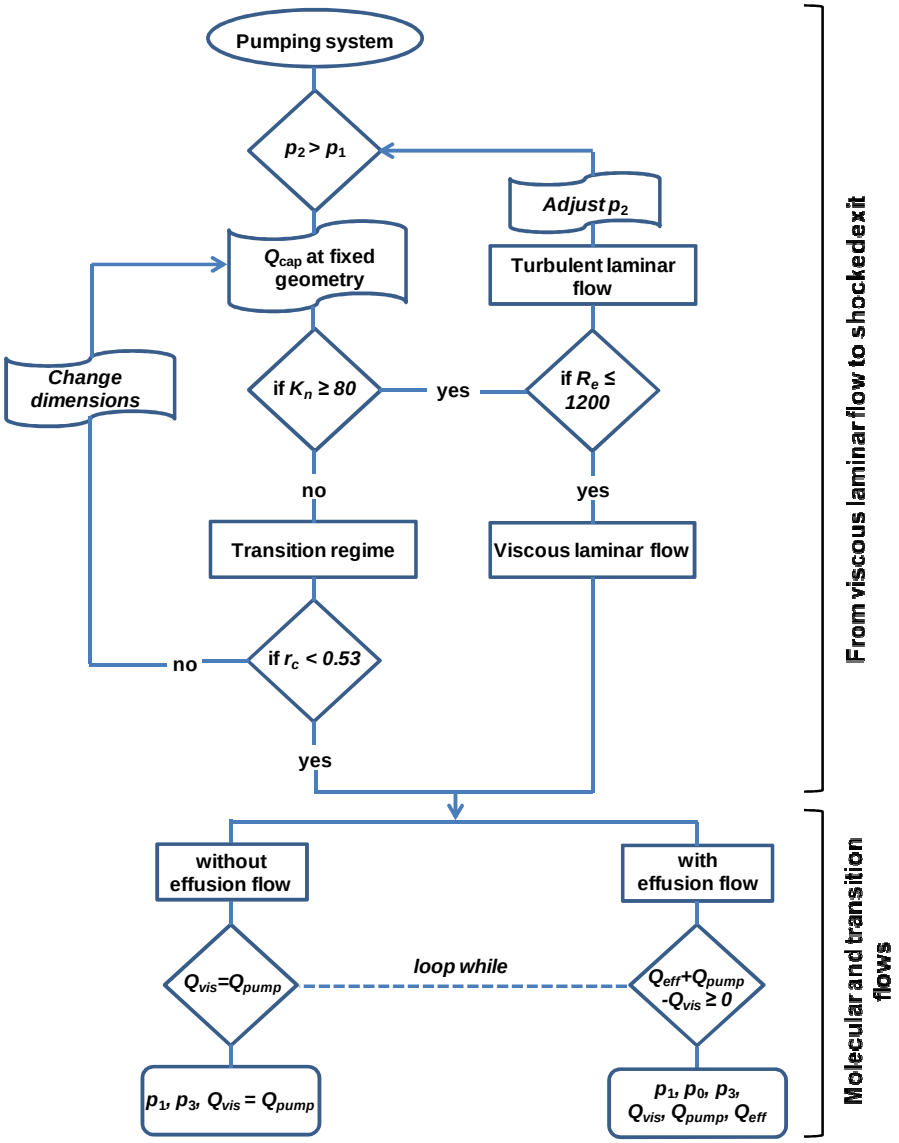

Figure 6.8. Simplified algorithm used for the solving of the flow equations

3.2.1 Connection between the ball-mill and the capillary

The pressure in the mill which will be measured using a pressure gauge, is the total pressure p_2 at the capillary entrance. Two flows are in series: viscous-laminar flow in the tube and shocked flow at the exit, both being connected by p_1 (Fig.6.6) which will be the parameter of calculation in order to equalize the two flows.

Knowing that the pressure p_1 should be lower than p_2 (and higher than p_0 which is very small), we define $p_1 = p_2$ / step, where the step in the interval [p_2 ; p_0] is such as: step = (p_2 - p_0) / 10. In the program, a loop determines the value of p_1 using the flow equations in particular the

relation of Hagen-Poiseuille (Eq.6.6) and the shocked flow formula (Eq.6.15). By solving the following flows equality:

$$Q_{\text{vis}} - Q_{\text{critical}} = \text{f}(p_1) = 0 \tag{6.19}$$

We deduce a direct expression for the calculation of p_1 which depends only on the pressure p_2 for a given gas species and temperature:

$$p_1 = \frac{C_{\text{choc}}}{2K_{\text{vis}}}\left[\sqrt{1+\left(\frac{2K_{\text{vis}}\,p_2}{C_{\text{choc}}}\right)^2} - 1\right] \tag{6.20}$$

The mill and the capillary are not linked in a direct way but by an intermediate tube which will be used as vibrations absorber of the movements of the mill. This quite large (i.d. 1.5 mm; length 1 m) tubing has been checked to have no effect on the calculations results (negligible pressure gradient).

The first calculated results (Table 6.1) show that in our case, the flow in the capillary will be always higher than the maximum effusion flow ($2.43\cdot10^{-6}$ mol.s^{-1} obtained for an effusion maximum pressure of 10^{-4} bar) as soon as the upward pressure exceeds 2 bar. But assuming the optimal conditions for measurements with the effusion cell, p_0 will lie between 10^{-5} and 10^{-6} bar. The effusion flow will then not exceed $2.43\cdot10^{-7}$ mol.s^{-1}. In this case, the upward pressure in the mill should not be lower than 400 mbar so that the condition of shocked flow could be maintained. Connecting a pump to the effusion cell is necessary for the evacuation of the excess flow arriving from the capillary when the upstream pressure is larger than 400 mbar. The above result seems to be less satisfying when the upstream pressure is lower than 250 mbar, because the flow regime in the capillary moves from viscous to transition and the residence time becomes higher. This feature can distort our mass spectrometric analysis of the vapor phase when containing reactive species because interactions with the capillary can take place. On one hand, this is due to the affinities of the constituents of the vapor phase with respect to the capillary. Moreover certain molecules can have very short life times as it is the case for the boron hydrides $\text{B}_\text{n}\text{H}_\text{m}$. The problem can be avoided while working with upstream pressures higher than the mentioned thresholds. At this stage, it is necessary to pump the excess flow introduced in the effusion cell by an additional primary pump.

Table 6.1. Flow calculation in the section: mill – effusion cell

p_2 (mbar)	p_1 (mbar)	Q_{cap}(mol.s^{-1})	D (Sccm)	$t_{residence}$ (s)	Kn_{cap}
10000	113,2	5,162.10^{-5}	10,89	0,10	3322,6
7943	71,40	3,257.10^{-5}	8,65	0,12	2633,2
5012	28,43	1,297.10^{-5}	5,46	0,19	1656,0
3981	17,94	8,182.10^{-6}	4,34	0,24	1313,9
2512	7,141	3,257.10^{-6}	2,74	0,39	827,6
1995	4,506	2,055.10^{-6}	2,17	0,49	657,0
1585	2,843	1,297.10^{-6}	1,73	0,61	521,6
1259	1,794	8,182.10^{-7}	1,37	0,77	414,2
1000	1,132	5,163.10^{-7}	1,09	0,97	328,9
794	0,714	3,257.10^{-7}	0,87	1,23	261,2
631	0,450	2,055.10^{-7}	0,69	1,54	207,4
501	0,284	1,297.10^{-7}	0,55	1,94	164,8
398	0,179	8,182.10^{-8}	0,43	2,44	130,9
316	0,113	5,163.10^{-8}	0,34	3,08	103,9
251	0,071	3,257.10^{-8}	0,27	3,87	82,6
200	0,045	2,055.10^{-8}	0,22	4,88	65,6
100	0,011	5,163.10^{-9}	0,11	9,73	32,9

3.2.2 Pumping system in the effusion cell

In order to choose the suitable characteristics of the primary pump the first approach is to look for the pumping of the total flow resulting from the capillary without taking into account the effusion flow. Thus the flow entering the effusion cell - depending only on the capillary upstream pressure p_2 - must be entirely evacuated by the primary pump connected to the effusion cell. The pressure p_3 at the pump entry and the effusion cell pressure p_0 (Fig.6.2) will depend on the capacity of the pump (volumic flow as expressed according to p_3).
From the pump data provided by the manufacturer (Alcatel 2015 SD), a fit was performed giving the volume flow versus the inward pressure of the pump (Fig.6.9): D / m^3.h^{-1} = f (p_3 / Pa).

Three areas are fitted as follows for which the maximum deviation is 12% from the pump flow characteristics:

$$\begin{aligned} &if \quad p_3 > 1 \qquad\qquad ; \; D = 1.4191 \times log(p_3) + 6.3424 \\ &if \quad p_3 \le (1.7838/7.027) ; \; D = 0 \\ &else \qquad\qquad\quad ; \; D = 7.027 \times p_3 - 1.7838 \end{aligned} \tag{6.21}$$

The re-constructed curve (recalculated points) represents the real values considered in the calculation. Deviations are due partly to the errors in the transformation of the curve provided by the manufacturer into a system of equations (Eq.6.21) and partially to the iteration solving.

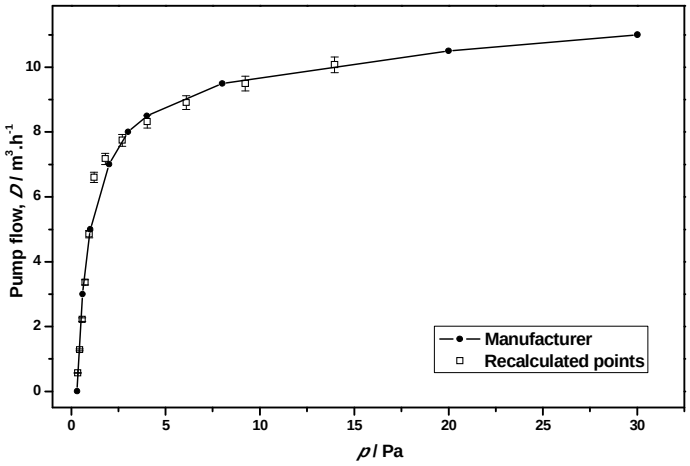

Figure 6.9. Original data characteristic of the pump 2015 SD according to Alcatel graph and our fitted values of the pumping flow

A scanning of the pressure p_3 (from 10^2 to 10^{-2} Pa with a step in power of -0.001) allows to determine the flow D or flow Q_{pump} (Eq.6.21 and 6.22) and the steady state pressure p_0 in the effusion cell (Eq.6.23). The conductance between the effusion cell and the pump depends on the fixed geometry and on the p_3 value. The calculation is performed for molecular and transition regimes. In the last case the problem is solved by iteration using the formula developed by DeMuth (Eq.6.16). The flow regime in the effusion cell–pump entry section is at each time determined by the Knudsen number K_{n}.

$$Q_{\text{pump}} = D \cdot p_3 / (3600RT) \tag{6.22}$$

$$p_0 = p_3 + \frac{Q_{\text{pump}}}{C_{\text{cell}}} \tag{6.23}$$

C_{cell} is the cell conductance related to its pumping tube deduced starting from the Eq.6.7 for a molecular regime, such as:

$$C_{\text{cell}} = \frac{sC}{\sqrt{2\pi MRT}} \tag{6.24}$$

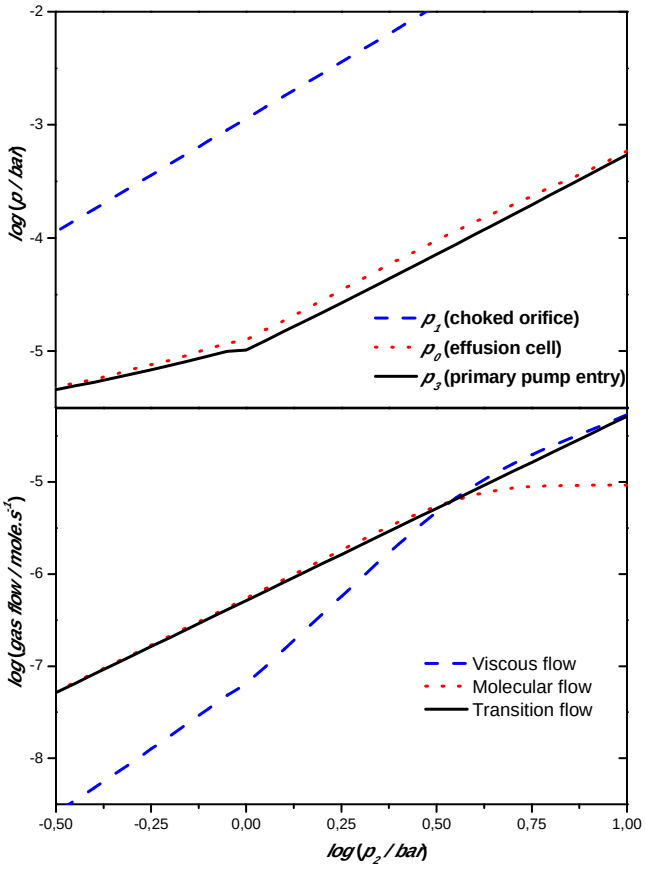

Figure 6.10. Gas flow regimes in the effusion cell pumping line and the various pressures in the effusion cell, at the pump entry as a function of the upstream pressure p_2 at the capillary entrance (without taking into account on the effusion flow in the flow balance)

Now it remains to find the suitable p_3 (and the corresponding pressure p_0) which corresponds to the capillary flow for an imposed p_2. To calculate the steady-state pressures p_3 (pump entry) and p_0 (effusion cell) as a function of the upward constant pressure p_2, we solved for each value of a variable pressure p_3 the equality of flows between the capillary and the pump entry (loop with precision criterion). Various pressures p_2 will be considered in a second loop. The results are presented in the figure 6.10.

In figure 6.10, the flow resulting from the capillary is directly evacuated by the primary pump. The indicated molecular and viscous flows parts are deduced from transition flow calculation. For a pressure upstream of 1.6 bar, the Knudsen number in the cell takes the value 2.8, corresponding to the beginning of the change of the flow regime (molecular to transition). The flow curve obtained is in agreement with the model suggested by DeMuth, i.e. a quasi-asymptotic transition flow to molecular and viscous regimes.

In the present case, the acceptable maximal upstream pressure p_2 is approximately 3 bars, and is limited by the maximum pressure allowed in the effusion cell. This limit is directly de-

pendent on the choice of the primary pump and its connection line to the cell. The pressure p_1 remains 10 times higher than the pressure p_0, and the exit of the capillary remains chocked.

By comparing the two pressures p_0 and p_3, the difference between these two pressures reflects an adaptable functioning of the additional pump upon the pressure p_2. Note, the slope changing is due to the pumping mode (Fig.6.9): from quasi-linear mode to logarithmic mode. At this point, it was also observed the most important relative error.

In this part, we have considered a line of direct flow (from the capillary to the pump evacuation) without taking into account the effusion flow towards the mass spectrometer. Doing so it enables us to choose the capacity of the primary pump for low and high upstream pressures (p_2 from 100 mbar to 10 bar). At high pressure, we noted that its role is to evacuate the main part of the flow. Note that the flow in the capillary becomes of transition type below an upstream pressure equal to 250 mbar. For the next section where the effusion flow is introduced in the set of equations, the pressure range of p_2 will be varied between 3000 and 250 mbar.

3.2.3 Flow balance in the effusion cell

The real working of the entire flow-lines must take account of all flows: capillary, effusion cell and pump. The evaluation of the optimal pressure p_3 and the pressure p_0 (effusion cell) will be made starting from the steady state of the flow i.e. the relation: $Q_{\mathrm{eff}} = Q_{\mathrm{vis}} - Q_{\mathrm{pump}}$. The test was carried out using various loops to determine the pressure p_3 corresponding to each value of p_2, and based on the inequality: $Q_{\mathrm{pump}} + Q_{\mathrm{eff}} - Q_{\mathrm{vis}} \geq 0$, which means that the pump must evacuate at least the excess flow injected by the capillary to the effusion cell. It is also a condition to avoid condensation phenomena on the walls of the cell in particular water vapor.

Moreover, for taking into account the transition flow which can occur indeed at the level of the connection tube between the cell and the pump entry, the equation of the transition regime is used. The calculation of the pressure p_0 cannot be done any more simply as in the preceding part because the relation between these two pressures is more complex. Initially we calculated for each imposed pressure p_3 two values $p_0\mathrm{min}$ and $p_0\mathrm{max}$ respectively from the only molecular flow and the only viscous flow equations. Varying p_0 between these two limits we find the exact flow at the pump entry. Thus Q_{trans} (transition flow) is used to compute the flow in the tube section between the effusion cell and the pump.

The results showed that the molecular flow regime entered into the transition flow regime in the pumping line for an upstream pressure p_2 above 2 bar (Fig.6.11). Conversely, below 350 mbar, the pumped flow becomes very weak.

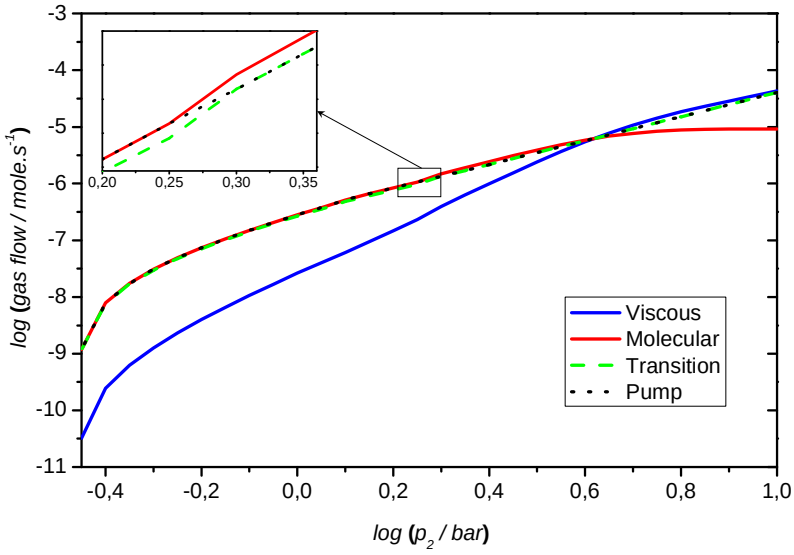

Figure 6.11. Variation of the flow regimes in the line effusion cell-pump as a function of the pressure p_2.

The intersection of flows represents equal contributions of viscous and molecular flows in the transition flow equation at the Knudsen number equal 14. At the pressure p_2 equal 1.9 bar, we observe the beginning of the transition flow. Below this pressure, a slight deviation is observed between the transition flow and the real pump flow. This is probably due to the application of the DeMuth model for Knudsen numbers between 3 to 80 (as cited in the literature) instead of 2 to 45 in the case of the DeMuth model determinations.

As the contributions of these two flows are always appearing in the transition flow relation, the transition flow relation can be applied in the full pressure range.

4 Results and discussion

4.1 Choice of the capillary tubing

The programmed software provides a set of rough data that we have used in this paragraph to build the experimental device. In the case of hydrogen gas, we note that an increase of the capillary length (from 1 to 3 m) makes it possible to work with low pressures p_0 in the effusion cell and high upstream pressures p_2 up to 4 bar. For the diameter of the capillary, calculation shows that as small as possible diameter is needed. The commercially distributed capillary 0.15 mm inner diameter fulfils satisfactorily the requirements fixed for our system of introduc-

tion. In our case, the input pressure p_2 could vary from 0.1 to 2.5 bar for ideal working conditions of both the milling device and the spectrometric measurement.

The capillary flow, in the case of N_2 gas, is equal to 3 Sccm for an upstream pressure of 2.5 bar with vacuum downstream. By using air, the manufacturer had given an indicative value 2 to 3 Sccm for 1 bar upstream and vacuum downstream. In the case of H_2, this same volumic flow is already reached with an upstream pressure of approximately 1 bar. The apparent "fluidity" of H_2 is due to its low viscosity compared to N_2 which suggests working with low upstream pressures in our experiments where the main gas will be H_2. In the followings the presented results are for the case of hydrogen gas.

For an adiabatic flow at the capillary orifice exit, the gas escape velocity is limited by the local sound velocity. At this stage, the pressures p_1/p_0 ratio should be maintain lower than the critical ratio (r_c) in order to avoid the transition regime and adiabatic expansion. Besides, the shocked exit for the gas can be established only if the pressure p_1 is in the viscous regime as attested by the Knudsen number.

Figure 6.12(a) shows the flow regime along the capillary represented by the variation of the Knudsen number in the capillary before the chocked exit for various upstream pressures. For the last millimeters before the capillary exit, the gas undergoes a very fast expansion which could affect the isentropic viscous regime at the exit. This regime change becomes more marked below 0.5 bar. This is in agreement with our estimations of the chocked exit based on the calculation of the critical ratio.

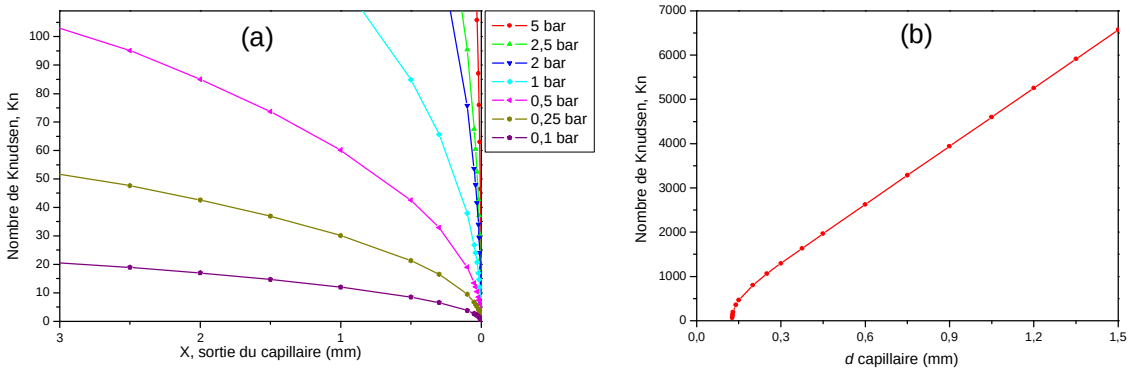

Figure 6.12. Variation of the Knudsen number upon: (a) the pressure along the capillary, (b) the diameter of the capillary for an upstream pressure of 1 bar

A capillary of small size is more convenient for this study in order to avoid a viscous flow of turbulent type. Although the flow regime in the capillary is in general viscous-laminar, where the pressure p_2 is lower than 250 mbar, the transition regime occurs at the exit, corresponding to a pressure p_1 equal to 0.07 mbar.

This limit will be that of the lowest pressure p_1 corresponding to the validity of our calculations. This pressure p_1 low limit, will give lowest p_2 limit. Below this pressure limit, the capillary is working, but measurements will not be related to calculation. According to these calculations, it appears that even for low upstream pressures the effusion flow is always negligible compared to the flow issued from the capillary for an upstream pressure lower than 400 mbar. Below this value near 320 mbar, the pump reaches its pumping limits because the pumping flow tends to zero value. At that time the pump may feed the effusion cell with backwards flows.

We confirm our assumption that the set up of an additional pump is essential in addition to the effusion flow. The pressure in the effusion cell, measurable by the mass spectrometer, will depend on the flow steady state. To be able to regulate this pressure for better optimizing the measurement conditions (increase the Knudsen cell pressure up to ≈ 10^{-5} bar) it is necessary to associate a valve with adjustable conductance to the pumping line.

4.2 Flows control in an effusion cell with a pumping system

The figure 6.13 presents the variation of the logarithm of the different pressures as a function of the upstream pressure p_2. It highlights the variation of the difference between the two pressures p_0 and p_3 in particular for values of upstream pressures increasingly high. The same situation was observed in the case of a device without effusion flow (Fig.6.10). This fact is due to the increase of the pumped flow due to the increase of the pressure gradient (Table 6.2) between the effusion cell and the primary pump.

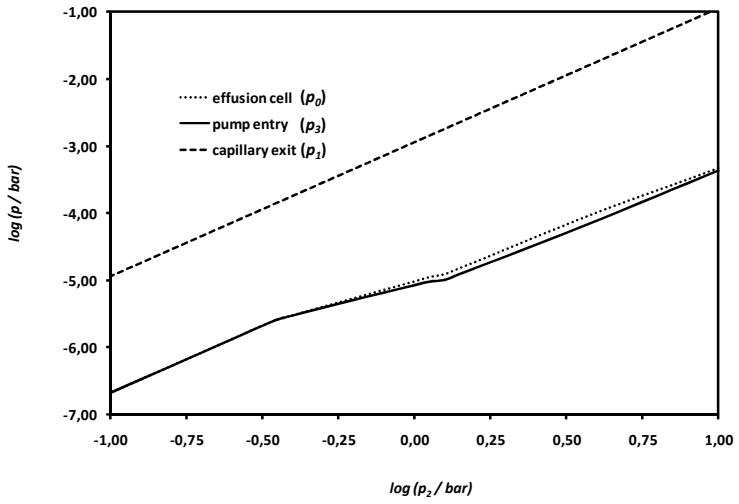

Figure 6.13. Variation of the different pressures as a function of the upstream pressure p_2

Table 6.2. Pressure gradient between the cell and the pump

p_2 (upstream)/ bar	p_0 (cell)/ bar	p_3 (pump)/ bar	Δp / bar
10,00	$4{,}74\ 10^{-4}$	$4{,}34\ 10^{-4}$	$3{,}97\ 10^{-5}$
8,91	$3{,}90\ 10^{-4}$	$3{,}51\ 10^{-4}$	$3{,}97\ 10^{-5}$
7,08	$2{,}67\ 10^{-4}$	$2{,}28\ 10^{-4}$	$3{,}91\ 10^{-5}$
5,62	$1{,}84\ 10^{-4}$	$1{,}48\ 10^{-4}$	$3{,}61\ 10^{-5}$
5,01	$1{,}52\ 10^{-4}$	$1{,}19\ 10^{-4}$	$3{,}31\ 10^{-5}$
3,98	$1{,}03\ 10^{-4}$	$7{,}77\ 10^{-5}$	$2{,}51\ 10^{-5}$
3,16	$6{,}81\ 10^{-5}$	$5{,}13\ 10^{-5}$	$1{,}69\ 10^{-5}$
2,51	$4{,}46\ 10^{-5}$	$3{,}41\ 10^{-5}$	$1{,}05\ 10^{-5}$
2,00	$2{,}91\ 10^{-5}$	$2{,}27\ 10^{-5}$	$6{,}40\ 10^{-6}$
1,58	$1{,}89\ 10^{-5}$	$1{,}53\ 10^{-5}$	$3{,}61\ 10^{-6}$
1,00	$9{,}70\ 10^{-6}$	$8{,}49\ 10^{-6}$	$1{,}21\ 10^{-6}$
0,71	$6{,}28\ 10^{-6}$	$5{,}82\ 10^{-6}$	$4{,}57\ 10^{-7}$
0,50	$4{,}07\ 10^{-6}$	$3{,}94\ 10^{-6}$	$1{,}32\ 10^{-7}$
0,40	$3{,}04\ 10^{-6}$	$3{,}01\ 10^{-6}$	$3{,}39\ 10^{-8}$

This graph confirms also that the pressure ratio p_0/p_1 is very small in the overall range of the upstream pressures planned for our study (0.1-10 bar). This feature is in agreement with the required conditions of chocked flow at the capillary exit. Consequently, the molecular flow criterion in the effusion cell is warranted.

As the gas flow in the molecular regime is characterized by independent flows of opposite directions [10], the partial pressures could be influenced by the presence of sources of gas in various places of the gas line. Consequently, the pump can have selective pumping effects for certain gases. To minimize these effects of back flow which could contain impurities, the use of a trap with liquid nitrogen before the primary pump will allow to improve the vacuum and to avoid any non desired condensations in the effusion cell, coming from the pump.

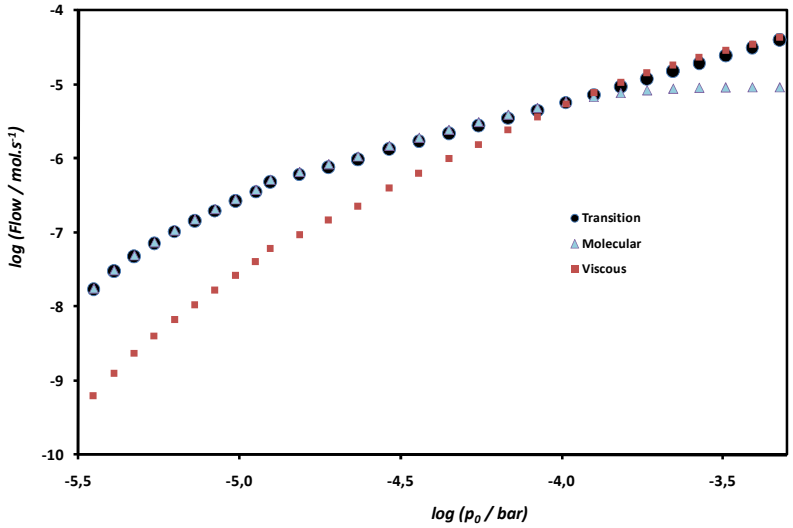

Figure 6.14. Variation of the transition flow and its viscous and molecular components between the effusion cell and pump entry according to the upstream pressure p_0 in the effusion cell.

Comparing the various existing regimes as a function of the pressure in the pumping line between the effusion cell and the pump (Fig.6.14) using the transition flow formula, we observe that the flow enters in the transition regime just before the pressure approaches the limit of operation of the effusion cell (≈ 10^{-4} bar).

By analysing the obtained values of flow, we note that the contribution of viscous flow in the pumping tube becomes negligible for upstream pressures p_2 lower than 1 bar which involves a pressure p_0 of about 10^{-5} bar.

The figure 6.15 shows the distribution of various flows in the “effusion cell” compartment upon the upstream pressure p_2 as well as the flow evacuated by the pump. It is to be noted that for upstream pressures lower than 0.4 bar the evacuated flow by the pump becomes negligible. The pump reaches its pumping capacity limit at the corresponding pressure limit.

At very low upstream pressures, flow resulting from the capillary is completely evacuated by the effusive flow. For these conditions we will maintain the valve of the pump close to avoid contaminations by any backward flow from the pump.

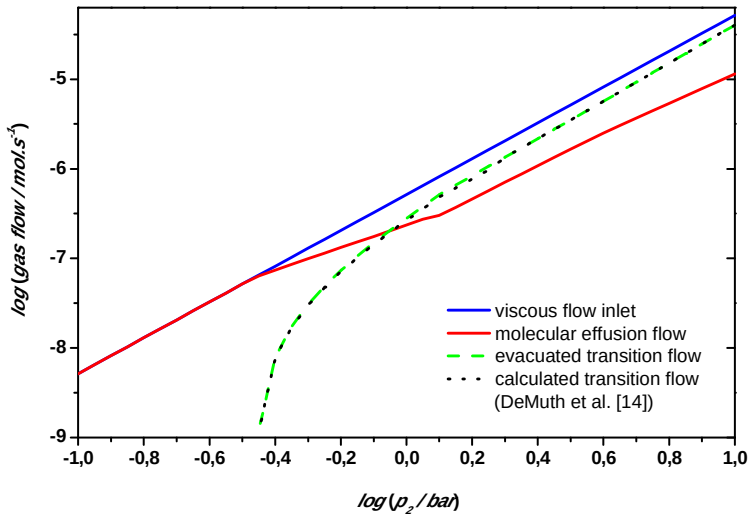

Figure 6.15. Relationship between different flows

Taking into account the transition flow equation in the pumping line section, brings a significant correction to the pump pressure and consequently to the effusion cell flow in particular for upstream pressures higher than 2 bar.

The transition regime occurs also at the capillary exit (the few last centimeters) for upstream pressures p_2 lower than 0.5 bar: the calculation of the Knudsen number for various upstream pressures and according to the distance along the capillary, shows that the transition flow could not be avoided. The chocked flow at the exit of the capillary remains, however, available because the viscous contribution is important and the ratio p_0/p_1 is very small. The transition flow becomes more pronounced for low upstream pressures. A molecular flow is also established in the capillary (near the exit) for upstream pressures lower than 100 mbar. The higher limit of the pressure p_2 is approximately 4 bar, which corresponds to a pressure p_0 near of the threshold pressure in the effusion cell when pumping. For ideal working conditions based on transition flow between the cell and the pump entry, we suggest to work at upstream pressures lower than 2.5 bar.

5 Construction of the reactor to be coupled to mass spectrometer

As the effusion cell assembly is expected to contain only gaseous species issued from the capillary tube, therefore its conception was simplified and consisted on a cylindrical chamber (h=68 mm, d=30 mm) with a screwed lid fitted with an orifice (i.d. 2 mm). The cell device is made in two parts: the main effusion cell and its pumping system (Fig.6.16). It will be also useful to measure the total pressure in the effusion cell in order to regulate the flow and cali-

brate the mass spectrometer. The upstream pressure of the capillary will be fixed using a flow controller with variable pressures in the range 0.1 - 2.5 bar.

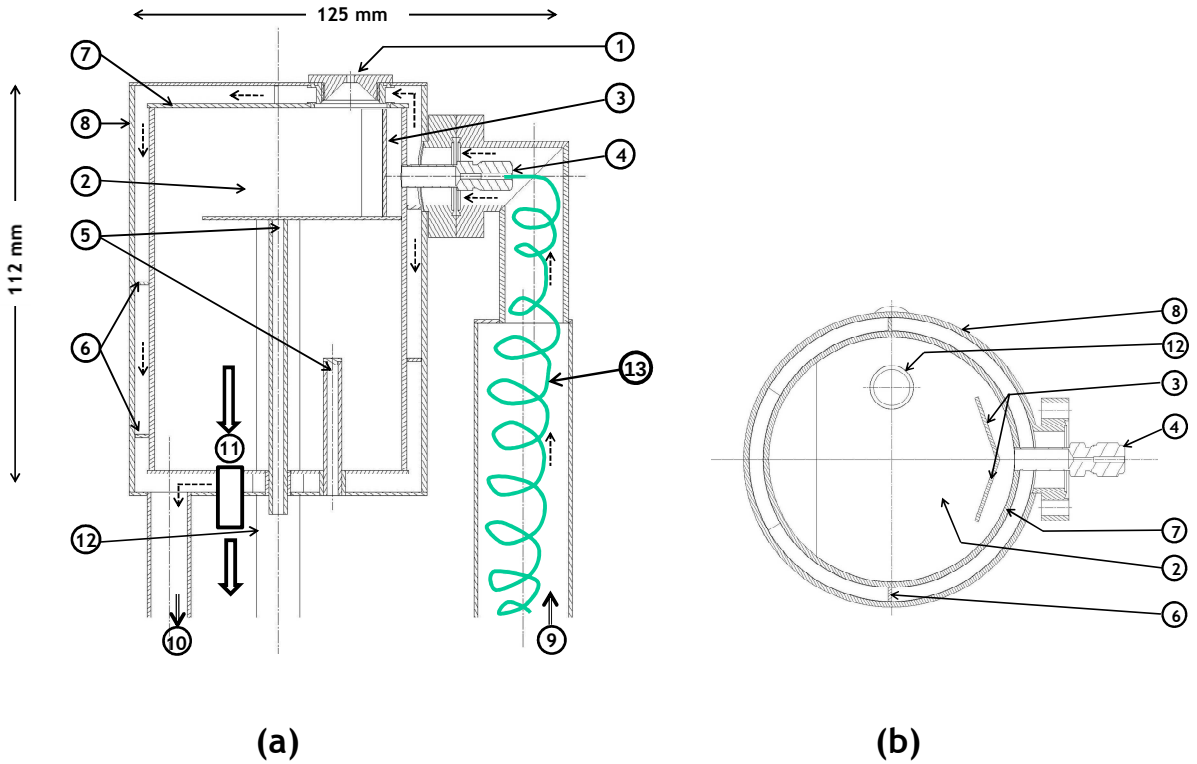

Figure 6.16. Schema of the effusion reactor-cell for hydrides: (a) Cross section; (b) Cross section of the top view. (1) effusion orifice; (2) cell compartment; (3) two reflector walls; (4) nut for capillary connection; (5) two tubings for K-type thermocouples; (6) baffles; (7) cell walls; (8) hot air envelope; (9)hot air entry; (10) hot air exit; (11) toward pumping system; (12) tube for pressure gauge (13) capillary tubing.

As determined in the flow calculation part, the excess flow is evacuated by the additional pump while only small amounts of the flow effuse toward the ionization chamber for its analysis by the mass spectrometer. The arriving flow from the capillary with chocked exit is deflected by two walls for allowing a scattered distribution of the flow across the cell compartment (Fig.6.16b). The evacuation exit of the cell has the same surface section as for the pumping tube (Ø 25 mm). The measurement of the temperature is performed directly in the cell at two levels by means of two K-type thermocouple through two tubings, while the pressure measurement in the cell is made by a “Baratron” capacitance gauge through a long tube (10 mm i.d.).

The cell is surrounded by an envelope for air heating circulation to obtain isothermal conditions (Fig.6.16a). Baffles were welded alternatively in the air heating compartment to allow the transmission of heat by convection. All parts of the cell made of stainless steel, are

welded and tested for air leaks. The cell is mounted on a vacuum flange for its set up to the spectrometer housing.

6 Conclusion

The present milling reactor has been constructed for two main purposes; – (i) analyse the behaviour of gaseous species that are desorbed or adsorbed from powder hydrides. – (ii) provide an access to kinetic constants which could be determined for the main decomposition-evaporation reactions.

Flow calculations were performed in order to propose a suitable architecture of the whole device (ball-mill, capillary tubing, tubes and pipes systems, effusion cell compartment, pumping system) compatible with the mass spectrometric detection in term of effused flows. Simulate theoretically the flows and define their regimes nature at each stage of the pipes and vessels system. This study highlights also the advantage of using a capillary for the connection between the mill and the spectrometer. Different working pressure conditions are associated its length, meanwhile the diameter choice has been demonstrated to be too sensitive to be varied.

Figure 6.17 shows the final architecture of the coupling of the milling device with the mass spectrometer. Under the present experimental conditions, steady-state flow will depend mainly on the real capacity of the pump and thus will fix the conditions of optimal pressure which can be reached to form an optimized molecular beam. Any upstream pressure fluctuation will be balanced by the evacuating pump in view of decreasing the effusion flow when the molecular beams are strong enough for mass spectrometry analysis. Other practical aspects will appear during our measurements, in particular the high solubility of hydrogen in steel vessels, even if only few effects at low working temperatures are attended. These apparent “leaks” could contribute to a pressure drop in the effusion cell.

The mill-effusion cell reactor is under construction which has required additional work in close cooperation with the technical service of SIMaP laboratory who made the technical set up and much methodological follow-up. The present reactor is complex as shown in figure 6.17, due to its innovative aspect. It will require additional accurate mechanical testing before to be hook-up to the mass spectrometer for safe working under hydrogen.

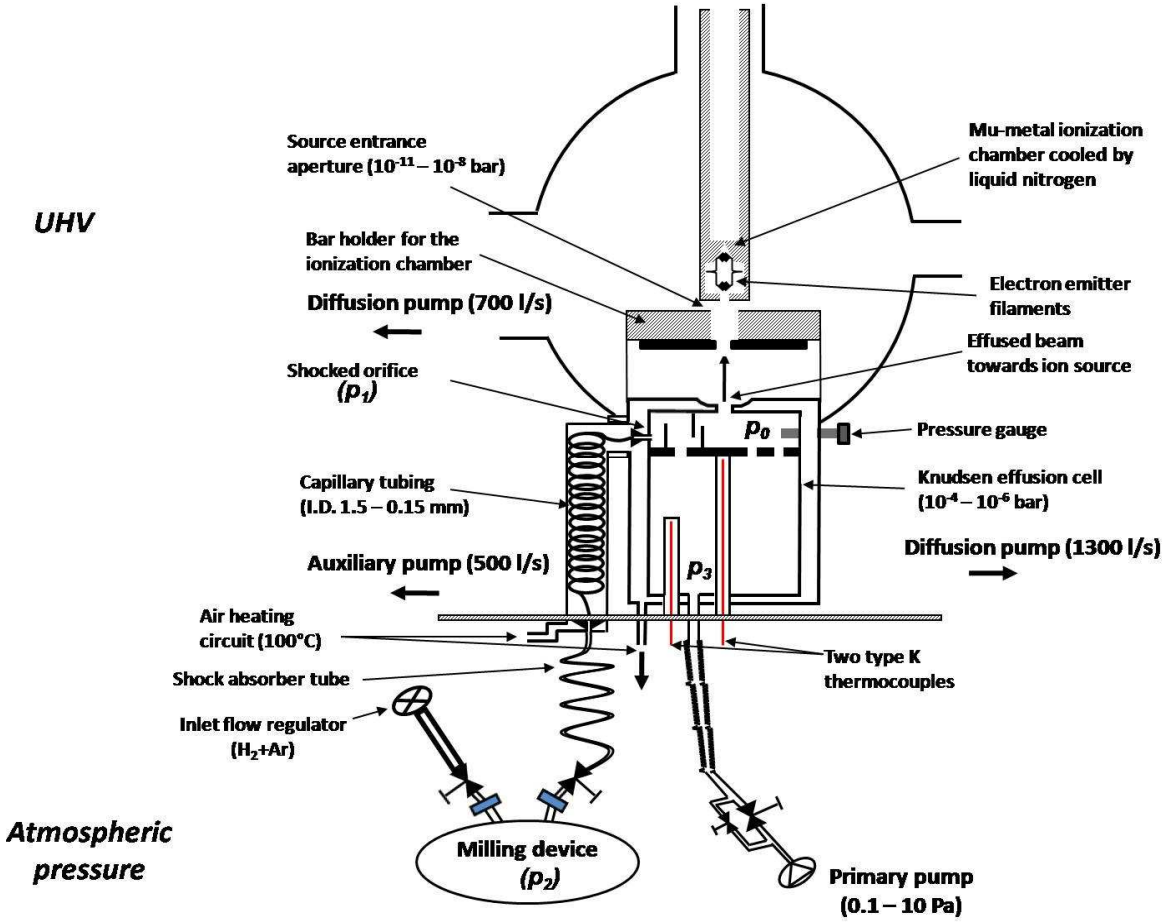

Figure 6.17. Schema of the coupled instruments for mass spectrometry measurements when milling the hydrides

References

[1] U. Bösenberg, S. Doppiu, L. Mosegaard, G. Barkhordarian, N. Eigen, A. Borgschulte, T.R. Jensen, Y. Cerenius, O. Gutfleisch, T. Klassen, M. Dornheim, R. Bormann, Acta Mater. 55 (2007) 3951-3958.
[2] Y.N. Shevchenko, N.N. Mal'tseva, V.A. Nazarenko, N.S. Kedrova, N.T. Kuznetsov, Journal Name: Dokl. Phys. Chem. (Engl. Transl.); (United States); Journal Volume: 290:4-6; Other Information: Translated from Dokl. Akad. Nauk SSSR; 290: No. 4-6, 1426-1430(Oct 1986) (1987) Medium: X; Size: Pages: 968-970.
[3] H.R. Ihle, C.H. Wu, Mass spectrometric Knudsen effusion measurements of vapor species in the lithium-hydrogen system, Proc. Symp. Fusion Technol., 7th Grenoble, EC, Center for Information and Documentation, Luxembourg, 1973, pp. 89-97.
[4] C. Chatillon, Revue de métallurgie(Paris) 95 (1998).
[5] P. Morland, C. Chatillon, P. Rocabois, High Temperature and Materials Science 37 (1997) 167-187.
[6] D. Bianchi, J.-P. Joly, A. Perrard, Le Vide, Science,Technique et Applications 286 (1997) 533-555.
[7] D.J. Santeler, Journal of Vacuum Science & Technology A: Vacuum, Surfaces, and Films 4 (1986) 348-352.
[8] H. Hertz, Ann. Physik. 17 (1882) 177.
[9] P. Clausing, Journal of Vacuum Science and Technology 8 (1971) 636-646.
[10] D.J. Santeler, Journal of Vacuum Science & Technology A: Vacuum, Surfaces, and Films 4 (1986) 338-343.
[11] R.J. Cole, Progress in Astronaut. and Aeronaut. 51 (1976) 261.
[12] R.P. Henry, Cours de science et technique du vide, 1968.
[13] J. Drowart, C. Chatillon, J. Hastie, D. Bonnell, Pure Appl. Chem. 77 (2005) 683-737.
[14] C. Chatillon, M. Heyrman, J. Phys. Chem. Solids 66 (2005) 488-493.
[15] S.F. DeMuth, J.S. Watson, Journal of Vacuum Science & Technology A: Vacuum, Surfaces, and Films 4 (1986) 344-347.

Appendix. *Flow calculation program*

```
'Calcul du flux dans le réacteur d'hydrures complexes'
Public Pi, T, Tc, MM, Pst, Rg, Delta, Nav, Ca, Reff, Leff, Leffeq, Clauseff, Rcell, Lcell, Lcelleq
Public Clauscell, Rcap, Lcap, Lcapeq, Clauscap, Pmoycap, Kncap1, Kncap2, Kncell, Ceff, Ccell
Public Qeff, Qcap, Qpompe, Qtrans, Qmolcell, Qviscell, Qviscap, P1, P2, P0, P01, P0moy, P0max, P0min, DeltaP0, P3
Public lambdacap1, lambdacap2, lambdacell
Public Eta, Kviscap, Kviscell, gamma, rc, Cchoc, Qchoc, Cchocmax, Qchocmax
Public lambdap, Dpompe, ecart1, ecart2, ecart3
Sub variables()

Pi = 3.14159265358979
'Dimensions en MKSA'
Tc = 150
T = 273.15 + Tc 'Temperature en K
Pst = 100000   'Pression standard en Pa (1 bar)
MM = 0.002    'kg pour H2(g)'
gamma = 7 / 5 'gar H2 diatomique
'régime visqueux
Eta = -1.0893 * 10 ^ -11 * T ^ 2 + 2.7796 * 10 ^ -8 * T + 1.59 * 10 ^ -6 'viscosité H2 à T (Pa.s)
Rg = 8.3145 ' constante des gaz parfait
Delta = 2.4 * 10 ^ -10 'diametre H2 en m (ref: CRC)
Nav = 6.02252 * 10 ^ 23 'nombre d'avogadro
Ca = 1.05   'coefficient de Demuth pour le regime de transition (ref: deMuth)

End Sub
Sub constantes()
variables

'Orifice d'effusion
Reff = 0.001  'en m' rayon de l'orifice d'effusion en m
Leff = 0.002  'en m' longueur de l'orifice en m
Leffeq = Leff * (1 + 1 / (3 + (3 * Leff) / (7 * Reff))) 'longueur equivalente orifice - correction de Santeler
Clauseff = 1 / (1 + (3 * Leffeq) / (8 * Reff)) 'coefficient de Clausing de l'orifice d'effusion
Ceff = Clauseff * Pi * Reff ^ 2 / ((2 * Pi * MM * Rg * T) ^ (1 / 2)) ' conductance orifice effusion en flux moleculaire (moles/s)
'cellule d'effusion
Rcell = 0.0125  'rayon DN40 ou DN25 en m'
Lcell = 1  'en m'
Lcelleq = Lcell * (1 + 1 / (3 + (3 * Lcell) / (7 * Rcell))) 'longueur equivalente orifice - correction de Santeler
Clauscell = 1 / (1 + (3 * Lcelleq) / (8 * Rcell)) 'coefficient de Clausing de l'orifice d'effusion
Ccell = Clauscell * Pi * Rcell ^ 2 / ((2 * Pi * MM * Rg * T) ^ (1 / 2)) ' conductance cellule effusion en flux moleculaire (moles/(Pa*s))
'capillaire
Rcap = 0.000075 'rayon en m
Lcap = 3 'longueur en m
Lcapeq = Lcap * (1 + 1 / (3 + 3 * Lcap / (7 * Rcap))) 'longueur equivalente
Clauscap = 1 / (1 + (3 * Lcapeq) / (8 * Rcap)) ' coefficient Clausing
```

```
'regime visqueux dans le capillaire
Kviscap = Pi * (Rcap ^ 4) / (16 * Eta * Lcap * Rg * T) 'conductance visqueuse Ar  en moles/s
'regime visqueux dans la cellule
Kviscell = Pi * (Rcell ^ 4) / (16 * Eta * Lcell * Rg * T) 'conductance visqueuse Ar  en moles/s
'choqué
rc = (2 / (gamma + 1)) ^ (gamma / (gamma - 1))
Cchocmax = (rc ^ (1 / gamma) * (2 * gamma * Rg * T * (1 - rc ^ ((gamma - 1) / gamma)) / ((gamma - 1)
* MM)) ^ (1 / 2)) * Pi * Rcap ^ 2 / (Rg * T) 'Conductance critique choquée sortie cap en moles/(Pa*s)
'Libre parcours moyen pour le regime de transition = Lm * P (en Pa)
lambdap = Rg * T / (2 ^ (1 / 2) * Pi * Delta ^ 2 * Nav)  'libre parcours moyen de H2(en m) = Lambdap /
P (en Pa)

End Sub
Sub cap() 'calcul de la pression en aval du capillaire quand on fixe la pression dans le broyeur
variables
constantes

j = 0
F = 0
Worksheets("feuil2").Cells(1 + F, 1).Value = "P2  (bar)"
Worksheets("feuil2").Cells(1 + F, 2).Value = "P0 cellule (bar)"
Worksheets("feuil2").Cells(1 + F, 3).Value = "P1 (Bar)"
Worksheets("feuil2").Cells(1 + F, 4).Value = "P3 (bar)"
Worksheets("feuil2").Cells(1 + F, 5).Value = "Qcap(mole/s)"
Worksheets("feuil2").Cells(1 + F, 6).Value = "Qchocmax (mol/s)"
Worksheets("feuil2").Cells(1 + F, 7).Value = "Q commerce"
Worksheets("feuil2").Cells(1 + F, 8).Value = "Qpompe"
Worksheets("feuil2").Cells(1 + F, 9).Value = "Qeff"
Worksheets("feuil2").Cells(1 + F, 10).Value = "Ecart2 Flux"
Worksheets("feuil2").Cells(1 + F, 11).Value = "Kn cell "
Worksheets("feuil2").Cells(1 + F, 12).Value = "D m3/h pomp"
Worksheets("feuil2").Cells(1 + F, 13).Value = "Kncap1 "
Worksheets("feuil2").Cells(1 + F, 14).Value = "Kncap2"
Worksheets("feuil2").Cells(1 + F, 15).Value = "ecart1"
Worksheets("feuil2").Cells(1 + F, 16).Value = "Qtrans"
Worksheets("feuil2").Cells(1 + F, 17).Value = "P0moy"
Worksheets("feuil2").Cells(1 + F, 18).Value = "P0min"
Worksheets("feuil2").Cells(1 + F, 19).Value = "P0max"
Worksheets("feuil2").Cells(1 + F, 20).Value = "Qviscell"
Worksheets("feuil2").Cells(1 + F, 21).Value = "Qmolcell"
Worksheets("feuil2").Cells(1 + F, 22).Value = "DeltaP0"

'les pressions sont calculées en Pa'

For i = 6 To 4 Step -0.05 'balayage P2 imposée
P2 = 10 ^ i 'pression au-dessus du broyeur

'P2 = 100000
'Calcul du flux dans capillaire (visqueux+choc)
'For j = 1 To 10000 Step 0.001 'balayage P1
```

```
'P1 = P2 / j
'Qcap = Kviscap * (P2 ^ 2 - P1 ^ 2)
'Qchocmax = P1 * Cchocmax
'ecart1 = Qchocmax - Qcap
'If ecart1 < 0 Then
'GoTo line1:
'End If
'Next j
'line1:
'P1 = P2 / (j - 0.001)

'calcul de p1 pour chaque pression p2 par la formule direct, meme resultat que la boucle ci-dessus désactivée
P1 = Cchocmax * (((1 + ((2 * Kviscap * P2 / Cchocmax) ^ 2)) ^ (1 / 2)) - 1) / (2 * Kviscap)

'For j = 0 To -1 Step -0.25 'balayage de P3 pression à l'entrée de la pompe
Qchocmax = P1 * Cchocmax 'flux critique
Qcap = Kviscap * (P2 ^ 2 - P1 ^ 2)
lambdacap1 = 2 * lambdap / (P1 + P2) 'libre parcours moyen dans le capillaire : entrée du capillaire vu que p1 est faible % p2
lambdacap2 = lambdap / P1          'libre parcours moyen dans le capillaire : sortie du du capillaire
Kncap1 = 2 * Rcap / lambdacap1
Kncap2 = 2 * Rcap / lambdacap2
Qcommerce = 3 * (10 ^ -6) * P2 / (60 * Rg * T) 'valable pour le gaz utilisé au cours des essais : N2 ou air

For k = 2 To -2 Step -0.0001 'balayage P1
P3 = 10 ^ k
If P3 < (1.7838 / 7.027) Then
Dpompe = 0
ElseIf P3 < 1 Then
Dpompe = 7.027 * P3 - 1.7838
Else
Dpompe = 1.4191 * Log(P3) + 6.3424
End If

Qpompe = Dpompe * (P3 / (3600 * Rg * T))
P0max = ((Qpompe / Kviscell) + P3 ^ 2) ^ (1 / 2)
P0min = P3 + (Qpompe / Ccell)
P0moy = (P0max + P0min) / 2

If P3 < 8.375 Then
DeltaP0 = P0max - P0min
Else
DeltaP0 = P0min - P0max
End If

lambdacell = 2 * lambdap / (P0moy + P3)
Kncell = 2 * Rcell / lambdacell
```

```
If Kncell <= 3 Then
P0 = P3 + (Qpompe / Ccell)
ElseIf Kncell > 80 Then
P0 = ((Qpompe / Kviscell) + P3 ^ 2) ^ (1 / 2)
Else: GoTo line4:
End If

GoTo line5:

line4:
For l = (P0moy + DeltaP0) To (P0moy - DeltaP0) Step -0.01
P0 = l
lambdacell = 2 * lambdap / (P0 + P3)
Kncell = 2 * Rcell / lambdacell
Qtrans = Kviscell * ((P0 ^ 2) - (P3 ^ 2)) * (1 - (Ca ^ (-Kncell))) + ((P0 - P3) * Ccell * ((Ca ^ (-Kncell))))
ecart1 = Qtrans - Qpompe
If ecart1 < 0 Then
GoTo line5:
End If
Next l

line5:

'A = Ca ^ (-Kncell)
'B = 1 - A
'P0 = ((((A * Ccell) ^ 2 + 4 * Kviscell * B * (P3 * (Kviscell * B * P3 + A * Ccell) + Qpompe)) ^ (1 / 2)) - A
* Ccell) / (2 * Kviscell * B)
'problem : Kn depend de P0

Qeff = Ceff * P0 'orifice d'effusion
'Condition état stationnaire
ecart2 = (Qpompe + Qeff) - Qcap
If ecart2 < 0 Then
GoTo line3:
End If
Next k

line3:

Qmolcell = (P0 - P3) * Ccell
Qviscell = Kviscell * (P0 ^ 2 - P3 ^ 2)
Qtrans = Kviscell * ((P0 ^ 2) - (P3 ^ 2)) * (1 - (Ca ^ (-Kncell))) + ((P0 - P3) * Ccell * ((Ca ^ (-Kncell))))

F = F + 1
Worksheets("feuil2").Cells(1 + F, 1).Value = P2 / Pst
Worksheets("feuil2").Cells(1 + F, 2).Value = P0 / Pst
Worksheets("feuil2").Cells(1 + F, 3).Value = P1 / Pst
Worksheets("feuil2").Cells(1 + F, 4).Value = P3 / Pst
Worksheets("feuil2").Cells(1 + F, 5).Value = Qcap
Worksheets("feuil2").Cells(1 + F, 6).Value = Qchocmax
```

```
Worksheets("feuil2").Cells(1 + F, 7).Value = Qcommerce
Worksheets("feuil2").Cells(1 + F, 8).Value = Qpompe
Worksheets("feuil2").Cells(1 + F, 9).Value = Qeff
Worksheets("feuil2").Cells(1 + F, 10).Value = ecart2
Worksheets("feuil2").Cells(1 + F, 11).Value = Kncell
Worksheets("feuil2").Cells(1 + F, 12).Value = Dpompe
Worksheets("feuil2").Cells(1 + F, 13).Value = Kncap1
Worksheets("feuil2").Cells(1 + F, 14).Value = Kncap2
Worksheets("feuil2").Cells(1 + F, 15).Value = ecart1
Worksheets("feuil2").Cells(1 + F, 16).Value = Qtrans
Worksheets("feuil2").Cells(1 + F, 17).Value = P0moy / Pst
Worksheets("feuil2").Cells(1 + F, 18).Value = P0min / Pst
Worksheets("feuil2").Cells(1 + F, 19).Value = P0max / Pst
Worksheets("feuil2").Cells(1 + F, 20).Value = Qviscell
Worksheets("feuil2").Cells(1 + F, 21).Value = Qmolcell
Worksheets("feuil2").Cells(1 + F, 22).Value = DeltaP0 / Pst

Next i
End Sub
Static Function Log10(X)
    Log10 = Log(X) / Log(10#)
End Function
```

GENERAL CONCLUSION AND OUTLOOK

Performed in the frame of the European Project “COSY-Project”, this work is a multidisciplinary study of hydrides for application as solid state hydrogen storage materials for industrial and governmental needs. The selected hydride materials have a gravimetric capacity between 7-14% H_2 corresponding, respectively, to the theoretical limits for pure MgH_2 and $LiBH_4$ compounds. Such important densities are the main motivation of the project coming out for vehicles and mobile devices applications. If the hydride materials are compared with pressurized H_2, this last requires tanks with a significant weight and awkward volume. Indeed, the compound $LiBH_4$ has the highest hydrogen capacity: - associated to 3 atoms when taking into account the main decomposition reaction, - and with the presence of Li, the lightest alkali-metal compound, comparing to other hydroborates. Nevertheless, for the understanding of its behaviour in applications, some thermodynamic and kinetic properties remain roughly unknown.

The compound $LiBH_4$ has two polymorphic structures: *ortho*-$LiBH_4$ (low temperature) and *hexa*-$LiBH_4$ (high temperature) with the transformation temperature T_{trs} = 113℃. The existing thermodynamic compiled data (SGTE, JANAF) consider the compound $LiBH_4$ as a single phase without taking into account the hexagonal and the liquid phases. This lack of data had led us to review the thermodynamic properties of this compound (essentially C_p, $\Delta_f H$ and ΔH_{trs}), and to perform vapour pressure measurements by mass spectrometry and Knudsen evaporation method.

To decrease the influence of the kinetics in the desorption process, we have mixed this compound with MgH_2. Hydride powders were reactivated by increasing their specific surface area using high-energy ball milling. We have also used some additives, Ti and Ni-based, in order to enhance the desorption reaction.

Our investigation (chapter 3) started with the study of hydride mixtures MgH_2-x$LiBH_4$ using – (i) a microstructural analysis at different compositions (0<x<3.5), - (ii) an analysis of their thermal behavior (thermal desorption by DTA) up to 500℃. Phases formed during milling or after thermal treatment were analyzed by XRD. The main results are:

- For powders with a crystallite size of 10 nm for MgH_2 and ~20 nm for $LiBH_4$. DTA measurements showed a clear decrease of the temperature of desorption of H_2 which was reduced by about 70℃.
- DSC analysis of the mixture MgH_2-$2LiBH_4$, demonstrated the existence of 4 thermal events where the last one is a two-steps process:

$$2LiBH_4(l) \xrightarrow{endo} 2LiH(s) + 2B(s) + 3H_2(g)$$
$$Mg(s) + 2B(s) \xrightarrow{exo} MgB_2(s)$$

  The existence of MgB_2 has been confirmed by scanning electron microscopy. After heat treatment at 500℃, XRD characterization s hows that the mixture is completely dehydrided with the formation of MgB_2, LiH and the Li-Mg solid solution. This suggests the presence of elemental B in the bulk, probably in amorphous form (no XRD detection).
- The study of the mixtures by DTA at various ratios ($0<x<3.5$) indicates that the melting point of $LiBH_4$ and the desorption temperatures of MgH_2 and $LiBH_4$ decrease by increasing MgH_2 contents. The formation of the phases Li-Mg and MgB_2, seems to depend on the composition. The composition x = 2 remains the most favorable showing a good compromise between hydrogen capacity of the mixture and its desorption temperatures.
- For the composition ratio x = 2 some additives were also tested in order to verify the improvement of the H_2 desorption reaction. Adding Ti-isopropoxide has a clear kinetic effect: a considerable decrease of the temperature of desorption of the mixture of about 70℃. This additive works by means of two components: metal oxide and hydrocarbon. Another additive was retained having a comparable behaviour as Ti-isopropoxide: a Ni based compound : Ni-NiF_2.

Chapter 4 approaches two aspects related to the lack of thermodynamic data in databanks as well as their reliability concerning the $LiBH_4$ compound.

- New calorimetric measurements allowed more refined description of the heat capacity, C_p, namely for the ortho-$LiBH_4$ phase (high temperature). New C_p function has been proposed for the hexagonal phase of this compound. The detected anomaly before phase transition has been considered as independent of the main polymorphous transition and attributed to increasing concentration of crystal defects (in relation with the deformation of the non-cubic lattice).

- On the basis of these new data, a critical assessment was made in order to complete the data banks or earlier compilations (JANAF). New enthalpies of the phase transition and of melting of the compound have been proposed. Gibbs energy function was derived, by means of CALPHAD approach, for each phase including the liquid phase. It must be emphasized the importance of these data because, in the case of the solid $LiBH_4$, they correspond to the decrease of the H_2 relative pressure of about 20% comparing to the current data (SGTE, SUB3 database), when considering the main decomposition reaction.

Phases stability and the decomposition reaction have been studied in the Li-B-H system, - (i) by heat treatment and XRD analysis, - (ii) by vapor pressure measurements using High *T* mass spectrometry and Knudsen evaporation method. In the chapter 5 we focused on the search of new gaseous species which could be present when cycling hydrides.

- In the Li-B-H phase diagram, we first focused on the study of the stability of the pseudo-ternary $LiBH_4$-LiH-B to check the main reaction of decomposition by hydrogen evolving. The three-phase system is stable in the *T* range up to 250℃, indicating no appearance of any melting or additional phase. A shift in $LiBH_4$ Bragg peaks was observed which is linked to the increase in defects or hypo-stoichiometry in agreement with our C_p measurements. The $B_{cry} \rightarrow B_{am}$ transformation probably takes place after annealing. Above the melting of $LiBH_4$, the liquid volume formation is more pronounced for B-rich samples. Two Bragg peaks have been also indexed for the phase $LiBH_2$ "boryl lithium", the crystal structure of which being issued from *ab-initio* calculations.
- An experimental work by mass spectrometry was undertaken in order to confirm or deny the presence of new gaseous species when evaporating $LiBH_4$ compound. The measurements carried out up to 205℃ show that H_2 is the major species with low concentrations of H, BH_3 and B_2H_5. BH_3 species were detected only when using a milled sample and at 205℃. At the temperature of study (100-205℃), B_2H_6 is thermodynamically more stable than BH_3. Even if B_2H_6 would have higher vapour pressure, its presence in our case is difficult to confirm due to an overlapping with molecular mass of N_2 found in high quantities in the background atmosphere of the mass spectrometer. The ion $B_2H_5^+$ could come from the dissociative ionisation of B_2H_6. Without any significant mass loss up to 205℃, we could not calibrate the mass spectrometer quantitative pressure data.

- Using a conventional Knudsen cell in a high *T* reactor, we have obtained total pressure data for the solid phase in the *T* up to 255℃. The melting of $LiBH_4$ under dynamic vacuum is accompanied by an overflowing, probably related to the presence of a sudden gas phase due to decomposition. The pressure over the liquid was evaluated in a sealed ampoule using a volumetric method. The sudden increase of the pressure over the liquid compared to the solid phase indicates limiting evaporation kinetics. By calculating the Motzfeldt evaporation coefficient, the very low value suggests that this kinetics could not be related to usual surface effects, but related to H_2 diffusion through surface layers of different composition such as LiH and/or B formed by decomposition of $LiBH_4$.

Chapter 6 presents a laboratory project related to the construction of a mechano-chemical milling-reactor system coupled to the mass spectrometer. This coupling has the goal to perform direct pressure measurements under milling effect for both H_2 desorption and absorption of hydride materials involving limited kinetics where the reaction rate can be enhanced by milling. The major challenge was how to perform the coupling between the output tube of the mill at "atmospheric pressure" and a specifically designed effusion cell "under high vacuum" for measurement of flow (and pressure) by the mass spectrometer. The connection will be through a capillary tube where the design of the experimental architecture is based on gas flow calculations. The calculations showed that the milling device will afford upward pressures from 0.1 to 2.5 bar with a standard capillary tube of 3 m length and 0.15 mm diameter. The mill is surrounded by a compartment for hot air circulation that enables *T* work of 100-250℃. The cell contains also a connected outer envelope for hot air circulation (*T* up to 150℃ at least to avoid water condensation). The re actor will require more technical testing and the set-up of pressure gauges - upward the capillary and downward the effusion cell - for steady flow calibration of the mass spectrometer in the presence of an additional pumping system for the evacuation of the excess flow from the effusion cell.

TITLE / TITRE

COMPLEX SOLID STATE REACTIONS FOR ENERGY EFFICIENT HYDROGEN STORAGE

ETUDE DES REACTIONS COMPLEXES EN PHASE SOLIDE POUR LE STOCKAGE D'HYDROGENE

ABSTARCT

Hydrides for solid-state hydrogen storage are one of the future solutions - pollutant free - for the storage and the transport of energy. Among the candidates, $LiBH_4$ was selected considering its high gravimetric hydrogen capacity (up to 13.6 wt.% H_2). This material has thermodynamic and kinetic properties insufficiently established to be included in future applications. Its decomposition can be facilitated within the presence of the hydride MgH_2. Thus, the composite MgH_2-$xLiBH_4$ ($0< x< 3.5$) reactivated by high energy ball-milling, was studied regarding its microstructural properties and stability of the phases. The desorption reaction of hydrogen, with or without additives, shows the appearance of additional phases accompanying the principal reaction. Heat capacity measurements of $LiBH_4$ revealed the presence of an abnormal behaviour before the polymorphous transition (T_{trs} = 386 K), attributed to the increase of crystal defects in agreement with the existence of a hypo-stoichiometric domaine $LiBH_{4-\varepsilon}$ observed at higher temperatures. The stability of the three-phase system $LiBH_4$-LiH-B was studied resulting to the principal reaction of decomposition: $LiBH_4(s,l) \rightarrow LiH(s) + B(s) + 1{,}5H_2(g)$. Vapour pressure measurements of $LiBH_4$ showed that H_2 is the major component of decomposition with minor species such as B_2H_6 and BH_3. The thermodynamic properties of $LiBH_4$ were critically assessed, gathering the new data with those existing in the literature, in the aim of modelling of reactions occurring in hydride mixtures.

***KEYWORDS**:* Hydrides Solid-State Reactions ; High Energy Ball-Milling ; Phases Stability ; Vapour Pressure Measurements ; Thermodynamic Properties

RESUME

Le stockage d'hydrogène en phase solide sous forme d'hydrures, est l'une des solutions non-polluantes futures pour le stockage et le transport de l'énergie. Parmi les matériaux candidats, $LiBH_4$ a été sélectionné vu sa capacité gravimétrique élevée en hydrogène (jusqu'à 13,6 % H_2 en masse). Ce matériaux possède des propriétés thermodynamiques et cinétiques insuffisamment établies pour comprendre son comportement dans les applications futures. Sa décomposition peut être facilitée en présence de l'hydrure MgH_2. Ainsi, le composite MgH_2-$xLiBH_4$ ($0<x<3{,}5$) réactivé par broyage à bille de haute énergie, a été étudié en terme de propriétés microstructurales et stabilité des phases. La réaction de désorption d'hydrogène, avec ou sans additifs, montre l'apparition de phases supplémentaires accompagnants la réaction principale. Des mesures de capacité calorifique du composé $LiBH_4$ ont révélés la présence d'une anomalie avant la transition de phase polymorphique (T_{trs} = 386 K), attribuée à l'augmentation de défauts dans le réseau cristallin en accord avec l'existence d'un domaine hypo-stœchiométrique $LiBH_{4-\varepsilon}$ observé à plus haute température. La stabilité du système triphasé $LiBH_4$-LiH-B a été étudiée et cette stabilité confirme la réaction principale de décomposition: $LiBH_4(s,l) \rightarrow LiH(s) + B(s) + 1{,}5H_2(g)$. Des mesures de pression de vapeur de $LiBH_4$ ont montré que H_2 est la composante majoritaire de décomposition avec des espèces mineures telles que B_2H_6 et BH_3. Une évaluation critique des propriétés thermodynamiques du composé $LiBH_4$ a été menée, incluant ces nouvelles données à celles issues de la littérature, dans le but de modéliser les réactions se produisant dans les mélanges d'hydrures.

MOTS-CLES: Réactions en Phase Solide des Hydrures ; Broyage à Bille de Haute Energie ; Stabilité des Phases ; Mesures de Pression de Vapeur ; Propriétés Thermodynamiques